Technische Universität München
TUM School of Engineering and Design

Prediction of Flame Dynamics and Thermoacoustic Interactions in Partially Premixed Combustors

Alexander Josef Eder

Vollständiger Abdruck der von der TUM School of Engineering and Design der Technischen Universität München zur Erlangung des akademischen Grades eines

DOKTORS DER INGENIEURWISSENSCHAFTEN
(DR.-ING.)

genehmigten Dissertation.

Vorsitz:
        Prof. Dr.-Ing. Harald Klein
Prüfende der Dissertation:
        1. Prof. Wolfgang Polifke, Ph.D.
        2. Senior Lecturer Dr. Andrea Giusti
        3. Hon.-Prof. Dr. Bruno Schuermans

»The work may be hard, and the discipline severe; but the interest never fails, and great is the privilege of achievement.«

— John Strutt, 3rd Baron Rayleigh, 1884

»One never notices what has been done; one can only see what remains to be done.«

— Marie Curie, 1894

»Wer es einmal soweit gebracht hat, daß er nicht mehr irrt, der hat auch zu arbeiten aufgehört.«

— Max Planck, 1922

»Life is like riding a bicycle. To keep your balance you must keep moving.«

— Albert Einstein, 1930

»Only those who dare to fail greatly, can ever achieve greatly.«

— John F. Kennedy, 1966

Abstract

Thermoacoustic combustion instabilities remain a significant challenge for the development of reliable, low-emission gas turbines. Predicting these self-excited instabilities requires thorough understanding of the interactions between unsteady heat release rate, acoustics, flow and mixture perturbations as well as entropy waves. This publication-based thesis aims to enhance the comprehension of flame dynamics and thermoacoustic interactions in technically relevant configurations, particularly partially premixed combustors. To this end, experimental post-processing techniques based on acoustic measurements and low-order network models are developed to enable a consistent prediction of flame dynamics, high-fidelity simulations with subsequent system identification are performed to predict the flame and entropy response, and an analytical framework is proposed to explain the underlying physics of entropy wave generation.

The state-of-the-art post-processing approach for determining the flame dynamics experimentally fails when being applied to test rigs with complex features, such as acoustic cross-communication bypassing the flame or an area contraction at the combustor outlet. To address this limitation, a novel method is developed that combines reactive transfer matrix measurements of the entire combustor with an accurate low-order network model of the rest rig. The Rolls-Royce scaled acoustic rig for low-emission technology (SCARLET), operated under realistic engine conditions, is used to demonstrate the capabilities of this physics-based method.

Furthermore, it is demonstrated that acoustic wave propagation in large eddy simulation (LES) is not relevant for the system identification (SI) of premixed flame dynamics. Specifically, the flame response, described in terms of the flame transfer function (FTF), can be accurately predicted without explicitly modeling the acoustic-flame interaction, i.e., by utilizing incompressible LES. This approach exhibits several advantages over their compressible counterpart, particularly in terms of the identification procedure and computational requirements.

In addition, the evaluation of the entropy transfer function (ETF) at various positions within the combustion chamber sheds light on the convective dispersion of entropy waves, revealing significant amplitudes at the combustor exit. By separating the entropy responses to equivalence ratio and velocity fluctuations utilizing multiple-input single-output (MISO) identification, the dominance of equivalence ratio fluctuations in this process is found, which aligns with the existing literature. It is demonstrated that entropy waves can even be generated in fully premixed combustors, specifically through wall heat losses resulting from unsteady heat transfer, but surprisingly also through the differential diffusion of hydrogen. To further investigate the generation of entropy waves, a consistent derivation of its analytical terms based on an arbitrary Lagrangian-Eulerian (ALE) framework is proposed.

Kurzfassung

Die Vorhersage thermoakustischer Verbrennungsinstabilitäten, die nach wie vor eine große Herausforderung für die Entwicklung zuverlässiger und emissionsarmer Gasturbinen darstellen, erfordert ein tiefgreifendes Verständnis der Wechselwirkungen zwischen instationärer Wärmefreisetzung, Akustik, Strömungs- und Mischungsstörungen sowie Entropiewellen. Die vorliegende publikationsbasierte Arbeit zielt darauf ab, das Verständnis der Flammendynamik und der thermoakustischen Wechselwirkungen in technisch relevanten Konfigurationen, insbesondere in technisch vorgemischten Brennkammern, zu verbessern. Zu diesem Zweck werden unter anderem experimentelle Post-Processing Routinen auf der Grundlage von akustischen Messungen und Netzwerkmodellen niedriger Ordnung entwickelt, um eine konsistente Vorhersage der Flammendynamik zu gewährleisten. Des Weiteren werden hochauflösende Simulationen mit anschließender Systemidentifikation durchgeführt, um die Flammen- und Entropieantworten vorherzusagen. Abschließend wird ein analytisches Framework vorgeschlagen, um die zugrundeliegende Physik der Entropiewellenerzeugung zu erklären.

Der gängigste Ansatz zur experimentellen Bestimmung der Flammendynamik erweist sich bei der Anwendung auf Prüfstände mit komplexen Elementen wie zusätzlichen akustischen Kommunikationspfaden oder einer Flächenkontraktion am Brennkammerauslass als unzureichend. Um dieser Einschränkung zu begegnen, wird eine neue Methode entwickelt, die Messungen der Übertragungsmatrix unter reaktiven Bedingungen mit einem Netzwerkmodell niedriger Ordnung kombiniert. Zur Verifikation der vorgeschlagenen Methode wird das Rolls-Royce Scaled Acoustic Rig for Low Emission Technology (SCARLET) unter realistischen Triebwerksbedingungen eingesetzt.

Des Weiteren wird dargelegt, dass die Ausbreitung akustischer Wellen in der Grobstruktursimulation (LES) für die anschließende Systemidentifikation (SI) der Dynamik vorgemischter Flammen ohne Relevanz ist. Es wird aufgezeigt, dass die Flammenantwort in Form einer Flammentransferfunktion (FTF) auch ohne der expliziten Modellierung der Akustik-Flamme-Interaktion akkurat vorhergesagt werden kann. Der inkompressible Simulationsansatz weist gegenüber seinem kompressiblen Äquivalent mehrere Vorteile hinsichtlich der Identifikation und der Anforderungen an den Berechnungsprozess auf.

Die Auswertung der Entropietransferfunktion (ETF) an verschiedenen Positionen innerhalb der Brennkammer erlaubt zudem Einblicke in die konvektive Dispersion der Entropiewellen und zeigt signifikante Amplituden am Brennkammerauslass. Die Trennung der Entropieantworten auf Schwankungen des Äquivalenzverhältnisses und der Geschwindigkeit mittels Multiple-Input Single-Output (MISO) Identifikation belegt die Dominanz von Äquivalenzverhältnisschwankungen, was mit der vorhandenen Literatur übereinstimmt. Es wird demonstriert, dass

Entropiewellen selbst in vollständig vorgemischten Brennkammern generiert werden können, insbesondere durch Wandwärmeverluste, die aus instationärem Wärmeübergang resultieren, sowie überraschenderweise auch durch die differenzielle Diffusion von Wasserstoff. Zur weiteren Untersuchung der Entstehungsmechanismen von Entropiewellen wird eine konsistente Herleitung der analytischen Terme auf Grundlage der Arbitrary Lagrangian-Eulerian (ALE) Methode vorgestellt.

Vorwort

It is with great gratitude and pleasure that I look back on the past three years of my doctoral studies in the Thermo-Fluid Dynamics (TFD) group at TUM. This research journey, which was mainly carried out in the framework of the DFG-funded project *NoiSI*, involved fruitful collaborations with Rolls-Royce Deutschland (RRD), the Combustion, Acoustics and Flow Physics (CAPS) Laboratory at ETH Zurich, and the Centre Européen de Recherche et de Formation Avancée en Calcul Scientifique (CERFACS). The successful completion of this project would not have been possible without the support, encouragement, and help of many people. I would like to take this opportunity to express my gratitude to them below.

When I was looking for a suitable position as research associate towards the end of my Master's degree, the most important factor for me was to find an exciting research topic. During my time in the TFD group, however, I realized that one thing is even more important than an exciting topic to work on: the supervisor. Wolfgang, I couldn't have found a better "Doktorvater" than you! Thank you for trusting me with this project, for always showing great interest in my research, for giving me the freedom to develop my own ideas, and providing me with feedback and advice whenever it was required (even the day before a paper deadline). Your respectful nature paired with high scientific standards for yourself and your group make you a very inspiring personality. I'm also grateful to Prof. Harald Klein for chairing the examination, and Dr. Andrea Giusti and Prof. Bruno Schuermans for reviewing my thesis.

I would further like to thank André Fischer, Claus Lahiri, Max Stauffer, and Ruud Eggels from Rolls-Royce Deutschland. Working with you guys has been a pleasure, and I really enjoyed the friendly working environment you created right from the beginning. I am also grateful for the opportunity to visit the RRD facility in Dahlewitz and the test rig located at the German Aerospace Center (DLR) in Cologne and for giving me an insight into the daily challenges of engineers in industry (which is a whole new world next to academia). I would also like to thank Prof. Nicolas Noiray, Prof. Bruno Schuermans, Audrey Blondé, and Bayu Dharmaputra from the CAPS lab for the fruitful collaboration, the invitation to visit your lab, and the support throughout the project. A special thanks goes to Bayu, my experimental counterpart working on entropy waves, for numerous discussions and constructive feedback. I am also indebted to CERFACS, particularly Laurent Gicquel, Gabriel Staffelbach, and Olivier Vermorel, for making the LES solver AVBP available at TUM and for providing HPC support. Also, thanks to everyone who helped me to get into AVBP quickly by answering my (hopefully not too stupid) questions, especially Thomas Lesaffre and Eléonore Riber. It was also a great opportunity to present the TFD group's research at the first AVBP User's Committee in Toulouse. I'm also very grateful to Prof. Matthew Juniper, who welcomed me to the University of Cambridge for a research stay at the end of my doctoral project. Cambridge is a very picturesque and inspiring

place and I am very glad that I had the opportunity to work there. Special thanks to Matthew Yoko and Alexandros Kontogiannis for making my time abroad (and in the gym) so enjoyable.

Being part of a research group with an excellent reputation in the international research community and the aforementioned trust of Wolfgang in my work allowed me to participate in numerous workshops, meetings, and conferences in Switzerland, Germany, USA, France, England, and Italy. During these trips, I had some very enriching experiences and discussions, such as with Prof. Thierry Poinsot, whom I would like to thank for a helpful clarification on combustion modeling during the Advanced Low NOx and Hydrogen Combustion Technologies Workshop in Florence, which solved a crucial problem in my simulations. Furthermore, Prof. Sébastien Candel, for his insightful comment after my talk at the Symposium on Thermoacoustics in Combustion in Zurich, where he pointed out that *»it is nice that someone shows what all is a problem«*. This further motivated my critical thinking in (not only) science-related topics. I would also like to thank Prof. Thierry Schuller and his colleagues at the Institut de Mécanique des Fluides de Toulouse (IMFT) for showing me a "real" flame during the Hydrogen Week in Toulouse - a rare experience for someone working primarily with numerical simulations.

I will never forget my time in the TFD group and thank my companions. From proofreading my papers and providing feedback during the rehearsal before conferences to engaging in enriching coffee kitchen discussions and hours of whiteboard sessions, your contributions have been instrumental. Special mention, Camilo F. Silva – the one who knows (almost) everything about thermoacoustics – for being a true mentor from day one. Writing nine (!) papers together says it all. I have really learned a lot from you, and not just scientifically. Also, Sagar Kulkarni and Philip Bonnaire, with whom I had a great time sharing offices, TFD-alumni Luis Tay-Wo-Chong, who shared his knowledge on the LES/SI methodology with me during several visits, Marcel Désor, with whom I collaborated a lot and who helped me with everything related to high performance computing and compilers, Moritz Merk, who shared his analytical and mathematical skills with me, which led to two joint first author papers, Korbinian Niebler, my desired successor for the course Simulation of Thermofluids with Open Source Tools (which I taught for six semesters), Axel Zimmermann and Marcin Rywik, it was a pleasure to generate gigabytes (when not terabytes) of data for your machine learning activities – keyword: data generation center –, Philipp Brokof, with whom I had twice-a-year Engineering Thermodynamics exam correction sessions that felt like a day off, Alex García, who helped me with questions related to chemical kinetics and with whom I spent hours discussing system identification, Edoardo Scoletta, who answered questions pertaining to hydrogen combustion at a time when I had no clue what its particularities were, Guillaume Fournier, who taught me the first steps in taX and made me a "TikZ figure advocate", Matthias Häringer, who taught me the basics and practical use of large eddy simulation and system identification in the first few months after I joined the TFD group, Grégoire Varillon, who put relentless efforts in combating any cake-supply-disruption (CSD), and Joachim Ottinger and Marian Hiestermann, my Santa Claus colleagues at our contemplative Einstandsfeier – none of our Einstandsfeiern would have been possible without the help of Jens Hümmer and the remaining workshop crew.

A research group cannot run smoothly without a well-functioning secretariat. Many thanks to Helga Bassett and Brigitte Blume for your great work, for your patience in explaining how to fill out the (frequently changing) forms correctly, for handling the mail, and for your daily support in all other organizational matters, including many formalities after submitting my thesis, and to Sigrid Schulz-Reichwald, who was a great help in all financial aspects of the project.

Munich, June 2024   Alexander J. Eder

Acknowledgment

Contents

List of Figures

Nomenclature

Roman letters

A, B, C, D, F	Polynomial filters [-]
B	Burner transfer matrix [-]
c	Speed of sound [m s^{-1}]
c_p	Isobaric heat capacity [J kg^{-1} K^{-1}]
$\mathcal{E}$	Entropy transfer function [-]
e	Additive disturbance/noise [-]
f, g	Acoustic wave amplitudes [-]
$\mathcal{F}$	Flame transfer function [-]
F	Flame transfer matrix [-]
G	Transfer function [-]
g	Impulse response [-]
J	Cost function [-]
L_j	Acoustic energy loss process [-]
p	Pressure [kg m^{-1} s^{-2}]
$\dot{Q}$	Heat release rate [W m^{-3}]
q	Shift operator [-]
R	Specific gas constant [-]
s	Sensible-plus-chemical entropy [J kg^{-1} K^{-1}]
T	Transfer matrix [-]
T	Temperature [K]
t	Time [s]
u	Flow velocity [m s^{-1}]
V	Volume [m^3]
x	Position vector [m]
x	Input [-]
y	Output [-]

Greek letters

α, β	Arbitrary scalars [-]
γ	Ratio of specific heats [-]

$\boldsymbol{\Theta}$	Parameter vector [-]
ϕ	Equivalence ratio [-]
ρ	Mass density [kg m^{-3}]
σ	Entropy wave amplitude [-]
τ	Time delay [s]
ω	Angular frequency [Hz]

Superscripts

$\overline{(\cdot)}$	Mean quantity
$(\cdot)'$	Fluctuating quantity
$(\cdot)^{-1}$	Inverse quantity
$\hat{(\cdot)}$	Predicted quantity

Subscripts

$(\cdot)_{\mathrm{ex}}$	Excitation
$(\cdot)_{\mathrm{ref}}$	Reference position
$(\cdot)_u$	Response to velocity fluctuations
$(\cdot)_\phi$	Response to equivalence ratio fluctuations

Dimensionless numbers

He	Helmholtz number
Le	Lewis number
Ma	Mach number

Abbreviations

ALE	Arbitrary Lagrangian-Eulerian
ARC	Analytically reduced chemistry
ARMAX	AutoRegressive Moving Average model with eXogenous inputs
ARX	AutoRegressive model with eXogenous input
BFTM	Burner-flame transfer matrix
BTM	Burner transfer matrix
CBSBC	Characteristics-based state-space boundary condition

CFD	Computational fluid dynamics
CFL	Courant-Friedrichs-Lewy condition
DNS	Direct numerical simulation
FDF	Flame describing function
FFT	Fast Fourier transform
FIR	Finite impulse response
FTF	Flame transfer function
FTM	Flame transfer matrix
ETF	Entropy transfer function
EWG	Entropy wave generator
ITA	Intrinsic thermoacoustic
LDI	Lean direct injection
LES	Large eddy simulation
LOM	Low-order model
LTI	Linear time-invariant
LPP	Lean premixed prevaporized
LQL	Lean-quench-lean
MBI	Model-based inference
MIMO	Multiple-input, multiple-output
MISO	Multiple-input, single-output
NGV	Nozzle guide vane
NSCBC	Navier-Stokes characteristic boundary condition
ODE	Ordinary differential equation
PDE	Partial differential equation
PRBS	Pseudo-random binary signal
Q1D	Quasi-one-dimensional
RANS	Reynolds-averaged Navier-Stokes
RQL	Rich-quench-lean
SAF	Sustainable aviation fuel
SCARLET	Scaled acoustic rig for low emission technology
SGS	Sub-grid scale
SI	System identification
SISO	Single-input single-output
SNR	Signal-to-noise ratio
TDIBC	Time-domain impedance boundary condition
TDLAS	Tunable diode laser absorption spectroscopy
URANS	Unsteady Reynolds-averaged Navier-Stokes
WMS	Wavelength modulation spectroscopy
xFDF	Extended flame describing function

1 Introduction

1.1 Gas turbines: Bridging energy needs and climate goals

One of the greatest challenges that humanity has to confront in the 21st century is climate change, with the overarching goal of halting global warming. As Kofi Annan aptly stated [52], *»[t]he world is reaching the tipping point beyond which climate change may become irreversible. If this happens, we risk denying present and future generations the right to a healthy and sustainable planet – the whole of humanity stands to lose.«*. To avoid reaching such a tipping point, the Paris Agreement [322] was signed by 195 parties, including 194 countries and the European Union, at the 2015 United Nations Climate Change Conference near Paris. The agreement sets a global goal to limit the rise in global mean temperature to "well below" 2 °C above pre-industrial levels, with efforts to limit the increase to 1.5 °C. Fig. 1.1 highlights the substantial rise in the annual mean temperature in Bavaria relative to the reference period from 1961 to 1990 [60]. This visual representation underscores the pressing necessity for climate change mitigation stipulated in the Paris Agreement. Reducing emissions is a key measure in this regard. As Emmanuel Macron [199] exaggeratedly stated in a speech before the Congress of the United States of America: *»[b]y polluting the oceans, not mitigating CO_2 emissions and destroying our biodiversity, we are killing our planet. Let us face it: there is no Planet B.«*. To escape from this "spiral of death", the design, development, deployment, and use of technologies aimed at reducing or suppressing pollutant emissions and utilizing fuels that enable a lower or even zero CO_2 footprint, will have a significant impact and help achieve the targeted goals of the Paris Agreement. In this context, it is essential to improve combustion technologies to
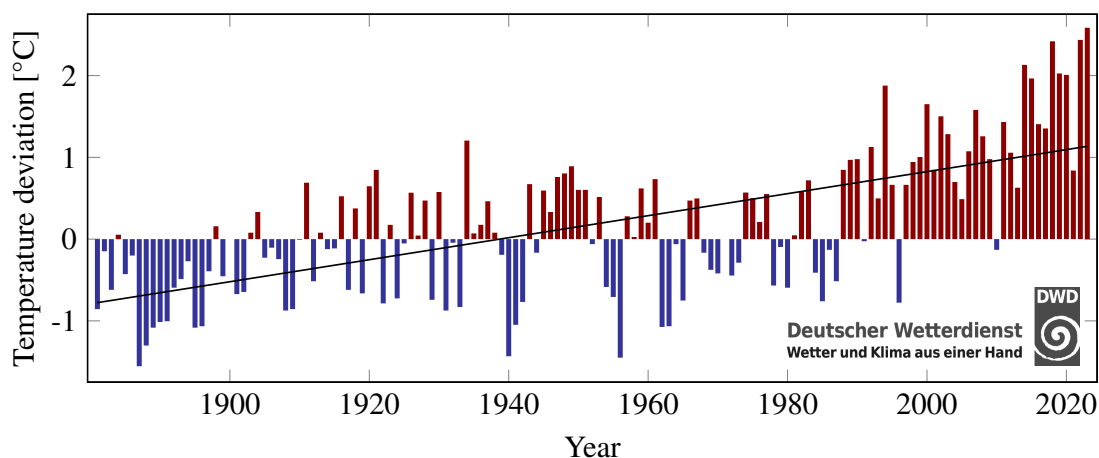
Figure 1.1: Positive (——) and negative (——) deviation of the annual mean temperature in Bavaria compared to the multi-annual mean of the reference period 1961-1990 (7.5 °C) and the linear trend between 1881 and 2023 (——, +1.9 °C). Data adopted from [60].

reduce their environmental impact in terms of emissions, as approximately 45 percent of these emissions (around 15 billion tons of CO_2) originate solely from the combustion of hydrocarbon fuels in the power generation and aviation sectors [148, 265]. It is anticipated that combustion devices, such as land-based gas turbines[1] and aero-engines, remain indispensable systems in the aforementioned sectors in the (near) future. Land-based gas turbines, for example, are expected to play a pivotal role in stabilizing the electrical grid by counterbalancing the unsteadiness in the supply of renewable energy sources [149]. They also offer solutions for storing excess energy through power-to-gas technologies [122]. For short- to long-haul civil aircraft (approximately 97 % of the industry's CO_2), as well as military aircraft in general, alternatives such as batteries or fuel cells are not (yet) viable [4]. Consequently, advancements in combustion technology are critical for the future of power and aviation industries, ensuring that humanity can meet energy needs while minimizing environmental impact.

Achieving low emissions and identifying novel pathways to cleaner combustion technologies are thus essential milestones in developing future gas turbines. These objectives can be accomplished through modifications to combustor[2] concepts and architectures, including lean direct injection (LDI) [306], lean premixed prevaporized (LPP) [146], and lean-quench-lean (LQL) as the successor of rich-quench-lean (RQL), as well as the adoption of alternative, *non*-fossil fuels, such as sustainable aviation fuels (SAF), hydrogen, and ammonia. Some of these novel combustion technologies, when employed in isolation or combination, are susceptible to thermoacoustic combustion instability [42, 163, 191, 194, 242, 314], which necessitates extensive basic and applied research, including experimental, numerical, and analytical approaches.

Thermoacoustic combustion instability is a self-excited instability that arises when constructive coupling between unsteady heat release rates and the acoustic field of the combustor leads to the production of acoustic energy of a rate that exceeds the dissipation of acoustic energy. Lord Rayleigh formulated this in his groundbreaking work in 1878 as follows [260]: *»If heat be periodically communicated to, and abstracted from, a mass of air vibrating (for example) in a cylinder bounded by a piston, the effect produced will depend upon the phase of the vibration at which the transfer of heat takes place. If heat be given to the air at the moment of greatest condensation, or taken from it at the moment of greatest rarefaction, the vibration is encouraged. On the other hand, if heat be given at the moment of greatest rarefaction, or abstracted at the moment of greatest condensation, the vibration is discouraged.«*. Thermoacoustic combustion instability is characterized by very large amplitudes of pressure oscillations (on the order of 10^5 Pa) and by pronounced peaks at one (or several) distinct frequencies, as shown in Fig. 1.2 for an aero-engine gas turbine combustor. This undesirable phenomenon can restrict operational flexibility and performance (e.g., through a limited operating range or reduced combustion efficiency [206]), increase heat load on the combustor liner (e.g., through flame impingement at the walls [76]), contribute to the formation of pollutants such as unburned hydrocarbons, carbon monoxide, and nitrogen oxides (e.g., through incomplete combustion), and, in extreme cases, may result in the immediate destruction of individual components or the entire system [68, 190, 242], as illustrated in Fig. 1.3. Preventing thermoacoustic combustion instability is therefore crucial to ensure the reliability and efficiency of advanced combustion systems.

---

[1]in the following, "gas turbine" is used as a generic term to refer to land-based (heavy-duty, industrial, aero-derivative) as well as aircraft gas turbine engines (i.e., turbojet and turbofan engines)

[2]"Combustor" means in the present thesis the whole unit between the compressor and turbine stages, including burner and combustion chamber.
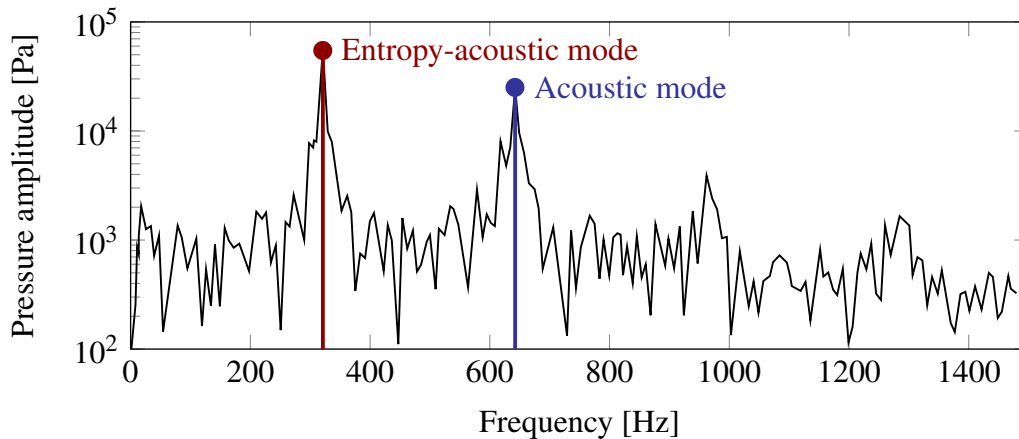
Figure 1.2: Typical spectrum of the pressure amplitude monitored at the outlet of an aero-engine gas turbine combustor during a thermoacoustic combustion instability. Data adopted from [220].

Multiple interaction mechanisms may be responsible for this constructive feedback. In addition to the "classical" feedback between acoustic waves and unsteady combustion that arises when pressure and heat release rate fluctuations are in phase [49, 192, 260] (see the second peak in Fig. 1.2), another potential driver of thermoacoustic instability in technically relevant configurations (i.e., upstream flow <u>and</u> mixture perturbations) is the presence of coherent temperature inhomogeneities in the burnt gas, which are commonly referred to as "hot spots", "entropy spots", or *entropy waves* [163, 252]. These inhomogeneities are typically generated in the flame region[3] and subsequently convect through the combustor. In gas turbines, entropy waves are accelerated in the turbine nozzle guide vane (NGV) succeeding the combustion chamber and are thereby converted to acoustic waves [163]. Some of these acoustic waves leave the combustor, contributing to the overall noise emissions [68, 145, 218]. However, some propagate back, interact with the fuel injection system and produce flow and mixture perturbations. These further perturb the flame heat release rate, as evidenced by the first peak in Fig. 1.2, thus closing a feedback loop. Each of the two mechanisms - the acoustic and the "mixed" entropy-acoustic (a third type will be introduced in Sec. 2.2) - can result in unstable modes, as demonstrated in [220] and shown in Fig. 1.2. Both the response of fluctuations in heat release rate and burnt gas temperature are therefore subsumed under the term *flame dynamics* in the present thesis. The development of predictive tools to mitigate thermoacoustic combustion instability in gas turbines necessitates a comprehensive understanding of both responses.

1.2 The scope and structure of this thesis

Since the early 1960s, extensive research has been conducted on thermoacoustic combustion instability, initially driven by the NASA Apollo program during the Cold War. The "Moon Race", sparked by John F. Kennedy's 1962 speech at Rice University with the historic words [166] *»[w]e choose to go to the moon in this decade«*, led among others to the pioneering develop-

---

[3]even if, in certain configurations, additional contributions may also arise from the dilution with cold air [220]

(a) New burner assembly   (b) Damaged burner assembly
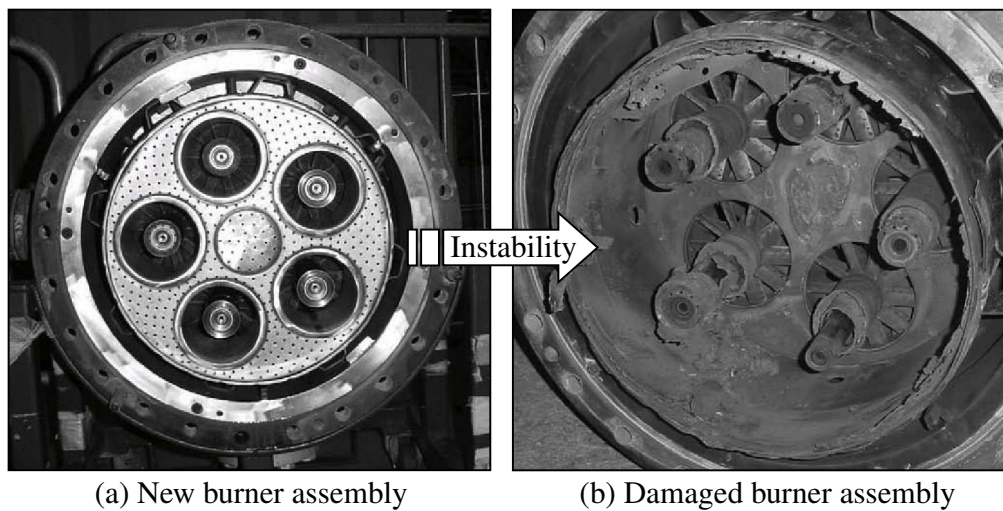
Figure 1.3: Burner assembly of a gas turbine combustor before and after an excessive thermoacoustic combustion instability [123]. Photos adopted from [140].

ment of the F-1 engine powering the Saturn V - an engine very susceptible to combustion instability [230]. Despite the long history of continued basic and applied research, thermoacoustic combustion instability remains a significant challenge in developing reliable, low-emission gas turbines. On the one hand, basic research is essential for understanding this self-excited instability, a complex phenomenon requiring knowledge from multiple disciplines, including thermodynamics, combustion fundamentals, fluid dynamics, and (thermo)acoustics. On the other hand, applied research is crucial because this instability is *»pathologically sensitive to very small design changes«* [98], making it unique to each burner and combustion chamber geometry. Consequently, predicting thermoacoustic combustion instability reliably in practical combustion devices remains challenging, with the earliest indications often emerging during full combustor or engine tests, typically in the late phase of an engine development program. Therefore, a thermoacoustic design process for aero-engine burners[4] has been proposed recently to confront this issue [99], schematically shown in Fig. 1.4. This process employs a two-step strategy: first, the flame dynamics is estimated and second, the acoustic field produced by the flame is assessed, taking into account the reflection of acoustic waves by the flame's enclosure. This is achieved through the use of a thermoacoustic solver. Theoretical considerations and derivations based on first principles or analytical models for flame dynamics are generally not applicable to such "real-world" problems [11, 33, 70, 186, 273, 278]. Consequently, (single-sector) measurements and simulations are required to estimate reduced-order models of flame dynamics, subsequently used for the stability prediction in thermoacoustic solvers. If the burner design is found to be stable, it advances to multi-sector or engine testing. Conversely, if the burner design is unstable, it is iterated. Therefore, there is a growing interest in developing flexible, consistent, and accurate tools for predicting flame dynamics with the objective of optimizing stability margins at an early stage of the design process. This is where the present work comes into play.

Large parts of this thesis originate from the joint DFG transfer project[5] *"NoiSI"* between the

---

[4]"Burner" means in the present thesis the upstream unit comprising swirler, fuel injectors, mixing tube and flame holder.

[5]DFG describes their transfer projects as follows [59]: *»Knowledge transfer funding options are intended to*
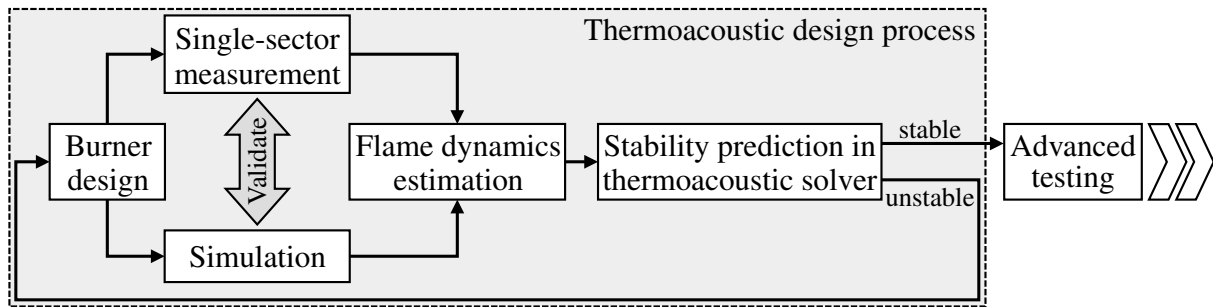
Figure 1.4: Principle of the thermoacoustic design process for an aero-engine burner. Based on [99]. Courtesy of Dr. André Fischer.

industrial partner Rolls-Royce Deutschland Ltd & Co KG (RRD) and the Thermo-Fluid Dynamics Group at the Technische Universität München (TUM). This joint project was complemented by informal collaborations with the Combustion, Acoustics and Flow Physics (CAPS) Laboratory at the ETH Zurich, and the Centre Européen de Recherche et de Formation Avancée en Calcul Scientifique (CERFACS) in Toulouse. The NoiSI project (acronym for **Noi**se + **S**ystem **I**dentification) was funded by the Deutsche Forschungsgemeinschaft and dealt with the dynamics of partially premixed[6] flames, particularly spray flames - the type of combustion in gas turbines.

The objective of the research described in this publication-based thesis is to enhance the comprehension of flame dynamics and thermoacoustic interaction mechanisms in technically relevant configurations. This is achieved by investigating both the flame <u>and</u> entropy response. In collaboration with RRD, the *flame response* was estimated experimentally and numerically in their high-pressure, liquid fuel test rig SCARLET, which houses an engine-like combustor powered by a full-scale burner. This project initially suffered from long computation times and problems with acoustic excitation in the compressible large eddy simulation (LES), resulting in unusable data for the subsequent system identification (SI). In PAPER-FTF [82] it was demonstrated that the acoustic wave propagation in the simulation is not relevant for the identification of premixed flame dynamics and therefore an incompressible formulation was used in the further course of this project. A conference paper [81] revealed significant discrepancies between experimental and numerical results in the flame response of SCARLET that could not be attributed solely to incorrect (or inaccurate) simulation results. The PAPER-MBI [84] showed that the state-of-the-art experimental post-processing approach is not valid for realistic configurations with test sections representing engine-like combustors. This thorough analysis led to the development and validation of a generalized, consistent framework for determining the flame response based on acoustic measurements and a low-order network model of the test rig. Together with the CAPS Laboratory, the *entropy response* was determined experimentally and numerically in their laboratory-scale, gaseous fuel combustor. Their novel laser-based measurement technique used in this rig was the first to measure entropy transfer functions over a wide frequency range, making them the perfect collaborators in this project. The dominance

---

support work on scientific questions in collaboration with an application partner (commercial enterprise or a non-commercial, non-profit institution) in the pre-competitive area. The aim is to apply the scientific findings and results generated by basic research. The projects are also expected to provide an impetus for pursuing new scientific questions in basic research.«

[6]also referred to as "technically premixed" or "practical premixed" in the literature

of equivalence ratio fluctuations was confirmed in PAPER-PP [83] (where CERFACS provided the software together with technical support for the high-fidelity simulations) by separating the entropy response to equivalence ratio and velocity perturbations using multiple-input single-output identification. In a subsequent measurement campaign at the CAPS Laboratory, "non-negligible" entropy wave generation was observed under fully premixed conditions, i.e., in the absence of global equivalence ratio fluctuations. The PAPER-FP [80] precisely addressed this finding using LES together with system identification and was able to confirm that unsteady wall heat transfer due to the massive water cooling of the combustor metal frame was the dominant source of entropy wave generation. Surprisingly, local variations in the equivalence ratio and local segregation of fuel components due to differential diffusion of hydrogen were found to be a second mechanism generating entropy waves in fully premixed flames. The PAPER-ALE [213] explains in detail the underlying physics of entropy wave generation using an analytical framework that allows the isolated analysis of the corresponding source terms.

This manuscript is intended to provide context and establish connection between the included papers, using the following structure: Chapter 2 provides a concise overview of the physical and theoretical background essential to grasp the essence of this thesis. It introduces the thermoacoustic feedback loops in a gas turbine combustor and elucidates the interaction mechanisms that drive thermoacoustic combustion instability. Since three papers, namely PAPER-FTF [82], PAPER-PP [83] and PAPER-FP [80], use system identification to estimate flame dynamics from time series generated with large eddy simulation, Chapters 3 and 4 are devoted to SI and LES, respectively. After that, in Chapter 5, a detailed cross-thematic discussion places the papers that comprise this thesis in the context of the existing literature, followed by an outlook in Chapter 6. Finally, Chapter 7 summarizes the five selected peer-reviewed papers included in this thesis.

2 A few (more) words about thermoacoustic combustion instability

This chapter provides a concise overview of thermoacoustic combustion instability, focusing on the underlying principles and mechanisms that drive such instability. The interconnection of these mechanisms is explored, highlighting the complex dynamics within gas turbine combustors. Recommended literature includes the Hyoit C. Hottel lecture by Candel [36] on the progress and challenges of thermoacoustic combustion instability and its control methods. For fundamentals, see the series of six lectures on thermoacoustic combustion instability by Polifke [248]. The doctoral thesis by Schuermans [271] offers insights into modeling and control, while the books by Lieuwen and Yang [192] and Culick [49] delve into the underlying physics of thermoacoustic combustion instability in technically relevant combustion systems. A comprehensive review of prediction and control is given by Poinsot [242].

2.1 Higgins, Rijke, Rayleigh and beyond

In 1777[1], Byron Higgins confined a small hydrogen flame in a tube, which produced *»very clear sounds«* depending on the tube's geometry: the phenomenon of a "singing flame" was discovered [131]. Higgins may have been the first to recognize that heat energy can be converted into acoustic oscillations. In 1859, Pieter Rijke placed a heated wire grid at a quarter of the length of an open vertical tube, observing a loud sound as long as the tube remained open [264]. Around a century after Higgins' observations, Lord Rayleigh developed a theory to explain this phenomenon [260, 261]. His words quoted in Chapter 1 are widely known as *Rayleigh's criterion*, which states that the unsteady flame adds energy to the acoustic field when the heat release rate $\dot{Q}'(\mathbf{x}, t)$ is in phase with the pressure $p'(\mathbf{x}, t)$ at the location of the heat source [260]. The criterion implies that the smaller the phase difference between the pressure and the heat release fluctuation rate, the greater the energy added to the instability. Mathematically, this is expressed as an integral in time and space:

$$\int_V \int_T p'(\mathbf{x}, t)\, \dot{Q}'(\mathbf{x}, t)\, \mathrm{d}t\mathrm{d}V > 0\,. \tag{2.1}$$

This expression describes *»conditions under which unsteady heat release adds energy to the acoustic field. However, even if energy is transferred from the combustion process to the acoustic field, this does not necessarily imply that the combustor is unstable«* [334]. An instability can only develop if the driving mechanisms are larger than the rate at which acoustic energy is dissipated due to the losses and damping mechanisms present in each *confined* combustion

---

[1]His work of 1777 was first recorded in 1802 [131].

system. Zinn and Lieuwen [334] summarize this inequality as follows:

$$\underbrace{\int_V \int_T p'(\mathbf{x}, t) \dot{Q}'(\mathbf{x}, t) \, \mathrm{d}t \mathrm{d}V}_{\text{Driving of oscillations}} \geq \underbrace{\int_V \int_T \sum_j L_j(\mathbf{x}, t) \, \mathrm{d}t \mathrm{d}V}_{\text{Damping of oscillations}}, \qquad (2.2)$$

with the acoustic energy loss processes L_j, such as vortex shedding (i.e., conversion of acoustic energy into vorticity) [18, 137], transmission of acoustic waves which then radiate to the environment [68], viscous and thermal dissipation of acoustic energy due to boundary layers [280], and passive damping devices such as bias flow liners [87, 183] or Helmholtz resonators [21, 72]. Equation (2.2) highlights that the potential for a thermoacoustic combustion instability fundamentally concerns the balance between driving and damping mechanisms.

2.2 Thermoacoustic feedback loops in a combustor

In gas turbine combustors, several driving mechanisms coexist and are interrelated. Depending on the underlying geometry of the system and the operating condition, either one or several mechanisms can drive thermoacoustic combustion instability, as already shown in Fig. 1.2. Before discussing the interaction mechanisms and the resulting feedback loops, it is necessary to define acoustic and entropy waves. Generally, both types of waves are small perturbations of flow variables traveling in a gaseous medium. Such flow variables can be separated into a time-invariant mean component, denoted as $\overline{(\cdot)}$, and a superimposed fluctuating component, denoted as $(\cdot)'$, where the amplitude of linear perturbations is small relative to the mean quantity,

$$p(\mathbf{x}, t) = \overline{p}(\mathbf{x}) + p'(\mathbf{x}, t), \qquad (2.3)$$

$$u(\mathbf{x}, t) = \overline{u}(\mathbf{x}) + u'(\mathbf{x}, t), \qquad (2.4)$$

$$s(\mathbf{x}, t) = \overline{s}(\mathbf{x}) + s'(\mathbf{x}, t), \qquad (2.5)$$

with the flow velocity u and the sensible-plus-chemical entropy s [200, 213]. The flow perturbations can be expressed as a combination of acoustic waves and entropy waves, where the
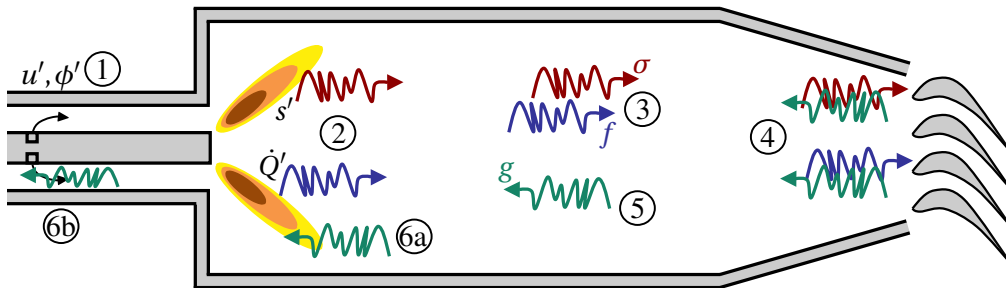
Figure 2.1: Schematic representation of acoustic wave propagation and entropy wave convection in a typical gas turbine combustor with succeeding nozzle guide vane (NGV). The upstream part of the burner has been omitted for clarity. (1) Flow and mixture perturbations, (2) generation of acoustic/entropy waves, (3) propagation of acoustic waves/transport of entropy waves, (4) transmission/reflection of acoustic waves/conversion of entropy waves to acoustic waves, (5) upstream propagation of acoustic waves, (6a) interaction of acoustic waves with flame, (6b) interaction of acoustic waves with fuel injection.

former propagate upstream and downstream, at speeds $\bar{c} + \bar{u}$ and $\bar{c} - \bar{u}$, respectively, while the latter are convected downstream with the mean flow velocity $\bar{u}$. A schematic of the propagation of acoustic waves and convection of entropy waves in a typical combustor is given in Fig. 2.1. The characteristic amplitudes of these waves can be related to the flow perturbations via

$$ f \equiv \frac{1}{2}\left(\frac{p'}{\overline{\rho c}} + u'\right), \qquad g \equiv \frac{1}{2}\left(\frac{p'}{\overline{\rho c}} - u'\right), \qquad \sigma \equiv \frac{1}{\gamma}\frac{p'}{\overline{p}} - \frac{\rho'}{\overline{\rho}} = \frac{s'}{c_p}, \qquad (2.6) $$

where γ is the heat capacity ratio, $c = \sqrt{\gamma R T}$ (with the specific gas constant R and the temperature T) is the speed of sound, ρ is the density, and c_p is the isobaric heat capacity.

In a premixed[2] combustion system such as the schematic in Fig. 2.1, thermoacoustic combustion instability may be classified into the following three types: acoustic, intrinsic thermoacoustic (ITA), and entropy-acoustic ("rumble"). Of these, only the latter involves the generation and convection of entropy waves.

1. *Acoustic*: This type of instability has been studied extensively in the past [36, 192, 242]. The structure of the feedback loop in acoustic-flow-flame interactions is simple: Acoustic waves are generated by the flame through volumetric gas expansion[3] and propagate along and across the combustor until they are transmitted and reflected by the confined environment (e.g., walls, inlet and outlet) depending on the boundary impedance, where the system acoustics controls the phase between velocity and pressure [253]. Subsequently, reflected waves impinge on the flame as well as interact with the fuel injection. In partially premixed flames, where the fuel is injected in close proximity to the burner outlet, the latter interaction results in the generation of spatial mixture inhomogeneities that are convected to the flame and subsequently modulate the heat release rate [141, 193, 268, 273]. This, in turn, generates acoustic waves, thereby closing a feedback loop.

2. *Intrinsic thermoacoustic:* This type of instability has only been discovered in the last decade [46, 89, 91, 134] and recently summarized in a review paper by Silva [285]. The most remarkable feature of ITA instability is that it does not require any confined environment. The ITA feedback loop is described as follows [29]: Acoustic waves are generated by the unsteady combustion process. The *upstream* propagating acoustic waves modulate the velocity immediately upstream of the flame and the equivalence ratio by interacting with the fuel injection, which generates fluctuations of the heat release rate, thereby closing the loop. This instability has not only been identified in premixed flames but also in spray flames [114]. The PAPER-FTF [82] indicates that a pronounced ITA resonance can significantly impair the estimation of flame dynamics.

3. *Entropy-acoustic:* This instability is associated with the feedback loop connecting downstream convecting entropy waves and upstream propagating acoustic waves [163, 164, 252, 268]. Once entropy waves are generated by the flame [283, 298, 301, 304, 323], they are transported (convected and dispersed) by the mean flow toward the exit of the combustor [119, 202, 219, 328] (PAPER-PP [83] and PAPER-FP [80]), where they are accelerated in the nozzle guide vane and thereby converted to acoustic waves [15, 54, 55].

---

[2]is used as a generic term for both "fully premixed" and "partially premixed" in the present work

[3]A perturbed heat source in a gas stream acts as a fluctuating volume source [252].

Some of the acoustic waves generated propagate back towards the flame and the fuel injectors, promoting velocity and equivalence ratio perturbations. These disturbances give rise to the generation of entropy waves in the reactive region, a phenomenon that is investigated in detail in PAPER-PP [83], PAPER-FP [80] and PAPER-ALE [213]. This type of instability is characterized by its low frequency [78, 220, 330]. It should be noted, however, that ITA modes may also occur at similar frequencies that correspond to convective time scales [7, 114, 223]. This potentially makes it more challenging to distinguish between these two types of modes [114].

2.3 Interconnection of mechanisms that drive instability

The interplay between flame, entropy waves, acoustic waves, flow and mixture perturbations described in Sec. 2.2 is shown schematically in Fig. 2.2. This interconnection holds for both fully and partially premixed flames, while the dotted boxes are not active in the case of fully premixed flames, where no fluctuations in the equivalence ratio are present. The transfer behavior of several elements (i.e., boxes) is required to describe how the *response* in terms of fluctuations in heat release rate $\dot{Q}'(\omega)$ and entropy $s'(\omega)$ is related to the fluctuating *signals*, i.e., velocity $u'(\omega)$ and equivalence ratio $\phi'(\omega)$ fluctuations at the burner outlet. Such a transfer behavior is generally described by a frequency-domain transfer function $G(\omega)$, which relates a signal $x(\omega)$ to its response $y(\omega)$, treating the element as a black-box (more details in Chapter 3),

$$y(\omega) = G(\omega)x(\omega) \,, \tag{2.7}$$

Figure 2.2: Interconnection of all relevant physical mechanisms of thermoacoustic combustion instability in a combustor with a partially premixed flame ($\phi' \neq 0$), including propagation (Prop.), transmission (Trans.) and convection (Conv.). The flame dynamics is characterized by individual transfer functions $\mathcal{F}_u(\omega)$ (response of $\dot{Q}'(\omega)$ to $u'(\omega)$), $\mathcal{F}_\phi(\omega)$ (response of $\dot{Q}'(\omega)$ to $\phi'(\omega)$), $\mathcal{E}_u(\omega)$ (response of $s'(\omega)$ to $u'(\omega)$) and $\mathcal{E}_\phi(\omega)$ (response of $s'(\omega)$ to $\phi'(\omega)$), as well as the "overall" transfer functions $\mathcal{F}(\omega)$ (response of $\dot{Q}'(\omega)$ to $u'(\omega)$) and $\mathcal{E}(\omega)$ (response of $s'(\omega)$ to $u'(\omega)$). Based on [255].

where ω is the angular frequency. As proposed by Huber and Polifke [141] for the heat release rate response and in the PAPER-PP [83] for the entropy response, a partially premixed flame may be expressed as a multiple-input multiple-output (MIMO) system as follows

$$\frac{\dot{Q}'(\omega)}{\overline{\dot{Q}}} = \mathcal{F}_u(\omega)\frac{u'_{\text{ref}}(\omega)}{\overline{u}_{\text{ref}}} + \mathcal{F}_\phi(\omega)\frac{\phi'_{\text{ref}}(\omega)}{\overline{\phi}_{\text{ref}}} \,, \tag{2.8}$$

$$\frac{s'(\omega)}{\overline{c}_p} = \mathcal{E}_u(\omega)\frac{u'_{\text{ref}}(\omega)}{\overline{u}_{\text{ref}}} + \mathcal{E}_\phi(\omega)\frac{\phi'_{\text{ref}}(\omega)}{\overline{\phi}_{\text{ref}}} \,, \tag{2.9}$$

where $\mathcal{F}_u(\omega)$ and $\mathcal{F}_\phi(\omega)$ are *flame transfer functions* (FTF) and $\mathcal{E}_u(\omega)$ and $\mathcal{E}_\phi(\omega)$ are *entropy transfer functions* (ETF), representing the individual (flame and entropy) responses to velocity and equivalence ratio perturbations, respectively, at a given reference position (typically the burner outlet). The heat release rate signal is volume-integrated, and the entropy signal is evaluated in the combustion chamber behind the flame, but in front of significant reductions in cross-sectional area, such as end contractions and nozzles. The transfer functions in Eqs. (2.8) and (2.9) are linear descriptions of the transfer behavior and, therefore, only valid in the limit of small perturbations.

In the case of a stiff fuel injection (constant fuel mass flow), velocity fluctuations at the injector caused by modulation of the air mass flow lead to phase-opposite equivalence ratio fluctuations at the injector [194, 235, 252] that are convected in the mixing duct toward the flame [268]. If, in addition to the stiff fuel injection, an acoustically compact mixing duct is present, a single-input single-output (SISO) system can be used to appropriately represent both the "overall" flame and entropy response [141, 319]. These overall responses $\mathcal{F}(\omega)$ and $\mathcal{E}(\omega)$, black-box representations of the gray boxes in Fig. 2.2, are related to the individual transfer functions via

$$\frac{\dot{Q}'(\omega)}{\overline{\dot{Q}}} = \underbrace{\left[\mathcal{H}_\phi(\omega)\mathcal{F}_\phi(\omega) + \mathcal{F}_u(\omega)\right]}_{\mathcal{F}(\omega)}\frac{u'_{\text{ref}}(\omega)}{\overline{u}_{\text{ref}}} \quad \Rightarrow \quad \frac{\dot{Q}'(\omega)}{\overline{\dot{Q}}} = \mathcal{F}(\omega)\frac{u'_{\text{ref}}(\omega)}{\overline{u}_{\text{ref}}} \,, \tag{2.10}$$

$$\frac{s'(\omega)}{\overline{c}_p} = \underbrace{\left[\mathcal{H}_\phi(\omega)\mathcal{E}_\phi(\omega) + \mathcal{E}_u(\omega)\right]}_{\mathcal{E}(\omega)}\frac{u'_{\text{ref}}(\omega)}{\overline{u}_{\text{ref}}} \quad \Rightarrow \quad \frac{s'(\omega)}{\overline{c}_p} = \mathcal{E}(\omega)\frac{u'_{\text{ref}}(\omega)}{\overline{u}_{\text{ref}}} \,, \tag{2.11}$$

with an additional transfer function $\mathcal{H}_\phi(\omega)$ representing the equivalence ratio response to velocity fluctuations at the burner outlet (see [108] for more detail). Equations (2.8) to (2.11) provide a complete description of the dynamics of partially premixed flames.

Once all relevant transfer functions have been determined, a comprehensive thermoacoustic stability analysis can be performed using a thermoacoustic solver, as outlined in Sec. 1.2, particularly Fig. 1.4. Depending on the combustor under investigation, one or more of the three thermoacoustic feedback loops from Chapter 2.1 may be identified: acoustic, ITA, and entropy-acoustic. These feedback loops are all included in the interconnecting network in Fig. 2.2, while the individual loops are extracted and illustrated in Fig 2.3. The differing importance of the upstream and downstream end reflection becomes evident in this context. While the acoustic feedback loop (Fig. 2.3 (a)) is closed by coupling between both boundaries, the entropy-acoustic loop (Fig. 2.3 (c)) requires only the downstream end for the entropy-acoustic conversion. As mentioned above, the ITA loop (Fig. 2.3 (b)) is independent of the boundary impedance.

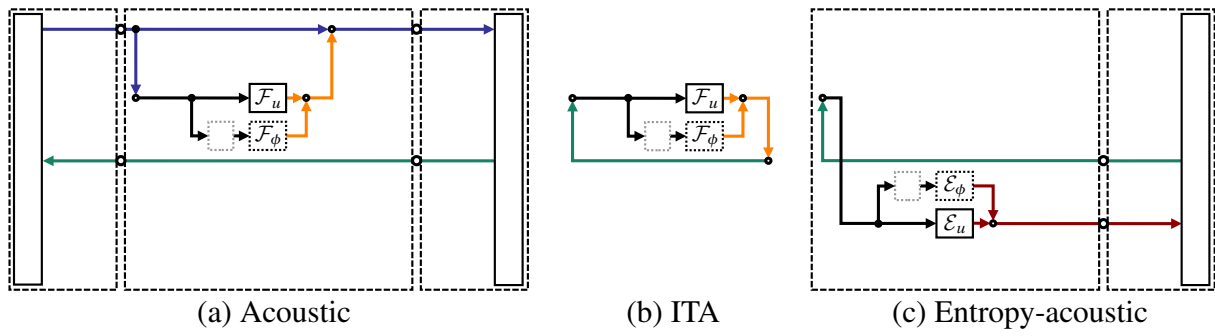(a) Acoustic   (b) ITA   (c) Entropy-acoustic

Figure 2.3: Network model representation of the essential interaction mechanisms of three types of thermoacoustic combustion instabilities. See Fig. 2.2 for a complete understanding of this figure. Based on [255].

3 System identification of LTI models

The black-box representation of flame dynamics introduced in Chapter 2 can be estimated using system identification. Keesman [162] defined the overarching objective of SI as *»the construction of mathematical models of the system under study based on noisy time series«*. In this context, "mathematical models" refer to "transfer functions", such as those introduced for the identification of flame dynamics in Eqs. (2.8) to (2.11). Nevertheless, the application of system identification methods is by no means limited to the latter. This chapter presents background information on dynamic systems, as illustrated in Fig. 3.1, and the modeling of the same, focusing on models used in the field of flame dynamics. For simplicity, only single-input single-output systems, such as those described by Eqs. (2.10) and (2.11), are discussed. However, extending this discussion to multiple-input single-output (MISO) or even multiple-input multiple-output systems is relatively straightforward due to the linearity of the problem [102, 295], which has been elucidated in the literature on reheat flames, for example [31, 269]. More detailed information on all aspects of system identification can be found in the books by Söderström and Stoica [291], Ljung [195], Keesman [162], and Tangirala [307].

3.1 Characterization of LTI systems

It is well known that a *causal*, *linear*, *time-invariant* (LTI) system such as the one shown in Fig. 3.1 (a) can be described by the following convolution integral [195]

$$y(t) = \int_0^\infty g(\tau)x(t-\tau)d\tau \, , \tag{3.1}$$

where $g(\tau)$ essentially characterizes how the system responds to a unit impulse at time τ, and the integral represents how the system responds to the entire input signal $x(t)$ over time. In general, a system is …

… *causal* if the output signal $y(t)$ at any given time depends solely on the values of the input signal at the present and past times $x(t-\tau)$, not on future values of the latter [307]. Mathematically, a system is causal if $y(t) = \mathrm{f}(x(t))$, $t \geq t_0$ implies $y(t) = \mathrm{f}(x(t))$, $t < t_0$, where t_0 is the present time.

… *linear* if it obeys the principle of superposition [162]. Mathematically, a system can be treated linear if it satisfies $\alpha x_1(t) + \beta x_2(t) = \alpha y_1(t) + \beta y_2(t)$, with two different input signals $x_1(t)$ and $x_2(t)$, two different output signals $y_1(t)$ and $y_2(t)$, and arbitrary scalars α and β. If a system is linear, its behavior can be entirely characterized by time delays (or its impulse response).
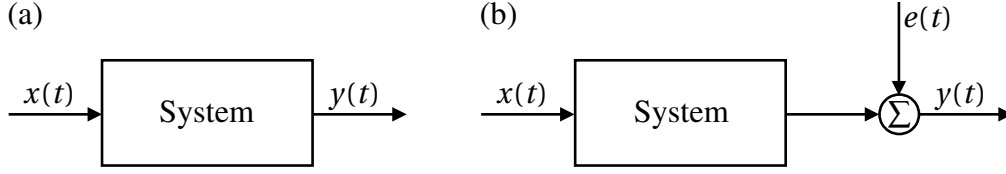
Figure 3.1: A system characterized as a black-box with a scalar input signal $x(t)$ and a scalar output signal $y(t)$ (a) without and (b) with an additive disturbance signal $e(t)$.

> … *time-invariant* if its behavior does not change over time. This implies that if the input signal is delayed or advanced in time, the output signal will also be delayed or advanced by the same amount, and the system's response will remain unaltered [162]. Mathematically, a system is time-invariant if $y(t) = \mathrm{f}(x(t))$ implies $y(t - \tau) = \mathrm{f}(x(t - \tau))$ for any linear function $\mathrm{f}(\cdot)$.

In practice, when dealing with sampled data, a *discrete*-time representation of Eq. (3.1) is typically employed [195],

$$y(t) = g(0)x(t) + g(1)x(t-1) + \ldots + g(N)x(t-N) = \sum_{k=0}^{N} g(k)x(t-k)\,, \tag{3.2}$$

where N is the number of sampled data points. By applying the backward shift operator q^{-k} to the input signal [162],

$$q^{-k}x(t) = x(t-k)\,, \tag{3.3}$$

the input-output system behavior, i.e., its dynamics, can be written as

$$y(t) = G(q)x(t)\,, \tag{3.4}$$

with the impulse response function (or transfer operator) $G(q)$,

$$G(q) = \sum_{k=0}^{N} g(k)q^{-k}\,. \tag{3.5}$$

Note that the frequency response function $G(\omega)$ in Eq. (2.7) corresponds to the z-transform (the equivalent of the Laplace transform for discrete-time systems [253]) of the impulse response function $G(q)$ in Eq. (3.5),

$$G(\omega) = \sum_{k=0}^{N} g(k)\exp(-i\omega k\Delta t)\,, \tag{3.6}$$

where Δt is the sampling interval and i is the imaginary unit. This mutual transformation also applies to the flame and entropy transfer functions in Eqs. (2.8) to (2.9) [247]. Given the existence of disturbances, such as turbulent noise in combustors [210, 211], it can be postulated that Eq. (3.4) may not provide an adequate representation of such a system. Therefore, an additive noise term $e(t)$ is included in Fig. 3.1 (b). The input-output behavior of the noise contribution is described by its own impulse response function $H(q)$, leading to the most general description of a SISO system:

$$\underbrace{y(t)}_{\text{Response}} = G(q)\underbrace{x(t)}_{\text{Signal}} + H(q)\underbrace{e(t)}_{\text{Noise}}\,. \tag{3.7}$$

A proper estimation of the impulse response functions $G(q)$ and $H(q)$ in Eq. (3.7) requires robust system identification methodologies, which typically encompass the following three steps [153].

1. Acquisition or generation of time series data that represents the input-output behavior of the system (more detail in Chapter 4).

2. Selection of a suitable model structure that captures the essential dynamics of the system. This model structure contains unknown parameters that need to be determined.

3. Estimation of the unknown model parameters by solving an optimization problem that minimizes the discrepancy between the model predictions and the observed data.

3.2 Selection of model structure

Expanding the impulse response functions $G(q)$ and $H(q)$ in Eq. (3.7) by means of polynomial filters, the most general model structure of a rational polynomial model reads [195]

$$A(q,\Theta)y(t,\Theta) = \underbrace{\frac{B(q,\Theta)}{F(q,\Theta)}}_{G(q,\Theta)} x(t) + \underbrace{\frac{C(q,\Theta)}{D(q,\Theta)}}_{H(q,\Theta)} e(t) , \qquad (3.8)$$

where $A(q,\Theta)$, $B(q,\Theta)$, $C(q,\Theta)$, $D(q,\Theta)$ and $F(q,\Theta)$ are polynomial filters, e.g.,

$$B(q) = b_0 + b_1 q^{-1} + \cdots + b_{n_b} q^{-n_b} , \qquad (3.9)$$

and Θ is a parameter vector containing the individual model coefficients such as $b_0,\ldots,b_{n_b}$, which are the prior *unknown* parameters. The employed set of polynomial filters determine specific model structures. Various models, such as the AutoRegressive model with eXogenous input (ARX) ($C(q,\Theta) = D(q,\Theta) = F(q,\Theta) = 1$), Output-Error (OE) ($A(q,\Theta) = C(q,\Theta) = D(q,\Theta) = 1$), AutoRegressive Moving Average model with eXogenous inputs (ARMAX) ($D(q,\Theta) = F(q,\Theta) = 1$), and Box-Jenkins ($A(q,\Theta) = 1$) are available to identify LTI systems and are special cases of Eq. (3.8). The finite impulse response (FIR) model structure is the simplest of this family of models, achieved by setting all filters except $B(q,\Theta)$ to unity:

$$y(t,\Theta) = B(q,\Theta)x(t) + e(t) . \qquad (3.10)$$

Here, the output $y(t)$ is estimated solely based on the convolution of the input $x(t)$ with the model coefficients $\Theta = \{b_0,\ldots,b_{n_b}\}$. A good estimate of the impulse response function $G(q,\Theta)$ can often be obtained with a small number of coefficients [249]. It is important to note that the trivial noise model $H(q,\Theta) = 1$ is used in this formulation, meaning no noise model is identified. The additive noise contribution $e(t)$ is assumed to be Gaussian white noise, a simplification that does not hold for turbulent flows in combustors. Indeed, turbulent noise is known to be colored noise [128, 172]. This erroneous assumption, i.e., assuming that turbulent noise is Gaussian white noise instead of colored noise, introduces a bias even in the filter $B(q,\Theta)$ [153, 210]. Nevertheless, in the context of limited time series length, which is typically the case in high-fidelity simulations, the results of the FIR and, for example, more advanced Box-Jenkins models

are comparable in terms of accuracy [153]. In this case, the identification error due to finite time series length dominates the bias introduced by the neglect of a proper noise model in FIR [209]. Consequently, the FIR model is widely used to estimate the flame dynamics [31, 81, 106–108, 142, 147, 171, 180, 274, 311, 329, 333] as well as in PAPER-FTF [82], PAPER-PP [83] and PAPER-FP [80].

3.3 Estimation of model parameters

The optimal values of the FIR coefficients $\mathbf{\Theta} = \{b_0, ..., b_{n_b}\}$ can be determined by solving a least-squares optimization problem [195]:

$$\hat{\mathbf{\Theta}} = \min_{\mathbf{\Theta}} J(\mathbf{\Theta}) = \min_{\mathbf{\Theta}} \frac{1}{N} \sum_{i=0}^{N} \left(y(t_i) - \hat{y}(t_i, \mathbf{\Theta}) \right)^2 , \qquad (3.11)$$

where $\hat{\mathbf{\Theta}}$ is the identified parameter vector, $J(\mathbf{\Theta})$ is the cost function to be minimized, y is the observed output signal, and $\hat{y}$ is the predicted output by the model. The estimation of the impulse response model using the FIR model structure (Eq. (3.10)) can be implemented by utilizing, for example, the `impulseest` function of the MATLAB® System Identification Toolbox™ [196] or the `impulseest` Python package [97].

4 Generation of time series data using large eddy simulation

The system identification methodology described in Chapter 3 is a *data-driven* approach to identifying the dynamics of LTI systems. Therefore, this approach - nowadays categorized as a form of *supervised learning* - requires the generation of input-output data in a preliminary step. In the special case of identifying the flame dynamics given in Eqs. (2.10) to (2.11) for combustor stability prediction, reactive computational fluid dynamics (CFD) simulations are most often performed to generate the required data set. Given that CFD is employed in the data generation step of SI (see Chapter 3 for the subsequent steps), this approach is commonly referred to as CFD/SI [247]. In the case of large eddy simulation being the preferred CFD method, one refers to LES/SI. For clarification, CFD/SI is *not* a hybrid method in the sense that CFD and SI are coupled during the simulation. Instead, CFD is first performed with a properly designed excitation time signal, then system identification is applied (see the three steps in Sec. 3.1).

In such data-driven approaches, the accuracy and reliability of the predicted models are ultimately contingent on the quality of the underlying data. There is a suitable phrase for this in computer science, namely "garbage in, garbage out". Using the example of the flame transfer function $\mathcal{F}(\omega)$ in Eq. (2.10), this means the following: Both the time series data of the velocity fluctuations at a reference position u'_{ref} (input signal) and the heat release rate fluctuations $\dot{Q}'$ (output signal) must be extracted from CFD. This data is then further used as input to a system identification model for estimating the FTF, such as the FIR model structure in Eq. (3.10). Consequently, if the CFD data is *poor*, the identified flame dynamics model will also be *poor*.

As a numerical method, CFD discretizes the Navier-Stokes equations, a set of partial differential equations (PDE) describing the motion of viscous fluid [95]. Typical physical and numerical assumptions made in CFD include the following [2, 75]: Newtonian fluid (i.e., shear stress is proportional to shear rate), ideal gas (i.e., no inter-particle interactions), Arrhenius model (i.e., reaction rate depends exponentially on temperature), zero body forces, zero external heat sources, and the Boussinesq approximation (i.e., density variations are only significant in the buoyancy term). There are three prominent strategies to handle the Navier-Stokes equations, namely Reynolds-averaged Navier-Stokes (RANS), direct numerical simulation (DNS), and large eddy simulation. These strategies differ mainly in how they treat (i.e., resolve or model) the different scales of turbulent structures and in the associated computational demands. On the one hand, RANS and URANS (unsteady formulation of RANS equations), which model all turbulent scales, are not sufficiently accurate to simulate the dynamics of flames [116, 147, 312]. On the other hand, DNS, which solves the full Navier-Stokes equations and resolves all scales of turbulence down to the Kolmogorov scale, remains impractical and unfeasible for flame dynamics identification, even for simple laboratory configurations. LES, which has been used

extensively in the scope of this doctoral project [57, 63, 80–83, 308], can be seen as the best of both worlds (RANS and DNS), where the governing equations are spatially filtered similarly to RANS [240, 244]. However, in contrast to RANS, the additional non-linear terms in the filtered LES equations refer only to the small-scale turbulent structures, which, according to Kolmogorov's theory of turbulence [168, 169], are more universal (i.e., less dependent on the geometry) and are therefore not resolved but modeled with subgrid-scale (SGS) models. Examples of such models include wall-adapting local eddy viscosity (WALE) [224], which is used in PAPER-FTF [82] and PAPER-FP [80], and SIGMA [227], which is used in the PAPER-PP [83]. The large turbulent scales, which are highly dependent on the flow problem itself, are resolved by LES without further modeling, similar to DNS. This should ensure the generation of *high-quality* input-output data, which in turn should facilitate the identification of *high-quality* models.

4.1   Large eddy simulation of premixed combustion

As mentioned above, combustion LES is the "unavoidable" tool for data generation within the LES/SI approach. Such data-driven modeling necessitates the acquisition of long time series (in the order of 10^2 ms), requiring the computational effort to be reduced as much as possible. To achieve this, global reaction mechanisms or analytically reduced chemistry (ARC) can be employed instead of detailed chemical kinetics [107]. Furthermore, the unity Lewis assumption for hydrocarbon combustion (Le = 1) [244] and simplified species diffusion instead of multi-component diffusion for hydrogen-enriched combustion (Le_i = const.) can be used. In addition, second-order accuracy in time and space is preferred over higher-order schemes [247], and, where feasible, the use of an incompressible flow model can further reduce computational demands [246]. Polifke's review paper [247] on CFD/SI provides additional best practice recommendations. In summary, the requirements for a combustion LES in the context of LES/SI may be slightly lower than those for "classical" investigations, emphasizing efficiency over accuracy.

4.1.1   Compressible and incompressible LES formalism

This section provides a concise technical comparison of two classes of LES formalism: compressible and incompressible (also known as "low Mach"). The compressible formalism can be further distinguished as time-implicit compressible (i.e., full compressible equations are solved implicitly to remove Courant-Friedrichs-Lewy (CFL) constraints) and time-explicit or fully compressible, where both account for acoustic wave propagation. The latter is the main difference to the incompressible formulation, where acoustics are removed from the governing equations. For a more detailed description of the difference between incompressible and implicit/explicit compressible see the review paper on LES of gaseous flames by Gicquel *et al.* [118]. Both formalism can be used for determining the dynamics, i.e. the FTF or flame describing function (FDF), of acoustically-compact, velocity-sensitive flames [82], although the use of incompressible LES may seem counterintuitive due to the neglect of acoustic wave propagation. A comprehensive discussion of the validity of incompressible LES for the identification of premixed flame dynamics is given in Sec. 5.2.

In the absence of acoustic waves, considerations about the finite speed of sound propagating through the fluid become superfluous. Velocity perturbations resulting from dilation mechanisms, such as thermal expansion due to heat release, are transported instantaneously, equivalent to an infinite speed of sound. Consequently, acoustic velocity perturbations upstream of the flame propagate infinitely fast from the inlet to the base of the flame, where they are convected along the flame. The resulting fluctuations in the heat release rate are thus interpreted as the flame's response to flow perturbations. It is crucial to note that solely purely axial perturbations are transported infinitely fast, while radial (perpendicular to the main flow) or azimuthal (around the flow axis) perturbations, as well as scalar quantities like temperature, are still convected, as they would be in a compressible LES. In addition to the physical distinctions, the assumption of incompressible flow may be less computationally demanding [174] and can significantly simplify the numerical setup since no *acoustic* boundary conditions are required in comparison to their compressible counterpart.

4.1.2 Acoustic boundary conditions for compressible LES

Giauque *et al*. [116] noted that *»the exact numerical procedure to introduce acoustic waves in a computation is a difficult topic and may lead to numerical artifacts«*. Consequently, a proper definition of inlet and outlet boundaries is crucial in compressible LES to accurately resolve the reflection and transmission of acoustic waves. Reflections can reduce the signal-to-noise ratio (SNR) and cause system resonances that corrupt the identification procedure. Consequently, sophisticated acoustic boundary conditions to mitigate such corruption have been developed since the 1990s [51, 152, 156, 197, 243, 254]. The Navier-Stokes characteristic boundary conditions (NSCBC) [243] utilized in PAPER-PP [83], necessitate the adjustment of model parameters, such as relaxation coefficients. This process is time-consuming and may require several iterations of trial and error. Additionally, NSCBCs are only partially non-reflective and even fully reflective at low frequencies [254, 282]. In contrast, time-domain impedance boundary conditions (TDIBC) [66, 152, 321], such as the characteristics-based state-space boundary conditions (CBSBC)[1] [152], employed in PAPER-FTF [82], offer full control over boundary impedances, aiding in finding a combination of inlet and outlet reflection coefficients that ensures a thermoacoustically stable system. It is important to note that acoustic impedance is an arbitrary quantity for identifying flame dynamics, with the sole restriction being that it assures thermoacoustic stability in the computational domain. While these boundary treatments typically control *longitudinal* modes, PAPER-FTF [82] introduces a methodology for mitigating self-excited *transverse* modes (a frequent problem in compressible LES [113, 129, 281, 311]), where the outlet formulation of CBSBC (with a reflection coefficient close to unity) is imposed at the perimeter of the combustor backplane. Implementing this approach at the side walls of the combustion chamber, similar to the "damping compliant walls" approach proposed by Ghani *et al*. [113], was found to influence flame dynamics. Further numerical tuning is often required in the compressible

---

[1]Based on an implementation in OpenFOAM [125], the CBSBCs were implemented and validated in the Rolls-Royce in-house code PRECISE [9]. The newly implemented boundary condition has been successfully applied in the compressible LES of a spray flame under realistic engine conditions resulting in a thermoacoustically stable condition [81]. However, the excitation signal imposed in the compressible LES for flame dynamics analysis did not perturb the flame with significant amplitude due to reflection of acoustic waves at the injector, resulting in a low signal-to-noise ratio. In addition, the compressible approach proved impractical due to its long computation time. These problems led to the study in PAPER-FTF [82].

LES to prevent the onset of unstable (longitudinal or transverse) thermoacoustic modes, such as "sponge layers" [139, 150], or modifying the pressure dependency of the heat release rate to effectively enforce the Rayleigh integral to be negative [86].

4.2 Broadband-excited LES for data generation

The fundamental concept underlying the LES/SI approach is to force a thermoacoustically stable simulation with an externally imposed *broadband* signal. This method *simultaneously* excites all frequencies of interest, enabling the generation of input-output data for subsequent flame dynamics identification from a *single* LES run.

4.2.1 Pre-processing: Design of excitation time series

Zhu *et al.* [333] emphasized that *»it is worthwhile to design the input signals carefully so as to generate data that are sufficiently informative«*, where "input signals" refer to "excitation signals" in the present terminology. Specific requirements must be met when broadband signals are designed, as discussed in more detail in the PAPER-FTF [82]. These requirements include a crest factor (peak-to-average power ratio) close to unity [195], low autocorrelation [210, 247, 309], low-pass filtered spectral characteristics with uniform amplitude over the frequency range of interest [101], continuous nature (as opposed to pseudo-random binary signals (PRBS)), and limited amplitudes to avoid triggering non-linear flame behavior. Signals based on Daubechies wavelets, as utilized in PAPER-FTF [82], PAPER-FP [80], and PAPER-PP [83], represent the optimal compromise of the requirements above [101]. Nevertheless, the PAPER-FTF [82] demonstrated that even an excitation signal with small amplitudes does not guarantee a linear flame response in compressible LES, indicating that the choice of excitation signals for compressible LES is not trivial and may require iterative adjustments to achieve a *linear* response.

4.2.2 Pre-processing: Setting up the LES

Once the excitation signal has been designed, the LES can be set up. The majority of these steps are similar to those encountered in any other LES, such as mesh generation (see PAPER-FTF [82], PAPER-PP [83], and PAPER-FP [80] for specific requirements in combustion LES), solver selection (e.g., incompressible or compressible formulation as discussed in Sec. 4.1.1), model selection for turbulence-combustion interactions, sub-grid Reynolds stresses, chemical kinetics and species transport, as well as selection of (acoustic,) flow and wall boundary conditions. In addition, there are some specific tasks for LES in the context of flame dynamics. These include the adaptation of the inflow boundary condition to handle the forcing signal (which functions with a variety of commercial and non-commercial solvers out of the box), and the definition of monitoring planes and integration volumes for the extraction of input-output data.

4.2.3 Processing: Running the LES

The actual processing (i.e., simulation) can be divided into four consecutive steps that must be carried out (steps 1-3 do not differ from any other combustion LES).

1. Running a cold flow LES until the system reaches a statistically steady state.

2. Igniting the cold flow LES, either by setting the entire combustion chamber to burnt gases or using more sophisticated methods, such as igniting a point or volume source.

3. Running the hot flow LES until the system reaches a statistically steady state, ensuring that all pressure wave amplitudes have properly decayed. It is crucial that the LES remains thermoacoustically stable, with no pronounced resonances or self-excited instability.

4. Running the forced hot flow LES with an imposed broadband excitation signal at the inlet to generate the necessary input-output data.

The generation of data involves the recording of input and output signals at regular time intervals during the last step. Such data extraction is exemplarily shown in Fig. 4.1. The excitation signal u'_{ex} induces velocity perturbations u'_{ref} at a reference position upstream of the reaction zone (input signal). These perturbations serve as the flame input, resulting in fluctuations in the heat release rate $\dot{Q}'$ and entropy s' (output signals), as discussed in Chapter 2. The input signal u'_{ref} is determined by area-averaging the axial flow velocity (black dashed line in Fig. 4.1), while the output signal $\dot{Q}'$ is obtained by volume-integrating the heat release rate (orange dashed line in Fig. 4.1). In contrast, entropy fluctuations s' are typically not directly accessible in LES. Similar

u'_{ex} u'_{ref} $\dot{Q}'$ T'

| Broadband excitation | Velocity input | Heat release rate output | Temperature output |
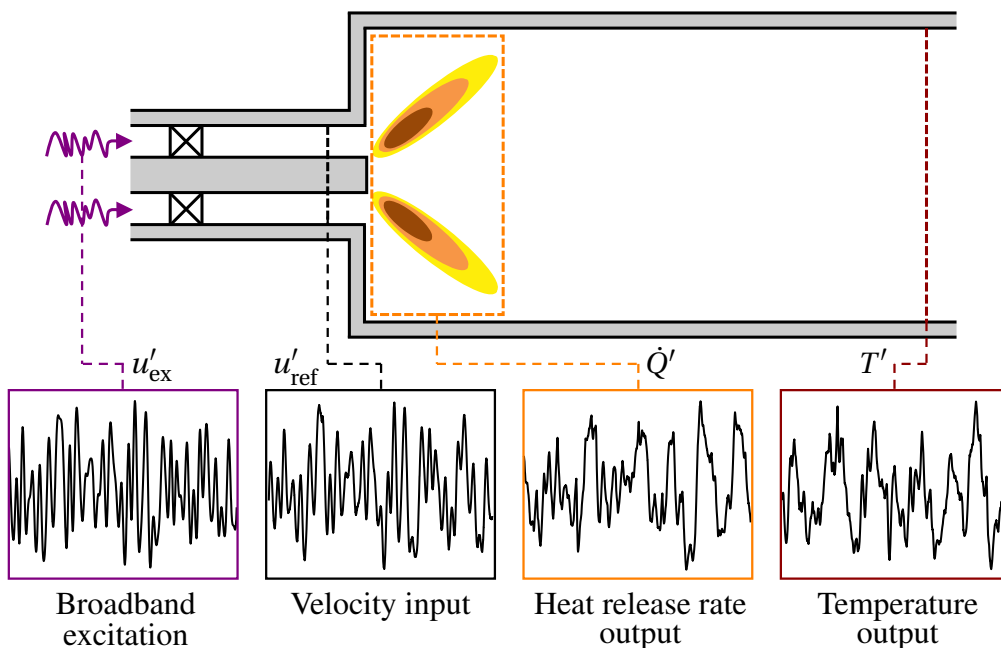
Figure 4.1: Excitation, input and output in the LES of a typical gas turbine combustor using the example of the SISO flame and entropy transfer functions in Eqs. (2.10) and (2.11).

as in experiments, temperature fluctuations T' can be determined instead [61, 327]. This substitution of s' by T' is based on the assumption that entropy disturbances can be approximated with the linearized expression for the ideal gas law, namely $\rho'/\overline{\rho} = p'/\overline{p} - T'/\overline{T}$, and by neglecting compositional inhomogeneities (which aligns with recent findings by Gentil *et al.* [112]) in the Gibbs equation as

$$\frac{s'}{\overline{c_p}} = \frac{1}{\gamma}\frac{p'}{\overline{p}} - \frac{\rho'}{\overline{\rho}} \approx \frac{T'}{\overline{T}} - \frac{\gamma-1}{\gamma}\frac{p'}{\overline{p}} \ . \tag{4.1}$$

Further assuming low Mach numbers and no large acoustic fluctuations (which is justified in premixed combustion) simplifies Eq. (4.1) to [61, 218, 252]

$$\frac{s'}{\overline{c_p}} \approx \frac{T'}{\overline{T}} \ . \tag{4.2}$$

The output signal T' (red dashed line in Fig. 4.1) is obtained by area-averaging the temperature fluctuations at a reference position downstream of the flame, typically near the combustor outlet (since solely entropy waves with significant strength leaving the combustor can contribute negatively to the rumble feedback cycle as described in Sec. 2.2). Additional monitoring planes can be deployed throughout the combustor to evaluate the convection and decay of entropy waves, as done in PAPER-PP [83] and PAPER-FP [80] and discussed in Sec. 5.3.

5 Contextualization and discussion of publications

This chapter puts the papers that comprise this thesis into perspective with the existing literature.

5.1 Challenges in the experimental prediction of flame dynamics in realistic test rigs

The key mechanism for predicting thermoacoustic combustion instability is the flame response to flow perturbations, as emphasized in Chapters 1 and 2. Determining the latter is particularly challenging under the harsh conditions of high-pressure, pre-heated test facilities comprising engine-like combustors with liquid fuel spray flames. There are two common approaches to determining flame response with *experimental measurements*: optical and acoustic. Both require external forcing (i.e., acoustic modulation of the air mass flow), with control over the excitation frequency and amplitude, typically utilizing sirens or loudspeakers to perturb the flame at distinct frequencies. The primary distinction between the two methodologies lies in how they extract information about the flame response.

The *optical approach* involves measuring the chemiluminescence intensity of free radicals, such as CH^* and OH^*, using a photomultiplier coupled with a band-pass filter to estimate the heat release rate, assuming proportionality between chemiluminescence intensity and heat release rate [165, 256]. This approach is straightforward for fully premixed flames [70], however, several studies [12, 23, 124, 184, 236, 273] have indicated that it leads to erroneous results when applied to flames subject to equivalence ratio fluctuations (i.e., partially premixed flames). This is because the chemiluminescence intensity of a single species reacts more strongly to equivalence ratio fluctuation than to mass flow perturbations, leading to a non-proportionality between chemiluminescence intensity and heat release rate [132, 133]. Schuermans *et al.* [275] extended this method by simultaneously measuring chemiluminescence intensity signals of different wavelength bands to relate both contributions to the fluctuations of heat release rate via an inverse method. However, this extended approach is highly sensitive to small measurement errors [276] and a discrepancy in gain persisted between the acoustic and optical data, despite the burner under investigation exhibiting comparatively less fluctuations in equivalence ratio. Consequently, the optical approach is not well suited for partially premixed flames. Rajendram Soundararajan *et al.* [258, 259] investigated the response of spray flames, assuming that equivalence ratio fluctuations are negligible as their flames behave quasi-premixed [257]. These findings are specific to their combustor (SICCA from the EM2C laboratory of CentralSupélec) and are not generalizable. Moreover, all of the aforementioned studies were conducted under atmospheric conditions. In contrast, high-pressure configurations include heat radiation from
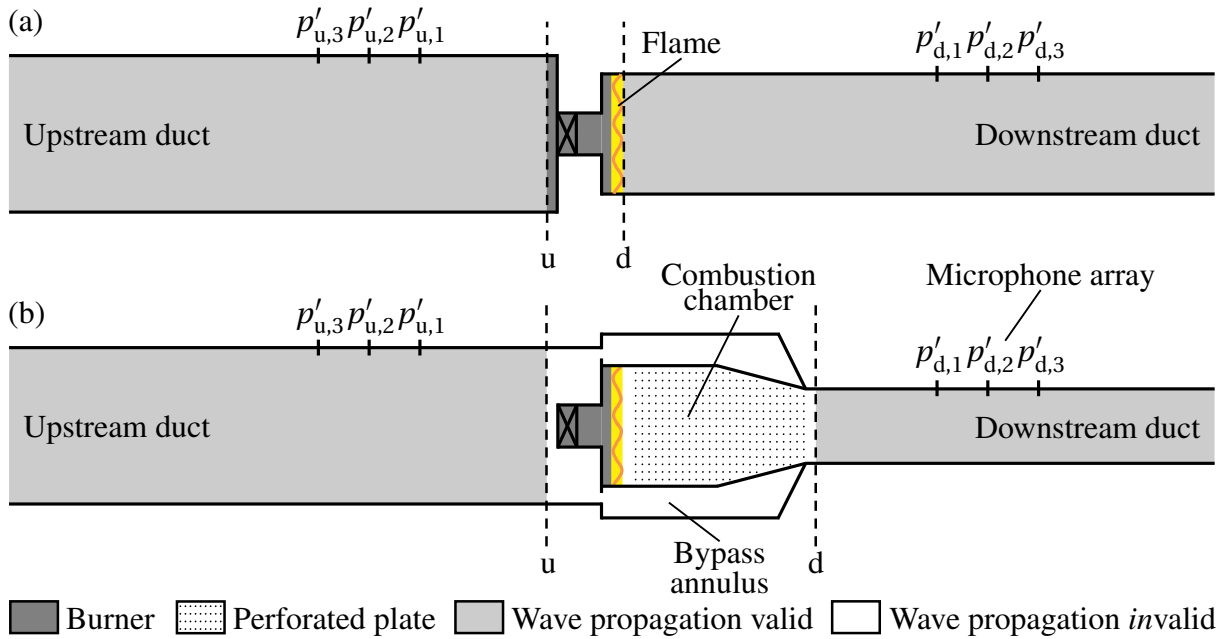
Figure 5.1: Schematic representation of (a) a simplistic test rig and (b) a realistic test rig with a gas turbine combustor as test section, both under reactive conditions. Sirens are not shown.

the combustor walls and a lower probability of formation of the chemical species associated with flame chemiluminescence [276], leading to even more complications and uncertainties. Furthermore, engine-like combustors often exhibit multiple flame regimes, including premixed and non-premixed combustion [167]. However, optical methods are limited to premixed flames due to saturation effects of their non-premixed counterpart on the optical sensor [276]. Another disadvantage is the difficulty of implementation in test rigs comprising complex combustors due to limited optical access caused by thick or curved pressure-resistant materials. This requires the use of endoscopes through the cooling annulus or perforated combustor walls [5]. In conclusion, the optical method is not adequate for the determination of flame dynamics in such test rigs.

The *acoustic approach* uses two arrays of microphones placed in measurement ducts upstream and downstream of the combustor to measure the resulting acoustic pressure fluctuations in response to acoustic excitation, as shown in Fig. 5.1. This method is more demanding than the optical approach in terms of experimental setup and data post-processing [23]. However, it does not suffer from the drawbacks of the former approach. In order to determine the flame dynamics from the measured pressure data, two modeling steps are required in the acoustic approach.

1. The acquired pressure fluctuations p' enable the reconstruction of upstream and downstream propagating plane acoustic waves (f and g in Eq. (2.6)) using an over-determined system of equations, assuming a constant speed of sound and no changes in cross-section between the individual microphones. The reconstructed acoustic waves are then used to relate the acoustic pressure and velocity fluctuations upstream and downstream of the combustor via a transfer matrix[1], which is a two-port, four-pole black-box representation of the combustor's acoustic behavior. This method builds on analogies between

---

[1]For more information on transfer matrices (not reintroduced in the present work) see [185, 234].

electrodynamics and acoustics established in the 1970s [47]. Munjal and Doige [221] developed the *two-source-location method* to determine transfer matrices of absorbing materials, pipeline elements, and mufflers, based on earlier studies on wave decomposition [43, 284, 315, 316]. Two measurement states are required to close the system of four unknown transfer matrix coefficients (four poles), typically achieved by upstream and downstream forcing. If only one forcing state is available, which results in an under-determined system, assumptions must be made to recover all elements of the transfer matrix [22]. Åbom [1] emphasized that the two test states must be acoustically independent. Peters *et al*. [237, 238] introduced the *multi-microphone method*, which was later extended to combustion applications by Paschereit and Polifke [232–234], using multiple microphones to minimize the impact of errors induced by turbulent flow and combustion noise. The method was further developed and validated by Schuermans [271–273] and *»is now a well established tool that proves to be the key experimental method in thermoa-coustic analysis [at Alstom]«* [275].

2. The flame transfer matrix must be extracted from the measured transfer matrix of the entire combustor, treating the elements between 'u' and 'd' in Fig. 5.1 as a black-box. Since a burner inherently stabilizes a flame, it is impossible to measure the transfer matrix of the flame without the burner.

The established approach in literature and practice [14, 23, 24, 98, 161, 204, 263, 270, 296] assumes that the measured transfer matrix $\mathbf{T}$ in the presence of combustion can be modeled as a series of the burner transfer matrix (BTM) $\mathbf{B}$ and flame transfer matrix (FTM) $\mathbf{F}$, resulting in $\mathbf{T} = \mathbf{FB}$. This transfer matrix is therefore known as the "burner-flame transfer matrix" (BFTM). To fully characterize the transfer behavior of the burner, an additional measurement at the same operating point without combustion is required. It is assumed that the acoustic transfer matrix of the burner remains unchanged by the combustion process [271, 273], which is justifiable for low Mach applications [8, 271]. In the case of hydrogen-enriched fuels, Blondé *et al*. [23] emphasized that the correct composition of the air-fuel mixture must be considered when calculating the speed of sound necessary for determining the burner transfer matrix. Rearranging the expression $\mathbf{F} = \mathbf{TB}^{-1}$ leads to the flame transfer matrix [271, 273]. This procedure of measuring two transfer matrices (with and without combustion, i.e., $\mathbf{B}$ and $\mathbf{T}$) must be performed for all operating conditions of interest. This approach may be referred to as *BFTM method* due to the key modeling assumption that the measured transfer matrix in the presence of combustion can be represented as a series of the burner and flame transfer matrices. The BFTM approach has been successfully applied to a variety of flame response studies, including investigations of the influence of steam content (humidity) and fuel composition [270] or the fuel-air mixture [14], non-linear response of fully and partially premixed[2] flames [44, 45], multi-jet burners operated with pure hydrogen and pure natural gas [22], and the effect of hydrogen enrichment on the dynamics of fully and partially premixed flames [23]. All of these studies have in common that they investigate simplified academic test rigs with a burner section placed between two ducts, as shown in Fig. 5.1 (a). In these specific cases, the assumptions of the BFTM approach hold.

Alanyalıoğlu *et al*. [5] and Eder *et al*. [81] in independent work pointed out that the state-of-the-art BFTM approach may fail for complex configurations with test sections representing gas

---

[2]Since the acoustic approach is based on a direct evaluation of the acoustic source, the degree of premixedness is irrelevant in contrast to the optical approach.

turbine-like combustors, such as the one depicted in Fig. 5.1 (b). However, the literature on such test rigs is scarce, with the exception of, e.g., [5, 81, 98, 262] and the PAPER-MBI [84]. The main differences between simplistic test rigs and these realistic and therefore more complex setups are the additional acoustic communication path between the upstream and downstream ducts through multi-perforated liners for effusion cooling and acoustic damping [176, 182, 183], a transition duct with a significant reduction in cross-sectional area at the combustor end, and more complex geometric features (such as multiple swirlers and complex burners with liquid fuel injection). The primary issue in the present context is that while the flame transfer matrix remains an intrinsic part of the transfer matrix measurement, the assumption of a simple matrix multiplication of burner and flame transfer matrices, as introduced above is, no longer consistent.

These inconsistencies are demonstrated in the PAPER-MBI [84] mathematically and by means of a low-order thermoacoustic network model (LOM) of the Rolls-Royce SCARLET[3] (SCaled Acoustic Rig for Low Emission Technology) test rig [98, 99], which comprises an engine-like combustor with a full-scale burner and is operated under realistic engine conditions. The corresponding LOM was built and solved with the open-source MATLAB® package taX[4] [88, 90] developed at TUM. The PAPER-MBI [84] presents a novel method for the *consistent* inference of the FTM in complex test rigs, such as SCARLET. This generalized method reduces to the BFTM approach as a special case. The *model-based inference* (MBI) method uses a LOM to approximate the internal system dynamics of the combustor. The FTM is solely inferred from the measured transfer matrix in the presence of combustion. The PAPER-MBI [84] applies the proposed method to SCARLET, demonstrating its capability and applicability in realistic problems. In addition, the transfer matrix measurement without combustion, which is employed in the BFTM approach to represent the burner geometry, is not required. This may significantly reduce the effort of a measurement campaign. Nevertheless, a follow-up study[5] [135] showed that the inclusion of a non-reactive transfer matrix (not necessarily at the exact same operating point) as a partial correction for systematic modeling errors may further improve the accuracy of the MBI method and thus the identified flame transfer matrix.

5.2 Incompressible LES: A valid tool for the numerical prediction of premixed flame dynamics?

The application of *numerical methods* for investigating thermoacoustic combustion instability can significantly reduce the number of test runs required in large-scale measurement campaigns.

---

[3]The SCARLET test rig is located in the HBK-3 (high-pressure combustion chamber) test facility at the DLR (German Aerospace Center) in Cologne, Germany. It was developed for efficient testing of aero-engine burners (including fuel spray nozzles) under realistic engine conditions at a low TRL (technology readiness level). The inlet conditions of the rig represent the outlet conditions of the compressor stage in the engine with a maximum pressure of 30 bar, a maximum preheating temperature of 950 K, and a maximum air mass flow of 4 kg/s. The rig is equipped with a back-pressure valve, two dampers, four sirens, two acoustic measurement sections (constant cross-sections) with an array of microphones, and an aero-engine combustion chamber (test section), allowing the use of the "acoustic approach". Further details pertaining to the experimental setup and the underlying network model can be found in the PAPER-MBI [84].

[4]gitlab.lrz.de/tfd/tax

[5]supervised by the author in the frame of a student thesis

5.2 Incompressible LES: A valid tool for the numerical prediction of premixed flame dynamics?

The long-term goal is thus to perform experiments only at selected operating points to validate numerical results. According to Poinsot's review paper [242], simulation methods for predicting thermoacoustic combustion instability can be classified into two categories: *self-excited LES* (referred to as "brute force LES" in [242]) and *forced LES* (referred to as "forced open-loop LES" in [242]; note that the latter terminology is misleading because a compressible LES is always a closed-loop due to inherent ITA feedback, even with non-reflecting boundary conditions [153]), as shown in Fig. 5.2.

The objective of the first approach, *self-excited LES* (see Fig. 5.2 (a)), is to simulate the thermoacoustic behavior of the entire combustor geometry, capturing the growth or damping of acoustic fluctuations and the potential evolution of limit cycle oscillations that are typical for a saturated thermoacoustic mode [16, 67]. This necessitates the utilization of *compressible* solvers, as the propagation of acoustic waves and their interaction with unsteady combustion processes are crucial to the onset of thermoacoustic combustion instability, as indicated by the Rayleigh criteria in Eqs. (2.1) and (2.2). To accurately capture all triggering and damping mechanisms of these self-excited oscillations, such as flow resonances in the plenum and longitudinal modes in the combustion chamber, it is necessary to spatially resolve all relevant geometric parts of the test rig, from inlet to outlet (e.g., full-length plenum [3, 40, 173] and all segments in annular systems [297]). This leads to potentially large computational domains [3, 173, 297, 305]. In addition, acoustic boundary conditions, such as inlet and outlet reflection coefficients, must match realistic values. Consequently, the computational domain is often extended until well-defined boundary impedances, such as those at choked [203] or open regions [187, 222], can be defined. Alternatively, experimentally obtained impedances can be imposed via time-domain impedance boundary conditions introduced in Sec. 4.1.2 [66, 152, 321]. For atmospheric rigs, extending the domain into the far field avoids the need to model the impedance at the combustor outlet [40, 104]. All these aspects of the self-excited LES play a decisive role in the prediction of thermoacoustic combustion instability, or as Gicquel *et al.* [118] succinctly summarize in their review paper, »*it will also depend on the modeler ability to properly treat the acoustic boundary conditions of its simulation*«. Additionally, the behavior of self-excited modes can vary based on initial conditions [244]. Furthermore, it is essential to note that only the dominant unstable mode can be detected, which limits comprehensive modal analysis of the combustor [247]. These and other issues related to the self-excited LES approach are further discussed by Polifke *et al.* [253] and Poinsot and Veynante [244].

The second approach, *forced LES* (see Fig. 5.2 (b)), follows the strategy of *divide et impera* ("divide and conquer") [245, 247], where modeling approaches of varying complexity are applied to multi-physics, multi-scale phenomena such as thermoacoustic combustion instability.
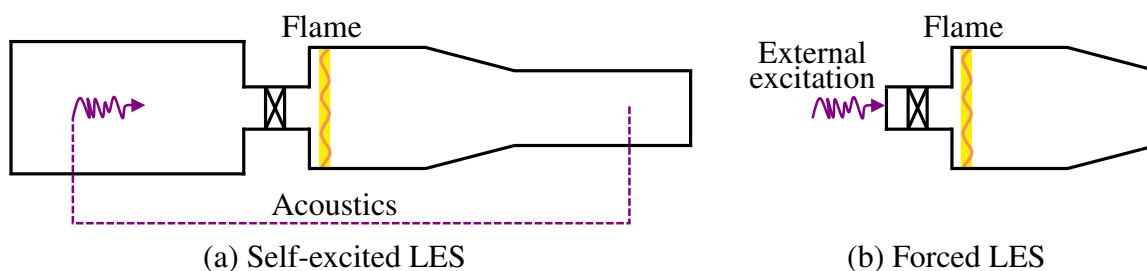

(a) Self-excited LES   (b) Forced LES

Figure 5.2: Numerical approaches to predict thermoacoustic combustion instability.

Following this idea, the *flame response problem* (which can be computed by LES) and the *acoustic problem* (which is handled by a thermoacoustic solver) are decoupled [118]. Instead of letting the acoustic feedback drive the flow, the LES is used as an amplifier of a stable flow by imposing excitation signals in a controlled manner [244] (see Fig. 5.2 (b) and recap Fig. 4.1). In comparison to the self-excited LES strategy, two additional posterior steps are necessary:

1. Estimation of a reduced-order flame response model from forced LES data utilizing analytical models [116, 320] or data-driven methods such as system identification [110, 311, 332] (see Chapter 3), artificial neural networks [151, 267, 308] or ordinary differential equation (ODE) models [62, 63].

2. Incorporation of the estimated linear (e.g., FTF) or non-linear (e.g., FDF [229] or extended flame describing function (xFDF) [126]) flame response as a sub-model in a thermoacoustic solver with a linearized description of acoustic wave propagation, such as low-order network models [26, 92, 163, 178, 252, 288, 299], finite-element or finite-volume methods [34, 226, 231, 287, 289], or Galerkin or state-space techniques [30, 175, 207, 271, 286], for linear stability analysis.

The initial investigations into extracting frequency-dependent flame characteristics from transient calculations and subsequent utilization of this information in linear acoustic analysis were conducted in the mid-1970s for one-dimensional laminar premixed flames [290]. Two decades later, Bohn *et al.* [27, 28] introduced a new method for predicting the transfer behavior of turbulent non-premixed flames and laminar premixed flames based on unsteady compressible reactive CFD. This method perturbs the mass flow rate at the air inlet of a steady-state solution with a sudden jump (i.e., a step function). The step response of the heat release rate is then transformed into the frequency domain using a Laplace transformation, thereby obtaining the frequency response of the flame. Krüger *et al.* [177, 178] further refined this approach by considering chemical kinetics and the interaction between turbulence and kinetics, enabling them to study turbulent premixed flames and even a gas turbine burner, where the estimated flame response is subsequently used in the stability analysis for both axial and circumferential directions. As early as 1999, they noted that »*the 3D-analysis of the combustion chamber and the flame is the key issue for successful analysis*« [178] and further emphasized that »*combustion driven oscillations can be predicted for this kind of gas turbine combustor using an acoustical network of four-pole elements*« [178]. Instead of forcing the flame with a step function and evaluating its step response, Polifke *et al.* [250, 253] proposed an alternative method that results in the unit impulse response of the perturbed system, which is then converted to the frequency domain via a *z*-transform (Eq. (3.6)). System identification, specifically a finite impulse response model structure as introduced in Eq. (3.10), was employed to time series data obtained from unsteady compressible CFD simulations with randomly perturbed boundary conditions. This approach, known as CFD/SI, was discussed in more detail in Chapter 4. They recognized a significant advantage over the self-excited approach, namely that »*it allows one to simulate only the element of interest and its immediate vicinity rather than the full thermoacoustic system complete with physically correct boundary conditions*«. Zhu *et al.* [332, 333] employed compressible CFD/SI with various types of excitation signals (harmonic, pulse, random binary, multi-sine) to identify the flame transfer function of a two-dimensional axisymmetric annular combustor with a spray atomizer. They proposed that more sophisticated CFD methods, such as LES, could be utilized for flame response identification in the future. The applicability of LES/SI (LES applied as CFD

method) was demonstrated in several studies on a three-dimensional turbulent swirl-stabilized burner by Tay-Wo-Chong *et al.* [309–312]. In the subsequent years, LES/SI became a well-established tool for the "forced LES approach" and is used extensively to identify the dynamics of fully premixed flames [13, 107, 179, 211, 313] (PAPER-FTF [82] and PAPER-FP [80]), partially premixed flames [58, 108, 180] (PAPER-PP [83]), spray flames [81], and autoignition flames [31, 106, 279].

A plethora of the studies mentioned so far rely on *compressible* CFD, which is still often considered the "established" approach for estimating the response of premixed flames [116, 127, 160, 205, 242, 244]. Five potential explanations for the continued prevalence of this thinking in the thermoacoustics community are given in the following.

1. A compressible simulation does not suppress fundamental effects such as acoustic wave propagation and is, therefore, closer to an experiment than its incompressible counterpart. This may be perceived as a more "natural" approach. It should be noted, however, that this is not a compelling argument for the use of compressible CFD, as experiments may encounter undesirable effects for the estimation of flame response due to their involvement of acoustics. These include acoustic, ITA and entropy-acoustic resonances (as discussed in Sec. 2.2 and schematically shown in Fig. 2.3), reflection, amplification or attenuation of the excitation signal, and even self-excited (longitudinal or transversal) modes, which can be circumvented by employing *incompressible* CFD as suggested by Polifke [246] and quantitatively demonstrated in the PAPER-FTF [82] (see Sec. 4.1.1 for technical details).

2. Some LES solvers have been historically or because of their primary field of application written in a compressible manner with no option for the user to switch to an incompressible formulation. Consequently, research groups and companies worldwide often employ only one of the two methods (see Tab. 3 in [118]). One could even argue that two distinct "camps" have formed.

3. Some of the earlier works [250, 253, 274] did not determine the flame response based on heat release rate fluctuations. Instead, they numerically employed the acoustic approach from Sec. 5.1. This treatment of combustors as an interconnection of acoustic multi-ports and the associated determination of the flame transfer matrix necessitates the inclusion of acoustic wave propagation in the numerical simulation, which requires a compressible formulation.

4. The numerical requirements for forced LES may be conflated with those of self-excited LES. Poinsot [242] elucidates the difference as follows, *»brute force LES consists in setting a computational domain as large as possible [...], matching all boundary conditions [...] and letting the LES solver compute the self-excited instability«*, whereas *»the second method uses LES only to compute the FTFs of a given flame«*. The fact that compressible solvers are mandatory for the self-excited approach (e.g., to match boundary conditions or let a thermoacoustic instability develop) does not necessarily imply that this also holds for the forced approach.

5. It is still widely held that determining the flame response necessitates the consideration of the acoustic-flame interactions in CFD [116]. However, since velocity disturbances

are expected to be the dominant mechanism for inducing heat release rate fluctuations in velocity-sensitive (i.e., no pressure and temperature sensitivity as in premixed flames), acoustically compact flames [71, 190], its response is governed by hydrodynamic processes and should be well captured in *incompressible* CFD with externally imposed axial flow oscillations [94].

Gentemann *et al.* [110] made a first attempt by employing CFD/SI on incompressible RANS data of a swirl-stabilized burner to identify the flame response. A subsequent comparison to compressible CFD/SI results revealed discrepancies [111], which were attributed to differences in the underlying solvers and a possible non-compactness of the flame. However, in non-reacting swirling flows, both LES formalisms showed good agreement when predicting unsteady hydrodynamic modes [64]. Similar agreement was observed in DNS of turbulent flames [53] and LES of turbulent flows in a swirl-stabilized combustor [174]. A comparative study by Treleaven *et al.* [317] based on LES of spray flames harmonically excited at two distinct frequencies yielded a match between both methodologies for the FTF phase at the higher forcing frequency. The discrepancies in gain and the lower frequency were attributed to differences in the computational setup. Without further evidence, they concluded that *»the calculation of the FTF is quite insensitive to the numerical method«* (i.e., compressible or incompressible solvers). Numerous studies conducted over the past decade on various premixed burners [13, 58, 107, 127, 179, 181, 313] (PAPER-FTF [82] and PAPER-FP [80]) have shown a high degree of *qualitative* agreement between the FTF obtained with incompressible CFD and experiments. The PAPER-FTF [82] presents a direct comparison of incompressible and compressible LES of a swirl-stabilized turbulent burner[6] to quantify these qualitative results and provide a definitive answer to whether both methods are equally applicable for the identification of (velocity-sensitive, acoustically compact) premixed flame response. To minimize systematic errors, the same grid, numerical schemes, turbulence-combustion model, and chemical kinetics were employed. It was demonstrated for the first time that the flame transfer functions up to the confidence intervals[7] are identical for both approaches. Furthermore, several challenges were encountered in the compressible LES, namely the occurrence of unstable transverse modes, resonances despite non-reflective boundary conditions, and a reduction in the signal-to-noise ratio that impaired system identification. In conclusion, the PAPER-FTF [82] confirms that acoustic wave propagation is irrelevant for the subsequent identification of premixed flame dynamics and thus recommends the use of *incompressible* CFD/SI.

Nevertheless, several applications exist where the use of compressible LES for identifying the flame response is unavoidable. These include acoustically non-compact flames (i.e., the burner and heat release zone are not small compared to the acoustic wavelength) [319], cases with non-compact distance between flame and fuel injection (i.e., the distance is not small compared

---

[6]The laboratory-scale BRS ("Beschaufelter RingSpalt") burner is a swirl-stabilized, perfectly premixed burner with an axial swirl generator mounted on a central bluff body, operated at atmospheric pressure. The operating points vary between 30 kW to 70 kW in thermal power and 0.7 to 0.9 in equivalence ratio. The combustion chamber has two quartz glass windows for OH* chemiluminescence measurements, allowing the use of the "optical approach" to determine the FTF. The burner was developed and experimentally investigated by Komarek and Polifke [170] at TUM. For further details on the experimental and numerical setup, see PAPER-FTF [82].

[7]The use of confidence intervals is crucial when evaluating the dynamics of *turbulent* flames due to their inherent stochasticity. Further information on the linear propagation of model uncertainties and confidence intervals can be found in [294].

to the acoustic wavelength, typically when the Helmholtz number He > 0.01) [319], pressure-sensitive flames, such as autoignition flames in reheat combustors [106], high flow velocities in the computational domain (e.g., in the region of fuel injection as in PAPER-PP [83], typically when Ma > 0.3 (change in density is non-negligible) [10]), and cases where acoustic transfer matrices are identified instead of the flame transfer function [103, 109, 212, 253]. It should be further noted that for practically relevant cases of burners that do not have a stiff fuel injection, and where the fuel system is resolved in CFD, the incompressibility assumption does not hold even for compact geometries, since pressure fluctuations can modulate the fuel supply.

5.3 The impact of entropy waves on thermoacoustic interactions in premixed combustors

In contrast to the extensive experimental (see Sec. 5.1) and numerical (see Sec. 5.2) investigations of the heat release rate response and the associated prediction of flame transfer functions over the past decades, the response of entropy fluctuations on flow disturbances has received comparatively less attention. In general, the role of entropy waves in the thermoacoustic feedback loop can be divided into three main phenomena, as already outlined in Sec. 2.2 and visualized in Fig. 2.1, namely the *generation* of entropy waves by unsteady combustion, the *convective transport and dispersion* of entropy waves along the combustion chamber to the outlet, and the acceleration of entropy waves due to mean flow gradients and the corresponding *conversion* to acoustic energy. Note that when fluid inhomogeneities, such as density and temperature disturbances, are convected through a region of non-uniform flow (e.g., an area contraction or downstream nozzle), acoustic waves are generated [35, 50, 203]. This is because the force required to accelerate a volume element depends on the density of the fluid. Consequently, a density inhomogeneity results in a change in the force required for acceleration, which in turn is compensated by a pressure perturbation that manifests itself as an acoustic wave [96]. It has been known since the early work of Keller *et al.* [163, 164] that such entropy-acoustic conversion can lead to thermoacoustic combustion instability in gas turbines. Polifke *et al.* [251, 252] demonstrated through low-order models that feedback originating from entropy wave generation may be either constructive or destructive, indicating that these waves can even stabilize the system. This finding was later confirmed by Goh and Morgans [120] using frequency-domain simulations.

5.3.1 Generation of entropy waves

Several studies [74, 218] have argued that heat release rate fluctuations contribute to the generation of entropy waves, suggesting a direct relationship between $\dot{Q}'$ and s'. This conclusion is supported by several analytically reduced quasi-one-dimensional (Q1D) models [69, 130, 188, 323]. However, these studies consider the flame to be a heat source *at rest*, neglecting flame movement. Strobio Chen *et al.* [301] and Meindl *et al.* [208] demonstrated in Q1D models and one- and two-dimensional simulations, respectively, that this neglect results in the non-physical generation of entropy waves. This conclusion has been widely accepted within the community [39, 106, 121, 215, 292, 293]. The PAPER-ALE [213] builds on these findings

and presents a unified and consistent description of entropy wave generation of *moving* sources from three-dimensional differential equations to the limit of Q1D jump conditions based on an arbitrary Lagrangian-Eulerian (ALE) framework [65]. This analytical framework enables the isolated analysis of the corresponding source terms for the first time.

Combustion-generated entropy waves have only recently become the subject of experimental investigation due to the development and adaptation of more sophisticated techniques for measuring exhaust gas temperature with sufficiently fine temporal resolution. Giusti *et al.* [119] used bare-wire thermocouples positioned in the combustor centerline to record temperature fluctuations of a non-premixed flame. The temperature signals were then fast Fourier transformed (FFT) to determine the frequency response up to 70 Hz. Wassmer *et al.* [324] measured entropy waves generated by a turbulent swirl-stabilized flame between 5 Hz and 50 Hz using a time-of-flight-based temperature measurement technique, which analyzes the time it takes for an acoustic wave to travel through a medium. This is based on the principle that the speed of sound is temperature-dependent. Weilenmann *et al.* [327] measured the linear and non-linear entropy transfer function of partially premixed CH_4-air flames with OH planar laser-induced fluorescence (PLIF) thermometry between 40 Hz and 90 Hz. However, this approach is not well-suited to the study of a wide range of operating conditions due to the substantial storage requirements for cross-sectional data and the corresponding post-processing demands [61]. Recently, Dharmaputra *et al.* [61] introduced the tunable diode laser absorption spectroscopy with wavelength modulation spectroscopy (TDLAS-WMS) for entropy wave measurements of partially premixed CH_4-H_2-air flames. This technique measured the ETF between 50 Hz and 250 Hz and offered compact data size, rendering it suitable for ETF measurements over a wide range of frequencies and operating conditions. Consequently, TDLAS-WMS became the experimental method of choice in PAPER-PP [83] and PAPER-FP [80] for validating numerical results.

It is widely established [163, 164, 220, 252, 268, 298, 301] that entropy waves are predominantly generated by fluctuations in the fuel concentration upstream of the flame. These fluctuations create locally richer and leaner pockets of the fresh mixture convecting towards the flame, which ultimately result in local changes in the adiabatic flame temperature, i.e., the generation of entropy waves [252]. This phenomenon was confirmed in numerical simulations of laminar partially premixed flames by Strobio Chen *et al.* [302] and Steinbacher *et al.* [298]. The PAPER-PP [83] builds upon these works and identifies the ETF of a *turbulent* partially premixed flame in the ETH burner[8] using LES/SI. The extraction of the temperature signal is described in Sec. 4.2.3. Numerical findings are complemented and validated by experimental data with the TDLAS-WMS method, with a similar experimental setup as in [61], but at a different operating point. The dominance of equivalence ratio fluctuations was revealed by separating the entropy response to equivalence ratio and velocity fluctuations through the use of MISO identification (see Eq. (2.9)), thereby confirming the consensus in the literature. In a subsequent measurement campaign at ETH Zurich, "non-negligible" entropy wave generation was observed at an oper-

---

[8]The laboratory-scale ETH burner is a swirl-stabilized burner operated under fully and partially premixed conditions. The water-cooled test rig has several quartz glass windows for optical access, as well as upstream and downstream microphones arrays, which allow both the use of the "optic approach" and "acoustic approach" to determine the FTF. Furthermore, it is equipped with the TDLAS-WMS technique for ETF measurements. The test rig is located in the CAPS laboratory at the ETH Zurich and was experimentally investigated by Schuermans *et al.* [277], Dharmaputra *et al.* [61] and Blondé *et al.* [23].

ating point with *fully* premixing, i.e., in the absence of fuel-air mixture inhomogeneities. The experimenters' first suspicion was *unsteady wall heat transfer* due to the massive water cooling of the combustor metal frame, while experimental investigation of the observed phenomenon was not possible [228]. The PAPER-FP [80] precisely addresses this problem using LES/SI and was able to confirm the hypothesis. Surprisingly, a second mechanism was found that generates entropy waves in fully premixed *hydrogen-enriched* flames, namely local variations in the equivalence ratio and local segregation of fuel components due to *differential diffusion of hydrogen*. The latter mechanism was quantified to be an order of magnitude smaller than the wall heat losses.

5.3.2 Convective transport and dispersion of entropy waves

In addition to the generation of entropy waves, both PAPER-PP [83] and PAPER-FP [80] investigate the convective transport and dispersion, which are as crucial as the underlying generation process. This thesis has repeatedly emphasized that only entropy waves of "significant" strength can contribute to the onset of a thermoacoustic combustion instability when being accelerated. Various relevant mechanisms associated with the dispersion of entropy waves have been discussed by Sattelmayer [268], Morgans *et al.* [218], Weilenmann *et al.* [326], Polifke [249], and Kaiser *et al.* [157–159]. However, the problem lacks generality, as each burner type exhibits different behavior due to its complex flow physics (e.g., swirl, flow separation, shear layers, recirculation, turbulence intensity), and unique geometry. On the one hand, early studies on convective dispersion of entropy waves by Sattelmayer [268], Eckstein and Sattelmayer [77], and Eckstein *et al.* [78] concluded that »*the strength of these entropy-related pressure waves is however too weak to significantly alter the dominating thermoacoustic mode*« [78][9]. On the other hand, Morgans *et al.* [219] revisited the convection model developed in [268] and found that entropy waves »*can survive the advection process sufficiently well for entropy-driven acoustic to be important*«. Most experimental, numerical and analytical studies on the convection and decay of entropy waves so far rely on the "canonical" configuration of a fully developed turbulent channel flow [41, 93, 119, 157–159, 218, 219, 268]. In this simplified configuration, dissipation is found to be negligible, and the dominant decay mechanism is shear dispersion. However, the transferability of these results to geometries of applied interest is questionable.

In a recent study, Weilenmann *et al.* [326] conducted experimental and LES work on complex, highly turbulent flows and found that the decay of entropy waves occurs significantly faster than predicted by models based on the assumption of shear dispersion [119]. This finding suggests that various dispersion mechanisms should be considered when developing new models. Xia *et al.* [328] studied the complex flow in a gas turbine combustor by solving an additional entropy transport equation with an artificially imposed entropy source term. They concluded that large-scale unsteady flow structures significantly impact the dispersion of entropy waves, leading to the attenuation of their strength. Nevertheless, when they scaled the reduced frequency response to typical high bulk flow velocities, they found that even with convective dispersion, the entropy waves likely retain sufficient strength at the combustor exit. The PAPER-PP [83]

---

[9]The "entropy-acoustic modes" investigated in [77, 78] were later identified by Ghani *et al.* [114] to be of ITA origin, meaning they do not involve the convection or decay of entropy waves in their feedback. See Sec. 2.2 for more information on both types of modes.

employs a methodology analogous to experimental methods such as the TDLAS-WMS technique. In this LES-based approach, temperature fluctuations at specific locations within the combustion chamber are "observed" (i.e., recorded on monitoring planes), rather than entropy source terms and corresponding transport equations or models being combined as in [328]. The temperature signals are employed in a subsequent SI step to identify the entropy transfer function at each location, thereby evaluating the attenuation of its gain. The study revealed that the gain decreases with increasing residence time across all frequencies above 100 Hz, but remains relatively unaffected at lower frequencies. Despite the presence of turbulent mixing, shear dispersion, and other decay mechanisms, the attenuation of entropy waves was found to be weak enough to ensure notable strength[10] at the combustor exit, potentially generating combustion noise and/or feeding a thermoacoustic combustion instability.

5.3.3 Conversion of entropy waves to acoustic energy

Many works have been devoted studying energy conversion between entropy and acoustic waves. Nevertheless, a considerable number of studies still rely on the linear one-dimensional theory proposed by Marble and Candel [203] in their seminal work in the 1970s, which examined subsonic and supersonic conditions in nozzle flows with and without shocks in the diffuser. These early models are based on the assumption of acoustic compactness, where the characteristic length of the contraction-expansion region is considered short with respect to the acoustic wavelengths of interest. Recently, De Domenico *et al.* [55] proposed an extension of this model to account for nozzles with non-isentropic flows, i.e., losses. Other studies have relaxed the compactness assumption [117, 300, 303], extended the model to non-linear effects in supersonic [144] and supercritical [143] nozzle flows, considered compositional inhomogeneities [56, 112, 200, 201], and applied the model to arbitrary nozzle shapes [216]. Of course, only models that account for mean flow effects can correctly predict entropy-acoustic modes [225].

In addition to some numerical simulations [17, 37, 73, 189, 217], only a few experimental facilities have been designed to study the entropy-acoustic energy conversion [15, 105, 119, 266, 325]. Among these, the entropy wave generator (EWG) test rig concept [15, 105, 266], originally developed by Bake *et al.* [15], is noteworthy because it allows for a transparent confrontation of theory with experiment. The EWG uses an electrical heating device to accurately control the generation of entropy waves (see the PAPER-ALE [213] for more detail on this generation mechanism), thereby avoiding the harsh environment created by combustion, e.g., as in [119]. Moreover, the non-reacting nature of the setup ensures the proper distinction between entropy-acoustic and "pure" acoustic (or ITA) mechanisms. In a recent study, Weilenmann and Noiray [325] employed a temperature-controlled pulsed jet-in-crossflow to generate entropy waves in a more realistic flow scenario than the heating wire. Future experiments may need to consider combustion as a mechanism for entropy wave generation instead of "artificial" sources, particularly when studying entropy-acoustic conversion in realistic gas turbine combustors, where flames are the primary source of entropy waves.

---

[10]To determine whether the entropy wave strength is strong enough to cause unstable entropy-acoustic modes (see Sec. 2.2), the identified entropy transfer function at the combustor exit can be incorporated into a low-order model of the test rig along with a model of a downstream nozzle (see Sec. 5.3.3).

A possible reason why these "artificial" entropy wave generators have been mainly used so far is that most studies did not focus on the closed feedback loop (i.e., thermoacoustic combustion instability) but rather aimed to determine how "loud" the entropy-acoustic conversion is (keyword: indirect combustion noise). An exception is the numerical study by Motheau *et al.* [220], who employed an extended Helmholtz solver with a flame modeled using the well-known $n - \tau$ model of Crocco [48]. In their study, parameters were extracted directly from LES, and a nozzle boundary condition accounted for the entropy-acoustic conversion.

36

6 Outlook

This publication-based thesis has contributed to the understanding of flame dynamics and thermoacoustic interactions in technically relevant configurations, such as partially premixed combustors. Thereby, a solid foundation is set for future advancements of flexible, consistent, and accurate tools for predicting flame dynamics. Three follow-up projects were identified and are outlined below.

1. The physics-based method to consistently infer flame dynamics from acoustic measurements proposed in the PAPER-MBI [84] could be combined with the data-driven procedure of *Bayesian inference* (see e.g., [32, 198] for mathematical details) to transform the qualitatively accurate models into quantitatively accurate models [155]. Juniper and Yoko [155] suggested to *»(i) tune their parameters by assimilating data from experiments; (ii) quantify the uncertainties in each model's parameters; (iii) quantify the evidence (the marginal likelihood) for each model; (iv) select the best model and (v) repeat for the next component until the model of the thermoacoustic system is complete«*. They demonstrated how such a framework, incorporating adjoint-based optimization of the first and second derivatives, can be used to infer the values of unknown model parameters [115, 155, 331]. This approach also allows for the quantification of the uncertainty in these unknown parameters and the resulting uncertainty in the model predictions [155, 331]. Given that both Bayesian and model-based inference are susceptible to modeling errors and require accurate network models with appropriate jump conditions for each element, developing improved models would enhance the effectiveness of these methods. A promising approach is the recently proposed Jacobian-based framework by Merk *et al.* [214]. This generalized framework derives highly accurate Q1D jump conditions with minimal assumptions, thereby increasing model flexibility by relaxing modeling assumptions. Moreover, specific components in gas turbine-like combustors, such as effusion cooling, may be more accurately represented in corresponding LOMs through the application of more sophisticated models such as those of Howe [136, 138], Jing and Sun [154] or Bellucci *et al.* [19, 20], as outlined by Lahiri [182] and Lahiri and Bake [183].

2. Another significant area of future work involves applying the LES/SI methodology used in PAPER-FTF [82], PAPER-PP [83], and PAPER-FP [80] to liquid fuel combustors operated under engine-like conditions. A preliminary attempt was made by Eder *et al.* [81] using the SCARLET combustor discussed in Sec. 5.1. The system identification results were robust and aligned with the harmonic analysis, thereby demonstrating the applicability of the methodology to spray flames, where prior work is scarce [147]. Nevertheless, various challenges were encountered in the LES of these types of flames, including spray and turbulence-combustion modeling under high pressure, modeling and resolution of effusion cooling, and external excitation under high pressure. Further in-depth investigations are required to fully address these issues.

3. The entropy transfer functions identified in PAPER-PP [83] and PAPER-FP [80] may be integrated into low-order network models of the underlying test rig. These LOMs require models for choked nozzles at the combustor outlet, as discussed in Sec. 5.3.3, to investigate the entropy-acoustic conversion and therefore predict whether the system is thermoacoustically unstable due to entropy-acoustic modes. The entropy response currently relies on "observations" of temperature fluctuations at a specific position within the combustor, similar to experimental measurements [61, 119, 324, 327], and therefore inherently includes the information about entropy wave transport up to the respective point of observation. Future work needs to focus on determining the entropy response based on the "source" of temperature fluctuations, which entails identifying the source term of entropy wave generation. The source term is then, together with a simple convection-diffusion model [6, 25, 324] for entropy wave transport, integrated into the LOM of the test rig, thereby making the model independent of the combustion chamber geometry. This approach requires the evaluation of the derived entropy source terms from the PAPER-ALE [213] by means of numerical simulations. One challenge is that the majority of CFD solvers operate within the Eulerian framework, whereas evaluating the entropy wave source terms necessitates the tracking of the local source within the arbitrary Eulerian-Lagrangian framework. The corresponding coordinate transform (see PAPER-ALE [213] for more information) introduces an additional source term, including the local flame displacement speed, which is directly related to the local flame speed [318]. This additional source term requires closure. In laminar flows, the laminar flame speed can be computed from the kinetics of the reaction mechanism. In turbulent reacting flows, many established combustion models, such as the G-equation model [100, 239], the thickened flame model [38], and the turbulent flame speed closure [241], approximate the turbulent flame speed as a function of the laminar flame speed. Given that "the devil is sometimes in the details", it is evident that the numerical application of the analytical framework proposed in the PAPER-ALE [213] requires further investigation.

In the future, incorporating these advancements into the thermoacoustic design process of new combustors will enable the mitigation of thermoacoustic combustion instability early in the gas turbine development program. More reliable predictions of flame dynamics and respective thermoacoustic interaction mechanisms can be achieved by leveraging advanced models and methodologies applied, improved, and developed in the present work. Ultimately, these improvements will contribute to the development of stable, efficient, and low-emission gas turbines that will bridge energy needs and the climate goals specified in the Paris Agreement.

7 Summary of papers

This chapter presents a summary of five selected peer-reviewed journal and conference papers carried out in the frame of this doctoral project. The papers published between 2023 and 2025 are not listed in chronological order, but rather in a way that follows the path of the contextualization and discussion in Chapter 5. In addition, the authors' contributions to each paper are indicated using the Contributor Roles Taxonomy (CRediT).

7.1 Model-based inference of flame transfer matrices from acoustic measurements in an aero-engine test rig

Label: PAPER-MBI [84]

Original abstract: Flame dynamics, represented as a flame transfer matrix (FTM), is not directly measurable in test rigs and must be deduced from transfer matrix measurements of the combustion system. The burner-flame transfer matrix (BFTM) approach for FTM estimation is based on local pressure signals from microphones located upstream and downstream of the combustor. It combines acoustic measurements in non-reacting and reacting conditions, with the latter implicitly including flame dynamics. A simple matrix operation yields the FTM. However, this approach assumes loss-free wave propagation at constant speed of sound with no change in cross-sectional area between the microphones and the burner/flame. The present work demonstrates the limitations of these assumptions when applied to a test rig with effusion cooling, bypass annulus, and end contraction. This work proposes a method to infer the FTM for complex combustors by combining reactive transfer matrix measurements of the entire combustor with an accurate low-order model (LOM) of the test rig. This generalized method reduces to the BFTM approach as a special case. The Rolls-Royce SCARLET test rig, operating under realistic engine conditions, is used to analyze the capabilities of the proposed model-based inference method and the limitations of the BFTM approach. First, a LOM based on SCARLET's geometry and operating point is formulated using a generic FTM. This model visualizes the limitations of the BFTM approach concerning various physical and geometrical parameters. Finally, experimental data is used to infer the FTM of SCARLET using the proposed approach.

Relevance for the thesis: This paper presents a network model-based approach for the consistent determination of flame response from acoustic measurements in engine-like thermoacoustic test rigs.

CRediT author statement: A. J. Eder: Conceptualization, Methodology, Software, Validation, Formal analysis, Investigation, Data curation, Writing - original draft, Writing - review & editing, Visualization, Project administration. **M. Merk:** Conceptualization, Methodology, Software, Validation, Formal analysis, Investigation, Data curation, Writing - original draft, Writing - review & editing, Visualization. **T. Hollweck:** Conceptualization, Software, Validation, Formal analysis, Investigation, Data curation, Writing - review & editing, Visualization. **A. Fischer:** Conceptualization, Validation, Formal analysis, Investigation, Data curation, Writing - review & editing draft. **C. Lahiri:** Conceptualization, Validation, Formal analysis, Investigation, Data curation, Writing - review & editing draft. **C. F. Silva:** Conceptualization, Writing - review & editing draft. **W. Polifke:** Conceptualization, Writing - review & editing, Supervision, Funding acquisition.

Status: Published in *Journal of Engineering for Gas Turbines and Power*.

Review process: Peer-reviewed, Scopus indexed, Web of Science indexed.

7.1 Model-based inference of flame transfer matrices from acoustic measurements in an aero-engine test rig

Comments: A first version of this publication was presented at the *ASME Turbo Expo 2024: Turbomachinery Technical Conference and Exposition* in London, UK, and published in the respective proceedings [84]. Parts of this publication were previously presented at the *Symposium on Thermoacoustics in Combustion* [81] in Zurich, Switzerland.

7.2 Incompressible versus compressible large eddy simulation for the identification of premixed flame dynamics

Label: PAPER-FTF [82]

Original abstract: The present work compares the respective advantages and disadvantages of compressible and incompressible computational fluid dynamics (CFD) formulations when used for the estimation of the acoustic flame response. The flame transfer function of a turbulent premixed swirl-stabilized burner is determined by applying system identification (SI) to time series data extracted from large eddy simulation (LES). By analyzing the quality of the results, the present study shows that incompressible simulations exhibit several advantages over their compressible counterpart with equal prediction of the flame dynamics. On the one hand, the forcing signals can be designed in such a way that desired statistical properties can be enhanced, while maintaining optimal values in the amplitude. On the other hand, computational costs are reduced and the implementation is fundamentally simpler due to the absence of acoustic wave propagation and corresponding resonances in the flame response or even self-excited acoustic oscillations. Such an increase in efficiency makes the incompressible CFD/SI modeling approach very appealing for the study of a wide variety of systems that rely on premixed combustion. In conclusion, the present study reveals that both methodologies predict the same flame dynamics, which confirms that incompressible simulation can be used for thermoacoustic analyses of acoustically compact velocity-sensitive flames.

Relevance for the thesis: This paper compares compressible and incompressible LES formulations for the identification of premixed flame dynamics. The comparison reveals that both methodologies are valid for this type of analysis; however, incompressible LES is found to be preferable due to its numerically easier handling.

CRediT author statement: A. J. Eder: Conceptualization, Methodology, Software, Validation, Formal analysis, Investigation, Data curation, Writing - original draft, Writing - review & editing, Visualization, Project administration. **C. F. Silva:** Conceptualization, Investigation, Writing - review & editing, Supervision. **Matthias Haeringer:** Conceptualization, Investigation, Writing - review & editing. **J. Kuhlmann:** Conceptualization, Writing - review & editing. **W. Polifke:** Conceptualization, Writing - review & editing, Supervision, Funding acquisition.

Status: Published in *International Journal of Spray and Combustion Dynamics*.

Review process: Peer-reviewed, Scopus indexed, Web of Science indexed.

Reference: <u>A. J. Eder</u>, C. F. Silva, M. Haeringer, J. Kuhlmann, and W. Polifke. Incompressible versus compressible large eddy simulation or the identification of premixed flame dynamics. *International Journal of Spray and Combustion Dynamics* 15(1):16–31, 2023. DOI: 10.1177/17568277231154204. Reproduced on p. 91 ff.

7.3 Identification of entropy waves in a partially premixed combustor

Label: PAPER-PP [83]

Original abstract: Unsteady combustion generates not only acoustic waves, but also fluctuations of the burnt gas temperature - referred to as entropy waves. These waves are convected by the mean flow through the combustor and result in conversion to acoustic energy when accelerated in an exit nozzle. The upstream traveling acoustic wave can then couple with the unsteady heat release of the flame and cause self-excited thermoacoustic instability, particularly at low frequencies ("rumble"). In this work, large eddy simulation (LES) is combined with system identification (SI) to determine the entropy transfer function (ETF) of a partially premixed, swirl-stabilized flame with hydrogen enrichment. We compare the single-input single-output (SISO) entropy transfer function identified from a broadband-forced LES with air mass flow modulation to the one obtained experimentally through tunable diode laser absorption spectroscopy with wavelength modulation spectroscopy (TDLAS-WMS) to measure temperature fluctuations. Then, multiple-input single-output (MISO) identification is applied to time series data obtained from simultaneous modulation of air and fuel mass flow to estimate the individual contributions of perturbations in velocity and equivalence ratio to entropy response. Equivalence ratio fluctuations are found to be the dominant generation mechanism of entropy waves. Finally, the entropy transfer function is identified at various positions in the combustion chamber to analyze the decay of entropy waves governed by convective dispersion.

Relevance for the thesis: This paper extends the methodology of PAPER-FP [80] to partially premixed flames. It confirms that equivalence ratio fluctuations are the dominant excitation mechanisms in partially premixed flames and reveals notable entropy wave strength at the combustor exit, potentially leading to thermoacoustic combustion instability and/or indirect combustion noise.

CRediT author statement: A. J. Eder: Conceptualization, Methodology, Software, Validation, Formal analysis, Investigation, Data curation, Writing - original draft, Writing - review & editing, Visualization, Project administration. **B. Dharmaputra:** Conceptualization, Validation, Formal analysis, Investigation, Data curation, Writing - review & editing. **A. M. Garcia:** Conceptualization, Methodology, Software, Writing - review & editing. **C. F. Silva:** Conceptualization, Writing - review & editing. **W. Polifke:** Conceptualization, Validation, Writing - review & editing, Supervision, Funding acquisition.

Status: Published in *Proceedings of the Combustion Institute*.

Review process: Peer-reviewed, Scopus indexed, Web of Science indexed.

Reference: A. J. Eder, B. Dharmaputra, A. M. Garcia, C. F. Silva, and W. Polifke. Identification of entropy waves in a partially premixed combustor. *Proceedings of the Combustion Institute* 40(1–4):105609, 2024. DOI:10.1016/j.proci.2024.105609, reproduced on p. 108 ff.

Comment: This publication was presented at the *Combustion Institute's 40th International Symposium* in Milan, Italy.

7.4 Generation of entropy waves by fully premixed flames in a non-adiabatic combustor with hydrogen enrichment

Label: PAPER-FP [80]

Original abstract: Thermoacoustic combustion instability is a major concern in gas turbine combustors with hydrogen-enriched fuels. Unsteady combustion not only generates acoustic waves but it may also result in fluctuations of burnt gas temperature, referred to as entropy waves. They are convected by the mean flow through the combustor and can cause indirect combustion noise when they are accelerated at the exit. In this work, we demonstrate that entropy waves occur in a fully premixed burner due to unsteady heat transfer at the combustion chamber wall. This mechanism of entropy generation is often neglected in the literature. This work shows an additional mechanism in CH_4-H_2-air flames, through which entropy may be created even in the fully premixed case. This is due to differential diffusion which generates local fluctuations in equivalence and carbon-to-hydrogen ratios. An adiabatic flame temperature is defined based on these two quantities to examine the influence of differential diffusion on the generation of entropy fluctuations. The generation of entropy waves is investigated by applying system identification (SI) to time series data obtained from a broadband forced large eddy simulation (LES) coupled with a heat conduction solver. The entropy transfer function (ETF) and flame transfer function (FTF) identified with LES/SI are then compared to experimental data obtained with tunable diode laser absorption spectroscopy with wavelength modulation spectroscopy (TDLAS-WMS) for measuring temperature fluctuations, and the multimicrophone method, respectively. After validating the computational setup, the entropy frequency response is identified at various positions within the combustion chamber, and the effects of generation and convective dispersion of entropy waves are qualitatively investigated. We show that a fully premixed turbulent system may exhibit significant entropy waves caused by wall heat losses and differential diffusion of hydrogen.

Relevance for the thesis: This paper takes advantage of the incompressible LES/SI approach studied in PAPER-FTF [82] and applies it to the identification of entropy response. It analyzes two sources of entropy waves in fully premixed combustion with hydrogen enrichment, namely wall heat losses and differential diffusion.

CRediT author statement: A. J. Eder: Conceptualization, Methodology, Software, Validation, Formal analysis, Investigation, Data curation, Writing - original draft, Writing - review & editing, Visualization, Project administration. **B. Dharmaputra:** Conceptualization, Validation, Formal analysis, Investigation, Data curation, Writing - review & editing. **M. Désor:** Conceptualization, Software, Investigation, Writing - review & editing. **A. M. Garcia:** Conceptualization, Methodology, Writing - review & editing. **C. F. Silva:** Conceptualization, Writing - review & editing. **B. Schuermans:** Conceptualization, Investigation, Writing - review & editing. **N. Noiray:** Conceptualization, Writing - review & editing, Supervision. **W. Polifke:** Conceptualization, Writing - review & editing, Supervision, Funding acquisition.

Status: Published in *Journal of Engineering for Gas Turbines and Power*.

Review process: Peer-reviewed, Scopus indexed, Web of Science indexed.

Reference: <u>A. J. Eder</u>, B. Dharmaputra, M. Désor, A. M. Garcia, C. F. Silva, B. Schuermans,

7.4 Generation of entropy waves by fully premixed flames in a non-adiabatic combustor with hydrogen enrichment

Comments: A first version of this publication was presented at the *ASME Turbo Expo 2023: Turbomachinery Technical Conference and Exposition* in Boston, Massachusetts, USA, and published in the respective proceedings [79]. This publication received the Best Paper Award from the Combustion, Fuels and Emissions Committee.

7.5 An arbitrary Lagrangian-Eulerian framework for the consistent analysis of entropy wave generation

Label: PAPER-ALE [213]

Original abstract: Entropy waves are generated in many technically relevant flow processes such as combustion, mixing, or convective heat transfer. When accelerated, entropy waves generate acoustic waves that contribute to the overall sound emission and can lead to self-excited thermoacoustic instabilities, especially at low frequencies. In order to reduce or prevent these undesirable byproducts of the flow, an understanding of the generation mechanisms of entropy waves is key. This study derives the analytical source terms of entropy disturbances for moving sources in general three-dimensional reactive flows. In this general setup, the consistent derivation of the generation mechanisms requires the tracking of the moving source for which an Arbitrary Lagrangian-Eulerian (ALE) framework is utilized. The derived differential equations provide a fundamental understanding of the underlying source mechanisms. In addition, the general three-dimensional differential equations are reduced to a quasi-one-dimensional jump condition to unify the analysis of the entropy wave generation. This unified framework is used for an in-depth analysis of a premixed flame, where all source terms that generate entropy disturbances are analyzed and their relative importance are quantified. The dominant contribution of unsteady heat addition per unit mass to the generation of entropy waves is reaffirmed for lean premixed flames. Finally, by comparison with the entropy generation mechanisms of a heated gauze at rest, it is emphasized once more that a heat source at rest is an invalid model for a premixed flame.

Relevance for the thesis: This paper consistently derives the sources of entropy wave generation in general three-dimensional reactive flows using an Arbitrary Lagrangian-Eulerian framework. These sources are quantitatively investigated for fully and partially premixed flames in PAPER-FP [80] and PAPER-PP [83], respectively.

CRediT author statement: M. Merk: Conceptualization, Methodology, Validation, Formal analysis, Writing - original draft, Writing - review & editing, Visualization. **A. J. Eder:** Conceptualization, Methodology, Validation, Formal analysis, Writing - original draft, Writing - review & editing, Visualization, Project administration. **W. Polifke:** Conceptualization, Methodology, Validation, Writing - review & editing, Supervision, Funding acquisition.

Status: Published in *Combustion and Flame*.

Review process: Peer-reviewed, Scopus indexed, Web of Science indexed.

Bibliography

[1] M. Åbom. A note on the experimental determination of acoustical two-port matrices. *Journal of Sound and Vibration*, 155(1):185–188, 1992. DOI: 10.1016/0022-460X(92)90655-H.

[2] P. W. Agostinelli. *Assessment of large eddy simulation in the conjugate heat transfer context for engine operability: application to hydrogen enrichment and spinning combustion technology.* Ph.D. thesis, Institut national polytechnique de Toulouse, Toulouse, France, 2022.

[3] P. W. Agostinelli, D. Laera, I. Chterev, I. Boxx, L. Gicquel, and T. Poinsot. Large eddy simulations of mean pressure and H2 addition effects on the stabilization and dynamics of a partially-premixed swirled-stabilized methane flame. *Combustion and Flame*, 249: 112592, 2023. DOI: 10.1016/j.combustflame.2022.112592.

[4] Air Transport Action Group. Waypoint 2050 2nd edition. URL: `https://atag.org/resources/waypoint-2050-2nd-edition-september-2021`, 2021. Accessed on: June 1, 2024.

[5] Ç. O. Alanyalıoğlu, H. Reinhardt, A. Fischer, C. Lahiri, H. Nicolai, and C. Hasse. Comparison of acoustic, optical, and heat release rate based flame transfer functions for a lean-burn injector under engine-like conditions. *International Journal of Spray and Combustion Dynamics*, 16(3):153–173, 2024. DOI: 10.1177/17568277241270403.

[6] A. Albayrak, R. S. Blumenthal, A. Ulhaq, and W. Polifke. An analytical model for the impulse response of laminar premixed flames to equivalence ratio perturbations. *Proceedings of the Combustion Institute*, 36(3):3725–3732, 2017. DOI: 10.1016/j.proci.2016.06.002.

[7] A. Albayrak, T. Steinbacher, T. Komarek, and W. Polifke. Convective scaling of intrinsic thermo-acoustic eigenfrequencies of a premixed swirl combustor. *Journal of Engineering for Gas Turbines and Power*, 140(4):041510, 2018. DOI: 10.1115/1.4038083.

[8] P. R. Alemela, D. Fanaca, F. Ettner, C. Hirsch, T. Sattelmayer, and B. Schuermans. Flame transfer matrices of a premixed flame and a global check with modelling and experiments. In *ASME Turbo Expo 2008: Power for Land, Sea, and Air*, volume 3A: Combustion, Fuels and Emissions, Parts A and B, pages 11–19, Berlin, Germany, 2008. American Society of Mechanical Engineers. DOI: 10.1115/GT2008-50111.

[9] M. S. Anand, R. Eggels, M. Staufer, M. Zedda, and J. Zhu. An advanced unstructured-grid finite-volume design system for gas turbine combustion analysis. In *ASME 2013 Gas Turbine India Conference*, page V001T03A003, Bangalore, India, 2014. American Society of Mechanical Engineers. DOI: 10.1115/GTINDIA2013-3537.

[10] J. D. Anderson and C. P. Cadou. *Fundamentals of aerodynamics*. McGraw Hill series in aeronautical and aerospace engineering. McGraw-Hill, New York, NY, USA, 7th edition, 2024. ISBN 978-1-266-07644-2.

[11] A. Andreini, B. Facchini, A. Giusti, and F. Turrini. Assessment of flame transfer function formulations for the thermoacoustic analysis of lean burn aero-engine combustors. *Energy Procedia*, 45:1422–1431, 2014. DOI: 10.1016/j.egypro.2014.01.149.

[12] M. P. Auer, C. Hirsch, and T. Sattelmayer. Influence of air and fuel mass flow fluctuations in a premix swirl burner on flame dynamics. In *ASME Turbo Expo 2006: Power for Land, Sea, and Air*, volume 1: Combustion and Fuels, Education, pages 97–106, Barcelona, Spain, 2006. American Society of Mechanical Engineers. DOI: 10.1115/GT2006-90127.

[13] A. Avdonin, A. Javareshkian, and W. Polifke. Prediction of premixed flame dynamics using LES with tabulated chemistry and Eulerian stochastic fields. *Journal of Engineering for Gas Turbines and Power*, 141(11):111024, 2019. DOI: 10.1115/GT2019-90140.

[14] S. Bade, M. Wagner, C. Hirsch, T. Sattelmayer, and B. Schuermans. Influence of fuel-air mixing on flame dynamics of premixed swirl burners. In *ASME Turbo Expo 2014: Turbine Technical Conference and Exposition*, volume 4A: Combustion, Fuels and Emissions, page V04AT04A023, Düsseldorf, Germany, 2014. American Society of Mechanical Engineers. DOI: 10.1115/GT2014-25381.

[15] F. Bake, C. Richter, B. Mühlbauer, N. Kings, I. Röhle, F. Thiele, and B. Noll. The entropy wave generator (EWG): a reference case on entropy noise. *Journal of Sound and Vibration*, 326(3):574–598, 2009. DOI: 10.1016/j.jsv.2009.05.018.

[16] R. Balachandran, B. O. Ayoola, C. F. Kaminski, A. P. Dowling, and E. Mastorakos. Experimental investigation of the nonlinear response of turbulent premixed flames to imposed inlet velocity oscillations. *Combustion and Flame*, 143(1–2):37–55, 2005. DOI: 10.1016/j.combustflame.2005.04.009.

[17] M. Bauerheim, I. Duran, T. Livebardon, G. Wang, S. Moreau, and T. Poinsot. Transmission and reflection of acoustic and entropy waves through a stator-rotor stage. *Journal of Sound and Vibration*, 374:260–278, 2016. DOI: 10.1016/j.jsv.2016.03.041.

[18] D. W. Bechert. Sound absorption caused by vorticity shedding, demonstrated with a jet flow. *Journal of Sound and Vibration*, 70(3):389–405, 1980. DOI: 10.1016/0022-460X(80)90307-7.

[19] V. Bellucci, C. O. Paschereit, and P. Flohr. Impedance of perforated screens with bias flow. In *8th AIAA/CEAS Aeroacoustics Conference*, Breckenridge, CO, USA, 2002. American Institute of Aeronautics and Astronautics. DOI: 10.2514/6.2002-2437.

[20] V. Bellucci, P. Flohr, and C. O. Paschereit. Numerical and experimental study of acoustic damping generated by perforated screens. *AIAA Journal*, 42(8):1543–1549, 2004. DOI: 10.2514/1.9841.

[21] V. Bellucci, P. Flohr, C. O. Paschereit, and F. Magni. On the use of Helmholtz resonators for damping acoustic pulsations in industrial gas turbines. *Journal of Engineering for Gas Turbines and Power*, 126(2):271–275, 2004. DOI: 10.1115/1.1473152.

[22] J. P. Beuth, J. M. Reumschüssel, J. G. R. von Saldern, D. Wassmer, B. Ćosić, C. O. Paschereit, and K. Oberleithner. Thermoacoustic characterization of a premixed multi jet burner for hydrogen and natural gas combustion. *Journal of Engineering for Gas Turbines and Power*, 146(4):041007, 2024. DOI: 10.1115/1.4063692.

[23] A. Blondé, B. Schuermans, K. Pandey, and N. Noiray. Effect of hydrogen enrichment on transfer matrices of fully and technically premixed swirled flames. *Journal of Engineering for Gas Turbines and Power*, 145(12):121009, 2023. DOI: 10.1115/1.4063415.

[24] B. C. Bobusch, J. P. Moeck, C. O. Paschereit, and S. Sadig. Thermoacoustic stability analysis of a kerosene-fueled lean direct injection combustor employing acoustically and optically measured transfer matrices. In *ASME Turbo Expo 2012: Turbine Technical Conference and Exposition*, volume 2: Combustion, Fuels and Emissions, Parts A and B, pages 781–794, Copenhagen, Denmark, 2012. American Society of Mechanical Engineers. DOI: 10.1115/GT2012-69034.

[25] B. C. Bobusch, B. Ćosić, J. P. Moeck, and C. Oliver Paschereit. Optical measurement of local and global transfer functions for equivalence ratio fluctuations in a turbulent swirl flame. *Journal of Engineering for Gas Turbines and Power*, 136(2):021506, 2013. DOI: 10.1115/1.4025375.

[26] D. Bohn and E. Deuker. An acoustical model to predict combustion driven oscillations. In *20th CIMAC International Congress on Combustion Engines*, London, UK, 1993. CIMAC.

[27] D. Bohn, G. Deutsch, and U. Krüger. Numerical prediction of the dynamic behaviour of turbulent diffusion flames. In *ASME 1996 International Gas Turbine and Aeroengine Congress and Exhibition*, volume 3: Coal, Biomass and Alternative Fuels; Combustion and Fuels; Oil and Gas Applications; Cycle Innovations, page V003T06A024, Birmingham, UK, 1996. American Society of Mechanical Engineers. DOI: 10.1115/96-GT-133.

[28] D. Bohn, Y. Li, G. Matouschek, and U. Krüger. Numerical prediction of the dynamic behaviour of premixed flames using systematically reduced multi-step reaction mechanism. In *ASME 1997 International Gas Turbine and Aeroengine Congress and Exhibition*, volume 2: Coal, Biomass and Alternative Fuels; Combustion and Fuels; Oil and Gas Applications; Cycle Innovations, page V002T06A034, Orlando, FL, USA, 1997. American Society of Mechanical Engineers. DOI: 10.1115/97-GT-265.

[29] S. Bomberg, T. Emmert, and W. Polifke. Thermal versus acoustic response of velocity sensitive premixed flames. *Proceedings of the Combustion Institute*, 35(3):3185–3192, 2015. DOI: 10.1016/j.proci.2014.07.032.

[30] M. Bothien, J. P. Moeck, A. Lacarelle, and C. O. Paschereit. Time domain modelling and stability analysis of complex thermoacoustic systems. *Proceedings of the Institution of Mechanical Engineers, Part A: Journal of Power and Energy*, 221(5):657–668, 2007. DOI: 10.1243/09576509JPE384.

[31] M. Bothien, D. Lauper, Y. Yang, and A. Scarpato. Reconstruction and analysis of the acoustic transfer matrix of a reheat flame from large-eddy simulations. *Journal of Engineering for Gas Turbines and Power*, 141(2):021018, 2018. DOI: 10.1115/1.4041151.

[32] G. E. Box and G. C. Tiao. *Bayesian inference in statistical analysis*. Wiley, New York, NY, USA, 1992. ISBN 978-0-471-57428-6.

[33] L. Boyer and J. Quinard. On the dynamics of anchored flames. *Combustion and Flame*, 82(1):51–65, 1990. DOI: 10.1016/0010-2180(90)90077-5.

[34] S. M. Camporeale, B. Fortunato, and G. Campa. A finite element method for three-dimensional analysis of thermo-acoustic combustion instability. *Journal of Engineering for Gas Turbines and Power*, 133(1):011506, 2011. DOI: 10.1115/1.4000606.

[35] S. Candel. *Analytical studies of some acoustic problems of fet engines*. Ph.D. thesis, California Institute of Technology, Pasadena, CA, USA, 1972.

[36] S. Candel. Combustion dynamics and control: Progress and challenges. *Proceedings of the Combustion Institute*, 29(1):1–28, 2002. DOI: 10.1016/S1540-7489(02)80007-4.

[37] A. Ceci, R. Gojon, and M. Mihaescu. Large eddy simulations for indirect combustion noise assessment in a nozzle guide vane passage. *Flow, Turbulence and Combustion*, 102 (2):299–311, 2019. DOI: 10.1007/s10494-018-9964-9.

[38] F. Charlette, C. Meneveau, and D. Veynante. A power-law flame wrinkling model for LES of premixed turbulent combustion part I: non-dynamic formulation and initial tests. *Combustion and Flame*, 131(1):159–180, 2002. DOI: 10.1016/S0010-2180(02)00400-5.

[39] Y. Chen, L. J. Ayton, and D. Zhao. Modelling of intrinsic thermoacoustic instability of premixed flame in combustors with changes in cross section. *Combustion Science and Technology*, 192(5):832–851, 2019. DOI: 10.1080/00102202.2019.1594799.

[40] Z. X. Chen, I. Langella, N. Swaminathan, M. Stöhr, W. Meier, and H. Kolla. Large eddy simulation of a dual swirl gas turbine combustor: Flame/flow structures and stabilisation under thermoacoustically stable and unstable conditions. *Combustion and Flame*, 203: 279–300, 2019. DOI: 10.1016/j.combustflame.2019.02.013.

[41] L. Christodoulou, N. Karimi, A. Cammarano, M. Paul, and S. Navarro-Martinez. State prediction of an entropy wave advecting through a turbulent channel flow. *Journal of Fluid Mechanics*, 882:A8, 2020. DOI: 10.1017/jfm.2019.799.

[42] I. Chterev and I. Boxx. Effect of hydrogen enrichment on the dynamics of a lean technically premixed elevated pressure flame. *Combustion and Flame*, 225:149–159, 2021. DOI: 10.1016/j.combustflame.2020.10.033.

[43] J. Y. Chung and D. A. Blaser. Transfer function method of measuring in-duct acoustic properties. I. Theory. *Journal of the Acoustical Society of America*, 68(3):907–913, 1980. DOI: 10.1121/1.384778.

[44] B. Ćosić, J. P. Moeck, and C. O. Paschereit. Nonlinear instability analysis for partially premixed swirl flames. *Combustion Science and Technology*, 186(6):713–736, 2014. DOI: 10.1080/00102202.2013.876420.

[45] B. Ćosić, S. Terhaar, J. P. Moeck, and C. O. Paschereit. Response of a swirl-stabilized flame to simultaneous perturbations in equivalence ratio and velocity at high oscillation amplitudes. *Combustion and Flame*, 162(4):1046–1062, 2015. DOI: 10.1016/j.combustflame.2014.09.025.

[46] E. Courtine, L. Selle, and T. Poinsot. DNS of intrinsic thermoacoustic modes in laminar premixed flames. *Combustion and Flame*, 162(11):4331–4341, 2015. DOI: 10.1016/j.combustflame.2015.07.002.

[47] L. Cremer. The second annual Fairey lecture: the treatment of fans as black boxes. *Journal of Sound and Vibration*, 16(1):1–15, 1971. DOI: 10.1016/0022-460X(71)90391-9.

[48] L. Crocco. Aspects of combustion stability in liquid propellant rocket motors. Part II: low frequency instability with bipropellants. High frequency instabilitiy. *Journal of American Rocket Society*, 22(1):7–16, 1952. DOI: 10.2514/8.4410.

[49] F. E. Culick. *Unsteady motions in combustion chambers for propulsion systems*. RTO AGARDograph. Research and Technology Organisation/North Atlantic Treaty Organisation, Neuilly-sur-Seine Cedex, France, 2006. ISBN 92-837-0059-7.

[50] N. A. Cumpsty and F. E. Marble. The generation of noise by the fluctuations in gas temperature into a turbine. Cambridge University Engineering Laboratory Report CUED/A TURBO/TR57, Cambridge, UK, 1974.

[51] G. Daviller, G. Oztarlik, and T. Poinsot. A generalized non-reflecting inlet boundary condition for steady and forced compressible flows with injection of vortical and acoustic waves. *Computers & Fluids*, 190:503–513, 2019. DOI: 10.1016/j.compfluid.2019.06.027.

[52] N. Davis. Kofi Annan: We must challenge climate-change sceptics who deny the facts. *The Guardian*, URL: https://www.theguardian.com/environment/2015/may/03/kofi-annan-interview-climate-change-paris-summit-sceptics?CMP=share_btn_url, 2015. Accessed on: June 1, 2024.

[53] J. de Charentenay, D. Thévenin, and B. Zamuner. Comparison of direct numerical simulations of turbulent flames using compressible or low-Mach number formulations. *International Journal for Numerical Methods in Fluids*, 39(6):497–515, 2002. DOI: 10.1002/fld.341.

[54] F. De Domenico, E. O. Rolland, and S. Hochgreb. Detection of direct and indirect noise generated by synthetic hot spots in a duct. *Journal of Sound and Vibration*, 394:220–236, 2017. DOI: 10.1016/j.jsv.2017.01.004.

[55] F. De Domenico, E. O. Rolland, and S. Hochgreb. A generalised model for acoustic and entropic transfer function of nozzles with losses. *Journal of Sound and Vibration*, 440: 212–230, 2019. DOI: 10.1016/j.jsv.2018.09.011.

[56] F. De Domenico, E. O. Rolland, J. Rodrigues, L. Magri, and S. Hochgreb. Compositional and entropy indirect noise generated in subsonic non-isentropic nozzles. *Journal of Fluid Mechanics*, 910:A5, 2021. DOI: 10.1017/jfm.2020.916.

[57] M. Désor, A. J. Eder, C. F. Silva, and W. Polifke. Influence of wall-to-wall radiative heat transfer on premixed flame dynamics. In *Symposium on Thermoacoustics in Combustion: Industry meets Academia*, Zurich, Switzerland, 2023.

[58] M. Désor, M. Haeringer, M. Hiestermann, K. K. Niebler, C. F. Silva, and W. Polifke. Application of an improved workflow for the identification of flame dynamics to swirl stabilized WET combustion. *Journal of Engineering for Gas Turbines and Power*, 147 (3):031003, 2025. DOI: 10.1115/1.4066364.

[59] Deutsche Forschungsgemeinschaft. Knowledge transfer. URL: `https://www.dfg.de/en/research-funding/funding-initiative/knowledge-transfer`, 2023. Accessed on: June 1, 2024.

[60] Deutscher Wetterdienst. Time series and trends. URL: `https://www.dwd.de/EN/ourservices/zeitreihen/zeitreihen.html`, 2024. Accessed on: June 1, 2024.

[61] B. Dharmaputra, S. Shcherbanev, A. Blondé, B. Schuermans, and N. Noiray. Entropy transfer function measurement with tunable diode laser absorption spectroscopy. *Proceedings of the Combustion Institute*, 39(4):4621–4630, 2022. DOI: 10.1016/j.proci.2022.07.083.

[62] G. Doehner, M. Haeringer, and C. F. Silva. Nonlinear flame response modelling by a parsimonious set of ordinary differential equations. *International Journal of Spray and Combustion Dynamics*, 14(1-2):17–29, 2022. DOI: 10.1177/17568277221094760.

[63] G. Doehner, A. J. Eder, and C. F. Silva. A parsimonious system of ordinary differential equations for the response modeling of turbulent swirled flames. *Combustion and Flame*, 266:113408, 2024. DOI: 10.1016/j.combustflame.2024.113408.

[64] J. Dombard, T. Poinsot, V. Moureau, N. Savary, G. Staffelbach, and V. Bodoc. Experimental and numerical study of the influence of small geometrical modifications on the dynamics of swirling flows. In *Proceedings of the Summer Program 2012*, pages 469–482, Stanford, CA, USA, 2012. Center for Turbulence Research.

[65] J. Donéa and A. Huerta. *Finite element methods for flow problems*. Wiley, Hoboken, NJ, USA, 2003. ISBN 978-0-471-49666-3.

[66] Q. Douasbin, C. Scalo, L. Selle, and T. Poinsot. Delayed-time domain impedance boundary conditions (D-TDIBC). *Journal of Computational Physics*, 371:50–66, 2018. DOI: 10.1016/j.jcp.2018.05.003.

[67] A. P. Dowling. Nonlinear self-excited oscillations of a ducted flame. *Journal of Fluid Mechanics*, 346:271–290, 1997. DOI: 10.1017/S0022112097006484.

[68] A. P. Dowling and Y. Mahmoudi. Combustion noise. *Proceedings of the Combustion Institute*, 35(1):65–100, 2015. DOI: 10.1016/j.proci.2014.08.016.

[69] A. P. Dowling and S. R. Stow. Acoustic analysis of gas turbine combustors. *Journal of Propulsion and Power*, 19(5):751–764, 2003. DOI: 10.2514/2.6192.

[70] S. Ducruix, D. Durox, and S. Candel. Theoretical and experimental determinations of the transfer function of a laminar premixed flame. *Proceedings of the Combustion Institute*, 28(1):765–773, 2000. DOI: 10.1016/S0082-0784(00)80279-9.

[71] S. Ducruix, T. Schuller, D. Durox, and b. Candel. Combustion dynamics and instabilities: elementary coupling and driving mechanisms. *Journal of Propulsion and Power*, 19(5): 722–734, 2003. DOI: 10.2514/2.6182.

[72] I. D. Dupère and A. P. Dowling. The use of Helmholtz resonators in a practical combustor. *Journal of Engineering for Gas Turbines and Power*, 127(2):268–275, 2005. DOI: 10.1115/1.1806838.

[73] I. Duran and S. Moreau. Numerical simulation of acoustic and entropy waves propagating through turbine blades. In *19th AIAA/CEAS Aeroacoustics Conference*, Berlin, Germany, 2013. American Institute of Aeronautics and Astronautics. DOI: 10.2514/6.2013-2102.

[74] I. Duran, S. Moreau, F. Nicoud, T. Livebardon, E. Bouty, and T. Poinsot. Combustion noise in modern aero-engines. *AerospaceLab*, (7):1–11, 2014. DOI: 10.12762/2014.AL07-05.

[75] L. Durand. *Development, implementation and validation of LES models for inhomogeneously premixed turbulent combustion*. Ph.D. thesis, Technische Universität München, Munich, Germany, 2007.

[76] D. Durox, T. Schuller, and S. Candel. Self-induced instability of a premixed jet flame impinging on a plate. *Proceedings of the Combustion Institute*, 29(1):69–75, 2002. DOI: 10.1016/S1540-7489(02)80013-X.

[77] J. Eckstein and T. Sattelmayer. Low-order modeling of low-frequency combustion instabilities in aeroengines. *Journal of Propulsion and Power*, 22(2):425–432, 2006. DOI: 10.2514/1.15757.

[78] J. Eckstein, E. Freitag, C. Hirsch, and T. Sattelmayer. Experimental study on the role of entropy waves in low-frequency oscillations in a RQL combustor. *Journal of Engineering for Gas Turbines and Power*, 128(2):264–270, 2006. DOI: 10.1115/1.2132379.

[79] A. J. Eder, B. Dharmaputra, M. Désor, C. F. Silva, A. M. Garcia, B. Schuermans, N. Noiray, and W. Polifke. Generation of entropy waves by fully premixed flames in a non-adiabatic combustor with hydrogen enrichment. In *ASME Turbo Expo 2023 Turbomachinery Technical Conference and Exposition*, volume 3B: Combustion, Fuels, and Emissions, page V03BT04A009, Boston, MA, USA, 2023. American Society of Mechanical Engineers. DOI: 10.1115/GT2023-102833.

[80] A. J. Eder, B. Dharmaputra, M. Désor, C. F. Silva, A. M. Garcia, B. Schuermans, N. Noiray, and W. Polifke. Generation of entropy waves by fully premixed flames in a non-adiabatic combustor with hydrogen enrichment. *Journal of Engineering for Gas Turbines and Power*, 145(11):111001, 2023. DOI: 10.1115/1.4063283.

[81] A. J. Eder, A. Fischer, C. Lahiri, M. Merk, M. Staufer, R. Eggels, C. F. Silva, and W. Polifke. Identification of the dynamics of a turbulent spray flame at high pressure. In *Symposium on Thermoacoustics in Combustion: Industry meets Academia*, Zurich, Switzerland, 2023.

[82] A. J. Eder, C. F. Silva, M. Haeringer, J. Kuhlmann, and W. Polifke. Incompressible versus compressible large eddy simulation for the identification of premixed flame dynamics. *International Journal of Spray and Combustion Dynamics*, 15(1):16–32, 2023. DOI: 10.1177/17568277231154204.

[83] A. J. Eder, B. Dharmaputra, A. M. Garcia, S. F. Camilo, and W. Polifke. Identification of entropy waves in a partially premixed combustor. *Proceedings of the Combustion Institute*, 40(1–4):105609, 2024. DOI: 10.1016/j.proci.2024.105609.

[84] A. J. Eder, M. Merk, T. Hollweck, A. Fischer, C. Lahiri, C. F. Silva, and W. Polifke. Model-based inference of flame transfer matrices from acoustic measurements in an aero-engine test rig. In *ASME Turbo Expo 2024 Turbomachinery Technical Conference and Exposition*, volume 3A: Combustion, Fuels, and Emissions, page V03AT04A040, London, UK, 2024. American Society of Mechanical Engineers. DOI: 10.1115/GT2024-124263.

[85] A. J. Eder, M. Merk, T. Hollweck, A. Fischer, C. Lahiri, C. F. Silva, and W. Polifke. Model-based inference of flame transfer matrices from acoustic measurements in an aero-engine test rig. *Journal of Engineering for Gas Turbines and Power*, 147(3):031022, 2025. DOI: 10.1115/1.4066366.

[86] J. Eigemann, C. Beck, and A. Kempf. A method to dampen acoustic waves in compressible reactive flow simulations. *Flow, Turbulence and Combustion*, 2024. DOI: 10.1007/s10494-024-00542-6.

[87] J. D. Eldredge and A. P. Dowling. The absorption of axial acoustic waves by a perforated liner with bias flow. *Journal of Fluid Mechanics*, 485:307–335, 2003. DOI: 10.1017/S0022112003004518.

[88] T. Emmert. *State space modeling of thermoacoustic systems with application to intrinsic feedback*. Ph.D. thesis, Technische Universität München, Munich, Germany, 2016.

[89] T. Emmert, S. Bomberg, and W. Polifke. Intrinsic thermoacoustic instability of premixed flames. *Combustion and Flame*, 162(1):75–85, 2015. DOI: 10.1016/j.combustflame.2014.06.008.

[90] T. Emmert, M. Meindl, S. Jaensch, and W. Polifke. Linear state space interconnect modeling of acoustic systems. *Acta Acustica united with Acustica*, 102(5):824–833, 2016. DOI: 10.3813/AAA.918997.

[91] T. Emmert, S. Bomberg, S. Jaensch, and W. Polifke. Acoustic and intrinsic thermoa-coustic modes of a premixed combustor. *Proceedings of the Combustion Institute*, 36(3): 3835–3842, 2017. DOI: 10.1016/j.proci.2016.08.002.

[92] S. Evesque and W. Polifke. Low-order acoustic modelling for annular combustors: Val-idation and inclusion of modal coupling. In *ASME Turbo Expo 2002: Power for Land, Sea, and Air*, volume 1: Turbo Expo 2002, pages 321–331, Amsterdam, The Netherlands, 2002. American Society of Mechanical Engineers. DOI: 10.1115/GT2002-30064.

[93] A. Fattahi, S. M. Hosseinalipour, and N. Karimi. On the dissipation and dispersion of entropy waves in heat transferring channel flows. *Physics of Fluids*, 29(8):087104, 2017. DOI: 10.1063/1.4999046.

[94] G. Febrer, Z. Yang, and J. McGuirk. A hybrid approach for coupling of acoustic wave effects and incompressible LES of reacting flows. In *47th AIAA/ASME/SAE/ASEE Joint Propulsion Conference & Exhibit*, San Diego, CA, USA, 2011. American Institute of Aeronautics and Astronautics. DOI: 10.2514/6.2011-6127.

[95] J. H. Ferziger, M. Perić, and R. L. Street. *Computational methods for fluid dynamics*. Springer, Cham, Switzerland, 4th edition, 2020. ISBN 978-3-319-99691-2.

[96] J. E. Ffowcs Williams and M. S. Howe. The generation of sound by density inhomo-geneities in low Mach number nozzle flows. *Journal of Fluid Mechanics*, 70(3):605–622, 1975. DOI: 10.1017/S0022112075002224.

[97] L. V. Fiorio, C. L. Remes, and Y. R. de Novaes. Impulseest: a Python package for non-parametric impulse response estimation with input-output data. *SoftwareX*, 15:100761, 2021. DOI: 10.1016/j.softx.2021.100761.

[98] A. Fischer and C. Lahiri. Ranking of aircraft fuel-injectors regarding low frequency thermoacoustics based on an energy balance method. In *ASME Turbo Expo 2021: Tur-bomachinery Technical Conference and Exposition*, volume 3B: Combustion, Fuels, and Emissions, page V03BT04A011, Virtual, Online, 2021. American Society of Mechanical Engineers. DOI: 10.1115/GT2021-59561.

[99] A. Fischer, C. Lahiri, and T. Doerr. Design, build, and commissioning of the new thermo-acoustics combustion test rig SCARLET. In *66. Deutscher Luft- und Raumfahrtkongress*, Munich, Germany, 2017. Deutsche Gesellschaft für Luft- und Raumfahrt.

[100] P. Flohr and H. Pitsch. A turbulent flame speed closure model for LES of industrial burner flows. In *Proceedings of the Summer Program 2000*, pages 169–179, Stanford, CA, USA, 2000. Center for Turbulence Research.

[101] S. Föller and W. Polifke. Advances in identification techniques for aero-acoustic scat-tering coefficients from large eddy simulation. In *18th International Congress on Sound and Vibration*, volume 4, pages 3122–3129, Rio de Janeiro, Brazil, 2011. International Institute of Acoustics & Vibration.

[102] S. Föller and W. Polifke. Identification of aero-acoustic scattering matrices from large eddy simulation: Application to a sudden area expansion of a duct. *Journal of Sound and Vibration*, 331(13):3096–3113, 2012. DOI: 10.1016/j.jsv.2012.01.004.

[103] S. Föller, R. Kaess, and W. Polifke. Reconstruction of acoustic transfer matrices from large-eddy-simulations of complex turbulent flows. In *14th AIAA/CEAS Aeroacoustics Conference (29th AIAA Aeroacoustics Conference)*, Vancouver, Canada, 2008. American Institute of Aeronautics and Astronautics.

[104] B. Franzelli, E. Riber, L. Y. Gicquel, and T. Poinsot. Large eddy simulation of combustion instabilities in a lean partially premixed swirled flame. *Combustion and Flame*, 159(2): 621–637, 2012. DOI: 10.1016/j.combustflame.2011.08.004.

[105] P. Gaetani, G. Persico, A. Spinelli, C. Sandu, and F. Niculescu. Entropy wave generator for indirect combustion noise experiments in a high-pressure turbine. In *11th European Conference on Turbomachinery Fluid Dynamics & Thermodynamics*, Madrid, Spain, 2015. European Turbomachinery Society.

[106] F. Gant, A. Cuquel, and M. R. Bothien. Autoignition flame transfer matrix: analytical model versus large eddy simulations. *International Journal of Spray and Combustion Dynamics*, 14(1-2):72–81, 2022. DOI: 10.1177/17568277221086261.

[107] A. M. Garcia, S. Le Bras, J. Prager, M. Haeringer, and W. Polifke. Large eddy simulation of the dynamics of lean premixed flames using global reaction mechanisms calibrated for CH4-H2 fuel blends. *Physics of Fluids*, 34(9):095105, 2022. DOI: 10.1063/5.0098898.

[108] A. M. Garcia, S. Le Bras, J. Prager, I. Boxx, and W. Polifke. Impact of H2-enrichment on the response of a partially premixed CH4-air flame to velocity and equivalence ratio fluctuations. *Combustion and Flame*, 268:113595, 2024. DOI: 10.1016/j.combustflame.2024.113595.

[109] A. Gentemann, A. Fischer, S. Evesque, and W. Polifke. Acoustic transfer matrix reconstruction and analysis for ducts with sudden change of area. In *9th AIAA/CEAS Aeroacoustics Conference and Exhibit*, Hilton Head, SC, USA, 2003. American Institute of Aeronautics and Astronautics. DOI: 10.2514/6.2003-3142.

[110] A. Gentemann, C. Hirsch, K. Kunze, F. Kiesewetter, T. Sattelmayer, and W. Polifke. Validation of flame transfer function reconstruction for perfectly premixed swirl flames. In *ASME Turbo Expo 2004: Power for Land, Sea, and Air*, volume 1: Turbo Expo 2004, pages 501–510, Vienna, Austria, 2004. American Society of Mechanical Engineers. DOI: 10.1115/GT2004-53776.

[111] A. M. Gentemann. *Identifikation von Akustischen Transfermatrizen Und Flammenfrequenzgängen Mittels Strömungssimulation*. Ph.D. thesis, Technische Universität München, Munich, Germany, 2006.

[112] Y. Gentil, G. Daviller, S. Moreau, N. Treleaven, and T. Poinsot. Theoretical analysis and numerical validation of the mechanisms controlling composition noise. *Journal of Sound and Vibration*, 585:118463, 2024. DOI: 10.1016/j.jsv.2024.118463.

[113] A. Ghani, T. Poinsot, L. Gicquel, and J.-D. Müller. LES study of transverse acoustic instabilities in a swirled kerosene/air combustion chamber. *Flow, Turbulence and Combustion*, 96(1):207–226, 2016. DOI: 10.1007/s10494-015-9654-9.

[114] A. Ghani, T. Steinbacher, A. Albayrak, and W. Polifke. Intrinsic thermoacoustic feedback loop in turbulent spray flames. *Combustion and Flame*, 205(7):22–32, 2019. DOI: 10.1016/j.combustflame.2019.03.039.

[115] A. Giannotta, M. Yoko, S. Cherubini, P. De Palma, and M. Juniper. Bayesian data assimilation of acoustically forced laminar premixed conical flames. In *Symposium on Thermoacoustics in Combustion: Industry meets Academia*, Zurich, Switzerland, 2023.

[116] A. Giauque, L. Selle, L. Gicquel, T. Poinsot, H. Buechner, P. Kaufmann, and W. Krebs. System identification of a large-scale swirled partially premixed combustor using LES and measurements. *Journal of Turbulence*, 6:1–21, 2005. DOI: 10.1080/14685240512331391985.

[117] A. Giauque, M. Huet, and F. Clero. Analytical analysis of indirect combustion noise in subcritical nozzles. *Journal of Engineering for Gas Turbines and Power*, 134(11): 111202, 2012. DOI: 10.1115/1.4007318.

[118] L. Y. Gicquel, G. Staffelbach, and T. Poinsot. Large eddy simulations of gaseous flames in gas turbine combustion chambers. *Progress in Energy and Combustion Science*, 38 (6):782–817, 2012. DOI: 10.1016/j.pecs.2012.04.004.

[119] A. Giusti, N. A. Worth, E. Mastorakos, and A. P. Dowling. Experimental and numerical investigation into the propagation of entropy waves. *AIAA Journal*, 55(2):446–458, 2017. DOI: 10.2514/1.J055199.

[120] C. S. Goh and A. S. Morgans. The influence of entropy waves on the thermoacoustic stability of a model combustor. *Combustion Science and Technology*, 185(2):249–268, 2013. DOI: 10.1080/00102202.2012.715828.

[121] H. S. Gopalakrishnan, A. Gruber, and J. P. Moeck. Computation and prediction of intrinsic thermoacoustic oscillations associated with autoignition fronts. *Combustion and Flame*, 254:112844, 2023. DOI: 10.1016/j.combustflame.2023.112844.

[122] M. Götz, J. Lefebvre, F. Mörs, A. McDaniel Koch, F. Graf, S. Bajohr, R. Reimert, and T. Kolb. Renewable power-to-gas: A technological and economic review. *Renewable Energy*, 85:1371–1390, 2016. DOI: 10.1016/j.renene.2015.07.066.

[123] C. J. Goy, S. R. James, and S. Rea. Monitoring combustion instabilities: E.ON UK's experience. In *Combustion instabilities in gas turbine engines: operational experience, fundamental mechanisms, and modeling*, pages 163–175. American Institute of Aeronautics and Astronautics, 2006. DOI: 10.2514/5.9781600866807.0163.0175.

[124] L. C. Haber, U. Vandsburger, W. R. Saunders, and V. K. Khanna. An examination of the relationship between chemiluminescent light emissions and heat release rate under non-adiabatic conditions. In *ASME Turbo Expo 2000: Power for Land, Sea, and Air*, volume 2: Coal, Biomass and Alternative Fuels; Combustion and Fuels; Oil and Gas Applications; Cycle Innovations, page V002T02A041, Munich, Germany, 2000. American Society of Mechanical Engineers. DOI: 10.1115/2000-GT-0121.

[125] M. Haeringer and W. Polifke. Hybrid CFD/low-order modeling of thermoacoustic limit cycle oscillations in can-annular configurations. *International Journal of Spray and Combustion Dynamics*, 14(1–2):143–152, 2022. DOI: 10.1177/17568277221085953.

[126] M. Haeringer, M. Merk, and W. Polifke. Inclusion of higher harmonics in the flame describing function for predicting limit cycles of self-excited combustion instabilitites. *Proceedings of the Combustion Institute*, 37(4):5255–5262, 2019. DOI: 10.1016/j.proci.2018.06.150.

[127] X. Han and A. S. Morgans. Simulation of the flame describing function of a turbulent premixed flame using an open-source LES solver. *Combustion and Flame*, 162(5):1778–1792, 2015. DOI: 10.1016/j.combustflame.2014.11.039.

[128] H. A. Hassan. Scaling of combustion-generated noise. *Journal of Fluid Mechanics*, 66 (03):445, 1974. DOI: 10.1017/S0022112074000292.

[129] T. Heggset, O. Meyer, L. Tay Wo Chong Hilares, A. Ciani, and A. Gruber. Numerical assessment of a rich-quench-lean staging strategy for clean and efficient combustion of partially decomposed ammonia in the constant pressure sequential combustion system. *Journal of Engineering for Gas Turbines and Power*, 146(8):081004, 2024. DOI: 10.1115/1.4063958.

[130] P. A. Hield, M. J. Brear, and S. H. Jin. Thermoacoustic limit cycles in a premixed laboratory combustor with open and choked exits. *Combustion and Flame*, 156(9):1683–1697, 2009. DOI: 10.1016/j.combustflame.2009.05.011.

[131] B. Higgins. On the sound produced by a current of hydrogen gas passing through a tube. *Journal of Natural Philosophy, Chemistry and the Arts*, 1(2):129–131, 1802.

[132] B. Higgins, M. Q. McQuay, F. Lacas, and S. Candel. An experimental study on the effect of pressure and strain rate on CH chemiluminescence of premixed fuel-lean methane/air flames. *Fuel*, 80(11):1583–1591, 2001. DOI: 10.1016/S0016-2361(01)00040-0.

[133] B. Higgins, M. Q. McQuay, F. Lacas, J. C. Rolon, N. Darabiha, and S. Candel. Systematic measurements of OH chemiluminescence for fuel-lean, high-pressure, premixed, laminar flames. *Fuel*, 80(1):67–74, 2001. DOI: 10.1016/S0016-2361(00)00069-7.

[134] M. Hoeijmakers, V. Kornilov, I. Lopez Arteaga, P. de Goey, and H. Nijmeijer. Intrinsic instability of flame-acoustic coupling. *Combustion and Flame*, 161(11):2860–2867, 2014. DOI: 10.1016/j.combustflame.2014.05.009.

[135] T. Hollweck. *Extended model-based inference of flame transfer matrices from acoustic measurements*. Semester thesis, Technische Universität München, Munich, Germany, 2024.

[136] M. S. Howe. On the theory of unsteady hhigh Reynolds number flow through a circular aperture. *Proceedings of the Royal Society of London A: Mathematical, Physical and Engineering Sciences*, 366(1725):205–223, 1979. DOI: 10.1098/rspa.1979.0048.

[137] M. S. Howe. The dissipation of sound at an edge. *Journal of Sound and Vibration*, 70 (8):407–411, 1980. DOI: 10.1016/0022-460X(80)90308-9.

[138] M. S. Howe. *Acoustics of fluid-structure interactions*. Cambridge University Press, 1998. ISBN 978-0-521-63320-8.

[139] F. Q. Hu. A stable, perfectly matched layer for linearized Euler equations in unsplit physical variables. *Journal of Computational Physics*, 173(2):455–480, 2001. DOI: 10.1006/jcph.2001.6887.

[140] Y. Huang and V. Yang. Dynamics and stability of lean-premixed swirl-stabilized combustion. *Progress in Energy and Combustion Science*, 35(4):293–364, 2009. DOI: 10.1016/j.pecs.2009.01.002.

[141] A. Huber and W. Polifke. Dynamics of practical premix flames, part I: model structure and identification. *International Journal of Spray and Combustion Dynamics*, 1(2):199–228, 2009. DOI: 10.1260/175682709788707431.

[142] A. Huber and W. Polifke. Dynamics of practical premix flames, part II: identification and interpretation of CFD data. *International Journal of Spray and Combustion Dynamics*, 1(2):229–249, 2009. DOI: 10.1260/175682709788707440.

[143] M. Huet. Nonlinear indirect combustion noise for compact supercritical nozzle flows. *Journal of Sound and Vibration*, 374:211–227, 2016. DOI: 10.1016/j.jsv.2016.03.028.

[144] M. Huet and A. Giauque. A nonlinear model for indirect combustion noise through a compact nozzle. *Journal of Fluid Mechanics*, 733:268–301, 2013. DOI: 10.1017/jfm.2013.442.

[145] M. Ihme. Combustion and engine-core noise. *Annual Review of Fluid Mechanics*, 49:277–310, 2017. DOI: 10.1146/annurev-fluid-122414-034542.

[146] A. Imamura, M. Yoshida, M. Kawano, N. Aruga, Y. Nagata, and M. Kawagishi. Research and development of a LPP combustor with swirling flow for low NOx. In *37th Joint Propulsion Conference and Exhibit*, Salt Lake City, UT, USA, 2001. American Institute of Aeronautics and Astronautics. DOI: 10.2514/6.2001-3311.

[147] A. Innocenti, A. Andreini, B. Facchini, and A. Peschiulli. Numerical analysis of the dynamic flame response of a spray flame for aero-engine applications. *International Journal of Spray and Combustion Dynamics*, 9(4):310–329, 2017. DOI: 10.1177/1756827717703577.

[148] International Energy Agency. CO2 emissions in 2022. URL: https://www.iea.org/reports/co2-emissions-in-2022, 2023. Accessed on: June 1, 2024.

[149] International Renewable Energy Agency. *Flexibility in conventional power plants*. Abu Dhabi, UAE, 2019. ISBN 978-92-9260-148-5.

[150] M. Israeli and S. A. Orszag. Approximation of radiation boundary conditions. *Journal of Computational Physics*, 41(1):115–135, 1981. DOI: 10.1016/0021-9991(81)90082-6.

[151] S. Jaensch and W. Polifke. Uncertainty encountered when modelling self-excited thermoacoustic oscillations with artificial neural networks. *International Journal of Spray and Combustion Dynamics*, 9(4):367–379, 2017. DOI: 10.1177/1756827716687583.

[152] S. Jaensch, C. Sovardi, and W. Polifke. On the robust, flexible and consistent implementation of time domain impedance boundary conditions for compressible flow simulations. *Journal of Computational Physics*, 314:145–159, 2016. DOI: 10.1016/j.jcp.2016.03.010.

[153] S. Jaensch, M. Merk, T. Emmert, and W. Polifke. Identification of flame transfer functions in the presence of intrinsic thermoacoustic feedback and noise. *Combustion Theory and Modelling*, 22(3):613–634, 2018. DOI: 10.1080/13647830.2018.1443517.

[154] X. Jing and X. Sun. Experimental investigations of perforated liners with bias flow. *The Journal of the Acoustical Society of America*, 106(5):2436–2441, 1999. DOI: 10.1121/1.428128.

[155] M. P. Juniper and M. Yoko. Generating a physics-based quantitatively-accurate model of an electrically-heated Rijke tube with Bayesian inference. *Journal of Sound and Vibration*, 535:117096, 2022. DOI: 10.1016/j.jsv.2022.117096.

[156] R. Kaess, A. Huber, and W. Polifke. A time-domain impedance boundary condition for compressible turbulent flows. In *14th AIAA/CEAS Aeroacoustics Conference (29th AIAA Aeroacoustics Conference)*, Vancouver, Canada, 2008. American Institute of Aeronautics and Astronautics. DOI: 10.2514/6.2008-2921.

[157] T. L. Kaiser and K. Oberleithner. Modeling the transport of fuel mixture perturbations and entropy waves in the linearized framework. *Journal of Engineering for Gas Turbines and Power*, 143(11):111001, 2021. DOI: 10.1115/1.4051714.

[158] T. L. Kaiser and K. Oberleithner. A global linearized framework for modelling shear dispersion and turbulent diffusion of passive scalar fluctuations. *Journal of Fluid Mechanics*, 915:A111, 2021. DOI: 10.1017/jfm.2021.151.

[159] T. L. Kaiser, N. Noiray, Q. Male, and K. Oberleithner. Modeling the convection of entropy waves in strongly non-parallel turbulent flows using a linearized framework. In *ASME Turbo Expo 2022: Turbomachinery Technical Conference and Exposition*, volume 3B: Combustion, Fuels, and Emissions, page V03BT04A039, Rotterdam, Netherlands, 2022. American Society of Mechanical Engineers. DOI: 10.1115/GT2022-82971.

[160] A. Kaufmann, F. Nicoud, and T. Poinsot. Flow forcing techniques for numerical simulation of combustion instabilities. *Combustion and Flame*, 131(4):371–385, 2002. DOI: 10.1016/S0010-2180(02)00419-4.

[161] J. Kaufmann, M. Vogel, J. Papenbrock, and T. Sattelmayer. Comparison of the flame dynamics of a premixed dual fuel burner for kerosene and natural gas. *International Journal of Spray and Combustion Dynamics*, 14(1-2):176–185, 2022. DOI: 10.1177/17568277221091405.

[162] K. J. Keesman. *System identification: an introduction*. Advanced textbooks in control and signal processing. Springer, London, UK, 2011. ISBN 978-0-85729-521-7.

[163] J. J. Keller. Thermoacoustic oscillations in combustion chambers of gas turbines. *AIAA Journal*, 33(12):2280–2287, 1995. DOI: 10.2514/3.12980.

[164] J. J. Keller, W. Egli, and J. Hellat. Thermally induced low-frequency oscillations. *Zeitschrift für angewandte Mathematik und Physik*, 36(2):250–274, 1985. DOI: 10.1007/BF00945460.

[165] J. O. Keller and K. Saito. Measurements of the combusting flow in a pulse combustor. *Combustion Science and Technology*, 53(2-3):137–163, 1987. DOI: 10.1080/00102208708947024.

[166] J. F. Kennedy. The address at Rice University on the nation's space effort. Rice University, URL: `https://www.rice.edu/jfk-speech`, 1962. Accessed on: June 1, 2024.

[167] E. Knudsen and H. Pitsch. Capabilities and limitations of multi-regime flamelet combustion models. *Combustion and Flame*, 159(1):242–264, 2012. DOI: 10.1016/j.combustflame.2011.05.025.

[168] A. N. Kolmogorov. The local structure of turbulence in incompressible viscous fluid for very large Reynolds numbers. *Doklady Akademii Nauk SSSR*, 30:301–304, 1942.

[169] A. N. Kolmogorov. A refinement of previous hypotheses concerning the local structure of turbulence in a viscous incompressible fluid at high Reynolds number. *Journal of Fluid Mechanics*, 13(01):82–85, 1962. DOI: 10.1017/S0022112062000518.

[170] T. Komarek and W. Polifke. Impact of swirl fluctuations on the flame response of a perfectly premixed swirl burner. *Journal of Engineering for Gas Turbines and Power*, 132(6):061503, 2010. DOI: 10.1115/1.4000127.

[171] K. Kostrzewa, J. Lepers, B. Noll, W. Krebs, M. Aigner, B. Prade, and M. Huth. Validation of advanced computational methods for determining flame transfer functions in gas turbine combustion systems. In *ASME Turbo Expo 2007: Power for Land, Sea, and Air*, volume 2: Turbo Expo 2007, pages 145–155, Montreal, Canada, 2007. American Society of Mechanical Engineers. DOI: 10.1115/GT2007-27267.

[172] S. Kotake and K. Takamoto. Combustion noise: Effects of the shape and size of burner nozzle. *Journal of Sound and Vibration*, 112(2):345–354, 1987. DOI: 10.1016/S0022-460X(87)80201-8.

[173] C. Kraus, L. Selle, and T. Poinsot. Coupling heat transfer and large eddy simulation for combustion instability prediction in a swirl burner. *Combustion and Flame*, 191: 239–251, 2018. DOI: 10.1016/j.combustflame.2018.01.007.

[174] M. Kraushaar. *Application of the compressible and low-Mach number approaches to large-eddy simulation of turbulent flows in aero-engines*. Ph.D. thesis, Université de Toulouse, Toulouse, France, 2011.

[175] W. Krebs, G. Walz, and S. Hoffmann. Thermoacoustic analysis of annular combustor. In *5th AIAA/CEAS Aeroacoustics Conference and Exhibit*, Bellevue, WA, USA, 1999. American Institute of Aeronautics and Astronautics. DOI: 10.2514/6.1999-1971.

[176] R. Krewinkel. A review of gas turbine effusion cooling studies. *International Journal of Heat and Mass Transfer*, 66:706–722, 2013. DOI: 10.1016/j.ijheatmasstransfer.2013.07.071.

[177] U. Krüger, S. Hoffmann, W. Krebs, H. Judith, D. Bohn, and G. Matouschek. Influence of turbulence on the dynamic behaviour of premixed flames. In *ASME 1998 International Gas Turbine and Aeroengine Congress and Exhibition*, volume 3: Coal, Biomass and Alternative Fuels; Combustion and Fuels; Oil and Gas Applications; Cycle Innovations, page V003T06A028, Stockholm, Sweden, 1998. American Society of Mechanical Engineers. DOI: 10.1115/98-GT-323.

[178] U. Krüger, J. Hüren, S. Hoffmann, W. Krebs, and D. Bohn. Prediction of thermoacoustic instabilities with focus on the dynamic flame behavior for the 3A-series gas turbine of siemens KWU. In *ASME 1999 International Gas Turbine and Aeroengine Congress and Exhibition*, volume 2: Coal, Biomass and Alternative Fuels; Combustion and Fuels; Oil and Gas Applications; Cycle Innovations, page V002T02A016, Indianapolis, IN, USA, 1999. American Society of Mechanical Engineers. DOI: 10.1115/99-GT-111.

[179] J. Kuhlmann, A. Lampmann, M. Pfitzner, and W. Polifke. Assessing accuracy, reliability and efficieny of combustion models for prediction of flame dynamics with large eddy simulation. *Physics of Fluids*, 34(9):095117, 2022. DOI: 10.1063/5.0098975.

[180] J. Kuhlmann, S. Marragou, I. Boxx, T. Schuller, and W. Polifke. LES based prediction of technically premixed flame dynamics and comparison with perfectly premixed mode. *Physics of Fluids*, 34(8):085125, 2022. DOI: 10.1063/5.0098962.

[181] H. Kutkan, A. Amato, G. Campa, L. Tay-Wo-Chong, and E. Æsøy. LES of turbulent premixed CH4/H2/air flames with stretch and heat loss for flame characteristics and dynamics. In *ASME Turbo Expo 2022: Turbomachinery Technical Conference and Exposition*, volume 3B: Combustion, Fuels, and Emissions, page V03BT04A021, Rotterdam, Netherlands, 2022. American Society of Mechanical Engineers. DOI: 10.1115/GT2022-82397.

[182] C. Lahiri. *Acoustic performance of bias flow liners in gas turbine combustors*. Ph.D. thesis, Technische Universität Berlin, Berlin, Germany, 2014.

[183] C. Lahiri and F. Bake. A review of bias flow liners for acoustic damping in gas turbine combustors. *Journal of Sound and Vibration*, 400:564–605, 2017. DOI: 10.1016/j.jsv.2017.04.005.

[184] M. Lauer and T. Sattelmayer. On the adequacy of chemiluminescence as a measure for heat release in turbulent flames with mixture gradients. *Journal of Engineering for Gas Turbines and Power*, 132(6):061502, 2010. DOI: 10.1115/1.4000126.

[185] J. Lavrentjev and M. Åbom. Characterization of fluid machines as acoustic multi-port sources. *Journal of Sound and Vibration*, 197(1):1–16, 1996. DOI: 10.1006/jsvi.1996.0514.

[186] C. J. Lawn and W. Polifke. A model for the thermoacoustic response of a premixed swirl burner, part II: the flame response. *Combustion Science and Technology*, 176(8): 1359–1390, 2004. DOI: 10.1080/00102200490461623.

[187] H. Levine and J. Schwinger. On the radiation of sound from an unflanged circular pipe. *Physical Review*, 73(4):383–405, 1948. DOI: 10.1103/PhysRev.73.383.

[188] M. Leyko, F. Nicoud, and T. Poinsot. Comparison of direct and indirect combustion noise mechanisms in a model combustor. *AIAA Journal*, 47(11):2709–2716, 2009. DOI: 10.2514/1.43729.

[189] M. Leyko, I. Duran, S. Moreau, F. Nicoud, and T. Poinsot. Simulation and modelling of the waves transmission and generation in a stator blade row in a combustion-noise framework. *Journal of Sound and Vibration*, 333(23):6090–6106, 2014. DOI: 10.1016/j.jsv.2014.06.034.

[190] T. Lieuwen. Modeling premixed combustion – acoustic wave interactions: a review. *Journal of Propulsion and Power*, 19(5):765–781, 2003. DOI: 10.2514/2.6193.

[191] T. Lieuwen and K. McManus. Introduction: combustion dynamics in lean-premixed prevaporized (LPP) gas turbines. *Journal of Propulsion and Power*, 19(5):721–721, 2003. DOI: 10.2514/2.6171.

[192] T. Lieuwen and V. Yang, editors. *Combustion instabilities in gas turbine engines: operational experience, fundamental mechanisms and modeling*, volume 210 of *Progress in astronautics and aeronautics*. American Institute of Aeronautics and Astronautics, Reston, VA, USA, 2005. ISBN 978-1-56347-669-3.

[193] T. Lieuwen and B. T. Zinn. The role of equivalence ratio oscillations in driving combustion instabilities in low nox gas turbines. *Symposium (International) on Combustion*, 27 (2):1809–1816, 1998. DOI: 10.1016/S0082-0784(98)80022-2.

[194] T. Lieuwen, H. Torres, C. Johnson, and B. T. Zinn. A mechanism of combustion instability in lean premixed gas turbine combustors. *Journal of Engineering for Gas Turbines and Power*, 123(1):182–189, 2001. DOI: 10.1115/1.1339002.

[195] L. Ljung. *System identification: theory for the user*. PTR Prentice Hall information and system sciences series. Prentice Hall PTR, Upper Saddle River, NJ, USA, 2nd edition, 1999. ISBN 0-13-656695-2.

[196] L. Ljung. System identification toolbox. User's guide, The MathWorks, Natick, MA, USA, 2022.

[197] G. Lodato, P. Domingo, and L. Vervisch. Three-dimensional boundary conditions for direct and large-eddy simulation of compressible viscous flows. *Journal of Computational Physics*, 227(10):5105–5143, 2008. DOI: 10.1016/j.jcp.2008.01.038.

[198] D. J. MacKay. *Information theory, inference, and learning algorithms*. Cambridge University Press, New York, NY, USA, 2003. ISBN 978-0-521-64298-9.

[199] E. Macron. Speech by the President of the Republic, Emmanuel Macron, at the Congress of the United States of America. Élysée, URL: https://www.elysee.fr/emmanuel-macron/2018/04/25/discours-demmanuel-macron-devant-le-congres-des-etats-unis-damerique, 2018. Accessed on: June 1, 2024.

[200] L. Magri. On indirect noise in multicomponent nozzle flows. *Journal of Fluid Mechanics*, 828:R2, 2017. DOI: 10.1017/jfm.2017.591.

[201] L. Magri, J. O'Brien, and M. Ihme. Compositional inhomogeneities as a source of indirect combustion noise. *Journal of Fluid Mechanics*, 799:R4, 2016. DOI: 10.1017/jfm.2016.397.

[202] Y. Mahmoudi, A. Giusti, E. Mastorakos, and A. P. Dowling. Low-order modeling of combustion noise in an aero-engine: the effect of entropy dispersion. *Journal of Engineering for Gas Turbines and Power*, 140(1), 2017. DOI: 10.1115/1.4037321.

[203] F. E. Marble and S. M. Candel. Acoustic disturbance from gas non-uniformities convected through a nozzle. *Journal of Sound and Vibration*, 55(2):225–243, 1977. DOI: 10.1016/0022-460X(77)90596-X.

[204] M. March, J. Renner, and T. Sattelmayer. Acoustic and optical investigations of the flame dynamics of rich and lean kerosene flames in the primary zone of an air-staged combustion test-rig. *Journal of Engineering for Gas Turbines and Power*, 146(1):011004, 2024. DOI: 10.1115/1.4063380.

[205] C. E. Martin, L. Benoit, Y. Sommerer, F. Nicoud, and T. Poinsot. Large-eddy simulation and acoustic analysis of a swirled staged turbulent combustor. *AIAA Journal*, 44(4): 741–750, 2006. DOI: 10.2514/1.14689.

[206] K. R. McManus, T. Poinsot, and S. M. Candel. A review of active control of combustion instabilities. *Progress in Energy and Combustion Science*, 19(1):1–29, 1993. DOI: 10.1016/0360-1285(93)90020-F.

[207] M. Meindl, A. Albayrak, and W. Polifke. A state-space formulation of a discontinuous Galerkin method for thermoacoustic stability analysis. *Journal of Sound and Vibration*, 481:115431, 2020. DOI: 10.1016/j.jsv.2020.115431.

[208] M. Meindl, C. F. Silva, and W. Polifke. On the spurious entropy generation encountered in hybrid linear thermoacoustic models. *Combustion and Flame*, 223:525–540, 2021. DOI: 10.1016/j.combustflame.2020.09.018.

[209] M. Merk. *Identification of combustion dynamics and noise of confined turbulent flames.* Ph.D. thesis, Technische Universität München, Munich, Germany, 2018.

[210] M. Merk, S. Jaensch, C. Silva, and W. Polifke. Simultaneous identification of transfer functions and combustion noise of a turbulent flame. *Journal of Sound Vibration*, 422: 432–452, 2018. DOI: 10.1016/j.jsv.2018.02.040.

[211] M. Merk, R. Gaudron, C. Silva, M. Gatti, C. Mirat, T. Schuller, and W. Polifke. Prediction of combustion noise of an enclosed flame by simultaneous identification of noise source and flame dynamics. *Proceedings of the Combustion Institute*, 37:5263–5270, 2019. DOI: 10.1016/j.proci.2018.05.124.

[212] M. Merk, C. F. Silva, W. Polifke, R. Gaudron, M. Gatti, C. Mirat, and T. Schuller. Direct assessment of the acoustic scattering matrix of a turbulent swirl combustor by combining system identification, large eddy simulation and analytical approaches. *Journal of Engineering for Gas Turbines and Power*, 141(2):021035, 2019. DOI: 10.1115/1.4040731.

[213] M. Merk, A. J. Eder, and W. Polifke. An arbitrary Lagrangian-Eulerian framework for the consistent analysis of entropy wave generation. *Combustion and Flame*, 262:113334, 2024. DOI: 10.1016/j.combustflame.2024.113334.

[214] M. Merk, F. Schily, A. J. Eder, and W. Polifke. A generalized Jacobian-based framework for the derivation of highly accurate thermoacoustic jump conditions. *Combustion and Flame (in preparation)*, 2024.

[215] Y. Méry. Dynamical response of a perfectly premixed flame and limit behavior for high power density systems. *Combustion and Flame*, 192:410–425, 2018. DOI: 10.1016/j.combustflame.2018.02.007.

[216] W. H. Moase, M. J. Brear, and C. Manzie. The forced response of choked nozzles and supersonic diffusers. 585:281–304, 2007.

[217] S. Moreau, C. Becerril, and L. Gicquel. Large-eddy-simulation prediction of indirect combustion noise in the entropy wave generator experiment. *International Journal of Spray and Combustion Dynamics*, 10(2):154–168, 2018. DOI: 10.1177/1756827717740775.

[218] A. S. Morgans and I. Duran. Entropy noise: a review of theory, progress and challenges. *International Journal of Spray and Combustion Dynamics*, 8(4):285–298, 2016. DOI: 10.1177/1756827716651791.

[219] A. S. Morgans, C. S. Goh, and J. A. Dahan. The dissipation and shear dispersion of entropy waves in combustor thermoacoustics. *Journal of Fluid Mechanics*, 733:R2, 2013. DOI: 10.1017/jfm.2013.448.

[220] E. Motheau, F. Nicoud, and T. Poinsot. Mixed acoustic–entropy combustion instabilities in gas turbines. *Journal of Fluid Mechanics*, 749:542–576, 2014. DOI: 10.1017/jfm.2014.245.

[221] M. L. Munjal and A. G. Doige. Theory of a two source-location method for direct experimental evaluation of the four-pole parameters of an aeroacoustic element. *Journal of Sound and Vibration*, 141(2):323–333, 1990. DOI: 10.1016/0022-460X(90)90843-O.

[222] R. M. Munt. The interaction of sound with a subsonic jet issuing from a semi-infinite cylindrical pipe. *Journal of Fluid Mechanics*, 83(4):609–640, 1977. DOI: 10.1017/S0022112077001384.

[223] M. Murugesan, B. Singaravelu, A. K. Kushwaha, and S. Mariappan. Onset of flame-intrinsic thermoacoustic instabilities in partially premixed turbulent combustors. *International Journal of Spray and Combustion Dynamics*, 10(3):171–184, 2018. DOI: 10.1177/1756827718758511.

[224] F. Nicoud and F. Ducros. Subgrid-scale stress modelling based on the square of the velocity gradient tensor. *Flow Turbulence and Combustion*, 62(3):183–200, 1999. DOI: 10.1023/A:1009995426001.

[225] F. Nicoud and K. Wieczorek. About the zero Mach number assumption in the calculation of thermoacoustic instabilities. *International Journal of Spray and Combustion Dynamics*, 1(1):67–111, 2009. DOI: 10.1260/175682709788083335.

[226] F. Nicoud, L. Benoit, C. Sensiau, and T. Poinsot. Acoustic modes in combustors with complex impedances and multidimensional active flames. *AIAA Journal*, 45(2):426–441, 2007. DOI: 10.2514/1.24933.

[227] F. Nicoud, H. B. Toda, O. Cabrit, S. Bose, and J. Lee. Using singular values to build a subgrid-scale model for large eddy simulations. *Physics of Fluids*, 23(8):085106, 2011. DOI: 10.1063/1.3623274.

[228] N. Noiray. Private communication, 2022.

[229] N. Noiray, D. Durox, T. Schuller, and S. Candel. A unified framework for nonlinear combustion instability analysis based on the flame describing function. *Journal of Fluid Mechanics*, 615:139–167, 2008. DOI: 10.1017/S0022112008003613.

[230] J. C. Oefelein and V. Yang. Comprehensive review of liquid-propellant combustion instabilities in F-1 engines. *Journal of Propulsion and Power*, 9(5):657–677, 1993. DOI: 10.2514/3.23674.

[231] C. Pankiewitz and T. Sattelmayer. Time domain simulation of combustion instabilities in annular combustors. *Journal of Engineering for Gas Turbines and Power*, 125(3): 677–685, 2003. DOI: 10.1115/1.1582496.

[232] C. O. Paschereit and W. Polifke. Characterization of lean premixed gas turbine burners as acoustic multi-ports. In *APS/DFD Meeting*, San Francisco, CA, USA, 1997. American Physical Society.

[233] C. O. Paschereit and W. Polifke. Investigation of the thermo-acoustic characteristics of a lean premixed gas turbine burner. In *ASME 1998 International Gas Turbine and Aeroengine Congress and Exhibition*, volume 3: Coal, Biomass and Alternative Fuels; Combustion and Fuels; Oil and Gas Applications; Cycle Innovations, page V003T06A057, Stockholm, Sweden, 1998. American Society of Mechanical Engineers. DOI: 10.1115/98-GT-582.

[234] C. O. Paschereit, B. Schuermans, W. Polifke, and O. Mattson. Measurement of transfer matrices and source terms of premixed flames. *Journal of Engineering for Gas Turbines and Power*, 124(2):239–247, 2002. DOI: 10.1115/1.1383255.

[235] A. Peracchio and W. Proscia. Non-linear heat-release / acoustic model for thermoacoustic instability in lean premixed combustors. *Journal of Engineering for Gas Turbines and Power*, 121(3):415–421, 1999. DOI: 10.1115/1.2818489.

[236] J. Peterleithner, N. V. Stadlmair, J. Woisetschläger, and T. Sattelmayer. Analysis of measured flame transfer functions with locally resolved density fluctuation and OH-chemiluminescence data. *Journal of Engineering for Gas Turbines and Power*, 138(3): 031504, 2016. DOI: 10.1115/1.4031346.

[237] M. C. Peters. *Aeroacoustic sources in internal flows*. Ph.D. thesis, Technische Universiteit Eindhoven, Eindhoven, Netherlands, 1993.

[238] M. C. Peters, A. Hirschberg, A. J. Reijnen, and A. P. Wijnands. Damping and reflection coefficient measurements for an open pipe at low Mach and low Helmholtz numbers. *Journal of Fluid Mechanics*, 256:499–534, 1993. DOI: 10.1017/S0022112093002861.

[239] N. Peters. The turbulent burning velocity for large-scale and small-scale turbulence. *Journal of Fluid Mechanics*, 384:107–132, 1999. DOI: doi.org/10.1017/S0022112098004212.

[240] U. Piomelli. Large-eddy simulation: achievements and challenges. *Progress in Aerospace Sciences*, 35(4):335–362, 1999. DOI: 10.1016/S0376-0421(98)00014-1.

[241] H. Pitsch. A consistent level set formulation for large-eddy simulation of premixed turbulent combustion. *Combustion and Flame*, 143(4):587–598, 2005. DOI: 10.1016/j.combustflame.2005.08.031.

[242] T. Poinsot. Prediction and control of combustion instabilities in real engines. *Proceedings of the Combustion Institute*, 36(1):1–28, 2017. DOI: 10.1016/j.proci.2016.05.007.

[243] T. Poinsot and S. K. Lele. Boundary conditions for direct simulation of compressible viscous flows. *Journal of Computational Physics*, 101(1):104–129, 1992. DOI: 10.1016/0021-9991(92)90046-2.

[244] T. Poinsot and D. Veynante. *Theoretical and numerical combustion*. Centre national de la recherche scientifique, Toulouse, France, 3rd edition, 2011. ISBN 978-2-7466-3990-4.

[245] W. Polifke. Divide et impera – combining CFD, system identification and system modelling to analyse thermo-acoustic combustion instabilities. In *3. NAFEMS CFD-Seminar: Simulation Gekoppelter Strömungsvorgänge (Multifield FSI)*, Wiesbaden, Germany, 2006. NAFEMS.

[246] W. Polifke. System identification for aero- and thermo-acoustic applications. In C. Schram, editor, *Advances in aero-acoustics and thermo-acoustics – VKI-LS*. von Karman Institute for Fluid Dynamics, Sint-Genesius-Rode, Belgium, 2011.

[247] W. Polifke. Black-box system identification for reduced order model construction. *Annals of Nuclear Energy*, 67:109–128, 2014. DOI: 10.1016/j.anucene.2013.10.037.

[248] W. Polifke. Six lectures on thermoacoustic combustion instability. In *21st CISM-IUTAM International Summer School on Measurement, Analysis and Passive Control of Thermoacoustic Oscillations*, Udine, Italy, 2015. DOI: 10.5281/zenodo.7932641.

[249] W. Polifke. Modeling and analysis of premixed flame dynamics by means of distributed time delays. *Progress in Energy and Combustion Science*, 79:100845, 2020. DOI: 10.1016/j.pecs.2020.100845.

[250] W. Polifke, A. Poncet, C. O. Paschereit, and K. Döbbeling. Determination of (thermo-) acoustic transfer matrices by time-dependent numerical simulation. In *7th International Conference on Numerical Combustion*, York, UK, 1998.

[251] W. Polifke, C. O. Paschereit, and K. Döbbeling. Suppression of combustion instabilities through destructive interference of acoustic and entropy waves. In *6th International Conference on Sound and Vibration*, pages 3319–3330, Copenhagen, Denmark, 1999.

[252] W. Polifke, C. O. Paschereit, and K. Döbbeling. Constructive and destructive interference of acoustic and entropy waves in a premixed combustor with a choked exit. *International Journal of Acoustics and Vibration*, 6(3):135–146, 2001. DOI: 10.20855/IJAV.2001.6.382.

[253] W. Polifke, A. Poncet, C. O. Paschereit, and K. Döbbeling. Reconstruction of acoustic transfer matrices by instationary computational fluid dynamics. *Journal of Sound and Vibration*, 245(3):483–510, 2001. DOI: 10.1006/jsvi.2001.3594.

[254] W. Polifke, C. Wall, and P. Moin. Partially reflecting and non-reflecting boundary conditions for simulation of compressible viscous flow. *Journal of Computational Physics*, 213(1):437–449, 2006. DOI: 10.1016/j.jcp.2005.08.016.

[255] W. Polifke, C. F. Silva, and C. Lahiri. Combustion noise and dynamics of partially premixed flames (NoiSI). DFG proposal (unpublished), 2020.

[256] R. Price, I. Hurle, and T. Sugden. Optical studies of the generation of noise in turbulent flames. *Symposium (International) on Combustion*, 12(1):1093–1102, 1969. DOI: 10.1016/S0082-0784(69)80487-X.

[257] P. Rajendram Soundararajan. *Investigation of combustion instabilities in annular combustors combining injector dynamics and flame describing functions in simplified configurations*. Ph.D. thesis, Université Paris-Saclay, Paris, France, 2022.

[258] P. Rajendram Soundararajan, D. Durox, A. Renaud, G. Vignat, and S. Candel. Swirler effects on combustion instabilities analyzed with measured FDFs, injector impedances and damping rates. *Combustion and Flame*, 238:111947, 2022. DOI: 10.1016/j.combustflame.2021.111947.

[259] P. Rajendram Soundararajan, D. Durox, A. Renaud, and S. Candel. Impact of spray dynamics on combustion instabilities investigated by changing the atomizer recess in a swirl combustor. *Combustion and Flame*, 252:112757, 2023. DOI: 10.1016/j.combustflame.2023.112757.

[260] J. W. S. Rayleigh. The explanation of certain acoustical phenomena. *Nature*, 18:319–321, 1878. DOI: 10.1038/018319a0.

[261] J. W. S. Rayleigh. *The theory of sound*, volume 2. Macmillan, London, UK, 2nd edition, 1896.

[262] H. Reinhardt, Ç. O. Alanyalıoğlu, A. Fischer, C. Lahiri, H. Nicolai, and C. Hasse. Simulation of the thermoacoustic response of an aero-engine gas turbine fuel injector using a hybrid CFD-CAA method. *Journal of Engineering for Gas Turbines and Power*, 145 (11):111016, 2023. DOI: 10.1115/1.4063335.

[263] J. Renner, M. March, C. Hirsch, and T. Sattelmayer. Flame dynamics in the lean burnout zone of an RQL combustion chamber – response to primary zone velocity fluctuations. *International Journal of Spray and Combustion Dynamics*, 14(3-4):238–250, 2022. DOI: 10.1177/17568277221128169.

[264] P. L. Rijke. Notiz über eine neue Art, die in einer an beiden Enden offenen Röhre enthaltene Luft in Schwingungen zu versetzen. *Annalen der Physik*, 183(6):339–343, 1859. DOI: 10.1002/andp.18591830616.

[265] H. Ritchie, P. Rosada, and M. Roser. Breakdown of carbon dioxide, methane and nitrous oxide emissions by sector. *Our World in Data*, URL: https://ourworldindata.org/emissions-by-sector, 2020. Accessed on: June 1, 2024.

[266] E. O. Rolland, F. De Domenico, and S. Hochgreb. Direct and indirect noise generated by entropic and compositional inhomogeneities. *Journal of Engineering for Gas Turbines and Power*, 140(8):082604, 2018. DOI: 10.1115/1.4039050.

[267] M. Rywik, A. Zimmermann, A. J. Eder, E. Scoletta, and W. Polifke. Spatially resolved modeling of the nonlinear dynamics of a laminar premixed flame with a multilayer perceptron - convolution autoencoder network. *Journal of Engineering for Gas Turbines and Power*, 146(6):061009, 2024. DOI: 10.1115/1.4063788.

[268] T. Sattelmayer. Influence of the combustor aerodynamics on combustion instabilities from equivalence ratio fluctuations. *Journal of Engineering for Gas Turbines and Power*, 125(1):11–19, 2003. DOI: 10.1115/1.1365159.

[269] A. Scarpato, L. Zander, R. Kulkarni, and B. Schuermans. Identification of multiparameter flame transfer function for a reheat combustor. In *ASME 2016 Turbo Expo: Turbomachinery Technical Conference and Exposition*, volume 4B: Combustion, Fuels and Emissions, page V04BT04A038, Seoul, Korea, 2016. American Society of Mechanical Engineers. DOI: 10.1115/GT2016-57699.

[270] S. Schimek, S. Göke, C. Schrödinger, and C. O. Paschereit. Flame transfer function measurements with CH4 and H2 fuel mixtures at ultra wet conditions in a swirl stabilized premixed combustor. In *ASME Turbo Expo 2012: Turbine Technical Conference and Exposition*, volume 2: Combustion, Fuels and Emissions, Parts A and B, pages 1335–1344, Copenhagen, Denmark, 2012. American Society of Mechanical Engineers. DOI: 10.1115/GT2012-69788.

[271] B. Schuermans. *Modeling and control of thermoacoustic instabilities*. Ph.D. thesis, École Polytechnique Fédérale de Lausanne, Lausanne, Switzerland, 2003.

[272] B. Schuermans, W. Polifke, and C. O. Paschereit. Modeling transfer matrices of premixed flames and comparison with experimental results. In *ASME 1999 International Gas Turbine and Aeroengine Congress and Exhibition*, volume 2: Coal, Biomass and Alternative Fuels; Combustion and Fuels; Oil and Gas Applications; Cycle Innovations, page V002T02A024, Indianapolis, IN, USA, 1999. American Society of Mechanical Engineers. DOI: 10.1115/99-GT-132.

[273] B. Schuermans, V. Bellucci, F. Guethe, F. Meili, P. Flohr, and C. O. Paschereit. A detailed analysis of thermoacoustic interaction mechanisms in a turbulent premixed flame. In *ASME Turbo Expo 2004: Power for Land, Sea, and Air*, volume 1: Turbo Expo 2004, pages 539–551, Vienna, Austria, 2004. American Society of Mechanical Engineers. DOI: 10.1115/GT2004-53831.

[274] B. Schuermans, H. Luebcke, D. Bajusz, and P. Flohr. Thermoacoustic analysis of gas turbine combustion systems using unsteady CFD. In *ASME Turbo Expo 2005: Power for Land, Sea, and Air*, volume 2: Turbo Expo 2005, pages 287–297, Reno, NV, USA, 2005. American Society of Mechanical Engineers. DOI: 10.1115/GT2005-68393.

[275] B. Schuermans, F. Guethe, and W. Mohr. Optical transfer function measurements for technically premixed flames. *Journal of Engineering for Gas Turbines and Power*, 132 (8):081501, 2010. DOI: 10.1115/1.3124663.

[276] B. Schuermans, F. Guethe, D. Pennell, D. Guyot, and C. O. Paschereit. Thermoacoustic modeling of a gas turbine using transfer functions measured under full engine pressure. *Journal of Engineering for Gas Turbines and Power*, 132(11):111503, 2010. DOI: 10.1115/1.4000854.

[277] B. Schuermans, J. Moeck, A. Blondé, B. Dharmaputra, and N. Noiray. The Rayleigh integral is always positive in steadily operated combustors. *Proceedings of the Combustion Institute*, 39(4):4661–4669, 2022. DOI: 10.1016/j.proci.2022.08.035.

[278] T. Schuller, D. Durox, and S. Candel. A unified model for the prediction of laminar flame transfer functions: comparisons between conical and V-flame dynamics. *Combustion and Flame*, 134(1-2):21–34, 2003. DOI: 10.1016/S0010-2180(03)00042-7.

[279] O. Schulz and N. Noiray. Autoignition flame dynamics in sequential combustors. *Combustion and Flame*, 192:86–100, 2018. DOI: 10.1016/j.combustflame.2018.01.046.

[280] G. Searby, A. Nicole, M. Habiballah, and E. Laroche. Prediction of the efficiency of acoustic damping cavities. *Journal of Propulsion and Power*, 24(3):516–523, 2008. DOI: 10.2514/1.32325.

[281] L. Selle, G. Lartigue, T. Poinsot, R. Koch, K.-U. Schildmacher, W. Krebs, B. Prade, P. Kaufmann, and D. Veynante. Compressible large eddy simulation of turbulent combustion in complex geometry on unstructured meshes. *Combustion and Flame*, 137(4): 489–505, 2004. DOI: 10.1016/j.combustflame.2004.03.008.

[282] L. Selle, F. Nicoud, and T. Poinsot. Actual impedance of nonreflecting boundary conditions: Implications for computation of resonators. *AIAA Journal*, 42(5):958–964, 2004. DOI: 10.2514/1.1883.

[283] B. Semlitsch, T. Hynes, I. Langella, N. Swaminathan, and A. P. Dowling. Entropy and vorticity wave generation in realistic gas turbine combustors. *Journal of Propulsion and Power*, 35(4):839–849, 2019. DOI: 10.2514/1.B37463.

[284] A. F. Seybert and D. F. Ross. Experimental determination of acoustic properties using a two-microphone random-excitation technique. *The Journal of the Acoustical Society of America*, 61(5):1362–1370, 1977. DOI: 10.1121/1.381403.

[285] C. F. Silva. Intrinsic thermoacoustic instabilities. *Progress in Energy and Combustion Science*, 95:101065, 2023. DOI: 10.1016/j.pecs.2022.101065.

[286] C. F. Silva and W. Polifke. A new class of Galerkin expansion models for the study of thermoacoustic instabilities. *Proceedings of the Combustion Institute*, 40(1–4):105242, 2024. DOI: 10.1016/j.proci.2024.105242.

[287] C. F. Silva, F. Nicoud, T. Schuller, D. Durox, and S. Candel. Combining a Helmholtz solver with the flame describing function to assess combustion instability in a premixed swirled combustor. *Combustion and Flame*, 160(9):1743–1754, 2013. DOI: 10.1016/j.combustflame.2013.03.020.

[288] C. F. Silva, T. Emmert, S. Jaensch, and W. Polifke. Numerical study on intrinsic thermoacoustic instability of a laminar premixed flame. *Combustion and Flame*, 162(9): 3370–3378, 2015. DOI: 10.1016/j.combustflame.2015.06.003.

[289] C. F. Silva, L. Magri, T. Runte, and W. Polifke. Uncertainty quantification of growth rates of thermoacoustic instability by an adjoint Helmholtz solver. *Journal of Engineering for Gas Turbines and Power*, 139(1):011901, 2017. DOI: 10.1115/1.4034203.

[290] V. A. Sklyarov and V. I. Furletov. Frequency characteristics of a laminar flame. *Journal of Applied Mechanics and Technical Physics*, 15:69–77, 1974. DOI: 10.1007/BF00850731.

[291] T. Söderström and P. Stoica. *System identification*. Series in systems and control engineering. Prentice Hall, Hertfordshire, UK, 1989. ISBN 0-13-881236-3.

[292] Y. Song, J. Li, and L. Yang. Effect of flame motion on longitudinal combustion instabilities. *Aerospace Science and Technology*, 122:107427, 2022. DOI: 10.1016/j.ast.2022.107427.

[293] Y. Song, X. Liu, J. Li, and L. Yang. Effect of the flame motion on azimuthal combustion instabilities. *Aerospace Science and Technology*, 130:107930, 2022. DOI: 10.1016/j.ast.2022.107930.

[294] C. Sovardi. *Identification of sound sources in duct singularities*. Ph.D. thesis, Technische Universität München, Munich, Germany, 2016.

[295] C. Sovardi, S. Jaensch, and W. Polifke. Concurrent identification of aero-acoustic scattering and noise sources at a flow duct singularity in low Mach number flow. *Journal of Sound Vibration*, 377:90–105, 2016. DOI: 10.1016/j.jsv.2016.05.025.

[296] N. Stadlmair and T. Sattelmayer. Measurement and analysis of flame transfer functions in a lean-premixed, swirl-stabilized combustor with water injection. In *54th AIAA Aerospace Sciences Meeting*, San Diego, CA, USA, 2016. American Institute of Aeronautics and Astronautics. DOI: 10.2514/6.2016-1157.

[297] G. Staffelbach, L. Y. Gicquel, G. Boudier, and T. Poinsot. Large eddy simulation of self excited azimuthal modes in annular combustors. *Proceedings of the Combustion Institute*, 32(2):2909–2916, 2009. DOI: 10.1016/j.proci.2008.05.033.

[298] T. Steinbacher, M. Meindl, and W. Polifke. Modeling the generation of temperature inhomogeneities by a premixed flame. *International Journal of Spray and Combustion Dynamics*, 10(2):111–130, 2018. DOI: 10.1177/1756827717738139.

[299] S. R. Stow and A. P. Dowling. A time-domain network model for nonlinear thermoacoustic oscillations. *Journal of Engineering for Gas Turbines and Power*, 131(3):031502, 2009. DOI: 10.1115/1.2981178.

[300] S. R. Stow, A. P. Dowling, and T. P. Hynes. Reflection of circumferential modes in a choked nozzle. *Journal of Fluid Mechanics*, 467:215–239, 2002. DOI: 10.1017/S0022112002001428.

[301] L. Strobio Chen, S. Bomberg, and W. Polifke. Propagation and generation of acoustic and entropy waves across a moving flame front. *Combustion and Flame*, 166:170–180, 2016. DOI: 10.1016/j.combustflame.2016.01.015.

[302] L. Strobio Chen, T. Steinbacher, C. Silva, and W. Polifke. On generation of entropy waves across a premixed flame. In *ASME 2016 Turbo Expo: Turbomachinery Technical Conference and Exposition*, volume 4A: Combustion, Fuels and Emissions, page V04AT04A049, Seoul, Korea, 2016. American Society of Mechanical Engineers. DOI: 10.1115/GT2016-57026.

[303] R. I. Sujith, G. A. Waldherr, and B. Zinn. An exact solution for one-dimensional acoustic fields in duct with an axial temperature gradient. *Journal of Sound and Vibration*, 184 (3):389–402, 1995. DOI: 10.1006/jsvi.1995.0323.

[304] Y. Sun, D. Zhao, S. Ni, T. David, and Y. Zhang. Entropy and flame transfer function analysis of a hydrogen-fueled diffusion flame in a longitudinal combustor. *Energy*, 194: 116870, 2020. DOI: 10.1016/j.energy.2019.116870.

[305] S. Tachibana, K. Saito, T. Yamamoto, M. Makida, T. Kitano, and R. Kurose. Experimental and numerical investigation of thermo-acoustic instability in a liquid-fuel aero-engine combustor at elevated pressure: validity of large-eddy simulation of spray combustion. *Combustion and Flame*, 162(6):2621–2637, 2015. DOI: 10.1016/j.combustflame.2015.03.014.

[306] R. Tacina, C. Wey, P. Laing, and A. Mansour. Sector tests of a low NOx, lean-direct-injection, multipoint integrated module combustor concept. In *ASME Turbo Expo 2002: Power for Land, Sea, and Air*, volume 1: Turbo Expo 2002, pages 533–544, Amsterdam, The Netherlands, 2002. American Society of Mechanical Engineers. DOI: 10.1115/GT2002-30089.

[307] A. K. Tangirala. *Principles of system identification: theory and practice*. CRC Press, Boca Raton, FL, USA, 2014. ISBN 978-1-4398-9602-0.

[308] N. Tathawadekar, A. Ösün, A. J. Eder, C. F. Silva, and N. Thuerey. Linear and nonlinear flame response prediction of turbulent flames using neural network models. *International Journal of Spray and Combustion Dynamics*, 16(3):93–103, 2024. DOI: 10.1177/17568277241262641.

[309] L. Tay-Wo-Chong. *Numerical simulation of the dynamics of turbulent swirling flames*. Ph.D. thesis, Technische Universität München, Munich, Germany, 2012.

[310] L. Tay-Wo-Chong and W. Polifke. Large eddy simulation-based study of the influence of thermal boundary condition and combustor confinement on premix flame transfer functions. *Journal of Engineering for Gas Turbines and Power*, 135(2):021502, 2013. DOI: 10.1115/1.4007734.

[311] L. Tay-Wo-Chong, T. Komarek, R. Kaess, S. Föller, and W. Polifke. Identification of flame transfer functions from LES of a premixed swirl burner. In *ASME Turbo Expo 2010: Power for Land, Sea, and Air*, volume 2: Combustion, Fuels and Emissions, Parts A and B, pages 623–635, Glasgow, UK, 2010. American Society of Mechanical Engineers. DOI: 10.1115/GT2010-22769.

[312] L. Tay-Wo-Chong, S. Bomberg, A. Ulhaq, T. Komarek, and W. Polifke. Comparative validation study on identification of premixed flame transfer function. *Journal of Engineering for Gas Turbines and Power*, 134(2):021502, 2012. DOI: 10.1115/1.4004183.

[313] L. Tay-Wo-Chong, A. Scarpato, and W. Polifke. LES combustion model with stretch and heat loss effects for prediction of premix flame characteristics and dynamics. In *ASME Turbo Expo 2017: Turbomachinery Technical Conference and Exposition*, volume 4A: Combustion, Fuels and Emissions, page V04AT04A029, Charlotte, NC, USA, 2017. American Society of Mechanical Engineers. DOI: 10.1115/GT2017-63357.

[314] J. E. Temme, P. M. Allison, and J. F. Driscoll. Combustion instability of a lean premixed prevaporized gas turbine combustor studied using phase-averaged PIV. *Combustion and Flame*, 161(4):958–970, 2014. DOI: 10.1016/j.combustflame.2013.09.021.

[315] C. W. To and A. G. Doige. A transient testing technique for the determination of matrix parameters of acoustic systems, I: theory and principles. *Journal of Sound and Vibration*, 62(2):207–222, 1979. DOI: 10.1016/0022-460X(79)90022-1.

[316] C. W. To and A. G. Doige. A transient testing technique for the determination of matrix parameters of acoustic systems, II: experimental procedures and results. *Journal of Sound and Vibration*, 62(2):223–233, 1979. DOI: 10.1016/0022-460X(79)90023-3.

[317] N. C. Treleaven, A. Garmory, and G. J. Page. The effects of turbulence on jet stability and the flame transfer function in a lean-burn combustor. *Combustion Science and Technology*, 192(11):2115–2137, 2020. DOI: 10.1080/00102202.2020.1777992.

[318] A. Trouvé and T. Poinsot. The evolution equation for the flame surface density in turbulent premixed combustion. *Journal of Fluid Mechanics*, 278:1–31, 1994. DOI: 10.1017/S0022112094003599.

[319] K. Truffin and T. Poinsot. Comparison and extension of methods for acoustic identification of burners. *Combustion and Flame*, 142(4):388–400, 2005. DOI: 10.1016/j.combustflame.2005.04.001.

[320] K. Truffin, B. Varoquié, and T. Poinsot. Measurements of transfer functions in reacting flows using large eddy simulations. In *10th International Congress on Sound and Vibration,*, pages 785–793, Stockholm, Sweden, 2003.

[321] P. Tudisco, R. Ranjan, S. Menon, S. Jaensch, and W. Polifke. Application of the time-domain impedance boundary condition to large-eddy simulation of combustion instability in a shear-coaxial, high pressure combustor. *Flow, Turbulence and Combustion*, 99 (1):185–207, 2017. DOI: 10.1007/s10494-017-9804-3.

[322] United Nations. Paris Agreement. *Treaty Series*, 3156:79–257, 2016.

[323] G. Wang, X. Liu, S. Wang, L. Li, and F. Qi. Experimental investigation of entropy waves generated from acoustically excited premixed swirling flame. *Combustion and Flame*, 204:85–102, 2019. DOI: 10.1016/j.combustflame.2019.03.005.

[324] D. Wassmer, B. Schuermans, C. Paschereit, and J. P. Moeck. Measurement and modeling of the generation and the transport of entropy waves in a model gas turbine combustor. *International Journal of Spray and Combustion Dynamics*, 9(4):299–309, 2017. DOI: 10.1177/1756827717696326.

[325] M. Weilenmann and N. Noiray. Experiments on sound reflection and production by choked nozzle flows subject to acoustic and entropy waves. *Journal of Sound and Vibration*, 492:115799, 2020. DOI: 10.1016/j.jsv.2020.115799.

[326] M. Weilenmann, Y. Xiong, and N. Noiray. On the dispersion of entropy waves in turbulent flows. *Journal of Fluid Mechanics*, 903:R1, 2020. DOI: 10.1017/jfm.2020.703.

[327] M. Weilenmann, U. Doll, R. Bombach, A. Blondé, D. Ebi, Y. Xiong, and N. Noiray. Linear and nonlinear entropy-wave response of technically-premixed jet-flames-array and swirled flame to acoustic forcing. *Proceedings of the Combustion Institute*, 38(4):6135–6143, 2021. DOI: 10.1016/j.proci.2020.06.233.

[328] Y. Xia, I. Duran, A. S. Morgans, and X. Han. Dispersion of entropy perturbations transporting through an industrial gas turbine combustor. *Flow, Turbulence and Combustion*, 100(2):481–502, 2018. DOI: 10.1007/s10494-017-9854-6.

[329] Y. Yang, N. Noiray, A. Scarpato, O. Schulz, K. M. Düsing, and M. Bothien. Numerical analysis of the dynamic flame response in Alstom reheat combustion systems. In *ASME Turbo Expo 2015: Turbine Technical Conference and Exposition*, volume 4A: Combustion, Fuels and Emissions, page V04AT04A048, Montreal, Quebec, Canada, 2015. American Society of Mechanical Engineers. DOI: 10.1115/GT2015-42622.

[330] Z. Yao, Y. Gao, M. Zhu, A. P. Dowling, and K. N. Bray. Combustion rumble prediction with integrated computational-fluid-dynamics/low-order-model methods. *Journal of Propulsion and Power*, 28(5):1015–1025, 2012. DOI: 10.2514/1.B34469.

[331] M. Yoko and M. P. Juniper. Data-driven modelling of thermoacoustic instability in a ducted conical flame. In *Symposium on Thermoacoustics in Combustion: Industry meets Academia*, Zurich, Switzerland, 2023.

[332] M. Zhu, A. P. Dowling, and K. N. Bray. Flame transfer function calculations for combustion oscillations. In *ASME Turbo Expo 2001: Power for Land, Sea, and Air*, volume 2: Coal, Biomass and Alternative Fuels; Combustion and Fuels; Oil and Gas Applications; Cycle Innovations, page V002T02A055, New Orleans, LA, USA, 2001. American Society of Mechanical Engineers. DOI: 10.1115/2001-GT-0374.

[333] M. Zhu, A. P. Dowling, and K. N. Bray. Transfer function calculations for aeroengine combustion oscillations. *Journal of Engineering for Gas Turbines and Power*, 127(1): 18–26, 2005. DOI: 10.1115/1.1806451.

[334] B. T. Zinn and T. C. Lieuwen. Combustion instabilities: basic concepts. In *Combustion instabilities in gas turbine engines: operational experience, fundamental mechanisms, and modeling*, volume 210 of *Progress in astronautics and aeronautics*, pages 3–26. American Institute of Aeronautics and Astronautics, 2005. DOI: 10.2514/5.9781600866807.0003.0026.

Supervised students

As part of this doctoral thesis, several student theses were conducted and written in the Thermo-Fluid Dynamics Group at TUM in the years 2021 to 2024 under the supervision of the author. Some of them were related to one or more of the topics discussed in this thesis, others were related to different research topics of the group. The author would like to express his sincere gratitude to all formerly supervised students for their commitment and support of this research project.

Name	Thesis title, type, submission year
Ioannis Beis	Accurate species transport in 1D laminar flames: H_2 combustion for clean gas turbine, Semester thesis, 2022.
Benjamin Gregg-Smith	On acoustic waves in 2D, Semester thesis, 2022.
Akshay Kulkarni	Study on pseudo time-stepping in LES with conjugate heat transfer in the context of confined turbulent flames, Semester thesis, 2023.
Vaman Neurekar	Assessment and optimization of species transport for methane-hydrogen flames in OpenFOAM, Semester thesis, 2023.
Nicolas Guzman	Numerical simulation and assessment of a turbulent swirl flame for thermoacoustic investigations using PRECISE-UNS, Master's thesis, 2024.
Thomas Hollweck	Extended model-based inference of flame transfer matrices from acoustic measurements [135], Semester thesis, 2024. Co-author of [84] and [85].
Benjamin Gregg-Smith	Implementation of a characteristics-based filter in OpenFOAM, HiWi, 2021.
Gregor Doehner	Development of a parsimonious system of ODEs for the response modeling of turbulent flames, HiWi, 2023. Author of [63].
Akash Shankdhar	Revision of the lab course "Simulation of Thermo-Fluids with Open Source Tools", HiWi, 2023.
Thomas Hollweck	Revision and supervision of the lab course "Simulation of Thermo-Fluids with Open Source Tools", HiWi, 2023–2024

Appendices

Alexander J. Eder[1,2]
Department of Engineering Physics and
Computation,
TUM School of Engineering and Design,
Technical University of Munich,
Garching D-85748, Germany
e-mail: alexander.eder@tum.de

Moritz Merk[1]
Department of Engineering Physics and
Computation,
TUM School of Engineering and Design,
Technical University of Munich,
Garching D-85748, Germany

Thomas Hollweck
Department of Engineering Physics and
Computation,
TUM School of Engineering and Design,
Technical University of Munich,
Garching D-85748, Germany

André Fischer
Combustion and Turbine Department,
Rolls-Royce Deutschland,
Blankenfelde-Mahlow, D-15827, Germany

Claus Lahiri
Combustion and Turbine Department,
Rolls-Royce Deutschland,
Blankenfelde-Mahlow D-15827, Germany

Camilo F. Silva
Department of Engineering Physics and
Computation,
TUM School of Engineering and Design,
Technical University of Munich,
Garching D-85748, Germany

Wolfgang Polifke
Department of Engineering Physics and
Computation,
TUM School of Engineering and Design,
Technical University of Munich,
Garching D-85748, Germany

Model-Based Inference of Flame Transfer Matrices From Acoustic Measurements in an Aero-Engine Test Rig

Flame dynamics, represented as a flame transfer matrix (FTM), is not directly measurable in test rigs and must be deduced from transfer matrix measurements of the combustion system. The burner-flame transfer matrix (BFTM) approach for FTM estimation is based on local pressure signals from microphones located upstream and downstream of the combustor. It combines acoustic measurements in nonreacting and reacting conditions, with the latter implicitly including flame dynamics. A simple matrix operation yields the FTM. However, this approach assumes loss-free wave propagation at constant speed of sound with no change in cross-sectional area between the microphones and the burner/flame. The present work demonstrates the limitations of these assumptions when applied to a test rig with effusion cooling, bypass annulus, and end contraction. This work proposes a method to infer the FTM for complex combustors by combining reactive transfer matrix measurements of the entire combustor with an accurate low-order model (LOM) of the test rig. This generalized method reduces to the BFTM approach as a special case. The Rolls-Royce SCARLET test rig, operating under realistic engine conditions, is used to analyze the capabilities of the proposed model-based inference method and the limitations of the BFTM approach. First, a LOM based on SCARLET's geometry and operating point is formulated using a generic FTM. This model visualizes the limitations of the BFTM approach concerning various physical and geometrical parameters. Finally, experimental data is used to infer the FTM of SCARLET using the proposed approach. [DOI: 10.1115/1.4066366]

1 Introduction

Lean-burn, low-emission combustion systems, such as modern aero-engines, are susceptible to thermoacoustic combustion instabilities that can restrict their operational range, increase wear, or even damage the engine [1,2]. To prevent these self-excited instabilities in future engine development programs, accurate and efficient prediction tools are essential. Low-order thermoacoustic network modeling [3–9] has been demonstrated to be an efficient technique for predicting thermoacoustic instabilities in confined combustion systems like aero-engine combustors. Such a low-order model encompasses the main geometric features of the combustion system and is based on the interconnection of compact (e.g., area

change, end reflection, flow splits, flame) and noncompact (e.g., duct) quasi-one-dimensional acoustic elements [10,11]. The local transfer behavior of each network element may be represented by its transfer matrix, which links the upstream and downstream acoustic pressure and velocity fluctuations, respectively. The transfer matrix can be described for many elements using simple analytical models based on linearized governing equations. However, transfer matrices extracted from numerical simulations or experimental measurements are used for elements with more complex dynamics.

The intricate dynamics of a flame require sophisticated methods to model with accuracy. Apart from simulation-based approaches [12–15], the flame transfer matrix (FTM) [16] is usually estimated using measured data from a thermoacoustic test rig. However, since a direct measurement of the FTM is not possible, it is usually postprocessed from measured pressure signals. In this setup, the model combustor is placed between two measurement ducts that are equipped with microphone arrays. A siren modulates the air mass flow of the thermoacoustically stable experimental setup, exciting the flame at distinct frequencies. The microphone arrays with a spatial distribution in the axial direction then measure the resulting acoustic pressure fluctuations. Starting from the measured pressure data, two modeling steps are required to estimate the FTM. First, the acquired pressure fluctuations enable the reconstruction of upstream and downstream propagating plane acoustic waves while assuming a constant speed of sound and no changes in cross section between the individual microphones. This technique was first proposed by Munjal and Doige [17] and later extended to the multimicrophone method (MMM) by Peters et al. [18]. Paschereit, Polifke and Schuermans [16,19–21] adopted it for combustion applications. The reconstructed acoustic waves may be utilized to relate the acoustic pressure and velocity fluctuations upstream and downstream of the combustor via a transfer matrix. This transfer matrix is a black-box representation of the acoustic behavior of the combustor. In a second step, the established approach for estimating the FTM combines two transfer matrices obtained from measurements in nonreacting ("cold") and reacting ("hot") conditions. This approach assumes that the transfer behavior of the hot burner can be expressed as a sequence of the cold burner transfer matrix and the flame. The FTM is then computed by simple matrix multiplication of the hot and cold burner transfer matrices [20,22]. This methodology has been successfully employed in various studies [23–26] on premixed flames in simplistic test rigs.

However, as pointed out in recent studies by Alanyalıoğlu [27] and Eder [28], this approach is not valid for complex configurations such as aero-engine combustors. The primary discrepancies to simplistic test rigs investigated in prior studies are an additional acoustic communication path between the upstream and the downstream duct via an effusion cooling bypass annulus and more complex combustion chamber geometries. While the FTM remains an intrinsic part of the hot measurement, the assumption that the hot burner transfer matrix is a simple sequence of the cold burner transfer matrix and the flame does not hold anymore. Therefore, the established approach is no longer applicable.

To remedy the limitations of the aforementioned approach, this work presents a novel method that provides a consistent inference of the FTM for complex test rigs. The proposed method combines acoustic transfer matrix measurements of the full combustor under hot conditions with a low-order thermoacoustic network model of the test rig. The capabilities of the model-based method are analyzed using the Rolls-Royce Scaled Acoustic Rig for Low Emission Technology (SCARLET) [29,30], which comprises a single sector aero-engine combustor and is operated under realistic engine conditions (high pressure, preheating temperatures and mass fluxes).

The paper is structured as follows. Section 2 describes the established method to postprocess the FTM from experimental measurements and introduces the model-based inference method. The experimental setup, acoustic transfer matrix measurements, and a low-order thermoacoustic network model of SCARLET are presented in Sec. 3. In Sec. 4, the network model is used to visualize the limitations of the established method for test rigs with complex

features like SCARLET. In addition, the model-based inference method is shown to be exact in the absence of modeling errors. In Sec. 5, the model-based inference method is applied to experimental data of SCARLET and the advantages and drawbacks of the novel method are discussed. Finally, the work is concluded in Sec. 6.

2 Modeling Approach

In experimental setups, many quantities of interest cannot be measured directly but must be postprocessed from the acquired data utilizing models. The quality and validity of the postprocessed quantities are therefore limited by the modeling assumptions used. It is essential to understand these limitations.

2.1 Determination of Transfer Matrices From Acoustic Pressure Measurements. The multimicrophone method [16,18–21,31] is a postprocessing technique to approximate the acoustic velocity and pressure perturbations at a reference point x_{ref} based on pressure signals acquired from an axially-distributed microphone array. Under the assumption of plane acoustic wave propagation at constant speed and no changes in cross section, the Fourier transformed pressure signals of the individual microphones

$$\begin{pmatrix} p'_1 \\ \vdots \\ p'_k \end{pmatrix} = \bar{\rho}\bar{c}\mathbf{A}\begin{pmatrix} f_{\text{ref}} \\ g_{\text{ref}} \end{pmatrix} \tag{1}$$

can be expressed in terms of the acoustic wave amplitudes $f = \left(p'/(\bar{\rho}\bar{c}) + u'\right)/2$ and $g = \left(p'/(\bar{\rho}\bar{c}) - u'\right)/2$ at x_{ref}. The matrix

$$\mathbf{A} = \begin{pmatrix} \exp\left(-\dfrac{i\omega}{\bar{c}+\bar{u}}\Delta x_1\right) & \exp\left(-\dfrac{i\omega}{\bar{c}-\bar{u}}\Delta x_1\right) \\ \vdots & \vdots \\ \exp\left(-\dfrac{i\omega}{\bar{c}+\bar{u}}\Delta x_k\right) & \exp\left(-\dfrac{i\omega}{\bar{c}-\bar{u}}\Delta x_k\right) \end{pmatrix} \tag{2}$$

accounts for the phase shift resulting from the acoustic wave propagation between the microphones and the reference point, $\Delta x_k = x_k - x_{\text{ref}}$. ω, p, ρ, c, and u are the angular frequency, pressure, density, speed of sound, and flow velocity. The superscripts $\bar{\psi}$ and ψ' denote the time-invariant mean value and a small perturbation of an arbitrary quantity ψ. Then, the approximated acoustic wave amplitudes at the reference point are retrieved as the least-squares minimization of Eq. (1), e.g., by applying the Moore–Penrose generalized inverse [32]

$$\begin{pmatrix} f_{\text{ref}} \\ g_{\text{ref}} \end{pmatrix} = \frac{1}{\bar{\rho}\bar{c}}(\mathbf{A}^H\mathbf{A})^{-1}\mathbf{A}^H\begin{pmatrix} p'_1 \\ \vdots \\ p'_k \end{pmatrix} \tag{3}$$

where $(\cdot)^H$ and $(\cdot)^{-1}$ are the Hermitian transpose and the matrix inverse. Finally, f_{ref} and g_{ref} can be decomposed into the pressure and velocity fluctuations at the x_{ref} via

$$\begin{pmatrix} \dfrac{p'_{\text{ref}}}{\bar{\rho}\bar{c}} \\ u'_{\text{ref}} \end{pmatrix} = \begin{pmatrix} 1 & 1 \\ 1 & -1 \end{pmatrix}\begin{pmatrix} f_{\text{ref}} \\ g_{\text{ref}} \end{pmatrix} \tag{4}$$

The transfer behavior of a system can be represented by a transfer matrix $\mathbf{T}$, which relates the pressure and the velocity perturbations at the boundaries of a system, generally defined as

$$\begin{pmatrix} \dfrac{p'}{\bar{\rho}\bar{c}} \\ u' \end{pmatrix}_j = \mathbf{T}\begin{pmatrix} \dfrac{p'}{\bar{\rho}\bar{c}} \\ u' \end{pmatrix}_i \tag{5}$$

Transfer matrices can be determined from acoustic measurements by enclosing a system between the reference points of two microphone arrays ($i = \text{u}, j = \text{d}$). Additionally, the measurement

of at least two acoustically independent test states is needed. See Åbom [33] for various possibilities of producing different test sets. For two test states A and B, the transfer matrix can be obtained using

$$\widetilde{\mathbf{T}} = \begin{pmatrix} \frac{p_d'^A}{\bar{\rho}\bar{c}} & \frac{p_d'^B}{\bar{\rho}\bar{c}} \\ u_d'^A & u_d'^B \end{pmatrix} \begin{pmatrix} \frac{p_u'^A}{\bar{\rho}\bar{c}} & \frac{p_u'^B}{\bar{\rho}\bar{c}} \\ u_u'^A & u_u'^B \end{pmatrix}^{-1} \quad (6)$$

Note that transfer matrices determined by the measurement procedure detailed in this section are denoted with $\widetilde{(\cdot)}$ throughout this work.

2.2 Estimation of the Flame Transfer Matrix From Two Measurements - the Burner-Flame Transfer Matrix Approach.

The flame transfer matrix $\mathbf{F}$ is an intrinsic part of the transfer matrix $\widetilde{\mathbf{T}}^h$ of the reactive ("hot") test rig. To extract $\mathbf{F}$ from the experimentally determined $\widetilde{\mathbf{T}}^h$, the established postprocessing approach [23–26] assumes that $\widetilde{\mathbf{T}}^h$ can be modeled as a series of the burner transfer matrix $\mathbf{B}$ and the flame transfer matrix $\mathbf{F}$

$$\mathbf{T}^h := \mathbf{F}\mathbf{B} \quad (7)$$

$\mathbf{T}^h$ is called burner-flame transfer matrix (BFTM) in this case. In addition, the burner transfer matrix $\mathbf{B}$ is assumed to remain unchanged by the combustion processes [22,34]. $\mathbf{B}$ is then determined by the transfer behavior $\widetilde{\mathbf{T}}^c$ of the nonreactive ("cold") test rig at the same inlet conditions

$$\widetilde{\mathbf{T}}^c := \mathbf{B} \quad (8)$$

Assuming that the model in Eq. (7) accurately represents the measured hot test rig ($\widetilde{\mathbf{T}}^h = \mathbf{T}^h$), the flame transfer matrix can be estimated via

$$\mathbf{F} = \widetilde{\mathbf{T}}^h \left(\widetilde{\mathbf{T}}^c\right)^{-1} \quad (9)$$

Analogously to $\widetilde{\mathbf{T}}^h$, $\widetilde{\mathbf{T}}^c$ is determined from experimental measurements using the MMM detailed in Sec. 2.1. Throughout this work, the method represented by Eq. (9) is referred to as the *BFTM approach* due to the key modeling assumption in Eq. (7).

Figure 1(*a*) shows a simple test rig consisting of a burner section between two ducts. In this simplistic case, the reference points of the
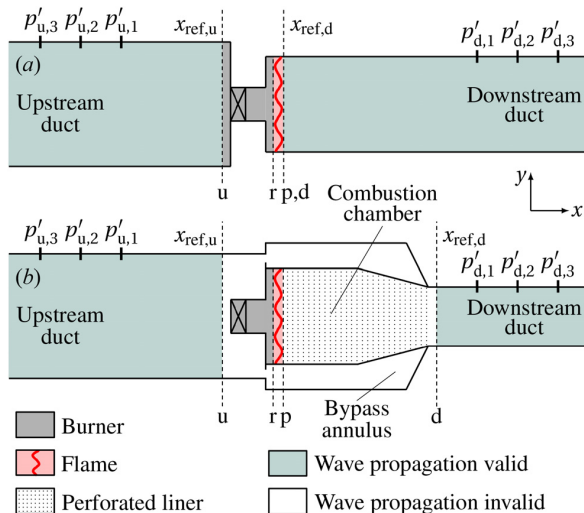
MMM can be chosen to enclose solely the burner and the flame. The assumptions of the BFTM approach hold. For combustor test rigs with complex features such as effusion cooling, bypass annulus, and downstream end contraction as shown in Fig. 1(*b*), the reference points of the MMM typically brackets the full combustor. Considering Fig. 1(*b*) it is evident that the transfer matrices $\widetilde{\mathbf{T}}^c$ and $\widetilde{\mathbf{T}}^h$ measured with the MMM should be recognized as the combustor transfer matrices $\widetilde{\mathbf{C}}^c$ and $\widetilde{\mathbf{C}}^h$ for the "cold" and "hot" operating conditions, respectively. In this case, the modeling assumption (Eq. (7)) of the BFTM postprocessing approach is no longer valid [27,28] and a new method is required to deduce $\mathbf{F}$ from $\widetilde{\mathbf{C}}^h$.

2.3 Model-Based Inference of the Flame Transfer Matrix in General Setups.

In general, the inference of $\mathbf{F}$, defined as (Fig. 2, top right)

$$\mathbf{v}_p = \mathbf{F}\,\mathbf{v}_r \quad (10)$$

from the measured hot combustor transfer matrix $\widetilde{\mathbf{C}}^h$, defined as (Fig. 2, top left)

$$\mathbf{v}_d = \widetilde{\mathbf{C}}^h \mathbf{v}_u \quad (11)$$

Requires a model that connects the states

$$\mathbf{v}_i = \begin{pmatrix} \frac{p'}{\bar{\rho}\bar{c}} \\ u' \end{pmatrix}_i \quad (12)$$

upstream ($i = r$, "reactants") and downstream ($i = p$, "products") of the flame to the states upstream ($i = u$) and downstream ($i = d$) of the combustor. This connector model (Fig. 2, center) is an interconnection of different transfer matrices representing the complexity of the underlying system. The subelements can be modeled individually, e.g., via low-order models (LOM), or provided from experimental measurements or numerical simulations. The resulting connector transfer matrix can be expressed by the general model [35]

$$\begin{pmatrix} \mathbf{v}_r \\ \mathbf{v}_d \end{pmatrix} = \begin{pmatrix} \mathbf{T}_{ru} & \mathbf{T}_{rp} \\ \mathbf{T}_{du} & \mathbf{T}_{dp} \end{pmatrix} \begin{pmatrix} \mathbf{v}_u \\ \mathbf{v}_p \end{pmatrix} \quad (13)$$
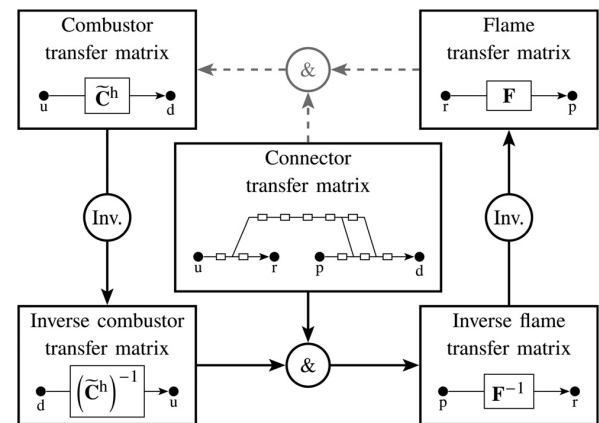

Fig. 1 Schematic representation of (*a*) a simplistic and (*b*) an aero-engine test rig under reactive conditions. Sirens are not shown. The indices "*u*," "*r*," "*p*," and "*d*" stand for upstream, reactants, products, and downstream, respectively.

Fig. 2 Visualization of the model-based inference method (solid arrows) to infer the flame transfer matrix (top right) from the measured combustor transfer matrix (top left) utilizing a connector model (center). "Inv." denotes the inversion of a transfer matrix and "&" the interconnection of two models. The gray dashed arrows display the methodology to calculate the system response from a known flame transfer matrix.

In Eq. (13), $\mathbf{v}_u$ and $\mathbf{v}_p$ are chosen as inputs while $\mathbf{v}_r$ and $\mathbf{v}_d$ are treated as outputs of the connector model. Note that this choice is arbitrary and could be changed. The connector model's subtransfer matrices $\mathbf{T}_{ru}$, $\mathbf{T}_{rp}$, $\mathbf{T}_{du}$ and $\mathbf{T}_{dp}$ each depend on the reflection and transmission coefficients of all subelements of the connector model. $\mathbf{T}_{ru}$, $\mathbf{T}_{rp}$, $\mathbf{T}_{du}$, and $\mathbf{T}_{dp}$ can be extracted utilizing existing low-order network toolboxes such as the open source MATLAB® package taX[2] [35] developed at TUM. Note that Eq. (13) is valid for connector models of arbitrary complexity.

To derive a closed-form representation of $\mathbf{F}$, the inverse hot combustor transfer matrix $\left(\widetilde{\mathbf{C}}^h\right)^{-1}$ (Fig. 2, lower left) is used as a closure model to remove $\mathbf{v}_u$ and $\mathbf{v}_d$ from the connector transfer matrix (Eq. (13)). Mathematically, this interconnection is expressed in the following two steps. First, the bottom row of Eq. (13) is used to substitute $\mathbf{v}_d$ in the definition of the inverse combustor transfer matrix

$$\begin{aligned} \mathbf{v}_u &= \left(\widetilde{\mathbf{C}}^h\right)^{-1}\mathbf{v}_d \\ &= \left(\widetilde{\mathbf{C}}^h\right)^{-1}\left(\mathbf{T}_{du}\mathbf{v}_u + \mathbf{T}_{dp}\mathbf{v}_p\right) \end{aligned} \tag{14}$$

This reveals an expression of the state $\mathbf{v}_u$ in terms of the state $\mathbf{v}_p$ only

$$\mathbf{v}_u = \left(\widetilde{\mathbf{C}}^h - \mathbf{T}_{du}\right)^{-1}\mathbf{T}_{dp}\,\mathbf{v}_p \tag{15}$$

Second, Eq. (15) is used to substitute $\mathbf{v}_u$ in the top row of Eq. (13). The result is the inverse flame transfer matrix $\mathbf{F}^{-1}$ (Fig. 2) that expresses the state $\mathbf{v}_r$ in sole dependence of the state $\mathbf{v}_p$

$$\mathbf{v}_r = \underbrace{\left[\mathbf{T}_{ru}\left(\widetilde{\mathbf{C}}^h - \mathbf{T}_{du}\right)^{-1}\mathbf{T}_{dp} + \mathbf{T}_{rp}\right]}_{\mathbf{F}^{-1}}\mathbf{v}_p \tag{16}$$

Finally, a simple matrix inversion provides the general rule for the inference of the FTM from the measured hot combustor transfer matrix

$$\mathbf{F} = \left[\mathbf{T}_{ru}\left(\widetilde{\mathbf{C}}^h - \mathbf{T}_{du}\right)^{-1}\mathbf{T}_{dp} + \mathbf{T}_{rp}\right]^{-1} \tag{17}$$

Throughout this work, the utilization of Eq. (17) is referred to as the *model-based inference* (MBI) method, where the individual steps to derive it are visualized in Fig. 2.

In contrast to the BFTM approach, described in Sec. 2.2, the MBI method does not require the additional measurement of the cold combustor transfer matrix $\widetilde{\mathbf{C}}^c$ at the same operating point as $\widetilde{\mathbf{C}}^h$ to infer the FTM, reducing the experimental effort. Therefore, the superscript "h" has been omitted throughout this section for simplicity. Note, however, that the MBI method relies heavily on the connector model's accurate representation of the internal combustor dynamics. Equation (17) shows that any modeling error in the connector transfer matrices $\mathbf{T}_{ru}$, $\mathbf{T}_{rp}$, $\mathbf{T}_{du}$, and $\mathbf{T}_{dp}$ directly impact the inferred $\mathbf{F}$. Therefore, the quality of the connector model must be ensured for reliable FTM predictions. In this work, the comparison of a measured cold combustor transfer matrix $\widetilde{\mathbf{C}}^c$ with the corresponding model

$$\mathbf{C}^c = \mathbf{T}_{dp}^c\left(\mathbf{I} - \mathbf{T}_{rp}^c\right)^{-1}\mathbf{T}_{ru}^c + \mathbf{T}_{du}^c \tag{18}$$

is used to indicate the accuracy of the connector model. Equation (18) is derived from the connector model (Eq. (13)) in the absence of a flame, $\mathbf{v}_p = \mathbf{I}\,\mathbf{v}_r$, where $\mathbf{I}$ is the identity matrix. The superscript "c" for the connector matrices $\mathbf{T}_{ru}$, $\mathbf{T}_{rp}$, $\mathbf{T}_{du}$, and $\mathbf{T}_{dp}$ denotes their evaluation for the cold combustor. See Appendix for a detailed derivation of the combustor model $\mathbf{C}^c$ (and $\mathbf{C}^h$).

Note that the MBI method applies not only to reduced-order network models—as used in the present work—but also to spatially resolved models based on linearized equations, e.g., Helmholtz equation, linearized Euler equations or linearized Navier-Stokes equation. In this case, the input and output state vectors $\mathbf{v}_u$, $\mathbf{v}_r$, $\mathbf{v}_p$, and $\mathbf{v}_d$ of the connector model include numerous states and Eq. (13) remains valid.

2.4 The Burner-Flame Transfer Matrix Approach—a Special Case of the Model-Based Inference Method. The postprocessing approach presented in Sec. 2.2 is a special case of the generalized MBI method proposed in Sec. 2.3. In the absence of an acoustic branch bypassing the flame, the transfer matrices $\mathbf{T}_{du}$ and $\mathbf{T}_{rp}$ of the connector model vanish ($\mathbf{T}_{du} = \mathbf{0}$, $\mathbf{T}_{rp} = \mathbf{0}$). Additionally, assuming a combustion chamber with constant cross section ($\mathbf{T}_{dp} = \mathbf{D}_{dp}$), Eq. (17) simplifies to

$$\mathbf{F} = \left(\mathbf{D}_{dp}^h\right)^{-1}\widetilde{\mathbf{C}}^h\left(\mathbf{T}_{ru}^h\right)^{-1} \tag{19}$$

Under the additional assumption that $\mathbf{T}_{ru}^h$ is not affected by the flame ($\mathbf{T}_{ru}^h = \mathbf{T}_{ru}^c = \mathbf{T}_{ru} = \mathbf{B}$) [22,34], $\mathbf{T}_{ru}^h$ can be deduced from the cold combustor transfer matrix $\widetilde{\mathbf{C}}^c = \mathbf{D}_{dp}^c\mathbf{T}_{ru}^h$ and Eq. (19) further reduces to

$$\mathbf{F} = \underbrace{\left(\mathbf{D}_{dp}^h\right)^{-1}\widetilde{\mathbf{C}}^h}_{\mathbf{FB}}\underbrace{(\widetilde{\mathbf{C}}^c)^{-1}\mathbf{D}_{dp}^c}_{\mathbf{B}^{-1}} \tag{20}$$

In this simple setup, the terms $\left(\mathbf{D}_{dp}^h\right)^{-1}\widetilde{\mathbf{C}}^h$ and $\left(\mathbf{D}_{dp}^c\right)^{-1}\widetilde{\mathbf{C}}^c$ are equal to the BFTM (Eq. (7)) and the burner transfer matrix (Eq. (8)), respectively. Accordingly, Eq. (20) is equivalent to the BFTM approach (Eq. (9)).

3 Thermoacoustic Test Rig

In this study, the BFTM approach (Sec. 2.2) and the proposed MBI method (Sec. 2.3) are used to estimate the flame transfer matrix from acoustic measurement data in an aero-engine test rig. The experimental setup and a thermoacoustic low-order network model of the rig are presented below.

3.1 Experimental Setup. The Rolls-Royce SCARLET test rig [29,30] comprises a single-sector aero-engine combustion chamber and is located in the HBK-3 (high-pressure combustion chamber) test facility at the DLR (German Aerospace Center) in Cologne, Germany. It was developed for efficient testing of liquid fuel injectors under realistic engine conditions. The inlet conditions of the rig represent the outlet conditions of the compressor stage in the engine with a maximum pressure of 30 bar, a maximum preheating temperature of 950 K, and a maximum air mass flow of 4 kg/s. The operating point investigated in this work is given in Table 1, where kerosene is used as the liquid fuel. The measurements aim to determine the cold and hot combustor transfer matrices $\widetilde{\mathbf{C}}^c$ and $\widetilde{\mathbf{C}}^h$, respectively, using the multimicrophone method described in Sec. 2.1. These measurements are conducted in an acoustically controlled environment and, therefore, guarantee a thermoacoustically stable operation.

Table 1 Operating condition of SCARLET

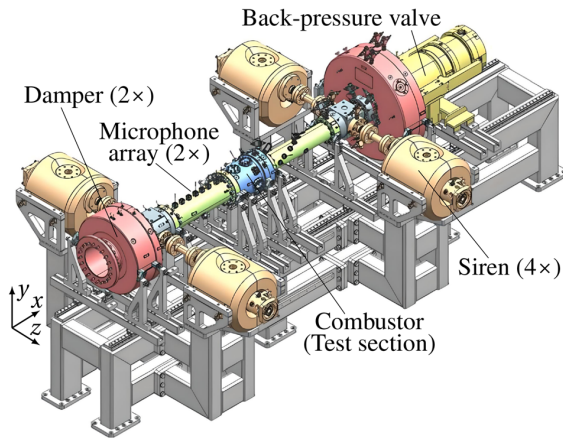| Parameter	Value	Unit
Inlet pressure	25	bar
Inlet mass flow	3	kg s^{-1}
Inlet temperature	825	K
Thermal power	4.2	MW

84

Fig. 3   Isometric view of SCARLET. Flow in *x*-direction.

The rig, shown in Fig. 3, consists of a back-pressure valve, two dampers, four sirens, two acoustic measurement sections (constant cross section) with an array of microphones, and an aero-engine combustion chamber (test section). A variable back-pressure valve restricts the total mass flow to adjust the pressure drop across the installed injector unit from about 2% to 4% to the inlet pressure. Upstream and downstream dampers ensure control of the acoustic boundaries, thus minimizing end reflections and dampening the occurrence of longitudinal modes. Two opposing sirens upstream and downstream of the test section provide sinusoidal acoustic excitation in the frequency range of approximately 100–1000 Hz, with the amplitude controlled by variations in the phase relation. The two acoustic measurement sections for reconstructing the upstream and downstream acoustic fields consist of five flush-mounted microphones each, whereas the downstream ones are water-cooled. The rig has approximately 200 static transducers to measure temperatures, static pressures, mass flows, and differences of static pressure with acquisition rates of 1 Hz. These measurements include upstream and downstream pressures, upstream temperature, pressure drops across the injector and liner, and air mass flow. The static pressures and pressure differences are measured at three radial positions and then averaged. The downstream temperature is not measured but estimated based on the fuel concentration, net caloric value of the fuel, upstream pressure, and upstream temperature, whereas the impact of wall cooling is neglected.

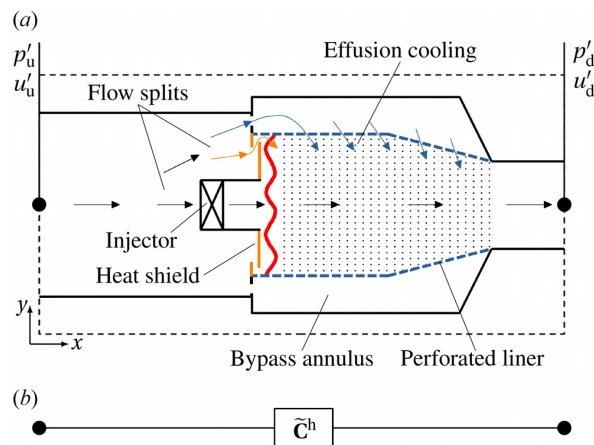The test section is shown schematically in Fig. 4(a). It is situated amidst the microphone arrays and consists of an injector unit with a fuel spray nozzle and five axial swirlers, and a combustion chamber with a bypass annulus for effusion cooling. The main air is split at the injector in three streams (through the injector for combustion, through the bypass annulus, and through the heat shield as cooling air). The combustion chamber walls are cooled by effusion cooling (transpiration cooling), achieved by moving air from the outer annulus through the liner structure (thousands of small holes). Due to its application in an aero-engine, the geometry of the single-sector axis-symmetrical combustor has a typical shape that tapers in diameter toward its outlet (i.e., turbine inlet). The entire test section (between the black dots) can be considered as a black-box by means of the combustor transfer matrix as shown in Fig. 4(b). The postprocessed combustor transfer matrices $\widetilde{\mathbf{C}}^{\mathrm{c}}$ (no flame) and $\widetilde{\mathbf{C}}^{\mathrm{h}}$ (flame) are shown in Fig. 5. All frequencies in this work are nondimensionalized using a Strouhal number for confidentiality

$$\mathrm{St} = f \frac{L_{\mathrm{ref}}}{u_{\mathrm{ref}}} \tag{21}$$

where f is the frequency, L_{ref} is the diameter of the injector, and u_{ref} is the bulk velocity of the inlet air stream.

3.2   Acoustic Network Model. The model-based inference of the flame transfer matrix presented in Sec. 2.3 combines acoustic transfer matrix measurements with an acoustic network model of the test rig. The network model of SCARLET used in this work is built using taX [35] and consists of 185 elements in total, including duct segments, area changes with and without pressure losses, converging and diverging junctions, and a compact flame element (in hot conditions). The *ducts* are modeled based on the one-dimensional acoustic wave equation [35] and are discretized with a third-order upwind scheme. The shortest wavelength of interest is highly resolved with 100 base points. Sudden *area changes* are represented with the $L - \zeta$ model [16,36]. The injector, bypass entry, effusion holes, and heat shield are penalized with a pressure loss coefficient ζ calculated from measured pressure differences, while effective and reduced lengths are set to zero [36]. Even though the geometry of the injector unit is highly complex, the axially arranged swirl vanes may be reasonably assumed to have acoustically transparent behavior [37]. Experimentally or numerically determined transfer matrices
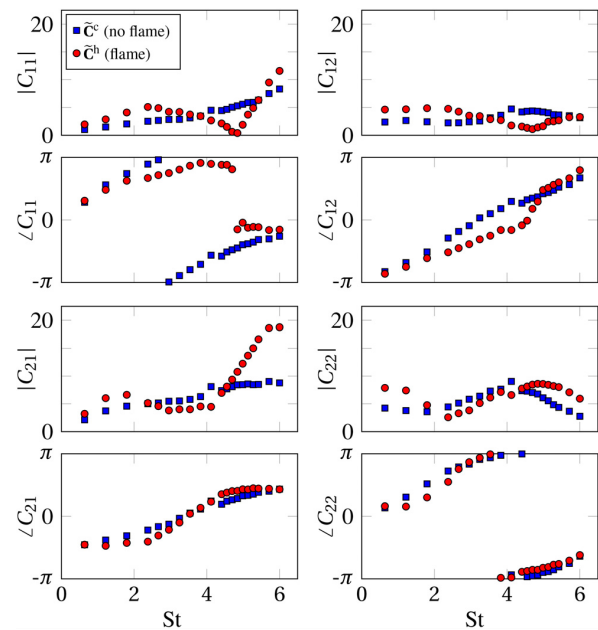

Fig. 4   (*a*) Schematic representation and (*b*) black-box model of the SCARLET test section in Fig. 3. The five axial swirlers are encompassed in the simplistic representation of the injector.

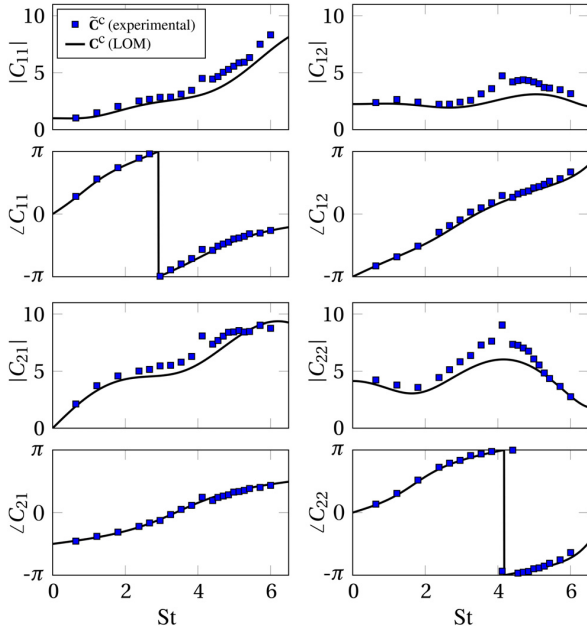**Fig. 5   Gain and phase of the coefficients of the experimental combustor transfer matrices of SCARLET**

Fig. 6 Gain and phase of the coefficients of the combustor transfer matrix for cold conditions obtained from experimental data $\tilde{\mathbf{C}}^c$ and LOM $\mathbf{C}^c$

should be used to increase the model's accuracy, especially at higher frequencies [20,38,39]. The convergent part of the combustion chamber is modeled as ten consecutive series of duct and area change. The real combustor has several thousand cooling holes in the acoustic liner. These holes are lumped into 20 branches in the LOM, each as a series of area change-duct-area change. Increasing the number of branches does not improve the results. The upstream and downstream boundaries are treated as nonreflective since they do not affect the determination of the combustor transfer matrix (acoustic/geometric changes outside the test section are irrelevant). Furthermore, the dependence of material properties on the temperature and mixture is neglected ($c_p \neq \mathrm{f}(T,Y_i) = $ const. and $R \neq \mathrm{f}(Y_i) = $ const., i.e., $\gamma = c_p/(c_p - R) \neq \mathrm{f}(T,Y_i) = $ const.) and low Mach numbers ($\mathcal{O}(\mathrm{M}^1)$) are assumed in all elements, which are common (yet questionable) assumptions made in thermoacoustic network models [14,40–42].

The acoustic network model in this work is based on geometrical information (lengths, diameters, areas) and static measurements (upstream and downstream pressure, upstream temperature, upstream mass flow) of SCARLET. The downstream temperature is estimated as described in Sec. 3. The flow splits are determined using low-order model calculations for the flow, and the effective surface area of the injector is approximated. The underlying model is physics-based and does not rely on spurious tuning parameters. This ensures a reasonably accurate modeling of the internal system dynamics, whereas fitting model parameters solely to global behavior (i.e., combustor transfer matrix) would violate this approach. A comparison of the cold combustor transfer matrix from measurements $\tilde{\mathbf{C}}^c$ and the acoustic network model $\mathbf{C}^c$ (Eq. (18)) is shown in Fig. 6. Both the gain and phase of the LOM are in quantitative agreement with experiments. Together with the physics-based approach of the LOM (internal system dynamics), this agreement ensures accurate modeling of the global behavior.

4 Limitations of the Burner-Flame Transfer Matrix Approach

The BFTM method, as described in Sec. 2.2, is appealing due to its simplicity and use of solely experimental input data. Unfortunately,
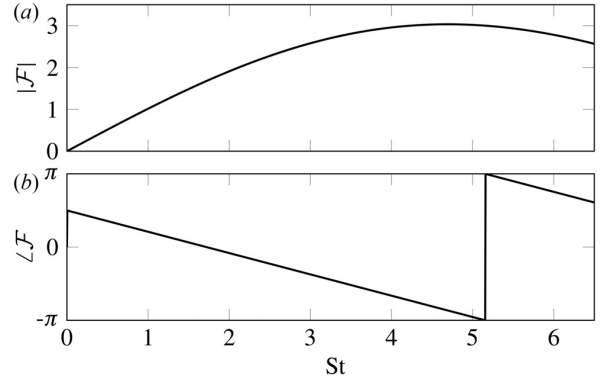

Fig. 7 (a) Gain and (b) phase of the generic flame transfer function $\mathcal{F}^*$

it is inconsistent for combustor geometries such as the present one with effusion cooling, bypass annulus, and downstream end contraction [27,28]. The goal of this section is to visualize this inconsistency.

A method is consistent if it can recover the reference solution without modeling errors, measurement inconsistencies, and uncertainties. To generate such a fully consistent dataset in combination with a known reference FTM, this section combines the LOM of SCARLET (see Sec. 3.2) with a generic FTM to generate $\tilde{\mathbf{C}}^h$. Additionally, $\tilde{\mathbf{C}}^c$ at the same operating point is generated using the LOM. Note that in this section, the transfer matrices $\mathbf{F}^*$, $\tilde{\mathbf{C}}^h$, and $\tilde{\mathbf{C}}^c$ are therefore purely analytical, while the flow quantities of the LOM are based on the realistic engine condition given in Table 1. The generic FTM has been generated using the Rankine–Hugoniot relations [5,20]

$$\mathbf{F}_{RH} = \begin{pmatrix} \dfrac{\rho_c c_c}{\rho_h c_h} & -\theta \mathrm{M}_h(1 + \mathcal{F}(\omega)) \\ -\gamma \theta \mathrm{M}_c & 1 + \theta \mathcal{F}(\omega) \end{pmatrix} \qquad (22)$$

where $\theta = (T_h/T_c - 1)$, T is the temperature, ρc is the acoustic impedance, M is the Mach number, and $\mathcal{F}(\omega)$ is the flame transfer function (FTF) of a velocity-sensitive flame used as closure for the heat release rate fluctuations. The FTF is defined as

$$\mathcal{F}(\omega) \equiv \frac{\dot{Q}'(\omega)/\overline{\dot{Q}}}{u_c'(\omega)/\bar{u}_c} \qquad (23)$$

where $\dot{Q}$ is the heat release rate and u_c is the velocity in the cold region upstream of the flame. This work uses a generic distributed time delay (DTD) model [43] of a partially premixed flame $\mathcal{F}^*$ as shown in Fig. 7. The corresponding generic FTM is obtained by incorporating $\mathcal{F}^*$ into Eq. (22) and is referred to as $\mathbf{F}^*$.

Figure 8 shows the FTMs postprocessed from the generic combustor transfer matrices of the SCARLET LOM via the BFTM approach (dash-dotted line) and the MBI method (solid line) and compares them to the reference solution $\mathbf{F}^*$. The MBI method is consistent, and its result coincides with the reference solution for the generic dataset used. In Fig. 8, $\mathbf{F}^*$ and the MBI results are represented by the same (solid) line. In contrast, the FTM postprocessed with the BFTM method shows large deviations from $\mathbf{F}^*$ in all transfer matrix coefficients. These discrepancies in the FTM originate solely from the inconsistency of the BFTM method for complex thermoacoustic test rigs like SCARLET and demonstrate furthermore its inapplicability in such cases.

In SCARLET, the inconsistency of the BFTM method is due to three features as summarized in Table 2—the area contraction at the end of the combustion chamber (C) as well as the acoustics (A) and the mean flow (M) bypassing the flame through the effusion holes. The following paragraph analyzes their contributions to the
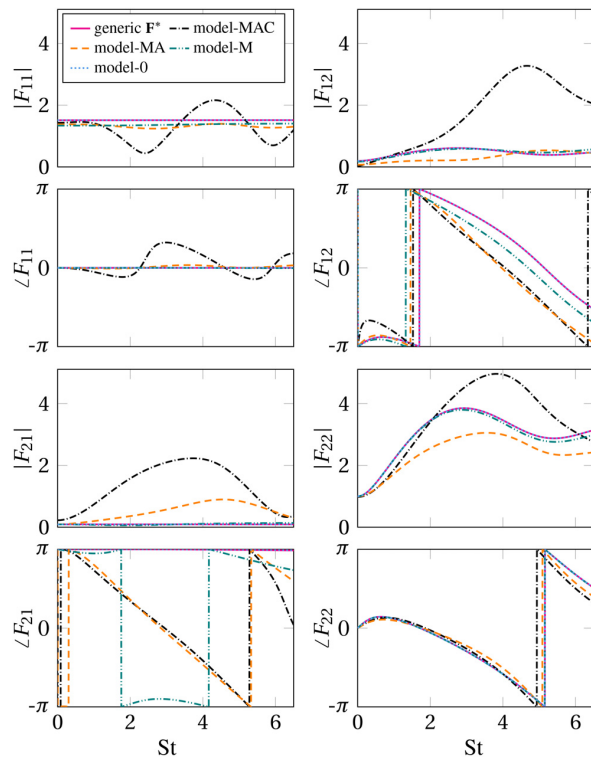
Fig. 8 Gain and phase of the coefficients of the generic $\mathbf{F}^*$ and the flame transfer matrices postprocessed from the generic SCARLET models detailed in Fig. 9 via the BFTM approach: model-MAC (original LOM), model-MA, model-M, and model-0. Note that model-0 and $\mathbf{F}^*$ overlap. The MBI result coincides with $\mathbf{F}^*$ in all cases and is therefore represented by the same solid line.

Table 2 Geometrical and flow features of different generic SCARLET low-order models used in this section. Important features are the meanflow bypass (M), the acoustic bypass (A) and the area contraction at the end of the combustion chamber (C).

	M	A	C
model-MAC	✓	✓	✓
model-MA	✓	✓	
model-M	✓		
model-0			

deviations of the BFTM method. Therefore, the SCARLET LOM is gradually adapted three times, removing the features M, A, and C. Figure 9 displays the corresponding generic SCARLET models. All other key features besides M, A, and C, like the FTM $\mathbf{F}^*$, mass flow splits, and pressure losses, remain unchanged. The SCARLET LOM detailed in Sec. 3.2 includes all features and is therefore awarded the
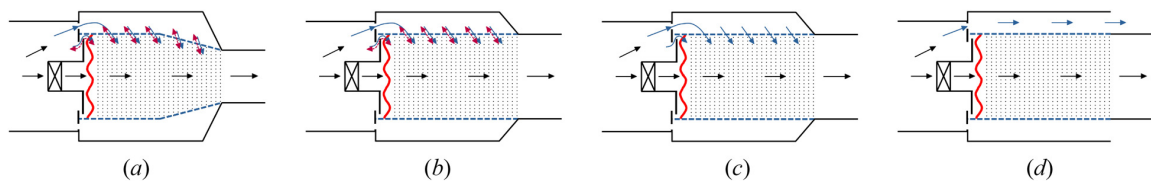
short name *model-MAC* (Fig. 9(*a*)). In the *model-MA* (Fig. 9(*b*)), the area contraction of the combustion chamber is removed by adapting the diameter of the downstream duct. The *model-M* (Fig. 9(*c*)) additionally eliminates the acoustic bypass through the effusion holes and the heat shield. This is achieved by inserting a fully reflective, acoustically energy-conserving element into each effusion hole and the heat shield. Finally, the *model-0* (Fig. 9(*d*)) also removes the bypass mean flow by venting all bypass air through a nozzle at the end of the bypass annulus.

The FTMs postprocessed with the BFTM approach for the generic SCARLET model-MAC, model-MA, model-M, and model-0 are visualized in Fig. 8 in addition to the MBI result. In the case of SCARLET, the area contraction at the end of the combustion chamber contributes most to the deviations of the BFTM method in all transfer coefficients of $\mathbf{F}^*$ (see the difference between model-MAC and model-MA). The magnitude of this deviation is directly linked to the area contraction and increases with stronger area contractions and vice versa. Compared to the deviations introduced by C, the deviations corresponding to the acoustic bypass (difference between model-MA and model-M) are smaller but yet in the same order of magnitude. This contribution's magnitude and frequency content depend strongly on the flow characteristics and the geometry of the bypass. Which of the two features, A or C, dominates the deviations in a given setup, and whether they partially cancel each other out, highly depends on the problem. Overall, both A and C should be assumed to invalidate the BFTM method for a specific setup unless proven otherwise. The final deviation of the cooling air reentering the combustion chamber (difference between model-M and model-0) is inferior to the other two effects. For model-0, the FTM postprocessed with the BFTM method coincides with the reference $\mathbf{F}^*$, proving that all features that render the BFTM method inconsistent have been removed.

5 Application to Experimental Measurements

The model-based inference method is applicable for complex thermoacoustic test rigs. As shown in Secs. 2.3 and 4, it is furthermore exact if the available combustor transfer matrix and the corresponding LOM are fully consistent. However, postprocessing of real experimental measurement data has to deal with combustor transfer matrices and LOMs subject to modeling and measurement errors. Therefore, the available combustor transfer matrices and the LOM are never fully consistent. This section discusses the capabilities and functionality of the model-based inference method in this case.

5.1 Flame Transfer Matrix of SCARLET. The model-based inference method relies on the accuracy of the LOM used. Therefore, to infer reliable results, it is necessary to ensure that the LOM well approximates the combustor's global and internal system dynamics. The accuracy of the LOM concerning the global dynamics of the combustor was assessed by first comparing the experimental combustor transfer matrix $\tilde{\mathbf{C}}^c$ with the corresponding model $\mathbf{C}^c$ (Eq. (18)) in Fig. 6. As a second measure for the accuracy of the LOM, this section computes the FTM using the BFTM method (Eq. (20)) with $\tilde{\mathbf{C}}^c$ and with $\mathbf{C}^c$, respectively. The results are plotted in Fig. 10. Note that although the BFTM method does not determine the correct FTM (see Sec. 4), the two FTMs of the BFTM method

Fig. 9 Schematic representation of the generic SCARLET models. Bypass mean flow and bypass acoustics are indicated by arrows and double arrows, respectively: (*a*) model-MAC, (*b*) model-MA, (*c*) model-M, and (*d*) model-0.
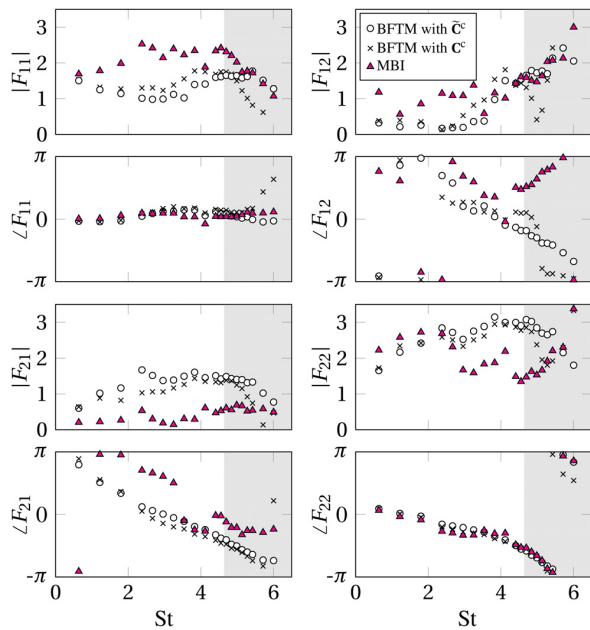
Fig. 10 Gain and phase of the coefficients of the flame transfer matrices of SCARLET computed with the MBI method and obtained with the BFTM approach using the experimental hot combustor transfer matrix $\tilde{\mathbf{C}}^h$ in combination with the experimental or modeled cold combustor transfer matrix $\tilde{\mathbf{C}}^c$ or $\mathbf{C}^c$, respectively, for comparison reasons and as an indicator for the accuracy of the LOM used

should coincide in case of a perfect model. The magnitude of discrepancy, on the other hand, will indicate to what extent inadequacies of the model $\mathbf{C}_c$ impact the determination of the FTM. Figure 10 shows a good agreement between the two FTMs for St ≤ 4.5. For St > 4.5, the two FTMs diverge in all coefficients, and it is concluded that the LOM is inaccurate in this frequency range. Figure 10 is therefore grayed out for St > 4.5.

Finally, the LOM described in Sec. 3.2 is used to infer the FTM from the experimental combustor transfer matrix $\tilde{\mathbf{C}}^h$ of SCARLET shown in Fig. 5. The model-based inference method uses the LOM to calculate the FTM of SCARLET. The resulting FTM is shown in Fig. 10 as triangles. Analogous to Sec. 4, the FTM coefficients of the BFTM approach and the model-based inference method differ from
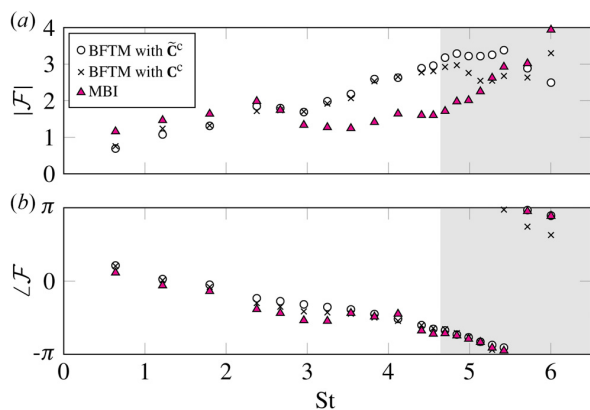

Fig. 11 (a) Gain and (b) phase of the flame transfer function of SCARLET computed with the MBI method and obtained with the BFTM approach using the experimental hot combustor transfer matrix $\tilde{\mathbf{C}}^h$ in combination with the experimental or modeled cold combustor transfer matrix $\tilde{\mathbf{C}}^c$ or $\mathbf{C}^c$, respectively

each other. This is expected due to the inconsistency of the BFTM method. However, in contrast to the ideal case in Sec. 4, the FTM of the model-based inference method is subject to modeling and measurement errors resulting in potential discrepancies between the experimental combustor transfer matrix $\tilde{\mathbf{C}}^h$ and the corresponding LOM. At this point, no quantitative statement can be made about the accuracy of the FTM due to the lack of a reference solution of SCARLET or a quantitative quality measure for the LOM applied. Qualitatively, a comparison between the FTM obtained with the model-based inference method and the BFTM approach shows similar effects as in Fig. 8. The phase of F_{11} is flattened. The coefficient F_{21} is strongly reduced in amplitude. The maximum amplitude of the coefficient F_{22} is shifted to lower Strouhal numbers, and at higher frequencies, the overall amplitude is reduced. The phase of coefficient F_{22} remains nearly unchanged. The outlier in the combustor transfer matrices $\tilde{\mathbf{C}}^c$ and $\tilde{\mathbf{C}}^h$ at St ≈ 4 (see Figs. 5 and 6) is present in all coefficients of the FTMs.

The inferred FTM in Fig. 10 suggests that the Rankine-Hugoniot relations (Eq. (22)) together with the FTF in Eq. (23) are applicable in the present case. For low Mach number flows ($M_c \ll 1$), the F_{22} element in Eq. (22) is commonly used to determine the flame dynamics via $\mathcal{F}(\omega) = 1/\theta(F_{22} - 1)$ [23–26]. Figure 11 shows the flame transfer function of SCARLET under these assumptions. The upcoming section discusses possible ways to enhance the quantification of model accuracy for the model-based inference method.

5.2 Discussion. The model-based inference method is a mathematically consistent approach to determining the FTM from the experimental combustor transfer matrices of complex thermoacoustic test rigs. However, its dependence on a LOM introduces a sensitivity to modeling errors. Any inaccuracies of the acoustic LOM will manifest as errors in the FTM. Therefore, it is crucial to ensure a good approximation of the global behavior and inner system dynamics of the combustor by the LOM.

Combining the model-based inference method with statistical procedures, such as Bayesian inference [44,45], may relax these constraints. Explicitly accounting for uncertainties in the experimental combustor transfer matrices and model input parameters would help to quantify the propagation of errors in the FTM. Additionally, the computation of uncertainty bounds for the FTM would visualize the reliability of the inferred result. Furthermore, quality measures could be systematically computed, facilitating the assessment of different LOMs in terms of their alignment with experimental combustor transfer matrices.

To ensure the fidelity of the internal system dynamics, it is imperative to construct the LOM with a high degree of physical realism. Introducing modeling assumptions, such as low Mach number flows or constant gas properties, should be avoided or chosen with meticulous care. In general, the LOM should be designed to minimize the number of uncertain input parameters, thereby enhancing its reliability in representing the intricacies of the system's internal system dynamics. If available, subelements or subsections of the LOM may be replaced by scattering matrices obtained from additional experiments or numerical simulations. In this case, the quality of the LOM would increase with the development of the combustor.

6 Conclusion and Outlook

This work focuses on the inference of the flame transfer matrix from experimental combustor transfer matrices of thermoacoustic test rigs with complex features, such as acoustic cross-communication bypassing the flame or area contractions at the combustion chamber outlet. The BFTM approach to postprocess the FTM simply combines the experimentally determined transfer matrices of the hot and cold burner at the same inlet conditions. Note that the BFTM approach achieves robustness by heavily constraining the internal system dynamics. This work shows that this approach is mathematically inconsistent for test rigs with complex features. Instead, a model-based inference method utilizing a LOM

to approximate the internal system dynamics of the combustor is proposed—a generalized framework to infer the FTM in complex setups. In addition, using a LOM can reduce the experimental effort as cold measurements are only required to validate the same but not at every operation point. The model-based inference method converges to the BFTM method in the absence of complex test rig features. The capabilities of the model-based inference method are analyzed by applying it to generic and experimental data sets of the Rolls-Royce SCARLET test rig operated under realistic engine conditions.

Formulating an accurate LOM is the most challenging part of the model-based inference method. A physics-based approach with minimal assumptions is used in this study. For future work, we propose to couple the MBI method with statistical procedures such as Bayesian inference. This coupling promises the systematic computation of quality measures to compare different LOMs, uncertainty bounds for the inferred FTM, and a reduced error propagation in the FTM.

Data Availability Statement

The datasets generated and supporting the findings of this article are obtainable from the corresponding author upon reasonable request.

Nomenclature

$\mathbf{B}$ = burner transfer matrix
$\mathbf{C}$ = combustor transfer matrix
c = speed of sound (m s^{-1})
$\mathbf{D}$ = duct transfer matrix
$\mathcal{F}$ = flame transfer function
$\mathbf{F}$ = flame transfer matrix
f, g = acoustic Riemann invariants
M = Mach number
p = pressure (kg m^{-1} s^{-2})
Q = heat release rate (W m^{-3})
St = Strouhal number
$\mathbf{T}$ = transfer matrix
u = velocity (m s^{-1})

Greek Symbols

γ = heat capacity ratio
θ = temperature ratio
ρ = density (kg m^{-3})
ω = angular frequency (Hz)

Subscripts

r = reactants
ref = reference position
p = products
u = upstream

Superscripts

c = cold
h = hot

$*$ = generic
$\sim$ = measurement

Abbreviations

BFTM = burner-flame transfer matrix
DTD = distributed time delay
FTF = flame transfer function
FTM = flame transfer matrix
LOM = low-order model
MBI = model-based inference
MMM = multi-microphone method

Appendix: Derivation of Combustor Transfer Matrix Models

Analogously to the derivations in Sec. 2.3, a model for the hot combustor matrix $\mathbf{C}^c$ can be derived by interconnecting the connector model (Fig. 2, center) with a known flame transfer matrix $\mathbf{F}$ (Fig. 2, upper right). For that purpose, the first row of Eq. (13) is used to substitute $\mathbf{v}_r$ in Eq. (10)

$$\begin{aligned} \mathbf{v}_p &= \mathbf{F}\mathbf{v}_r \\ &= \mathbf{F}\left(\mathbf{T}_{ru}^h \mathbf{v}_u + \mathbf{T}_{rp}^h \mathbf{v}_p\right) \end{aligned} \quad \Rightarrow \quad \mathbf{v}_p = \left(\mathbf{F}^{-1} - \mathbf{T}_{rp}^h\right)^{-1} \mathbf{T}_{ru}^h \mathbf{v}_u$$

(A1)

Subsequently, Eq. (A1) is used to replace $\mathbf{v}_p$ in the bottom row of Eq. (13) to retrieve $\mathbf{C}^h$

$$\mathbf{v}_d = \underbrace{\left[\mathbf{T}_{dp}^h \left(\mathbf{F}^{-1} - \mathbf{T}_{rp}^h\right)^{-1} \mathbf{T}_{ru}^h + \mathbf{T}_{du}^h\right]}_{\mathbf{C}^h} \mathbf{v}_u \qquad \text{(A2)}$$

This procedure is displayed in Fig. 2 by the gray dashed arrows. The cold combustor matrix model $\tilde{\mathbf{C}}^c$ is retrieved from Eq. (2) by replacing with the identity matrix $\mathbf{I}$ and evaluating $\mathbf{T}_{ru}$, $\mathbf{T}_{rp}$, $\mathbf{T}_{du}$, and $\mathbf{T}_{dp}$ for cold conditions

$$\mathbf{C}^c = \mathbf{T}_{dp}^c \left(\mathbf{I} - \mathbf{T}_{rp}^c\right)^{-1} \mathbf{T}_{ru}^c + \mathbf{T}_{du}^c \qquad \text{(A3)}$$

References

[1] Lieuwen, T., and Yang, V., eds., 2005, *Combustion Instabilities in Gas Turbine Engines*, Vol. 210, AIAA, Reston, VA.
[2] Poinsot, T., 2017, "Prediction and Control of Combustion Instabilities in Real Engines," Proc. Combust. Inst., **36**(1), pp. 1–28.
[3] Merk, H. J., 1957, "Analysis of Heat-Driven Oscillations of Gas Flows," Appl. Sci. Res., **6**(4), pp. 317–336.
[4] Bohn, D., and Deucker, E., 1993, "An Acoustical Model to Predict Combustion Driven Oscillations," 20th International Congress on Combustion Engines, CIMAC, London, UK, Mar. 17–20.
[5] Keller, J. J., 1995, "Thermoacoustic Oscillations in Combustion Chambers of Gas Turbines," AIAA J., **33**(12), pp. 2280–2287.
[6] Paschereit, C. O., and Polifke, W., 1997, "Characterization of Lean Premixed Gas Turbine Burners as Acoustic Multi-Ports," APS/DFD Annual Meeting, APS, San Francisco, NC, Nov. 23–25.
[7] Dowling, A. P., 1999, "Thermoacoustic Instability," 6th International Congress on Sound and Vibration, Copenhagen, Denmark, pp. 3277–3292.
[8] Eckstein, J., and Sattelmayer, T., 2006, "Low-Order Modeling of Low-Frequency Combustion Instabilities in Aeroengines," J. Propul. Power, **22**(2), pp. 425–432.
[9] Schuermans, B., Guethe, F., Pennell, D., Guyot, D., and Paschereit, C. O., 2010, "Thermoacoustic Modeling of a Gas Turbine Using Transfer Functions Measured Under Full Engine Pressure," ASME J. Eng. Gas Turbines Power, **132**(11), p. 111503.
[10] Munjal, M. L., 2014, *Acoustics of Ducts and Mufflers*, 2nd ed., Wiley, Chichester, UK.
[11] Emmert, T., 2016, "State Space Modeling of Thermoacoustic Systems With Application to Intrinsic Feedback," Ph.D. thesis, Technical University of Munich, Munich, Germany.
[12] Pankiewitz, C., Fischer, A., Hirsch, C., and Sattelmayer, T., 2003, "Computation of Transfer Matrices for Gas Turbine Combustors Including Acoustics/Flame Interaction," AIAA Paper No. 2003-3295.

[13] Bothien, M., Lauper, D., Yang, Y., and Scarpato, A., 2019, "Reconstruction and Analysis of the Acoustic Transfer Matrix of a Reheat Flame From Large-Eddy Simulations," ASME J. Eng. Gas Turbines Power, **141**(2), p. 021018.

[14] Gant, F., Cuquel, A., and Bothien, M. R., 2022, "Autoignition Flame Transfer Matrix: Analytical Model Versus Large Eddy Simulations," Int. J. Spray Combust. Dyn., **14**(1–2), pp. 72–81.

[15] Reinhardt, H., Alanyal Ioğlu, Ç. O., Fischer, A., Lahiri, C., Nicolai, H., and Hasse, C., 2023, "Simulation of the Thermoacoustic Response of an Aero-Engine Gas Turbine Fuel Injector Using a Hybrid CFD-CAA Method," ASME J. Eng. Gas Turbines Power, **145**(11), p. 111016.

[16] Schuermans, B., Polifke, W., and Paschereit, C. O., 1999, "Modeling Transfer Matrices of Premixed Flames and Comparison With Experimental Results," ASME Paper No. 99-GT-132.

[17] Munjal, M. L., and Doige, A. G., 1990, "Theory of a Two Source-Location Method for Direct Experimental Evaluation of the Four-Pole Parameters of an Aeroacoustic Element," J. Sound Vib., **141**(2), pp. 323–333.

[18] Peters, M. C. A. M., Hirschberg, A., Reijnen, A. J., and Wijnands, A. P. J., 1993, "Damping and Reflection Coefficient Measurements for an Open Pipe at Low Mach and Low Helmholtz Numbers," J. Fluid Mech., **256**, pp. 499–534.

[19] Paschereit, C. O., and Polifke, W., 1998, "Investigation of the Thermo-Acoustic Characteristics of a Lean Premixed Gas Turbine Burner," ASME Paper No. 98-GT-582.

[20] Paschereit, C. O., Schuermans, B., Polifke, W., and Mattson, O., 2002, "Measurement of Transfer Matrices and Source Terms of Premixed Flames," ASME J. Eng. Gas Turbines Power, **124**(2), pp. 239–247.

[21] Bellucci, V., Schuermans, B., Nowak, D., Flohr, P., and Paschereit, C. O., 2005, "Thermoacoustic Modeling of a Gas Turbine Combustor Equipped With Acoustic Dampers," ASME J. Turbomach., **127**(2), pp. 372–379.

[22] Schuermans, B., 2003, "Modeling and Control of Thermoacoustic Instabilities," Ph.D. thesis, École Polytechnique Fédérale de Lausanne, Lausanne, Switzerland.

[23] Schimek, S., Göke, S., Schrödinger, C., and Paschereit, C. O., 2012, "Flame Transfer Function Measurements With CH4 and H2 Fuel Mixtures at Ultra Wet Conditions in a Swirl Stabilized Premixed Combustor," ASME Paper No. GT2012-69788.

[24] Bobusch, B. C., Moeck, J. P., Paschereit, C. O., and Sadig, S., 2012, "Thermoacoustic Stability Analysis of a Kerosene-Fueled Lean Direct Injection Combustor Employing Acoustically and Optically Measured Transfer Matrices," ASME Paper No. GT2012-69034.

[25] Bade, S., Wagner, M., Hirsch, C., Sattelmayer, T., and Schuermans, B., 2014, "Influence of Fuel-Air Mixing on Flame Dynamics of Premixed Swirl Burners," ASME Paper No. GT2014-25381.

[26] Blondé, A., Schuermans, B., Pandey, K., and Noiray, N., 2023, "Effect of Hydrogen Enrichment on Transfer Matrices of Fully and Technically Premixed Swirled Flames," ASME J. Eng. Gas Turbines Power, **145**(12), p. 121009.

[27] Alanyal Ioğlu, C., Reinhardt, H., Fischer, A., Lahiri, C., Nicolai, H., and Hasse, C., 2023, "Comparison of Acoustic, Optic, and Heat Release Rate Based Flame Transfer Functions for a Lean-Burn Injector Under Engine-Like Conditions," Symposium on Thermoacoustics in Combustion, Zurich, Switzerland, Sept. 11–14.

[28] Eder, A. J., Fischer, A., Lahiri, C., Merk, M., Staufer, M., Eggels, R., Silva, C. F., and Polifke, W., 2023, "Identification of the Dynamics of a Turbulent Spray Flame at High Pressure," Symposium on Thermoacoustics in Combustion, Zurich, Switzerland, Sept. 11–14.

[29] Fischer, A., Lahiri, C., and Doerr, T., 2017, "Design, Build, and Commissioning of the New Thermo-Acoustics Combustion Test Rig SCARLET," Rolls-Royce Deutschland, Report No. DLRK2017-450116.

[30] Fischer, A., and Lahiri, C., 2021, "Ranking of Aircraft Fuel-Injectors Regarding Low Frequency Thermoacoustics Based on an Energy Balance Method," ASME Paper No. GT2021-59561.

[31] Lavrentjev, J., Åbom, M., and Bodén, H., 1995, "A Measurement Method for Determining the Source Data of Acoustic Two-Port Sources," J. Sound Vib., **183**(3), pp. 517–531.

[32] Ben-Israel, A., and Greville, T. N. E., 2003, Generalized Inverses: Theory and Applications, 2nd ed., Springer, New York.

[33] Åbom, M., 1992, "A Note on the Experimental Determination of Acoustical Two-Port Matrices," J. Sound Vib., **155**(1), pp. 185–188.

[34] Schuermans, B., Bellucci, V., Guethe, F., Meili, F., Flohr, P., and Paschereit, C. O., 2004, "A Detailed Analysis of Thermoacoustic Interaction Mechanisms in a Turbulent Premixed Flame," ASME Paper No. GT2004-53831.

[35] Emmert, T., Meindl, M., Jaensch, S., and Polifke, W., 2016, "Linear State Space Interconnect Modeling of Acoustic Systems," Acta Acust. United Acust., **102**(5), pp. 824–833.

[36] Gentemann, A., Fischer, A., Evesque, S., and Polifke, W., 2003, "Acoustic Transfer Matrix Reconstruction and Analysis for Ducts With Sudden Change of Area," AIAA Paper No. 3142.

[37] Kim, K. T., Lee, J. G., Quay, B. D., and Santavicca, D. A., 2010, "Spatially Distributed Flame Transfer Functions for Predicting Combustion Dynamics in Lean Premixed Gas Turbine Combustors," Combust. Flame, **157**(9), pp. 1718–1730.

[38] Van Horn, E. M., and Scarborough, D. E., 2022, "Low-Frequency Acoustic Response of Gas Turbine Perforated Plate and Axial Swirler," ASME J. Eng. Gas Turbines Power, **144**(5), p. 051008.

[39] Meindl, M., Merk, M., Fritz, F., and Polifke, W., 2019, "Determination of Acoustic Scattering Matrices From Linearized Compressible Flow Equations," J. Theor. Comput. Acoust., **27**(3), p. 1850027.

[40] Dowling, A. P., 1995, "The Calculation of Thermoacoustic Oscillation," J. Sound Vib., **180**(4), pp. 557–581.

[41] Dowling, A. P., and Stow, S. R., 2003, "Acoustic Analysis of Gas Turbine Combustors," J. Propul. Power, **19**(5), pp. 751–764.

[42] Strobio Chen, L., Bomberg, S., and Polifke, W., 2016, "Propagation and Generation of Acoustic and Entropy Waves Across a Moving Flame Front," Combust. Flame, **166**, pp. 170–180.

[43] Polifke, W., 2020, "Modeling and Analysis of premixed flame Dynamics by Means of Distributed Time Delays," Prog. Energy Combust. Sci., **79**, p. 100845.

[44] MacKay, D. J., 2003, Information Theory, Inference, and Learning Algorithms, Cambridge University Press, New York.

[45] Yoko, M., and Juniper, M. P., 2023, "Data-Driven Modelling of Thermoacoustic Instability in a Ducted Conical Flame," Symposium on Thermoacoustics in Combustion, Zurich, Switzerland, Sept. 11–14.

90

Original Research Article

Incompressible versus compressible large eddy simulation for the identification of premixed flame dynamics

Alexander J Eder ⓘ **, Camilo F Silva, Matthias Haeringer** ⓘ **,
Johannes Kuhlmann and Wolfgang Polifke**

Abstract

The present work compares the respective advantages and disadvantages of compressible and incompressible computational fluid dynamics (CFD) formulations when used for the estimation of the acoustic flame response. The flame transfer function of a turbulent premixed swirl-stabilized burner is determined by applying system identification (SI) to time series data extracted from large eddy simulation (LES). By analyzing the quality of the results, the present study shows that incompressible simulations exhibit several advantages over their compressible counterpart with equal prediction of the flame dynamics. On the one hand, the forcing signals can be designed in such a way that desired statistical properties can be enhanced, while maintaining optimal values in the amplitude. On the other hand, computational costs are reduced and the implementation is fundamentally simpler due to the absence of acoustic wave propagation and corresponding resonances in the flame response or even self-excited acoustic oscillations. Such an increase in efficiency makes the incompressible CFD/SI modeling approach very appealing for the study of a wide variety of systems that rely on premixed combustion. In conclusion, the present study reveals that both methodologies predict the same flame dynamics, which confirms that incompressible simulation can be used for thermoacoustic analyses of acoustically compact velocity-sensitive flames.

Introduction

Investigating thermoacoustic combustion instability is crucial for the development of reliable, low-emission gas turbine engines. In these systems, combustion technology moves towards lean operating conditions in order to satisfy emission regulations on pollutants. Identification of a flame transfer function (FTF) is a key ingredient in the thermoacoustic stability analysis[1], as it is a necessary input for acoustic network models[2]. The acoustic response of turbulent premixed burners can be described by a single-input-single-output[3] black box model, with velocity perturbations at a reference position as input and global heat release rate response as output. Given that perfectly premixed flames or configurations with an acoustically

stiff fuel injector located very close to the burner outlet[4] are studied, the flame response is defined as

$$\mathcal{F}(\omega) \equiv \frac{\dot{Q}'(\omega)/\bar{\dot{Q}}}{u'_{\text{ref}}(\omega)/\bar{u}_{\text{ref}}}. \tag{1}$$

Department of Engineering Physics and Computation, TUM School of Engineering and Design, Technical University of Munich, Garching, Germany

Corresponding author:
Alexander J Eder, Department of Engineering Physics and Computation, TUM School of Engineering and Design, Technical University of Munich, Boltzmannstr. 15, 85748 Garching, Germany.
Email: alexander.eder@tum.de

The established way in thermoacoustic studies to identify such a flame response is to use either experiment[5–8] or compressible large eddy simulation (LES)[9–12], where the flame is acoustically forced with a harmonic or broadband signal from an upstream or downstream position. Simultaneously, the velocity perturbations at the reference position and the global heat release signal are monitored. Such a procedure may be seen as "natural" and, accordingly, widespread in the thermoacoustic community. For example the works of Kaufmann et al.[13], Giauque et al.[1], and Han and Morgans[14] mention:

The following requirements must be matched by the LES tool to obtain reliable information for flame transfer functions in gas turbines: 1) The full three dimensional compressible Navier Stokes equations must be solved on unstructured meshes for complex geometries. Kaufmann et al. (2002)[13]

To determine the transfer function of a burner, the usual procedure is to introduce an acoustic wave into the burner (usually through the inlet) and measure the perturbation of heat release. Giauque et al. (2005)[1]

The need to include acoustic waves when considering the flame response means that compressible CFD approaches are typically chosen for flame response investigations. Han and Morgans (2015)[14]

Although the aforementioned procedures are correct, they leave aside incompressible computational fluid dynamics (CFD) as an alternative in the calculation chain. Compressible CFD is characterized by the speed of sound. Numerically, this implies that small time steps are required to fulfill the acoustic Courant-Friedrichs-Lewy (CFL) number condition, which entails high computational costs, at least for explicit (density-based) codes.

Han and Morgans[14] (third quote above) correctly recovered the response of a fully premixed flame subjected to velocity forcing with *in*compressible simulation, where they thereby overcome the above mentioned drawbacks of compressible simulation. For doing so, the flame is assumed to be insensitive to pressure fluctuations, which is valid for gaseous fuels[15]. In the case of perfectly premixed combustion at low Mach numbers, heat release rate fluctuations induced by flow perturbations are expected to be dominant, since the effect of pressure, temperature, and strain rate perturbations—induced by the associated acoustic wave—are rather weak[15,16]. Accordingly, the flame dynamics is governed by hydrodynamic processes and should be well represented by incompressible solvers.

Note that the FTF in equation (1) describes the heat release rate fluctuations produced by velocity disturbances. Accordingly, imposing axial velocity (incompressible) perturbations enables the evaluation of the flame response with incompressible solvers.[17] The response of the

unsteady heat release rate to such velocity perturbations can then be investigated for various forcing frequencies[14] or a frequency band of interest using broadband excitation[4]. Incompressible CFD[14,17–21] has been used as an alternative to compressible CFD for the flame response evaluation. Research groups and companies around the world often use either the one or the other method as shown by Gicquel et al.[22], who presented an overview of reacting LES codes based on the compressible and incompressible formulation, respectively.

Gentemann[23] identified a FTF from CFD/SI using a compressible and incompressible Reynolds-averaged Navier-Stokes (RANS) approach in Fluent. He observed deviations in the gain between the two, mainly in the regions of maxima and minima. He questioned the compactness of the flame and attributed the observed mismatch to differences in the respective solvers. A first comparison between compressible and incompressible LES in the field of premixed combustion was carried out by Ma and Kempf[24]. They compared the velocity fields obtained from LES with experiments, while studying a self-excited combustion instability. In the incompressible LES, the effect of combustion instability on the flow was emulated by applying external forcing at the frequency of the instability. The authors observed that the fluctuating velocity fields match well experimental results, once such an external forcing is applied. Additionally, the observed mean and fluctuating velocity fields agree well with the experimental counterparts when compressible LES is considered. Dombard et al.[25] compared the two LES variants for unsteady hydrodynamic activities in non-reacting swirling flows. They found that both solvers properly capture the observed hydrodynamic modes. Treleaven et al.[26] presented a direct comparison of the forcing methods in compressible and incompressible LES for the investigation of swirl number fluctuations, but without evaluating the flame response. A recent LES study by Treleaven et al.[27] compared the FTF computed with a compressible and incompressible approach by imposing a sine wave excitation for two specific frequencies at the inlet, where only the phase at the higher forcing frequency matches. They attributed this difference to differences in the computational setup. Without clear evidence, they concluded that the FTF identification is insensitive to the choice of numerical method (i.e. compressible or incompressible solvers).

To the best knowledge of the authors, the present study is the first to directly compare and analyze the flame response obtained with compressible and incompressible LES (regardless of the method used for estimating the FTF), where a broad range of frequencies are investigated, and where the weaknesses and uncertainties of each methodology are discussed. The present paper closes this gap and present such a direct comparison. It is expected that systemic errors—which can result from comparing different numerical setups—are excluded, because same grid,

numerical schemes, turbulent combustion model, and chemistry mechanism are used.

The paper is structured as follows: In section "Modeling approaches" we first introduce the acoustic modeling of longitudinal combustion chambers, in order to point out fundamental differences between compressible and incompressible CFD. We also introduce relevant system identification (SI) theory. Subsequently, section "Turbulent premixed swirl burner" presents the swirl-stabilized burner and the numerical setup. In section "Unforced flow/flame validation" the unforced flow fields and flame shapes of both LES variants are compared as a basis for further dynamic investigations. In section "Flame response to velocity perturbations of the premixed swirl burner," we apply broadband and harmonic forcing to the statistically steady-state LES solution and evaluate the respective input and output behavior. Finally, we compare the flame response data computed with compressible and incompressible LES. We discuss advantages and weaknesses of each method and make recommendations for the use of CFD in the context of system identification.

Modeling approaches

To better understand the differences between compressible and incompressible formulations in CFD codes, this section presents fundamentals in thermoacoustics. Besides the introduction to acoustic wave propagation, resonances, instabilities and feedback-loops, the differences in compressible and incompressible CFD for the subsequent system identification are discussed. Emphasis is put on signal generation and quality criteria.
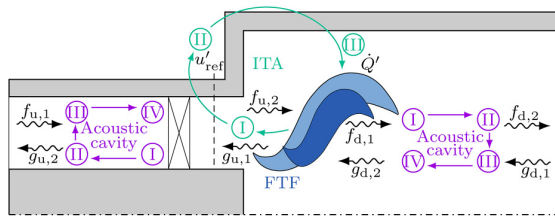

Figure 1. Sketch of plane acoustic wave propagation in a generic swirl burner with (fully or partially) reflecting boundaries. The outer acoustic loop (acoustic cavity) and the internal feedback loop (ITA) are shown in violet and green, respectively. Acoustic cavity: (I) generated acoustic waves g_u and f_d through unsteady volumetric gas expansion, (II) acoustic wave propagation to upstream/downstream boundary, (III) acoustic wave reflection at upstream/downstream boundary, and (IV) acoustic wave propagation of reflected acoustic waves f_u and g_d through the flame; ITA: (I) generated acoustic waves g_u through unsteady volumetric gas expansion, (II) acoustic wave g_u causes acoustic velocity perturbations at the reference position, and (III) acoustic velocity perturbations are coupled with global heat release rate fluctuations via FTF.

Thermoacoustic modeling in longitudinal combustion chambers

One-dimensional (1D) acoustics, which models the propagation of plane acoustic waves in 1D systems, is described by characteristic wave amplitudes f and g (also called "Riemann invariants" in the mathematical context). We refer to them simply as "acoustic waves" in this work. f and g are related to the primitive acoustic variables p, u, ρ, and c via

$$f = \frac{1}{2}\left(\frac{p'}{\bar{\rho}\bar{c}} + u'\right) \qquad \text{and} \qquad g = \frac{1}{2}\left(\frac{p'}{\bar{\rho}\bar{c}} - u'\right), \quad (2)$$

where p' and u' are fluctuations in pressure and velocity and $\bar{\rho}$ and $\bar{c}$ are temporal averaged density and speed of sound, respectively. Conversely, p' and u' are related to f and g by

$$u' = f - g \qquad \text{and} \qquad p' = \bar{\rho}\bar{c}\,(f + g). \quad (3)$$

The reflection of acoustic waves at the boundaries (inlet and outlet) is described by the so-called reflection coefficient $R(\omega)$, which is the ratio of the characteristic wave amplitudes f and g

$$R_u(\omega) = \frac{\hat{f}_u}{\hat{g}_u} \qquad \text{and} \qquad R_d(\omega) = \frac{\hat{g}_d}{\hat{f}_d}, \quad (4)$$

where the subscripts "u" and "d" refer to the upstream (combustor inlet) and downstream boundary (combustor outlet), respectively, and $\hat{(\cdot)} = (\cdot)' e^{-i\omega t}$ label variables in the frequency domain assuming harmonic oscillations. The reflection coefficient, which is complex valued, describes the gain and phase between the incident and outgoing acoustic wave. This formalism is suitable only for waves impinging normally to the boundary, which is justified in 1D systems.

The above described (fully or partially) reflection of acoustic waves at the combustor boundaries closes the so-called *outer acoustic loop* of the system, shown in violet in Figure 1 for a generic swirl burner. It is explained as follows. First, the flame causes fluctuations in heat release rate (I), which are associated with an unsteady volumetric gas expansion. Such volumetric pulsations generate acoustic waves g_u and f_d traveling upstream and downstream of the flame (II), respectively. The acoustic waves are then reflected at the boundaries (III), depending on the reflection coefficients R_u and R_d. The downstream and upstream traveling reflected acoustic waves f_u and g_d hit the flame (IV) and close the loop. This loop can be also seen as an acoustic cavity (combustor) loop since it depends on the boundaries of the combustor (e.g. open end, choked nozzle, or sinter plate).

An intuitive but invalid point of view, which is still present in the thermoacoustic community, is the following. It is often believed that breaking the acoustic cavity loop, that is, allowing all acoustic waves to leave the domain

through the boundaries, leads to a thermoacoustically stable system. A so-called anechoic system is modeled in CFD by incorporating non-reflective acoustic boundary conditions[28,29] ($R_u = R_d = 0$). It might be believed that such an anechoic system is unconditionally stable. However, this is a consequence of neglecting the *internal acoustic loop*, usually known as the intrinsic thermoacoustic (ITA) feedback loop[30–33] (shown in green in Figure 1). The previously described unsteady volumetric gas expansion of the flame (I), produced by the unsteady heat release rate $\dot{Q}'$, causes an acoustic wave g_u to travel in the upstream direction, which in turn modulates the acoustic velocity at the reference position u'_{ref} (II). These velocity perturbations are coupled via the FTF with fluctuations of global heat release rate $\dot{Q}'$ (III), which close the ITA feedback loop. As a result, the stability of a system (as the one depicted in Figure 1) with anechoic boundary conditions is governed by the stability of the ITA loop, as the outer acoustic loop—referred in the following simply as acoustic loop—does not exist for such boundaries. Partially reflecting boundaries, on the other hand, allow both acoustic and ITA loops to co-exist and interact.

It is well known that resonances of acoustic modes lead to peaks in the power spectral distribution of acoustic pressure[34–36]. Similarly, it should be clear that resonances of ITA modes may create additional peaks[37,30,38]. Importantly, resonances may develop into self-excited instability if any parameter that affects the flame dynamics or the pressure distribution within the system is changed. Examples are fuel composition or inlet/outlet reflection coefficients.

Compressible and incompressible CFD

The main difference between a compressible and incompressible CFD formulation is the absence of acoustic wave propagation in the latter. This absence causes acoustic velocity perturbations associated to dilation mechanisms to be transported instantaneously (i.e. $c \to \infty$) from one point in the domain to another. Acoustic velocity or pressure perturbation upstream of the flame propagate infinitely fast from the inlet to the flame base. Subsequently, the flame base disturbances are convected along the flame. In addition to these convective disturbances, restoration mechanisms[39]—which are a consequence of flame propagation and flame anchoring—are also produced instants after and transported along the flame sheet. The overall fluctuations of the heat release can be thus understood as the flame response to acoustic forcing. Note that in the context of an incompressible formulation, the terminology *acoustic* perturbation or *acoustic* forcing can be misleading. In the context of an incompressible simulation in the present paper, such a terminology is exclusively associated with purely axial perturbations that are transported infinitely fast. Note that radial or azimuthal perturbations in the flow, or scalar quantities in general (e.g. temperature), are

still transported by convection as in the compressible CFD. Besides the differences in physics, the incompressibility assumption simplifies the numerical setup drastically, since no definition of acoustic boundary conditions is required. Furthermore, acoustic-driven resonances—associated with the acoustic or ITA loop—are avoided.

Acoustic boundary conditions in compressible CFD. To resolve the acoustic wave propagation accurately, special attention goes to the boundary conditions in the compressible CFD, which determine the reflection coefficients defined in equation (4). As discussed above, the intuitive idea of using non-reflective boundary conditions to achieve a thermoacoustically stable system is not generally applicable. Depending on the system under investigation, different combinations of (frequency-dependent) reflection coefficients at the inlet and outlet can lead to a thermoacoustically stable system. This does not necessarily have to be the combination $R_u = R_d = 0$. Therefore, non-reflective boundary conditions should not be always considered optimal acoustic boundary conditions for flame response identification.

A general and very flexible method to prescribe frequency-dependent reflection coefficients $R(\omega)$ is to represent them as a state-space model. These characteristics-based state-space boundary conditions (CBSBC), introduced by Jaensch et al.[29], are an extension of the partially non-reflective (NSCBC[40]) and fully non-reflective (NSCBC with plane wave masking[28]) boundary conditions. In the CBSBC framework, the outgoing acoustic wave f_d serves as input to a state-space model that characterizes a linear time-invariant (LTI) system. The following is an example of an outlet boundary:

$$\dot{\mathbf{x}} = A\mathbf{x} + Bf_d,$$
$$g_d = C\mathbf{x} + Du, \tag{5}$$

with input f_d and output g_d. The system is also characterized by the state vector $\mathbf{x}$ and state-space matrices A, B, C, D. For a given dynamic response of the boundary, the state-space matrices should be evaluated in a calibration step before carrying out CFD[29].

Different ways of forcing in compressible CFD exist. For example, when considering an inlet boundary, forcing can be performed by imposing either a velocity perturbation (Dirichlet boundary condition, i.e. hard wall) or an acoustic wave via CBSBC condition[13]. The latter is used in the present paper because it allows full control of the boundary acoustic reflection. Forcing in the incompressible CFD is done via velocity forcing in the present paper.

System identification

The current paper makes use of the well-established CFD/SI approach[41], where high-fidelity CFD is combined with tools from system identification to characterize the

response of the flame to velocity perturbations over the entire frequency range of interest with a *single* broadband-excited CFD simulation. It has to be mentioned that the combustion system under investigation has to be thermoacoustically stable and must not develop resonances or self-excited instability. Otherwise the (linear) SI procedure described in the following should not be applied, since linearity together with time invariance is a prerequisite for the analyzed system[41]. Once the (thermoacoustically stable) simulation reaches a statistically steady-state after ignition, a broadband signal is imposed at the upstream boundary to generate a time series of acoustic velocity perturbations $u'_{ref} = [u'_0, \ldots, u'_N]$ (input signal) and heat release rate fluctuations $\dot{Q}' = [\dot{Q}_0, \ldots, \dot{Q}_N]$ (output signal). Input and output signals are then evaluated by correlation analysis, which is a specific kind of system identification[3].

For sufficiently small excitation amplitudes[1], the flame response modeled with CFD is considered linear[3,42]. It can be modeled by two equivalent approaches: the FTF in the frequency domain (equation (1)) or the finite impulse response in the time domain[41]. In practice, a finite number of impulse response coefficients h_k give sufficiently accurate results. The finite impulse response is written as

$$\frac{\dot{Q}'_n}{\bar{\dot{Q}}} = \frac{1}{\bar{u}_{ref}} \sum_{k=0}^{n_h} h_k u'_{ref,n-k}, \qquad n = n_h, \ldots, N. \quad (6)$$

The impulse response is typically not known a priori and has to be estimated from time series data u' and $\dot{Q}'$ via an optimal linear least square estimator[3], known as the Wiener-Hopf equation. For more information see Silva et al.[38], Since the unit impulse response and FTF are fundamentally equivalent, they can be converted into each other via z-transform

$$\mathcal{F}(\omega) = \sum_{k=0}^{n_h} h_k e^{-i\omega k \Delta t}, \qquad \text{where } \omega \in \mathbb{C}. \quad (7)$$

The signal used for perturbing the flame over a large range of frequencies has to fulfill specific quality criteria. One of them is the crest factor

$$C_r = \sqrt{\frac{\max_n \left(\left(\frac{u'_{ref}}{\bar{u}_{ref}} \right)^2 \right)}{\frac{1}{N} \sum_{n=1}^{N} \left(\frac{u'_{ref}}{\bar{u}_{ref}} \right)_n^2}}, \quad (8)$$

which relates the ratio of the largest absolute value of the signal to the root mean square (RMS) value of it. The crest factor is one of the most important quality measures in signal processing with a theoretical optimum of unity[3]. This value is desirable to avoid outlier peaks in the time series, as they can trigger nonlinear mechanisms in the response. A discrete random binary signal (DRBS), for example, has a maximum utilization of the signal power due to binary amplitudes of either 1 or -1, which leads to $C_r = 1$.
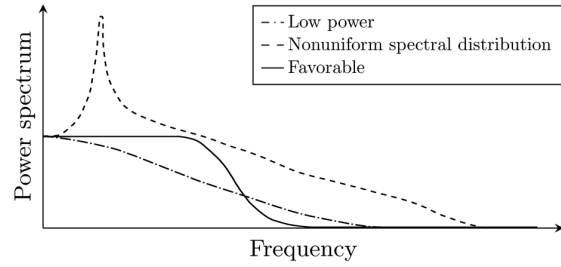

Figure 2. Power spectrum of three different broadband signals. Examples of a low power signal, a signal with nonuniform spectral distribution, and a favorable signal.

Another quality measure of interest evaluates the level of correlation of the signal with itself, namely autocorrelation, estimated as follows[43,41,44]

$$\gamma \equiv \frac{1}{N-k} \sum_{i=1}^{N-k} \left(u'_{ref,i} - \bar{u}_{ref} \right) \left(u'_{ref,i+k} - \bar{u}_{ref} \right), \quad (9)$$

where k is a certain time lag. Low values of γ result in high statistical independence. Furthermore, a good signal typically shows broadband, low-pass filtered spectral characteristics with uniform amplitude in the frequency range of interest[45] (see black curve in Figure 2). In systems with noise, low power (see dash-dotted curve in Figure 2) may lead to poor identification quality, mainly because of a low signal-to-noise ratio (SNR). SNR is defined as [46]

$$SNR \equiv \frac{RMS \left(\dot{Q}'_{u'} \right)}{RMS \left(\dot{Q}'_{turb} \right)}, \quad (10)$$

where $\dot{Q}'_{u'}$ denotes the heat release rate fluctuations resulting purely from acoustic excitation and $\dot{Q}'_{turb}$ stands for the heat release rate fluctuations produced by turbulence (variance of pure noise). From equation (10) it might be concluded that a high SNR (and therefore high forcing amplitudes) is appropriate for CFD/SI, as long as a nonlinear response is not triggered. Note that peaks in the amplitude content (which lead to high SNR) can trigger nonlinear flame behavior at specific frequencies (see dashed curve in Figure 2). Note also that a proper signal exhibits a uniform amplitude spectrum along the frequency band of interest (see the solid curve in Figure 2), resulting in an uniform SNR per frequency. This uniform distribution of SNR is desirable, since the influence of noise can be considered similar within the frequency band of interest.

Turbulent premixed swirl burner

Experimental setup

In the present work, the turbulent swirl-stabilized laboratory-scale combustor shown in Figure 3 is studied
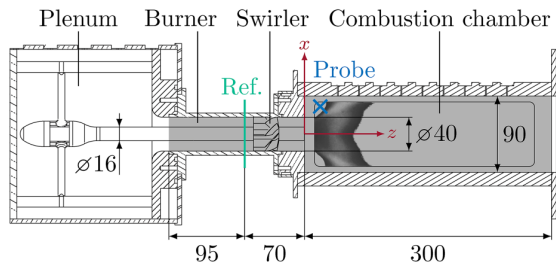
Figure 3. Experimental setup of the BRS burner[7] test rig with a pressure probe located at (40 0 15) mm. The shaded area represents the part resolved with LES. Dimensions are given in mm.

for the comparison of compressible and incompressible LES. The perfectly premixed BRS burner test rig includes an axial swirl generator with eight vanes mounted on a central bluff body, which is characterized by a theoretical swirl number $S = 0.74$[7]. The circular plenum is located upstream of an annular flow passage (called burner). The squared combustion chamber downstream of the burner features two quartz glass windows for chemiluminescence measurements and houses a perforated plate at the combustor outlet. The swirler position near the burner outlet results in a small pressure drop between the swirler and combustion chamber, which means that the swirler can be considered acoustically transparent[47].

The burner was developed and experimentally investigated by Komarek and Polifke[7]. It was operated under perfectly premixed conditions of methane and air. The experimental data in the present work always refers to the 30 kW thermal power rating and $\phi = 0.77$ equivalence ratio configuration. OH* chemiluminescence was measured with an intensified CMOS camera.[7] A recorded time of about 4 s was averaged to determine the steady-state average of OH* emissions. The velocity signal at the reference position was obtained by Constant Temperature Anemometry (CTA) measurements. Compressible LES with AVBP[9,48], and incompressible LES with Fluent[19,20] and OpenFOAM 5.x[21] of the BRS burner were carried out in previous studies on the dynamics of premixed flames. Both incompressible and compressible studies showed good agreement of the predicted FTF when compared with experimental data.

Numerical setup

Large eddy simulations using the open source C++ library OpenFOAM 5.x[49] are performed. The fully compressible Navier-Stokes equations using the reactingFoam solver are solved, where the density is a function of temperature *and* pressure $\rho(T, p)$. For the incompressible simulation, the original solver was customized for the treatment of

incompressible flows, where the density is only a function of the temperature $\rho(T)$[21]. In terms of implementation, the pressure is split into a hydrodynamic pressure and a constant thermodynamic pressure[50]. Kinetic energy terms and the mechanical work term $\frac{\partial p}{\partial t}$ are removed from the energy equation. Other terminologies like "low Mach number" or "weakly-compressible" formulations are also common for such incompressible solvers, where the acoustics are effectively removed from the governing equations[22]. With the approximation that density is only a function of temperature, an incompressible solver can still capture the time-averaged flame shapes and flow fields of a thermoacoustically stable condition as validated in previous studies[24,51,19] and also shown in section "Unforced flow/flame validation."

The shaded area in Figure 3 represents the numerical domain resolved in the LES with a reference position for the FTF identification as in the experiment at $z = -70$ mm. The CFD/SI approach does not require resolving the whole combustion system. Therefore, in order to reduce computational costs[41], only the vicinity of the flame has to be resolved in the simulation, whereas the effect of the system boundaries may be considered by impedance boundary conditions (e.g. CBSBC). For system identification, these do not have to be realistic, but must ensure a thermoacoustically stable configuration.

The governing equations are solved on an unstructured grid consisting of approximately 5 million cells (predominantly hexagonal) with refinement zones in the swirler and flame region. A typical cell size in the latter is 500–600 μm, which is close to the laminar flame thickness of about 460 μm. In terms of Pope's criterion[52], over 90% of the turbulent kinetic energy are resolved as shown in a previous study[21]. Similarly, a grid independence study was previously performed[21]. A fully implicit second-order accurate Euler scheme is used, which was found to be sufficient for CFD/SI[41]. The time step is fixed at $\Delta t = 1 \times 10^{-6}$ s for both simulations, which yields a maximum hydrodynamic CFL number of 0.3. A PIMPLE-consistent algorithm (with three outer iterations) is employed to solve the pressure–velocity coupling in the compressible simulation without being restricted by the acoustic CFL number, and PISO-consistent is used in the incompressible case (both use three inner iterations). The additional three outer iterations increase the runtime of the compressible LES by almost this factor. The wall-adapting local eddy-viscosity (WALE) sub-grid model[53] without using a wall function is applied to close the Favre-filtered Navier-Stokes equations of mass, momentum, species mass fraction, and energy at atmospheric conditions. An extended version of the dynamic thickened flame model[54–57], with local sensor S and an efficiency function, is used to take turbulence-flame interaction into account. The dynamically thickened flame front is resolved with $n = 7$ cells

Table 1. Numerical boundary conditions for the compressible and incompressible simulation. The perimeter in the backplane is shown in Figure 5.

Boundary condition	Type	Details
Inlet (comp.)	CBSBC velocity inlet	$U_{inlet} = 11.3$ m/s, $R_{inlet} = 0$
Inlet (incomp.)	Velocity inlet	$U_{inlet} = 11.3$ m/s
Outlet (comp.)	CBSBC pressure outlet	$p_{outlet} = 101325$ Pa, $R_{outlet} = 0$
Outlet (incomp.)	Total pressure outlet	$p_{outlet} = 101325$ Pa
Burner/swirler	Adiabatic no-slip wall	–
Combustor wall	Isothermal no-slip wall	$T_{wall} = 600$ K
Backplane	Isothermal no-slip wall	$T_{wall} = 600$ K
Backplane damper (comp.)	CBSBC isothermal no-slip wall	$T_{wall} = 600$ K, $R_{wall} = 0.95$

Inlet   Swirler   Backplane   Outlet   Burner   Combustor wall
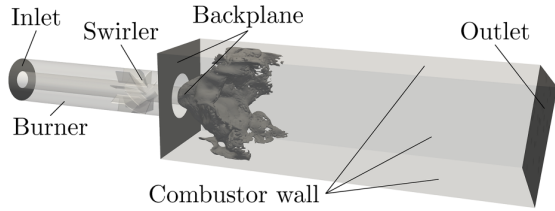
Figure 4. Numerical setup and boundary conditions of the BRS burner. The flame is visualized by an iso-surface of the CH_4 concentration.

and a maximum thickening factor $F_{max} < 10$ is kept[56]. The thickening factor is defined as

$$F = 1 + \left(n \frac{\Delta_{LES}}{\delta_l^0} - 1 \right) S, \qquad (11)$$

where Δ_{LES} is the LES filter width and δ_l^0 is the laminar flame thickness defined from the temperature profile gradient[55]. The thickened flame model is not affected by the choice of compressible or incompressible solvers[58]. The chemical reactions are modeled with the two-step global mechanism 2S_CH4_BFER by Franzelli and Riber[59]. The species and energy equations are modeled with unity Lewis number and Schmidt number $Sc = 0.7$ for all species, which is a common approximation for hydrocarbon combustion[60].

For the identification of flame dynamics, a frequency-limited (1000 Hz) Daubechies wavelets-based signal (DWBS)[45] is imposed at the upstream end of the computational domain. The cut-off frequency $f_{cut} \approx 630$ Hz and a constant amplitude spectrum up to around 500 Hz (maximum frequency of interest in the present study) is achieved. The maximum amplitude of the signal is 10% of the mean inlet velocity $\bar{u}_{inlet} = 11.3$ m/s. A similar excitation amplitude has shown linear flame response in previous studies of the swirl-stabilized BRS burner[19,21]. Note that identical signals were used for the compressible and incompressible LES.

The boundary conditions are shown in Figure 4 and indicated in Table 1. The combustor walls and the bluff body plane are set to no-slip isothermal walls

with a fixed temperature of 600 K. The combustor wall temperature is an estimated value based on measurements of a similar burner configuration as mentioned in Tay-Wo-Chong et al.[48], Previous studies[61–63] show that wall heat transfer in the combustion chamber is very important for correct modeling of the flame shape (and therefore the flame dynamics) in swirl-stabilized combustors. Uncertainty in wall temperature in the experiment might cause deviations in the flame response evaluation with LES[64]. The burner section including the swirler is treated as an adiabatic no-slip wall, which is sufficient as the reaction only takes place inside the combustion chamber. CBSBC are used for the compressible LES due to the advantages discussed in section "Modeling approaches". To overcome an unstable transverse chamber mode in the compressible LES, CBSBC with a reflection coefficient near one ($R_{wall} = 0.95$) is used at a small outer slit of the backplane to suppress the amplifying mode, as shown in Figure 5. The results of the simulation with and without transverse mode damping are properly discussed in section "Unforced flow/flame validation." After an iterative "trial and error" procedure with different combinations of upstream and downstream reflection coefficients[2], the use of non-reflective boundaries at the inlet and outlet turned out to be a good choice, as they assure in the present case thermoacoustic stability.

Unforced flow/flame validation

Unstable transverse mode in the compressible LES

A transverse mode at approximately $f = 4170$ Hz develops in the combustion chamber during unforced compressible simulations as shown in Figure 6. The mode matches with the first transverse eigenmode of the combustion chamber $f_{1T} = \frac{c}{2H} = 4139$ Hz, where $H = 0.09$ m and $c = \bar{c}_{chamber} = 745$ m/s. This high-frequency instability is self-exciting and was not observed in the experiments, but similar observations were made in previous numerical studies.[48,65,66] Several types of initialization were tested, but the instability developed regardless of the procedure used. Therefore, it is concluded that the unstable mode is

not a numerical instability, but physically correct in an acoustically ideal environment such as a computational domain. On the other hand, quartz windows are not perfectly sealed (i.e. there is leakage of combustion chamber) and geometry features in the experiment are not ideal compared to a numerical model: corners are not perfectly sharp and chamber walls exhibit certain roughness, which enhance acoustic dissipation. Such additional losses might explain why the mode was not observed in experiments.

Figure 6 shows that the pressure perturbations start to increase after around 30 ms and continue increasing up to a limit cycle. The pressure is measured on a probe located at (40 0 15) mm, illustrated in Figure 3. Velocity perturbations are slightly affected once the pressure perturbations start to increase. Velocity amplitudes reach up to 50% $\bar{u}_{inlet}$. Similarly, the global heat release rate is also affected, as the high-frequency instability affects the shape and overall dynamics of the flame. The measured input and output signals are thus corrupted and cannot be used for system identification.
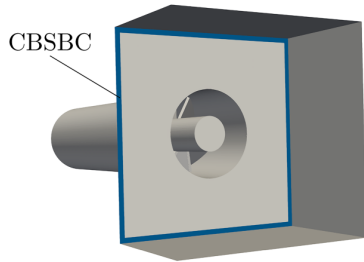

Figure 5. Unstable transverse mode is suppressed with an impedance boundary condition (CBSBC) imposed at the perimeter (blue) of the combustion chamber backplane.

In order to suppress the high-frequency instability, the acoustic behavior of the four chamber walls was originally manipulated, where a reflection coefficient near one ($R_{wall} = 0.95$) was imposed with the CBSBC method. A similar approach with "soft NSCBC" walls was presented and applied by Ghani et al.[66]. However, in the present case, this approach turned out to influence the flame dynamics, as observed with harmonic analysis and broadband SI (not shown in the present paper). It was concluded that such an approach is not adequate for later flame dynamics analysis and is therefore not used in the present study.

The selected damping approach is the following. The outlet formulation of CBSBC with $R_{wall} = 0.95$ is imposed at the perimeter of the combustion chamber backplane, as shown in Figure 5. An acoustic slit with a width of four numerical cells, where only acoustic flux is allowed, turned out to sufficiently suppress the transverse mode without influencing the flame dynamics, as analyzed by several harmonically excited simulations (not shown in the present paper). With the reflection coefficient close to unity, the slot is slightly acoustically softer than the rest of the (acoustically hard) combustor wall. The excellent performance of this arrangement is shown in Figure 6 (blue). This damping strategy was inspired by the ones used in industrial gas turbines[67]. Compared to the latter, which considers Helmholtz or quarter-wave resonators, we do not use holes in the backplane, but an acoustic slit in order to avoid influencing the flow field.

Comparison of time-averaged flow/flame quantities in the compressible and incompressible LES

An obligatory test for the correctness of a CFD simulation is the comparison of velocity profiles at different axial
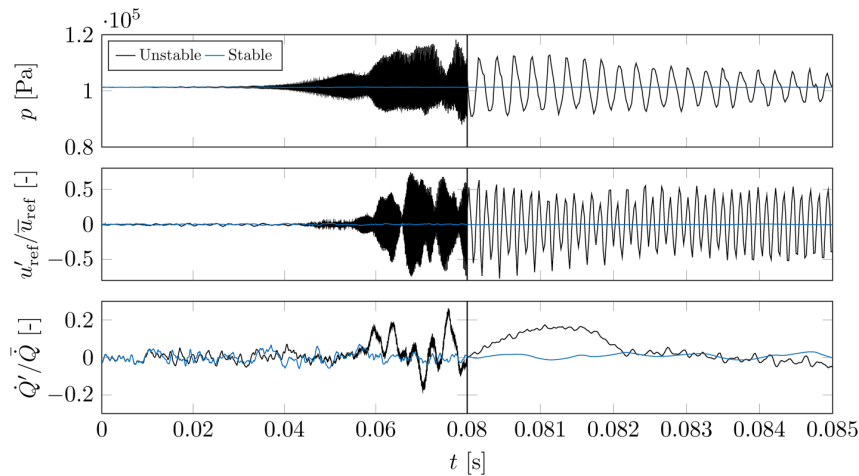

Figure 6. Pressure fluctuation (top), input velocity signal (middle) and output heat release rate signal (bottom) of the unstable and stable compressible LES. Pressure probe is located at (40 0 15) mm in the combustion chamber (illustrated in Figure 3). Note the non-equidistant time axis.

positions. The associated time-averaging was carried out over 100 ms in the compressible and incompressible cases. Profiles of time-averaged and RMS axial velocity components at different positions downstream the combustion chamber entry are compared, as illustrated in Figure 7.

The RMS velocity is calculated as $u_{z,\sigma} = \sqrt{\overline{u_z'^2}} = \sqrt{\frac{1}{N}\sum_i^N (u_z - \overline{u_z})^2}$, where N is number of samples for time averaging. Note that the comparison is limited to CFD, as no velocity measurements (PIV) are available for the 30 kW thermal power configuration[20]. Therefore, due to the lack of experimental data of velocity for the present case, the prediction of flame-turbulence interaction cannot be considered fully validated. However, the agreement between compressible and incompressible LES is very good. Time-averaged axial velocity and temperature fields of both LES are shown in Figure 8 together with surface streamlines and iso-contours of the heat release rate, respectively. The velocity fields show classical flow features of a swirl burner, namely a strongly pronounced central recirculation zone (CRZ) downstream of the bluff body and a weaker outer recirculation zone (ORZ) typical for V-shaped flames. The flame shapes are also present in the temperature fields, which exhibit relatively low temperatures in the ORZ compared to the burnt gases. Overall, both fields are in good agreement in the LES.

Time-averaged heat release rate fields from both simulations were line-of-sight (LOS) integrated along the width of the combustion chamber. A comparison between time-averaged OH* chemiluminescence emission measurements from the experiment and the normalized heat release rate from LES is feasible because heat release rate $\dot{Q}$ is proportional to light emission intensity of OH* in perfectly premixed systems[68]. Figure 9 shows the spatial distribution of the normalized (with its maximum) time-averaged OH*
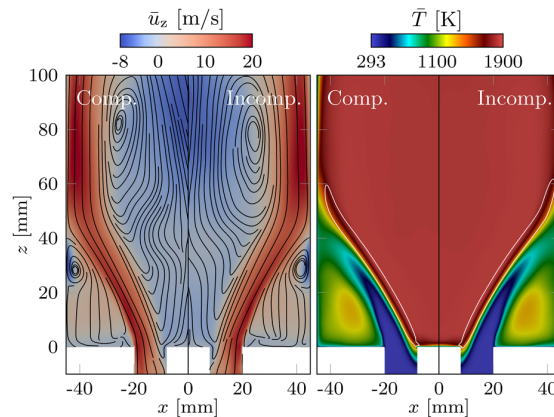
Figure 8. Time-averaged fields of axial velocity with surface streamlines (left) and temperature (right) of compressible and incompressible LES. White iso-contours refer to the heat release rate of level 2×10^8 W/m^3.

chemiluminescence emission measurements from the experiment and the normalized heat release rate from LES. The cage of the combustion chamber, where the quartz windows are mounted, is represented with a shaded area in the images of the simulations. The flame angle at the bluff body, as well as the flame length, is correctly reproduced in both LES. Each flame shows the characteristic stabilization in the inner shear layer only, which is known as a "V-shaped" flame. Capturing the flame length and shape are essential features for the correct identification of flame dynamics[69].

The simulated flame shapes stand in good agreement with that of the experiment and no differences between the compressible and incompressible LES are visible. The heat release rate distributions of LES are normalized with the area under the curve of the experimental distribution (reference area) since the amount of burnt fuel (or produced heat release) in experiments and simulations should be equivalent. The agreement between the experiment and LES is very good from approximately 0.045 m behind the chamber entry (see Figure 9 right). A possible reason for the mismatch at the burner outlet is the missing optical access in the experimental setup. This would explain the zero value until 0.01 m. The heat release at the burner mouth is higher in LES, whereas the OH* chemiluminescence emissions could not be measured directly at the bluff body plane, because the cage of the quartz windows limited the view field of the camera. For a better agreement in the close vicinity of the combustion chamber entry, a more advanced modeling approach for the wall temperature boundary conditions (i.e. conjugate heat transfer) at the backplane has to be used in LES[62,63]. However, a correct modeling is very challenging because there is no reliable data on wall temperatures from the experiment. In any case, the agreement between compressible and
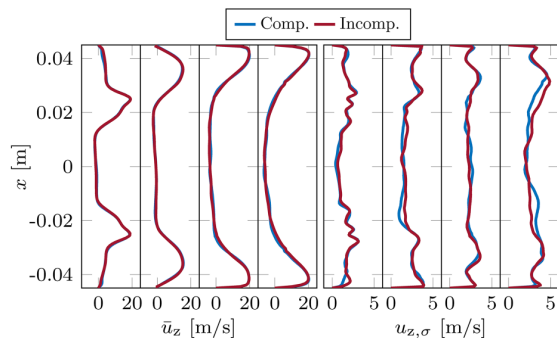

Figure 7. Profiles of time-averaged (left) and RMS (right) axial velocity components of compressible and incompressible LES at various measurement planes (z=20, 40, 60 and 80 mm) downstream of the combustion chamber entry.
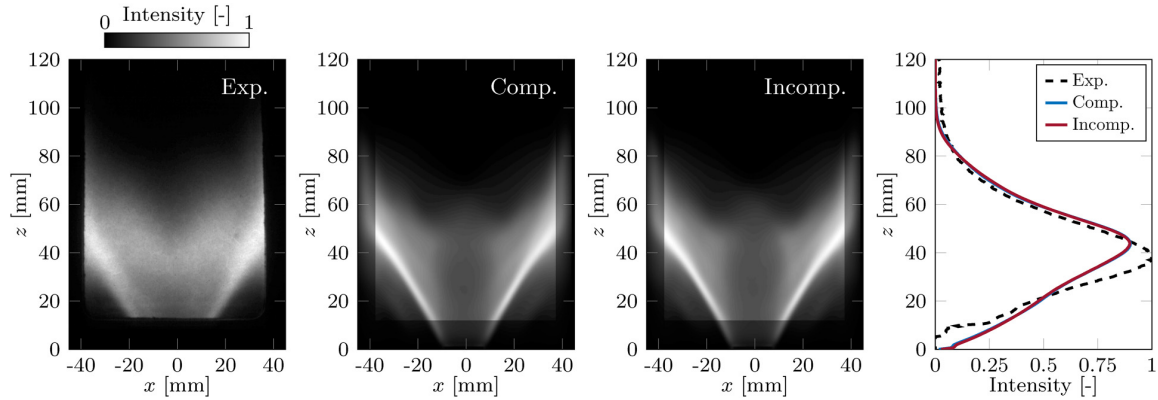
Figure 9. Comparison of experimental time-averaged LOS integrated OH* chemiluminescence image with time-averaged LOS integrated heat release rate field $\dot{Q}$ from compressible and incompressible LES. The normalized spatial distribution of heat release rate from experiment, compressible and incompressible LES is shown in addition. Note that the blue and red lines overlap.

incompressible LES is excellent, which is of higher priority than agreement with the experiment in the present study.

Flame response to velocity perturbations of the premixed swirl burner

Since the steady-state results shown in the previous section match very well, the corresponding flame dynamics is analyzed in this section. Compressible and incompressible LES are excited with broadband signals to identify with one simulation the flame response over the frequency range up to 500 Hz. The compressible LES is forced with an acoustic wave f_{ex} and the incompressible LES is forced with an acoustic velocity perturbation u'_{ex}, where the subscript "ex" stand for excitation. Both methods are compared directly with each other and validated with experimental data. For additional numerical validation, results from harmonic excitation at specific frequencies are used. First, the quality of the generated time series data is evaluated. Afterwards, the FTF is identified with harmonic analysis and a finite impulse response model.

Evaluation of input and output signals

As stated above, compressible and incompressible LES are excited with a broadband signal with maximum amplitude $f_{ex}/\bar{u}_{ex} = 0.1$ (compressible) and $u'_{ex}/\bar{u}_{ex} = 0.1$ (incompressible) in order to generate time series for subsequent system identification. The probability density function (PDF) of both excitation signals is shown in Figure 10 (left column). In a turbulent flame, the amplitude of the excitation signal has a significant effect on the identification of flame dynamics, even in the linear flame regime. If the excitation amplitude is chosen too low, the SNR (excitation signal compared to turbulent noise) is too low and a clear

identification of the FTF is no longer possible. Therefore, the amplitude has to be chosen such it assures linear flame behavior on the one hand and keeps the SNR high enough for an accurate system identification procedure on the other. The amplitudes $f_{ex}/\bar{u}_{ex} = 0.1$ (compressible) and $u'_{ex}/\bar{u}_{ex} = 0.1$ (incompressible) are selected, as illustrated in Figure 10.

Note that it is not the amplitude of the excitation signal (imposed at the inlet boundary), but the amplitude of the velocity perturbations at the reference position (input signal) what is of primary interest for flame perturbation and also FTF identification. The PDF of the compressible and incompressible input signal is shown in Figure 10 (right column), where the incompressible PDF is marked as reference. Note that, in contrast to the incompressible case, the input signal in the compressible case—and therefore the associated PDF—is different from its corresponding excitation signal. Differences between the excitation and input signals in the compressible LES are also observed with the power spectrum of the latter, shown in the middle column in Figure 10. Its peaks at three specific frequencies (110 Hz, 260 Hz and 470 Hz) are a manifestation of resonances within the system. The dominant peak at $f_{PSD,1}$ is associated with the first ITA mode of the anechoic BRS burner, identified with the $-\pi$ criterion from the FTF shown in Figure 13. The intrinsic thermoacoustic feedback loop, explained in section "Modeling approaches", causes a resonance in the system, which is clearly observed in the power spectrum. Such high resonances cause significant differences between excitation and input signals. Note that the flame does not respond to the imposed excitation signal, but to the input signal extracted upstream of the flame. The disparity between the two signals must be taken into account during pre-processing when generating an excitation signal. It may be necessary to iteratively modify the excitation signal until the input signal exhibits the desired features.
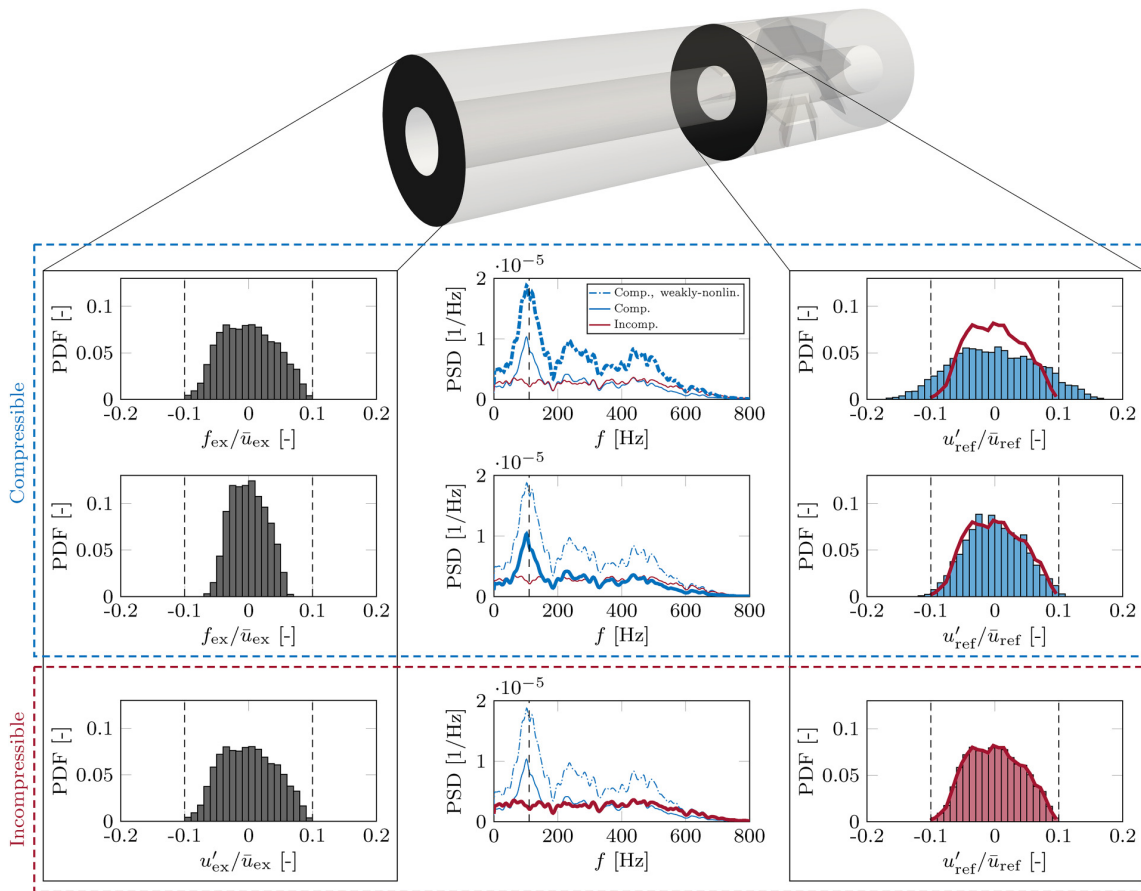
Figure 10. Influence of intrinsic thermoacoustic (ITA) feedback loop on input signal. Left column: PDF of excitation signals (imposed at inlet boundary). Middle column: PSD of weakly-nonlinear compressible, compressible and incompressible LES . Note hat the same three PSDs are shown in each figure in the middle column for comparison purposes. The thick line highlights the case that corresponds to each row (top: weakly-nonlinear compressible; middle: compressible; bottom: incompressible). Right column: PDF of input signals (evaluated at reference position) with PDF of incompressible LES (solid, red) as comparison.

A strong ITA resonance as shown in Figure 10 (middle column) is linked to high amplitudes of the g wave, which is simply explained with equation (3). In the specific case of $f_{\mathrm{ex}}/\bar{u}_{\mathrm{ex}} = 0.1$, this leads to maximum amplitudes of the input signal up to $u'_{\mathrm{ref}}/\bar{u}_{\mathrm{ref}} > 0.17$, which may cause a nonlinear flame response that cannot be investigated by linear identification models. To check nonlinearity of the compressible LES, a harmonic excitation at $140\,\mathrm{Hz}$ is used. The amplitude of the excitation signals is again $f_{\mathrm{ex}}/\bar{u}_{\mathrm{ex}} = 0.1$ (compressible) and $u'_{\mathrm{ex}}/\bar{u}_{\mathrm{ex}} = 0.1$ (incompressible). The input signal of the compressible LES in Figure 11 (dashed blue) shows already an amplitude of $u'_{\mathrm{ref}}/\bar{u}_{\mathrm{ref}} \approx 0.2$. Two indications for nonlinear flame behavior are found. First, the output signal of the compressible LES (dashed blue) shows a typical non-harmonic shape. Second, frequencies $f \neq f_{\mathrm{ex}}$ get excited, which are shown in the power spectra of input and output signal in

Figure 11 (see detailed view). To conclude, the compressible LES ($f_{\mathrm{ex}}/\bar{u}_{\mathrm{ex}} = 0.1$) shows weakly-*nonlinear* behavior.

The amplitude of the excitation signal in the compressible LES has to be scaled to establish comparability with the incompressible LES and to avoid nonlinear flame behavior. Therefore, the amplitude of the excitation signal is adjusted to realize $u'/\bar{u} = 0.1$ at the reference position. Input and output signals and power spectra of the linear compressible LES (afterwards simply called "compressible LES") and the incompressible LES are now comparable, as shown in Figure 11.

The amplitude of the broadband excitation signal is scaled from $f_{\mathrm{ex}}/\bar{u}_{\mathrm{ex}} = 0.1$ to $f_{\mathrm{ex}}/\bar{u}_{\mathrm{ex}} = 0.065$. This downscaling results in the same broadband signal for compressible and incompressible simulation, but different amplitudes. The PDF of the down-scaled excitation signal
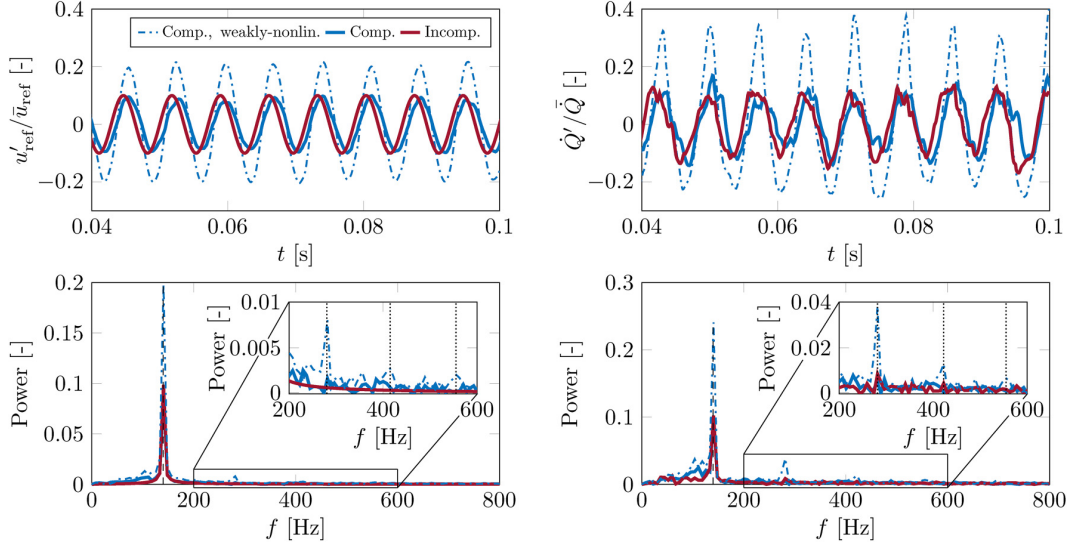
Figure 11. Harmonic analysis of input signals (left) and output signals (right) for weakly-nonlinear compressible, compressible and incompressible LES at 140 Hz in time domain (top) and frequency domain (bottom).

Table 2. Crest factor C_r of the input signals.

Input signal	C_r
Compressible, weakly-nonlinear	1.17
Compressible, linear	1.11
Incompressible	1.10

is shown in Figure 10 (left column). The corresponding input signal (right column) of the compressible LES now leads to a similar PDF as in the incompressible case with maximum amplitudes $u'_{ref}/\bar{u}_{ref} \approx 0.1$. The peak in the frequency domain (middle column) also decreases in amplitude, but persists because the resonance in the compressible LES does not disappear. Note that there is no peak in the PSD of the incompressible signal, which is beneficial for the quality of the signal. The difference in PDF of the input signals can be quantified with the crest factor (see equation (8)) of the input signals of weakly-nonlinear compressible, compressible, and incompressible LES, as shown in Table 2. The compressible and incompressible input signals have a similar C_r and therefore show a better utilization of the signal power compared to the weakly-nonlinear compressible LES, which has a higher crest factor. Finally, the autocorrelation γ of the input signals is evaluated according to equation (9) and shown in Figure 12. The signals of the two compressible simulations have a similar autocorrelation behavior, where both exhibit correlation with itself up to around 40 time lags. The autocorrelation of the incompressible LES decays to zero within 10 time lags. Thus, the resonances in the compressible simulations significantly increase (i.e.
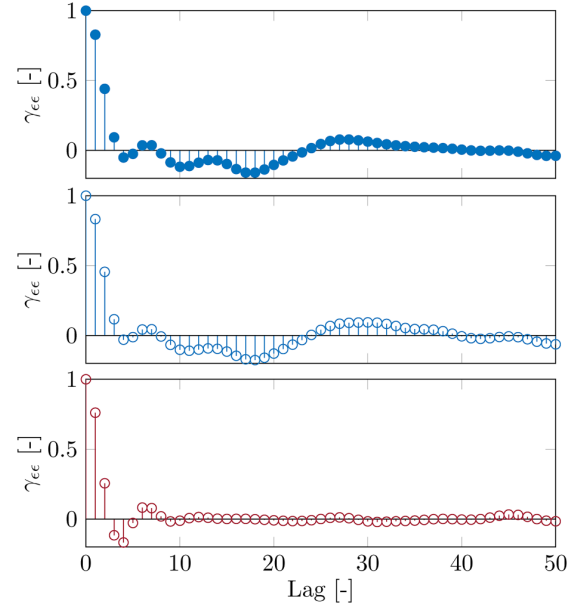

Figure 12. Autocorrelation γ of the weakly-nonlinear compressible (top), compressible (middle) and incompressible (bottom) input signals.

degrade) the autocorrelation. Overall, the incompressible signal has the highest signal quality. The input signal of the compressible LES shows the same crest factor as the incompressible signal and comparable amplitudes in the PSD, only the autocorrelations differ significantly. The input signal of the weakly nonlinear compressible LES
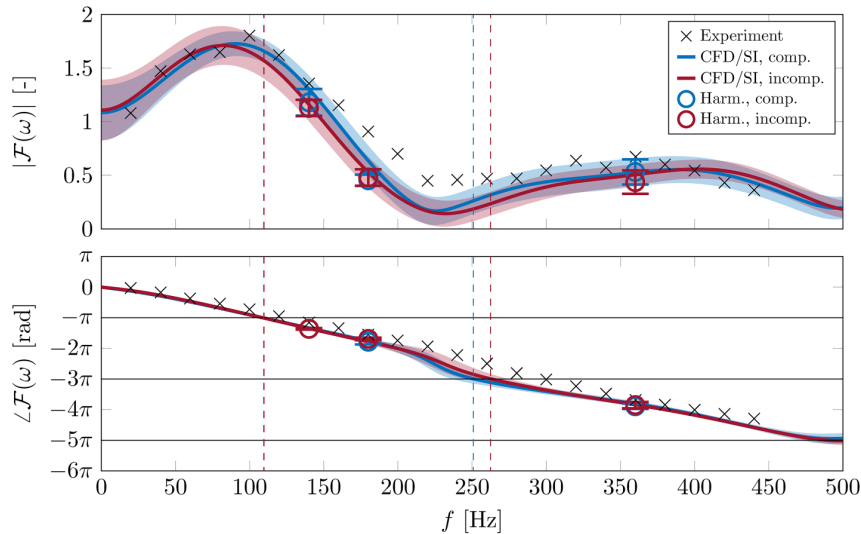
Figure 13. Frequency response from experiment, compressible CFD/SI and incompressible CFD/SI with the respective $\sigma = 1.96$ confidence intervals. Vertical lines (solid, black) indicate ITA frequencies according to the $-\pi$ criterion for the compressible (dashed, blue) and incompressible (dashed, red) case.

shows the poorest quality in all three aspects compared to the two linear signals.

With the evaluation of the input and output signals, the following becomes clearer:

(i) The quality of the excitation signal in the incompressible simulation can be directly tuned/adjusted due to the absence of acoustic wave propagation. The input signal is equivalent to the excitation signal in the incompressible case, which leads to the conclusion that the power spectra are also equivalent (not shown in Figure 10).

(ii) The input signal and excitation signal may differ significantly from each other in a compressible LES, as a result of acoustic resonances in the system (see equation (3)). The more dominant the outgoing acoustic wave g—which can occur in an anechoic system with ITA resonances—the larger the difference between the incoming acoustic wave f and the velocity perturbations u'. With increased (acoustic or ITA) resonances in a compressible LES, the quality of the excitation signal is deteriorated, which may affect the accuracy of system identification.

(iii) The PDF support of the input signal, which quantifies the occurrence of amplitudes in the time series, can be seen as a first indicator of nonlinear flame behavior.

Identification of flame response from compressible and incompressible LES

The main objective of the present work is to ascertain if compressible and incompressible CFD/SI predicts the same flame response. For this reason, the FTF is identified from both data sets and then compared with experimental measurements.

Uncertainty in system identification promoted by turbulent combustion may be important if broadband forcing is performed. Note that the spectral distribution of combustion noise is detrimental for system identification, as the input signals may exhibit low SNR per frequency. Therefore, as a first step, harmonic forcing of compressible and incompressible LES at specific frequencies 140 Hz, 180 Hz and 360 Hz is investigated. The excitation amplitude of the compressible LES is chosen such that the amplitude at the reference position (i.e. of the input signal) equals $u'_{\text{ref}}/\bar{u}_{\text{ref}} = 0.1$. Gain and phase of time series data is analyzed using a fast Fourier transform (FFT) based approach. The harmonic time-series data (≈ 300 ms) is split into parts of eight consecutive periods, where each part overlaps with seven periods from the previous part. This procedure is used to compute the standard deviation from a large data set, which is necessary because of the noise introduced by turbulent combustion. The harmonic results with respective standard deviation of 1.96 σ (95% confidence interval) are shown in Figure 13. Both, the magnitude and phase of the compressible and incompressible LES at each of the frequencies under investigation agree very well.

After harmonic analysis, the LES is excited with a broadband signal to obtain a FTF up to 500 Hz. The finite impulse response (FIR) identification is applied to a 500 ms time series generated by compressible and incompressible LES, where the first 30 ms are cut as a transient phase. A polynomial order $n_h = 39$ is considered for both simulations. The FTFs with 1.96 σ confidence intervals[70] from compressible

and incompressible CFD/SI are compared with experimental measurements in Figure 13. The gain of the transfer functions from CFD/SI stands in overall good agreement with each other and with experimental values. It approaches unity in the low frequency limit[71] and features the overall low-pass behavior with excess in gain at 90 Hz followed by a local minimum at 220 Hz[72,73]. At 200 Hz both CFD/SI results have a slightly smaller gain than in experiment. This mismatch might be caused by the sensitivity of the sum (see equation (7)) to uncertainties in h_k when the sum approaches zero (cancellation effects in the Nyquist plot as discussed in more detail by Polifke[42]).

The small disagreement between the FTFs of compressible and incompressible CFD/SI may have different origins. A likely reason is the inherent stochasticity of the system under evaluation: a turbulent flame. Such a stochastic system introduces uncertainties in the flame response estimation. Note, however, that differences in the prediction lie in the confidence interval of the respective counterpart. Both methodologies show the typical characteristic features of a premixed FTF[42], as discussed in detail above. Both results resolve the first and second maximum of the FTF gain very well. Furthermore, the phase, which is essential for an accurate thermoacoustic analysis[1], matches very well the experimental data. It decreases nearly monotonically with a slight deviation around 250 Hz, which is close to the local minimum in gain.

To further analyze the system dynamics, the $-\pi$ criterion can be used to characterize the ITA modes in the anechoic environment[30,37,32]. The frequencies with a phase corresponding to an odd multiple of $-\pi$ are evaluated. The ITA frequencies extracted from compressible CFD/SI ($f_{ITA1} = 109.5$ Hz and $f_{ITA2} = 250.8$ Hz) and incompressible CFD/SI ($f_{ITA1} = 109.7$ Hz and $f_{ITA2} = 262.4$ Hz) match very well. These frequencies correspond to the peaks observed in the PSD of the compressible simulations in Figure 10 (middle column). The overall good agreement in FTF gain and phase will lead to similar thermoacoustic stability predictions, which can be analyzed in detail by incorporating the FTFs into a reduced order network model of the burner (not done in the present work).

Conclusion

In the present work, the FTF of an acoustically compact premixed burner was identified. In this context, compressible simulation is often the choice for generating the required time series. However, as shown by many authors[14,17–21], incompressible simulation is a well suited alternative. We demonstrated for the first time that both methodologies predict the same flame response to upstream velocity perturbations, reproduce the experimental results equally well, and show the characteristic features of the FTF in fully premixed combustion. For a direct comparison of the flame dynamics in both methods, the same

computational setup (i.e. grid, numerical schemes, turbulent combustion model, chemistry mechanism) was used in the present study to exclude systematic errors. One might conclude that both compressible and incompressible CFD are valid methods for analyzing the dynamics of acoustically compact velocity sensitive flames, provided that an excitation level is assured that results in *linear* flame response and aleatoric uncertainty from the stochastic nature of the identification method is considered. However, the current work reveals significant challenges in compressible simulation for FTF identification.

The present study demonstrated explicitly that there is no need of including acoustic wave propagation in the CFD formulation, since flame-acoustics interaction, for an acoustically compact premixed flame, has no influence on the latter. Excluding the acoustics from the governing equations allows the incompressible simulation to circumvents acoustic resonances and feedback loops in the system. This is equivalent to a perfectly thermoacoustically stable system without any resonances. Besides, statistically steady-state flow and flame quantities (i.e. velocity temperature, heat release rate) were shown to be equivalent.

In the compressible simulation, on the other hand, depending on the reflection coefficients (non-reflecting, fully reflecting, partially reflecting) the amplitude of thermoacoustic modes—either of ITA or acoustic origin—can be amplified by resonances[38], which increases the SNR and therefore corrupts the subsequent identification procedure. Due to acoustic wave propagation, sophisticated acoustic boundary conditions[40,28,29] are required in compressible simulation to obtain a thermoacoustically stable system. Note that even these systems exhibit acoustic modes, which are manifested as peaks in the power spectrum. A key message of this work is that a forcing signal with small amplitudes does *not* guarantee an input signal (upstream velocity perturbation) with small amplitudes (i.e. linear flame response) and similar signal quality, which is detrimental for the identification of the linear flame response with high confidence and accuracy. It is emphasized that the choice of the excitation amplitude in compressible LES is not trivial and may need iterative adjustment until linear response is obtained.

Implicit pressure-based solvers are used in the present work, where there is no acoustic CFL number constraint besides numerical stability limitations and accuracy. Nevertheless, the computational effort is by a factor 3 higher in our compressible simulations. The extent to which incompressible simulations are computationally more efficient depends highly on the underlying numerics[22] and is not object of the present work.

In conclusion, we recommend the *incompressible* CFD/SI approach for studies on flame response identification in acoustically compact, premixed flames due to the above-mentioned difficulties for the compressible counterpart. While LES was used in the present work, the

outcome generalizes to other CFD methods like RANS or direct numerical simulation (DNS). It should be further noted that not all signal quality criteria are of the same significance for the identification of flame dynamics. In the present study, for example, an identical FTF up to the confidence interval is obtained with compressible and incompressible input signals, even though they exhibit a different degree of autocorrelation. The impact of individual quality features like crest factor, power spectrum, and autocorrelation of the input signal on the system identification of premixed flames needs further investigation. In addition, the study should be extended to non-compact flames, since acoustic compactness cannot be assumed in many applied combustors.

Acknowledgements

Declaration of conflicting interests

The authors declared no potential conflicts of interest with respect to the research, authorship, and/or publication of this article.

Funding

ORCID iDs

Alexander J Eder ⬤ https://orcid.org/0000-0003-4451-9034
Matthias Haeringer ⬤ https://orcid.org/0000-0001-5286-0756

Notes

1. *Sufficiently small* may be a vague statement. The actual transition between linear and nonlinear flame response is highly dependent on the specific burner setup (e.g. thermal power, equivalence ratio) and the flame topology. A rough linear limit for a turbulent swirl burner is 10% of the mean inlet velocity[46].
2. Within this process, both LES and an acoustic low-order network model according to Silva et al.[38] were used.

References

1. Giauque A, Selle L, Gicquel L et al. System identification of a large-scale swirled partially premixed combustor using LES and measurements. *J Turbul* 2005; 6: 1–21.
2. Dowling AP and Stow SR. Acoustic analysis of gas turbine combustors. *J Propuls Power* 2003; 19: 751–764.
3. Ljung L. *System identification: theory for the user.* 2nd ed. Upper Saddle River, NJ, USA: Prentice Hall PTR, 1999.
4. Huber A and Polifke W. Dynamics of practical premix flames, part I: model structure and identification. *Int J Spray Combust Dyn* 2009; 1: 199–228.
5. Birbaud AL, Durox D, Ducruix S et al. Dynamics of confined premixed flames submitted to upstream acoustic modulations. *Proc Combust Inst* 2007; 31: 1257–1265.
6. Durox D, Schuller T, Noiray N et al. Experimental analysis of nonlinear flame transfer functions for different flame geometries. *Proc Combust Inst* 2009; 32: 1391–1398.
7. Komarek T and Polifke W. Impact of swirl fluctuations on the flame response of a perfectly premixed swirl burner. *J Eng Gas Turbines Power* 2010; 132.
8. Gatti M, Gaudron R, Mirat C et al. Impact of swirl and bluff-body on the transfer function of premixed flames. *Proc Combust Inst* 2019; 37: 5197–5204.
9. Tay-Wo-Chong L, Bomberg S, Ulhaq A et al. Comparative validation study on identification of premixed flame transfer function. *J Eng Gas Turbines Power* 2012; 134. DOI: 10.1115/1.4004183.
10. Krediet HJ, Beck CH, Krebs W et al. Saturation mechanism of the heat release response of a premixed swirl flame using LES. *Proc Combust Inst* 2013; 34: 1223–1230.
11. Merk M, Silva CF, Polifke W et al. Direct assessment of the acoustic scattering matrix of a turbulent swirl combustor by combining system identification, large eddy simulation and analytical approaches. *J Eng Gas Turbine and Power* 2019; 141. DOI: 10.1115/1.4040731.
12. Schulz O and Noiray N. Autoignition flame dynamics in sequential combustors. *Combust Flame* 2018; 192: 86–100.
13. Kaufmann A, Nicoud F and Poinsot T. Flow forcing techniques for numerical simulation of combustion instabilities. *Combust Flame* 2002; 131: 371–385.
14. Han X and Morgans AS. Simulation of the flame describing function of a turbulent premixed flame using an open-source LES solver. *Combust Flame* 2015; 162: 1778–1792.
15. Lieuwen T. Modeling premixed combustion – acoustic wave interactions: a review. *J Propuls Power* 2003; 19: 765–781.
16. Ducruix S, Schuller T, Durox D et al. Combustion dynamics and instabilities: elementary coupling and driving mechanisms. *J Propuls Power* 2003; 19: 722–734.
17. Febrer G, Yang Z and McGuirk J. A hybrid approach for coupling of acoustic wave effects and incompressible LES of reacting flows. In *47th AIAA/ASME/SAE/ASEE joint propulsion conference & exhibit.* paper no. AIAA2011-6127, San Diego, CA, USA: AIAA. doi:10.2514/6.2011-6127.
18. Gentemann A, Hirsch C, Kunze K et al. Validation of flame transfer function reconstruction for perfectly premixed swirl flames. In *Proceedings of ASME turbo expo 2004.* paper no. GT2004-53776, Vienna, Austria: ASME. doi:10.1115/GT2004-53776.
19. Tay-Wo-Chong L, Scarpato A and Polifke W. LES combustion model with stretch and heat loss effects for prediction

of premix flame characteristics and dynamics. In *Proceedings of ASME turbo expo 2017*. paper no. GT2017-63357, Charlotte, NC, USA: ASME. doi:10.1115/GT2017-63357.

20. Avdonin A, Javareshkian A and Polifke W. Prediction of premixed flame dynamics using LES with tabulated chemistry and eulerian stochastic fields. *J Eng Gas Turbines Power* 2019; 141. DOI: 10.1115/GT2019-90140.

21. Kuhlmann J, Lampmann A, Pfitzner M et al. Assessing accuracy, reliability and efficieny of combustion models for prediction of flame dynamics with large eddy simulation. *Phys Fluids* 2022; 34. DOI: 10.1063/5.0098975.

22. Gicquel LYM, Staffelbach G and Poinsot T. Large eddy simulations of gaseous flames in gas turbine combustion chambers. *Prog Energy Combust Sci* 2012; 38: 782–817.

23. Gentemann A. *Identifikation von akustischen Transfermatrizen und Flammenfrequenzgängen mittels Strömungssimulation*. PhD Thesis, TU München, Germany, 2006.

24. Ma T and Kempf AM. Compressible and incompressible large eddy simulation of a premixed dump combustor. In *Proceedings of ASME turbo expo 2011*. Paper no. GT2011-45304, Vancouver, BC, Canada: ASME, pp. 331–341. doi:10.1115/GT2011-45304.

25. Dombard J, Poinsot T, Moureau V et al. Experimental and numerical study of the influence of small geometrical modifications on the dynamics of swirling flows. In *Proceedings of the 2012 summer program*. CA, USA: Center for Turbulence Research, NASA Ames/Stanford Univ.

26. Treleaven NCW, Su J, Garmory A, et al. An efficient method to reproduce the effects of acoustic forcing on gas turbine fuel injectors in incompressible simulations. *Flow Turbul Combust* 2019; 103: 417–437.

27. Treleaven NCW, Garmory A and Page GJ. The effects of turbulence on jet stability and the flame transfer function in a llean-burn combustor. *Combust Sci Technol* 2020; 192: 2115–2137.

28. Polifke W, Wall C and Moin P. Partially reflecting and non-reflecting boundary conditions for simulation of compressible viscous flow. *J Comput Phys* 2006; 213: 437–449.

29. Jaensch S, Sovardi C and Polifke W. On the robust, clexible and consistent implementation of time domain impedance boundary conditions for compressible flow simulations. *J Comput Phys* 2016; 314: 145–159.

30. Hoeijmakers M, Kornilov V, Lopez Arteaga I et al. Intrinsic instability of flame-acoustic coupling. *Combust Flame* 2014; 161: 2860–2867.

31. Bomberg S, Emmert T and Polifke W. Thermal versus acoustic response of velocity sensitive premixed flames. *Proc Combust Inst* 2015; 35: 3185–3192.

32. Courtine E, Selle L and Poinsot T. DNS of intrinsic thermoacoustic modes in laminar premixed flames. *Combust Flame* 2015; 162: 4331–4341.

33. Silva CF. Intrinsic thermoacoustic instabilities. *Prog Energy Combust Sci* 2023; 95. DOI: 10.1016/j.pecs.2022.101065.

34. Strahle WC. Combustion noise. *Prog Energy Combust Sci* 1978; 4: 157–176.

35. Hegde UG, Reuter D and Zinn BT. Sound generation by ducted flames. *AIAA J* 1988; 26: 532–537.

36. Chakravarthy SR, Shreenivasan OJ, Boehm B et al. Experimental characterization of onset of acoustic instability in a nonpremixed half-dump combustor. *J Acoust Soc Am* 2007; 122: 120–127.

37. Emmert T, Bomberg S and Polifke W. Intrinsic thermoacoustic instability of premixed flames. *Combust Flame* 2015; 162: 75–85.

38. Silva CF, Merk M, Komarek T et al. The contribution of intrinsic thermoacoustic feedback to combustion noise and resonances of a confined turbulent premixed flame. *Combust Flame* 2017; 182: 269–278.

39. Blumenthal RS, Subramanian P, Sujith RI et al. Novel perspectives on the dynamics of premixed flames. *Combust Flame* 2013; 160: 1215–1224.

40. Poinsot T and Lele SK. Boundary conditions for direct simulation of compressible viscous flows. *J Comput Phys* 1992; 101: 104–129.

41. Polifke W. Black-box system identification for reduced order model construction. *Ann Nucl Energy* 2014; 67C: 109–128.

42. Polifke W. Modeling and analysis of premixed flame dynamics by means of distributed time delays. *Prog Energy Combust Sci* 2020; 79. DOI: 10.1016/j.pecs.2020.100845.

43. Tay-Wo-Chong L. *Numerical simulation of the dynamics of turbulent swirling flames*. PhD Thesis, TU München, Germany, 2012.

44. Merk M, Jaensch S, Silva CF et al. Simultaneous identification of transfer functions and combustion noise of a turbulent flame. *J Sound Vib* 2018; 422: 432–452.

45. Foeller S and Polifke W. Advances in identification techniques for aero-acoustic scattering coefficients from large eddy simulation. In *18th international congress on sound and vibration (ISCV18)*. Rio de Janeiro, Brazil, pp. 3122–3129.

46. Jaensch S, Merk M, Emmert T et al. Identification of flame transfer functions in the presence of intrinsic thermoacoustic feedback and noise. *Combust Theory Model* 2018; 22: 613–634.

47. Kim KT, Lee HJ, Lee JG et al. Flame transfer function measurement and instability frequency prediction using a thermoacoustic model. In *Int'l gas turbine and aeroengine congress & exposition*. paper no. GT2009-60026, Orlando, FL, USA, pp. 799–810. doi:10.1115/GT2009-60026.

48. Tay-Wo-Chong L, Komarek T, Kaess R et al. Identification of flame transfer functions from LES of a premixed swirl burner. In *Proceedings of ASME turbo expo 2010*. Paper no. GT2010-22769, Glasgow, UK: ASME, pp. 623–635. doi:10.1115/GT2010-22769.

49. Weller HG, Tabor G, Jasak H et al. A tensorial approach to computational continuum mechanics using object-oriented techniques. *Comput phys* 1998; 12: 620–631.

50. Nichols JW, Schmid PJ and Riley JJ. Self-sustained oscillations in variable-density round jets. *J Fluid Mech* 2007; 582: 341–376.

51. Han X, Li J and Morgans AS. Prediction of combustion instability limit cycle oscillations by combining flame describing function simulations with a thermoacoustic network model. *Combust Flame* 2015; 162: 3632–3647.

52. Pope SB. Ten questions concerning the large-eddy simulation of turbulent flows. *New J Phys* 2004; 6. DOI: 10.1088/1367-2630/6/1/035.

53. Nicoud F and Ducros F. Subgrid-scale stress modelling based on the square of the velocity gradient tensor. *Flow Turbul Combust* 1999; 62: 183–200.

54. Colin O, Ducros F, Veynante D et al. A thickenend flame model for large eddy simulation of turbulent premixed combustion. *Phys Fluids* 2000; 12: 1843–1863.

55. Légier JP, Poinsot T and Veynante D. Dynamically thickened flame LES model for premixed and non-premixed turbulent combustion. In *Proceedings of the 2000 summer program.* CA, USA: Center for Turbulence Research, NASA Ames/Stanford Univ., pp. 157–168.

56. Charlette F, Meneveau C and Veynante D. A power-law flame wrinkling model for LES of premixed turbulent combustion, part I: non-dynamic formulation and initial tests. *Combust Flame* 2002; 131: 159–180.

57. Wang G, Boileau M and Veynante D. Implementation of a dynamic thickened flame model for large eddy simulations of turbulent premixed combustion. *Combust Flame* 2011; 158. DOI: 10.1016/j.combustflame.2011.04.008.

58. Benard P, Lartigue G, Moureau V et al. Large-eddy simulation of the lean-premixed PRECCINSTA burner with wall heat loss. *Proc Combust Inst* 2019; 37: 5233–5243.

59. Franzelli B, Riber E, Gicquel LYM et al. Large eddy simulation of combustion instabilities in a lean partially premixed swirled flame. *Combust Flame* 2012; 159: 621–637.

60. Poinsot T and Veynante D. *Theoretical and numerical combustion.* 3rd ed. Paris, France: CNRS, 2012.

61. Tay-Wo-Chong L and Polifke W. Large eddy simulation-based study of the influence of thermal boundary condition and combustor confinement on premix flame transfer functions. *J Eng Gas Turbines Power* 2013; 135. DOI: 10.1115/1.4007734.

62. Agostinelli PW, Laera D, Boxx I et al. Impact of wall heat transfer in large eddy simulation of flame dynamics in a swirled combustion chamber. *Combust Flame* 2021; 234. DOI: 10.1016/j.combustflame.2021.111728.

63. Agostinelli PW, Laera D, Chterev I et al. On the impact of H2-enrichment on flame structure and combustion dynamics of a lean partially-premixed turbulent swirling flame. *Combust Flame* 2022; 241. DOI: 10.1016/j.combustflame.2022.112120.

64. Kulkarni S, Guo S, Silva CF et al. Confidence in flame impulse response estimation from large eddy simulation with uncertain thermal boundary conditions. *J Eng Gas Turbines Power* 2021; 143. DOI: 10.1115/1.4052022.

65. Selle L, Lartigue G, Poinsot T et al. Compressible large eddy simulation of turbulent combustion in complex geometry on unstructured meshes. *Combust Flame* 2004; 137: 489–505.

66. Ghani A, Poinsot T, Gicquel L et al. LES study of transverse acoustic instabilities in a swirled kerosene/air combustion chamber. *Flow Turbul Combust* 2016; 96: 207–226.

67. Bothien M, Theuer A and Imfeld J. *Helmholtz damper and gas turbine with such a Helmholtz damper.* Patent EP 3 029 376 A1, Baden, Switzerland, 2014.

68. Higgins B, McQuay MQ, Lacas F et al. Systematic measurements of OH chemiluminescence for fuel-lean, high-pressure, premixed, laminar flames. *Fuel* 2001; 80: 67–74.

69. Schuller T, Durox D and Candel S. A unified model for the prediction of laminar flame transfer function: comparisons between conical and V-flame dynamics. *Combust Flame* 2003; 134: 21–34.

70. Sovardi C. *Identification of sound sources in duct singularities.* PhD Thesis, TU München, Germany, 2016.

71. Polifke W and Lawn CJ. On the low-frequency limit of flame transfer functions. *Combust Flame* 2007; 151: 437–451.

72. Hirsch C, Fanaca D, Reddy P et al. Influence of the swirler design on the flame transfer function of premixed flames. In *Proceedings of ASME turbo expo 2005.* Paper no. GT2005-68195, Reno, NV, USA: ASME, pp. 151–160. doi:10.1115/GT2005-68195.

73. Palies P, Schuller T, Durox D et al. Modeling of premixed swirling flames transfer functions. *Proc Combust Inst* 2011; 33: 2967–2974.

Identification of entropy waves in a partially premixed combustor

Alexander J. Eder [a],*, Bayu Dharmaputra [b], Alex M. Garcia [a], Camilo F. Silva [a], Wolfgang Polifke [a]

[a] Technical University of Munich, TUM School of Engineering and Design, Department of Engineering Physics and Computation, Garching 85748, Germany
[b] ETH Zurich, Department of Mechanical and Process Engineering, CAPS Laboratory, Zurich 8092, Switzerland

ARTICLE INFO

ABSTRACT

Unsteady combustion generates not only acoustic waves, but also fluctuations of the burnt gas temperature — referred to as entropy waves. These waves are convected by the mean flow through the combustor and result in conversion to acoustic energy when accelerated in an exit nozzle. The upstream traveling acoustic wave can then couple with the unsteady heat release of the flame and cause self-excited thermoacoustic instability, particularly at low frequencies ("rumble"). In this work, large eddy simulation (LES) is combined with system identification (SI) to determine the entropy transfer function (ETF) of a partially premixed, swirl-stabilized flame with hydrogen enrichment. We compare the single-input single-output (SISO) entropy transfer function identified from a broadband-forced LES with air mass flow modulation to the one obtained experimentally through tunable diode laser absorption spectroscopy with wavelength modulation spectroscopy (TDLAS-WMS) to measure temperature fluctuations. Then, multiple-input single-output (MISO) identification is applied to time series data obtained from simultaneous modulation of air and fuel mass flow to estimate the individual contributions of perturbations in velocity and equivalence ratio to entropy response. Equivalence ratio fluctuations are found to be the dominant generation mechanism of entropy waves. Finally, the entropy transfer function is identified at various positions in the combustion chamber to analyze the decay of entropy waves governed by convective dispersion.

1. Introduction

Unsteady combustion may generate coherent temperature fluctuations in the burnt gas [1], also known as *entropy waves*. These inhomogeneities are convected through the combustion chamber and attenuated by turbulent mixing and spatial variations in the velocity field [2,3]. In aero-engine combustors, where convective dispersion is slow relative to the residence time, entropy waves often reach the turbine stage with high amplitudes, where they are accelerated [4–6]. This acceleration results in a mode conversion into pressure oscillations [7]. On the one hand, the downstream traveling acoustic waves add to the overall noise emissions of an aircraft as indirect combustion noise [6]. On the other hand, the upstream propagating acoustic waves might interact constructively with the unsteady combustion and cause thermoacoustic combustion instability, particularly at low frequencies ("rumble") [1,8]. This coupling is achieved through multiple connected mechanisms involving fluctuations of entropy, pressure, velocity and fuel concentration [8].

In this work, lean *partially premixed* (or technically premixed) turbulent flames are considered, where the fuel is injected close to the burner outlet resulting in spatial mixture inhomogeneities at the flame. Equivalence ratio fluctuations can contribute to combustion instability

only if driven in a coherent manner by the combustion process and pressure oscillations, thus closing a positive feedback loop [9,10]. Coherent fluctuations in fuel concentration originate from pressure and velocity fluctuations at the location of the fuel injection [11], which are convected to the flame [2]. These locally richer and leaner pockets of fresh mixture cause local changes in the adiabatic flame temperature, i.e. entropy waves [8]. In the absence of equivalence ratio fluctuations, entropy waves may occur due to unsteady wall heat loss (dominant effect) or differential diffusion, as shown in our previous study on entropy waves in a fully premixed non-adiabatic combustor with hydrogen enrichment [12]. These mechanisms are coherent with velocity fluctuations.

The two excitation mechanisms mentioned above and their interaction result in a frequency-dependent response of entropy to flow perturbations, known as entropy transfer function (ETF). The model of a partially premixed combustion system with an acoustically stiff fuel injection (large pressure drop across fuel injectors) located in acoustically compact distance (much shorter than the acoustic wavelength) to the burner outlet reduces to a single-input single-output (SISO) model structure [11,13] (see Fig. 1(a)). This black-box model implicitly accounts for fluctuations in equivalence ratio caused by
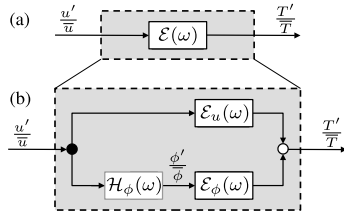

Fig. 1. Black-box model structure of (a) overall entropy transfer function $\mathcal{E}(\omega)$ and (b) individual contributions $\mathcal{E}_\phi(\omega)$ and $\mathcal{E}_u(\omega)$ in a partially premixed combustor with stiff and acoustically compact fuel injection. $\mathcal{H}_\phi(\omega)$ relates fluctuations in equivalence ratio ϕ' and velocity u'.

velocity perturbations at the fuel injector. For the configuration considered here, the forcing of air mass flow determines the overall ETF in partially premixed flames [14]. In this work, high-fidelity large eddy simulation (LES) is combined with system identification (SI) [15] to determine the frequency response of entropy waves. The simulations are complemented by tunable diode laser absorption spectroscopy with wavelength modulation spectroscopy (TDLAS-WMS) [14] to measure the overall ETF.

This study aims at enhancing the understanding of entropy response in partially premixed flames by separating the contributions of equivalence ratio and velocity fluctuations, respectively, as shown in Fig. 1(b). Therefore, a multiple-input single-output (MISO) structure is introduced for the ETF, similar to that proposed by Huber and Polifke [11] for the flame transfer function (FTF), which describes the response of heat release rate to perturbation in velocity and equivalence ratio. The data for the MISO approach is generated by a LES with simultaneous excitation of the air and fuel mass flow with uncorrelated broadband signals. The next section describes the experimental and numerical setup of the combustor used in this work. Section 3 provides information on the methodology for SISO and MISO model identification. Section 4 presents the ETF obtained by LES/SI and experiments and analyzes the individual transfer functions. Finally, the decay of entropy waves along the combustor is investigated.

2. Experimental and numerical setup

2.1. The ETH combustor

To investigate the entropy response of partially premixed flames to modulations in air mass flow, experimental results are compared to acoustically forced large eddy simulation. In this section, a brief overview of the laboratory-scale test rig [14,16] of a turbulent swirl combustor shown in Fig. 2(a) is provided. The test rig has a modular layout and consists of a square air plenum and combustion chamber (62×62 mm^2), an annular burner (100 mm length) equipped with an axial swirler, and a motor-driven adjustable outlet orifice to ensure thermoacoustic stable conditions. Some of these modules consist of air-cooled quartz windows for optical access, the rest of water-cooled aluminum walls.

The air is supplied at ambient temperature and pressure through the plenum and subsequently passes through eight axial swirl vanes. The methane-hydrogen fuel mixture is injected in two stages at approximately choked conditions (unity Mach number) as jet-in-cross-flow[1] into the turbulent swirling air flow within the burner annulus downstream of the swirler. Both stages consist of four small injection holes (0.8 mm diameter), positioned at 90 degree increments around the

center body. A large pressure drop across the injectors ensures acoustically stiff fuel injection. The short distance (50 mm and 22 mm) between the injector stages and the burner outlet (also known as burner mouth) leads to spatial and temporal inhomogeneities of equivalence ratio before combustion.

The air mass flow is mono-frequently excited through an upstream loudspeaker. Six G.R.A.S. microphones are located between loudspeaker and burner to reconstruct the acoustic field. Two different lasers centered at around 1392 nm and 1469 nm that targets the H$_2$O absorption spectra are employed for the TDLAS-WMS method. The beams are combined together with a fiber combiner. Optical access for the laser beam is located 280 mm downstream of the burner outlet as shown in Fig. 2(a). The laser beam passes the hot gas section and is detected by a photodiode. The raw signals from the photodiode are converted to temperature signals. The ETF is then obtained by dividing these signals by the reconstructed acoustic velocity. A more detailed description of the TDLAS-WMS setup and algorithm are presented in [14].

The methane-hydrogen-fired combustor (59% hydrogen by volume) was operated at an equivalence ratio of $\phi = 0.78$ and an air mass flow of 18.2 g/s resulting in a thermal power of 43.7 kW. The operating condition considered in this work corresponds to "OP 3" in [16] and provides additional measurement data including line-of-sight integrated OH* chemiluminescence and planar laser-induced fluorescence of the OH radical (OH-PLIF). The flame images are compared with the numerical results in Section 4.1.

2.2. LES setup

Large eddy simulations of the ETH combustor shown in Fig. 2 are performed using the massively parallel explicit cell-vertex AVBP code (www.cerfacs.fr/avbp7x/index.php), which solves the multi-species compressible Navier–Stokes equations. Subgrid Reynolds stresses are modeled using the SIGMA turbulent closure [17] without wall functions. A second-order (in both space and time) Lax–Wendroff scheme is used to discretize the convective terms, found to be sufficient for LES/SI applications [15]. The time step is fixed to $\Delta t = 1.3 \times 10^{-8}$ s, assuring an acoustic Courant-Friedrichs-Lewy (CFL) number below 0.8 (corresponds to a hydrodynamic CFL number below approx. 0.4). The computational domain shown in Fig. 2(b) consists of the burner (axial swirler, fuel injectors and mixing duct) and 300 mm of the combustion chamber and is spatially discretized with 72.8 million tetrahedral elements. The grid is shown in Fig. 2(c) and refined as follows: $\Delta x = 80$ μm in the injectors and fuel jets, $\Delta x = 250$ μm in the swirler and flame region (laminar flame thickness is about 397 μm), $\Delta x = 300$ μm in the mixing duct, and $\Delta x = 400$ μm at the combustor walls.

Inlet and outlet boundaries are modeled with the Navier–Stokes characteristic boundary conditions (NSCBC) [18] imposing mass flow rates (see numbers in Section 2.1) and ambient pressure, respectively, with relaxation coefficients $K_{air} = 5.0 \times 10^4$ s^{-1}, $K_{fuel} = 5.0 \times 10^5$ s^{-1} and $K_{outlet} = 5.0 \times 10^2$ s^{-1}. The inlet and outlet impedances are set to ensure thermoacoustic stability and do not have to correspond to their actual values in the experiment. To suppress a self-excited transverse chamber mode, a characteristic zero mass-flux boundary condition with relaxation towards a target temperature is imposed at the perimeter of the backplane as successfully applied by Eder et al. [19]. Heat loss $\dot{q} = (T_{wall} - T_\infty)/R_w$ is imposed at the remaining backplane, combustion chamber side walls and the center body tip, where the thermal resistance R_w is adjusted to ensure wall temperatures around $T_{wall} = 850$ K.

The analytically reduced chemistry (ARC) mechanism presented and validated by Laera et al. [20] for CH$_4$-H$_2$-air combustion is employed. It consists of 20 transported species, 166 reactions, and 9 quasi-steady-state species derived from the detailed GRI-Mech 3.0. Supplementary material in [20] offers further information on the ARC mechanism.

---

[1] The momentum flux ratio is estimated based on LES results as $J = \left(\rho_{fuel} u_{fuel}^2\right) / \left(\rho_{air} u_{air}^2\right) \approx 100$.
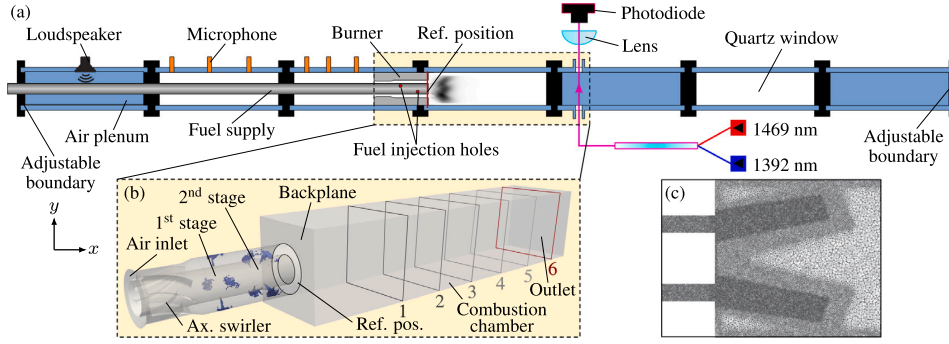
Fig. 2. (a) Schematic of the swirl combustor equipped with TDLAS-WMS and microphone arrays for ETF measurement. The reference position for velocity reconstruction is indicated at the burner outlet. Stiff fuel injection of the CH_4-H_2 mixture into the turbulent swirling air flow is done inside the burner (partially premixing). (b) Computational domain used in LES with instantaneous iso-contours of H_2 to visualize the staged fuel injection together with the reference positions for velocity and temperature reconstruction (position 6 indicates location of ETF measurement). (c) Grid refinement in the flame region.

Transport properties are described by a constant mixture Prandtl number and constant Schmidt numbers for each species [20] to account for differential diffusion. Turbulence-combustion interaction is modeled with the dynamic thickened flame (DTFLES) model [21], where the flame is thickened based on a flame sensor (5 points in the flame are specified as target resolution). The model parameters (laminar flame speed, laminar flame thickness, reaction rates) are functions of the equivalence ratio.

3. Methodology

3.1. Entropy disturbances

Based on the linearized Gibbs equation and neglecting compositional inhomogeneities [22], together with the linearized expression for the ideal gas law $\rho'/\overline{\rho} = p'/\overline{p} - T'/\overline{T}$, entropy fluctuations s' can be approximated by fluctuations of the temperature T' and pressure p',

$$\frac{s'}{c_p} = \frac{1}{\gamma}\frac{p'}{\overline{p}} - \frac{\rho'}{\overline{\rho}} \approx \frac{T'}{\overline{T}} - \frac{\gamma - 1}{\gamma}\frac{p'}{\overline{p}}, \tag{1}$$

where ρ, c_p and γ are the density, the specific isobaric heat capacity and the heat capacity ratio, respectively, and $(\cdot)'$ are small fluctuations around its temporal mean value $\overline{(\cdot)}$. Assuming low Mach numbers and no large amplitude acoustic fluctuations, the contribution of pressure fluctuations (second term on the right-hand side of Eq. (1)) is known to be small in premixed flames. This simplifies the right-hand side of Eq. (1) to [6,8,14]

$$\frac{s'}{c_p} \approx \frac{T'}{\overline{T}}. \tag{2}$$

The time series of the temperature fluctuations are inferred in the experiment using TDLAS-WMS at a reference position (0.28 m from the burner outlet). In the LES, they are recorded as an area-integral at several planes along the combustion chamber (and also at the measurement position). The reference position in the experiment was chosen to be sufficiently far from the reaction zone, while still ensuring that the temperature variations were detectable. In technically relevant applications, entropy waves are only problematic if they have sufficient amplitudes at the combustor exit/turbine inlet to make a relevant contribution to the overall engine noise or trigger a self-excited feedback loop.

3.2. Entropy transfer function

The frequency-dependent response of coherent fluctuations of the burnt gas temperature to coherent velocity fluctuations can be related for small amplitudes using an entropy transfer function,

$$\frac{T'}{\overline{T}} \equiv \mathcal{E}(\omega)\frac{u'_{ref}}{\overline{u}_{ref}}, \tag{3}$$

where u_{ref} is the velocity at a reference location (burner outlet), $\mathcal{E}(\omega)$ is the entropy transfer function, and $\omega = 2\pi f$ is the Fourier transform variable (angular frequency). The transfer function in Eq. (3) can be understood as the overall entropy response, which contains both the mechanisms of equivalence ratio and velocity fluctuations. In partially premixed combustion systems with stiff fuel injection (constant fuel mass flow), velocity fluctuations at the injector (caused by modulation of the air mass flow) lead to phase-opposite equivalence ratio fluctuations at the injector [8,23,24] that are convected in the mixing duct toward the flame [2]. If, in addition to the stiff fuel injection, an acoustically compact mixing duct is present (both are given in the present configuration), a single-input single-output model structure for the entropy response is justified [11,13]. In both the experiment and a first LES, the overall ETF in Eq. (3) is determined by an upstream modulation of the air mass flow via mono-frequency (experiment) and broadband (LES) forcing. The experimental and numerical results are compared in Section 4.1.

As proposed by Huber and Polifke [11] for the flame transfer function, a multiple-input single-output model structure is utilized in the present work for the ETF,

$$\frac{T'}{\overline{T}} \equiv \mathcal{E}_\phi(\omega)\frac{\phi'_{ref}}{\overline{\phi}_{ref}} + \mathcal{E}_u(\omega)\frac{u'_{ref}}{\overline{u}_{ref}}, \tag{4}$$

where $\mathcal{E}_\phi$ (independent of impedance and position of the fuel injector) and $\mathcal{E}_u$ represent the individual entropy responses to equivalence ratio and velocity fluctuations at the burner outlet (reference position). In Eq. (4) all mechanisms generating entropy waves by global equivalence ratio fluctuations at the burner outlet are represented by $\mathcal{E}_\phi$. All generation mechanisms of entropy waves present in the system due to perturbations of the incoming flow at the flame base (e.g. wall heat losses [12,25,26], differential diffusion [12], dilution jets [25] or incomplete combustion [26]) are represented by $\mathcal{E}_u$. Separating the input quantities permits independent consideration of both excitation mechanisms. The present experimental setup is not equipped for excitation in the fuel supply duct and therefore is not suitable for the MISO analysis. However, simultaneous broadband forcing of air and fuel mass flow is applied in a second LES. Uncorrelated excitation signals for both channels (air and fuel mass flow) allow to distinguish the individual contributions using MISO identification [11,27] even if the eventual input signals (u'_{ref}, ϕ'_{ref}) exhibit a certain correlation [28]. The reader may refer to [11,28] for further information on the MISO identification. The individual contributions $\mathcal{E}_\phi$ and $\mathcal{E}_u$ are identified from LES data in Section 4.2.
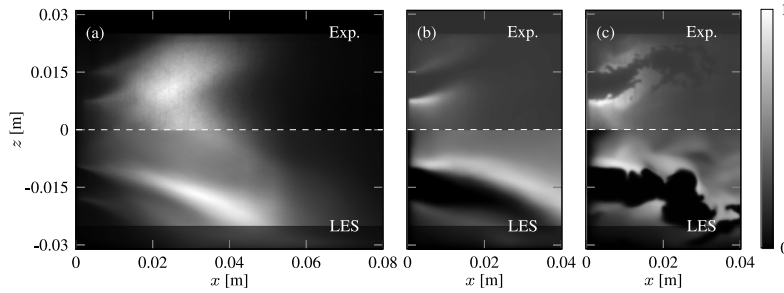
Fig. 3. Comparison of flame shapes between experiment [16] (top) and LES (bottom), with (a) line-of-sight (LOS) integration of time-averaged OH* chemiluminescence image (Exp.) and HRR (LES), (b) time-averaged OH-PLIF signal (exp.) and OH mass fraction $\overline{Y}_{OH}$ (LES), and (c) instantaneous OH-PLIF (exp.) and OH mass fraction Y_{OH} (LES).

Under the same assumptions as in Eq. (3) (stiff and acoustically compact fuel injection), the overall ETF is related to the two contributions $\mathcal{E}_\phi$ and $\mathcal{E}_u$ via [29]

$$\frac{T'}{\overline{T}} \equiv \underbrace{\left[\mathcal{H}_\phi(\omega)\mathcal{E}_\phi(\omega) + \mathcal{E}_u(\omega)\right]}_{\mathcal{E}(\omega)} \frac{u'_{ref}}{\overline{u}_{ref}} \; . \tag{5}$$

The transfer function $\mathcal{H}_\phi(\omega)$ represents the equivalence ratio response to velocity fluctuations at the burner outlet and can be obtained with system identification from the LES with only air mass flow forcing (ϕ'_{ref} and u'_{ref} are correlated) via

$$\frac{\phi'_{ref}}{\overline{\phi}_{ref}} \equiv \mathcal{H}_\phi(\omega) \frac{u'_{ref}}{\overline{u}_{ref}} \; . \tag{6}$$

Eq. (5) is used in Section 4.3 to validate the MISO model (Eq. (4)) with experimental data.

4. Results and discussion

4.1. Comparison of flame shapes

A comparison of time-averaged and instantaneous flame images from LES and optical measurements, respectively, is shown in Fig. 3. The mean fields in LES are time-averaged over a duration of 35 ms. Although OH* light intensity is not a quantitative indicator for heat release rate in partially premixed flames (non-linear response of OH* to ϕ') [30], it may serve as a qualitative measure to compare the shape and characteristics of the flame from experiment and LES. As shown in Fig. 3(a), the high volume fraction of hydrogen in the fuel ($X_{H_2} = 0.59$) causes a short flame with dominant M-shape that exhibits pronounced reactions in the inner and outer shear layer, which is well captured in LES. Furthermore, time-averaged and instantaneous OH-PLIF images (experiment) are compared with OH mass fractions (LES), see Fig. 3(b) and (c), respectively. Both flames show an accumulation of OH in the inner shear layer, more pronounced in the LES. As noticeable in Fig. 3(a) and (b), the flame length is clearly overestimated compared to experiments, which may be partially attributed to the simplifications of the thermal boundary modeling and associated inaccuracies in the absolute wall temperature and heat distribution. Further. Nevertheless, the agreement between experiment and LES was found to be acceptable for the subsequent entropy response analysis.

4.2. Overall entropy response

In the first step, the air mass flow is excited in experiment and LES to determine from the temperature signal at the measurement position (0.28 m from the burner outlet) the overall entropy transfer function as introduced in Eq. (3). The frequency response $\mathcal{E}(\omega)$ is typically shown in gain and phase representation (Bode plot), $\mathcal{E}(\omega) = |\mathcal{E}(\omega)|e^{i\angle\mathcal{E}(\omega)}$, where $\omega \in \mathbb{R}$ is the (real-valued) angular frequency. Fig. 4 shows the
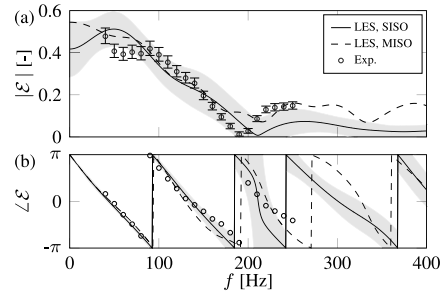

Fig. 4. (a) Gain and (b) phase of overall entropy transfer functions obtained from experiment, and SISO and MISO identification. The error bars and shaded areas represent 95% confidence intervals.

ETF estimated with a finite impulse response (FIR) filter [15,31] from time series data of upstream velocity (burner outlet) and downstream temperature fluctuations. The error bars indicate the standard deviation of $\sigma = 1.96$ (95% confidence interval according to Sovardi et al. [32]) for the measured and predicted transfer functions to account for the aleatoric uncertainty of the spectroscopic database and the coefficients of the system identification, respectively. Since system identification is a data-driven method, the confidence intervals become smaller with increasing data size (length of the time series). The predicted gain of the ETF in Fig. 4(a) shows quantitative agreement with experiment. It exhibits an overall low-pass behavior due to the convective nature of entropy waves and decays towards zero gain after a local maximum around 250 Hz. Possible reasons for the non-monotonically decaying gain are presented in [14] for a similar flame, such as hydrodynamic perturbations generated at the swirler, which might constructively or destructively interact with the equivalence ratio perturbations at the injector locations, or the existence of large coherent structures in swirling flows. As shown in Section 4.4, this characteristic feature vanishes when identifying the ETF at more upstream positions, suggesting that it is related to a mechanism caused by convective dispersion.

The predicted and measured ETF phases are shown in Fig. 4(b). The following presents a simplified argument for the low frequency-limit of a lean flame, where the flame is assumed to be the sole source of entropy generation. The low-frequency limit $\omega \to 0$ can be thought of as a change in one quantity (e.g. $\delta\dot{m}_{air}$) resulting in a new steady state of the system [33]. Since an increase in air mass flow ($\delta\dot{m}_{air}$, i.e. $\delta u > 0$) corresponds to an increased amount of air available for combustion relative to the fuel (excess air becomes more pronounced), the burnt gas temperature ($\delta T < 0$) reduces. Therefore u' and T' are out of phase and $\angle\mathcal{E}(\omega \to 0) \to \pm\pi$, which is consistent with results
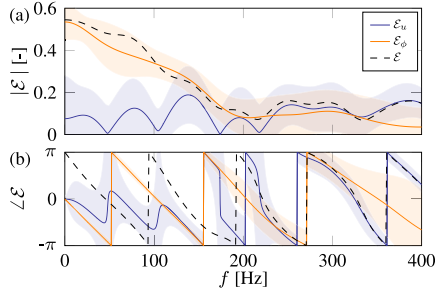
Fig. 5. (a) Gain and (b) phase of individual entropy transfer functions $\mathcal{E}_u$ and $\mathcal{E}_\phi$ from MISO identification. The shaded areas represent 95% confidence intervals. $\mathcal{E}$ is reconstructed via Eq. (5).
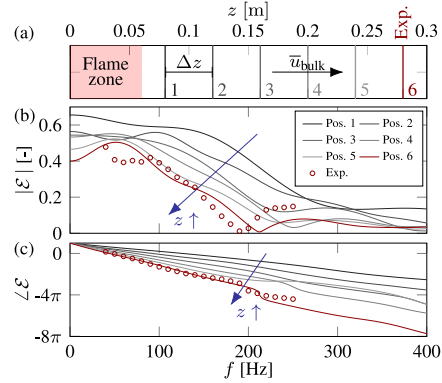

Fig. 6. (a) Sampling positions 1 to 6 in the combustion chamber. Position 6: location of the experimental measurements. (b) Gain and (c) phase of overall entropy transfer functions. Confidence intervals (not shown) are comparable to Fig. 4.

from LES/SI and experiment[2]. In addition, the slope of the phase is very well predicted, indicating accurate modeling of the bulk velocity transport in the LES. The phase of the ETF corresponds to the time delay between the acoustic perturbation at the reference position and the temperature fluctuations at the measuring point, which matches well with the expected convective time delay.

4.3. MISO identification of entropy response

In the next step, simultaneous air and fuel mass flow forcing is applied in LES using uncorrelated excitation signals for the two channels [11]. The individual entropy responses to equivalence ratio and velocity fluctuations at the burner outlet are directly obtained from multiple-input single-output (inputs: ϕ'_{ref} and u'_{ref}, output: T') identification using a FIR model structure. The overall number of model parameters (see e.g. [34] for more information on their choice and estimation), i.e. FIR coefficients, is approximately doubled in comparison to the SISO model (Section 4.2). This results in larger confidence intervals for the same time series length [27] (see [32] for more information on the uncertainty propagation), shown in Fig. 5. Eq. (5) is utilized to reconstruct the overall ETF from the individual contributions $\mathcal{E}_\phi$ and $\mathcal{E}_u$. The reconstructed ETF, additionally shown in Fig. 4 (dashed line), exhibits very similar gain and phase as the ETF obtained with SISO identification (solid line). This validates the MISO methodology and the underlying separation of excitation mechanisms. Some of the differences between the estimated entropy responses may be attributed to the comparably larger confidence intervals of the individual responses $\mathcal{E}_\phi$ and $\mathcal{E}_u$ discussed below.

The contribution from fluctuations in equivalence ratio $\mathcal{E}_\phi$ is significantly larger and dominates the overall entropy response $\mathcal{E}$ over almost the entire frequency range, particularly below 200 Hz. This finding supports the arguments found in the literature [1,2,8,26] that equivalence ratio fluctuations are the dominant mechanism for the generation of entropy waves in partially premixed flames. The contribution of entropy response due to velocity fluctuations $\mathcal{E}_u$ (see Fig. 5) exhibits a similar order of magnitude and shape as observed in our previous study on the fully premixed configuration of the same combustor (different operating point) [12]. This is reasonable, as the studied combustor involves severe wall heat losses and considerable differential diffusion due to the high volume fraction of hydrogen.

4.4. Convective transport of entropy waves

The decay of entropy waves is just as crucial as their actual excitation mechanisms discussed in the previous two subsections, as entropy waves only affect the thermoacoustic feedback cycle due to mode conversion if they are not fully attenuated during the convection through the combustor. Various relevant mechanisms associated with dispersion and dissipation are discussed in the works of Sattelmayer [2], Morgans et al. [5], Weilenmann et al. [35], Polifke [36], Kaiser and Oberleithner [37,38] and Kaiser et al. [39], whereas each burner type exhibits different behavior due to its complex flows (e.g. swirl, flow separation, central vortex core) and unique geometry. This repeatedly leads to contradictory conclusions in the literature on the importance of entropy waves in technically relevant combustors [6,35]. Consequently, the decay of entropy waves in the present turbulent swirl combustor is assessed in the following.

We record coherent temperature fluctuations to upstream air mass flow modulations at five additional monitoring planes (see positions 1 to 6 in Fig. 2(b) or Fig. 6(a)) between the reaction zone and the measurement position to identify the overall entropy responses via Eq. (3) at these locations, shown in Fig. 6. The gain exhibits a continuous decrease with increasing residence time in the combustor over the entire frequency range. Nevertheless, for low frequencies (below 100 Hz), the gain is less affected by the attenuation in the combustion chamber and remains similar to regions close to the reaction zone. The phase in Fig. 6(b) has been unwrapped to visualize the convective nature of entropy waves. The phase change along the combustor matches the predicted convective transport, which is constant for a constant bulk velocity $\bar{u}_{bulk}$ and equal delays $\Delta\tau$ between each of the six positions.

It is beyond the scope of this work to rank the strength of the entropy waves found at the combustor outlet in terms of their relevance to thermoacoustic instability, but Fig. 6 clearly emphasizes that turbulent mixing, shear dispersion and further decay mechanisms in the present combustor are not properly suppressing entropy waves.

5. Conclusion

This work employs both large eddy simulations combined with system identification (LES/SI) and laser-based experiments (TDLAS-WMS) to determine the entropy transfer function of a partially premixed flame. The predicted and measured entropy response shows remarkable agreement in both the gain and phase. Furthermore, the well predicted phase slope suggests a correct modeling of the bulk flow in LES. Subsequently, the individual contributions of entropy

---

[2] Note that the phase of the ETF in the original experimental work by Dharmaputra et al. [14] (Figs. 6 and 7) is erroneously shifted by π.

response to equivalence ratio and velocity fluctuations are analyzed utilizing multiple-input single-output identification with time series data obtained from simultaneous air and fuel mass flow forcing in LES. The fluctuations of equivalence ratio are found to be the dominant mechanisms for the generation of entropy waves even in the presence of strong water cooling with severe wall heat losses and significant differential diffusion (59% hydrogen by volume) [12], suggesting that this finding is generalizable to other configurations in premixed combustion. Furthermore, this is consistent with literature [1,2,8,26].

In addition, we numerically analyzed the convective transport of entropy waves in the generic partially premixed swirl combustor by evaluating entropy transfer functions on various planes in the combustion chamber. It is demonstrated that the attenuation is weak enough to ensure significant entropy wave strength at the combustor exit. For low-frequencies ($f < 100$ Hz), the gain of the entropy response is comparable to regions shortly downstream of the reaction zone.

To the authors' best knowledge, this is the first time that the dominance of equivalence ratio fluctuations on the generation of entropy waves has been investigated and confirmed *quantitatively* in accordance with [1,2,8,26] using MISO identification, i.e. that the individual excitation mechanisms are studied, and that the entropy transfer function of a partially premixed flame is determined numerically.

Novelty and significance statement

The novelty of this research is the determination of entropy transfer functions in a partially premixed combustor by large eddy simulation combined with system identification. Numerical findings are complemented by experimental data obtained with the Tunable Diode Laser Absorption Spectroscopy with Wavelength Modulation Spectroscopy method (TDLAS-WMS). By further separating the entropy responses to equivalence ratio and velocity fluctuations utilizing multiple-input single-output identification, the dominance of equivalence ratio fluctuations in this process is revealed. Furthermore, the evaluation of entropy transfer functions across various positions within the combustion chamber sheds light on the decay of entropy waves, revealing significant amplitudes at the combustor exit. The presented analysis yields new insights into both generation and transport of entropy waves in partially premixed combustion systems.

CRediT authorship contribution statement

Alexander J. Eder: Conceptualization, Methodology, Software, Validation, Formal analysis, Investigation, Data curation, Writing - original draft, Writing - review & editing, Visualization. **Bayu Dharmaputra:** Conceptualization, Validation, Formal analysis, Investigation, Data curation, Writing - review & editing. **Alex M. Garcia:** Conceptualization, Methodology, Software, Writing - review & editing. **Camilo F. Silva:** Conceptualization, Writing - review & editing. **Wolfgang Polifke:** Conceptualization, Validation, Writing - review & editing, Supervision, Funding acquisition.

Declaration of competing interest

The authors declare that they have no known competing financial interests or personal relationships that could have appeared to influence the work reported in this paper.

Acknowledgments

References

[1] J.J. Keller, Thermoacoustic oscillations in combustion chambers of gas turbines, AIAA J. 33 (12) (1995) 2280–2287.

[2] T. Sattelmayer, Influence of the combustor aerodynamics on combustion instabilities from equivalence ratio fluctuations, J. Eng. Gas Turbines Power 125 (1) (2003) 11–19.

[3] Y. Xia, I. Duran, A.S. Morgans, X. Han, Dispersion of entropy perturbations transporting through an industrial gas turbine combustor, Flow Turbl. Combust. 100 (2) (2018) 481–502.

[4] A.P. Dowling, Y. Mahmoudi, Combustion noise, Proc. Combust. Inst. 35 (1) (2015) 65–100.

[5] A.S. Morgans, C.S. Goh, J.A. Dahan, The dissipation and shear dispersion of entropy waves in combustor thermoacoustics, J. Fluid Mech. 733 (2013).

[6] A.S. Morgans, I. Duran, Entropy noise: A review of theory, progress and challenges, Int. J. Spray Combust. Dyn. 8 (4) (2016) 285–298.

[7] F.E. Marble, S.M. Candel, Acoustic disturbance from gas non-uniformities convected through a nozzle, J. Sound Vib. 55 (2) (1977) 225–243.

[8] W. Polifke, C.O. Paschereit, K. Döbbeling, Constructive and destructive interference of acoustic and entropy waves in a premixed combustor with a choked exit, Int. J. Acoust. Vib. 6 (3) (2001) 135–146.

[9] T.C. Lieuwen, B.T. Zinn, The role of equivalence ratio oscillations in driving combustion instabilities in low NOx gas turbines, Symp. (Int.) Combust. 27 (2) (1998) 1809–1816.

[10] B. Schuermans, V. Bellucci, F. Guethe, F. Meili, P. Flohr, O. Paschereit, A detailed analysis of thermoacoustic interaction mechanisms in a turbulent premixed flame, in: ASME Turbo Expo 2004, ASME, Vienna, Austria, 2004, 539-551.

[11] A. Huber, W. Polifke, Dynamics of practical premix flames, part I: model structure and identification, 2, Int. J. Spray Combust. Dyn. 1 (2) (2009) 199–228.

[12] A.J. Eder, B. Dharmaputra, M. Désor, C.F. Silva, A.M. Garcia, B. Schuermans, N. Noiray, W. Polifke, Generation of entropy waves by fully premixed flames in a non-adiabatic combustor with hydrogen enrichment, J. Eng. Gas Turbines Power 145 (11) (2023) 111001.

[13] K. Truffin, T. Poinsot, Comparison and extension of methods for acoustic identification of burners, Combust. Flame 142 (4) (2005) 388–400.

[14] B. Dharmaputra, S. Shcherbanev, A. Blondé, B. Schuermans, N. Noiray, Entropy transfer function measurement with tunable diode laser absorption spectroscopy, Proc. Combust. Inst. 39 (4) (2022) 4621–4630.

[15] W. Polifke, Black-box system identification for reduced order model construction, Ann. Nucl. Energy 67C (2014) 109–128.

[16] A. Blondé, B. Schuermans, K. Pandey, N. Noiray, Effect of hydrogen enrichment on transfer matrices of fully and technically premixed swirled flames, J. Eng. Gas Turbines Power 145 (12) (2023) 121009.

[17] F. Nicoud, H.B. Toda, O. Cabrit, S. Bose, J. Lee, Using singular values to build a subgrid-scale model for large eddy simulations, Phys. Fluids 23 (8) (2011) 085106.

[18] T. Poinsot, S.K. Lele, Boundary conditions for direct simulation of compressible viscous flows, J. Comput. Phys. 101 (1) (1992) 104–129.

[19] A.J. Eder, C.F. Silva, M. Haeringer, J. Kuhlmann, W. Polifke, Incompressible versus compressible large eddy simulation for the identification of premixed flame dynamics, Int. J. Spray Combust. Dyn. 15 (1) (2023) 16–32.

[20] D. Laera, P. Agostinelli, L. Selle, Q. Cazères, G. Oztarlik, T. Schuller, L. Gicquel, T. Poinsot, Stabilization mechanisms of CH4 premixed swirled flame enriched with a non-premixed hydrogen injection, Proc. Combust. Inst. 38 (4) (2021) 6355–6363.

[21] O. Colin, F. Ducros, D. Veynante, T. Poinsot, A thickenend flame model for large eddy simulation of turbulent premixed combustion, Phys. Fluids 12 (7) (2000) 1843–1863.

[22] Y.Y. Gentil, G. Daviller, S. Moreau, T. Poinsot, Combustion composition noise mechanism analysis, in: AIAA AVIATION 2023 Forum, AIAA, San Diego, CA, USA, 2023.

[23] A. Peracchio, W. Proscia, Non-linear heat-release / acoustic model for thermoacoustic instability in lean premixed combustors, J. Eng. Gas Turbines Power 121 (3) (1999) 415–421.

[24] T. Lieuwen, H. Torres, C. Johnson, B.T. Zinn, A mechanism of combustion instability in lean premixed gas turbine combustors, J. Eng. Gas Turbines Power 123 (1) (2001) 182–189.

6

[25] T. Poinsot, Prediction and control of combustion instabilities in real engines, Proc. Combust. Inst. 36 (1) (2017) 1–28.

[26] L. Strobio Chen, S. Bomberg, W. Polifke, Propagation and generation of acoustic and entropy waves across a moving flame front, Combust. Flame 166 (2016) 170–180.

[27] J. Kuhlmann, S. Marragou, I. Boxx, T. Schuller, W. Polifke, LES based prediction of technically premixed flame dynamics and comparison with perfectly premixed mode, Phys. Fluids 34 (8) (2022) 085125.

[28] A. Huber, Impact of Fuel Supply Impedance and Fuel Staging on Gas Turbine Combustion Stability (Ph.D. thesis), Technical University of Munich, Munich, Germany, 2009.

[29] B. Ćosić, S. Terhaar, J.P. Moeck, C.O. Paschereit, Response of a swirl-stabilized flame to simultaneous perturbations in equivalence ratio and velocity at high oscillation amplitudes, Combust. Flame 162 (4) (2015) 1046–1062.

[30] B. Schuermans, F. Guethe, W. Mohr, Optical transfer function measurements for technically premixed flames, J. Eng. Gas Turbines Power 132 (8) (2010) 081501.

[31] L. Ljung, System Identification: Theory for the User, second ed., Prentice Hall PTR, Upper Saddle River, NJ, USA, 1999.

[32] C. Sovardi, S. Jaensch, W. Polifke, Concurrent identification of aero-acoustic scattering and noise sources at a flow duct singularity in low mach number flow, J. Sound Vib. 377 (2016) 90–105.

[33] W. Polifke, C.J. Lawn, On the low-frequency limit of flame transfer functions, 3, Combust. Flame 151 (3) (2007) 437–451.

[34] S. Jaensch, M. Merk, T. Emmert, W. Polifke, Identification of flame transfer functions in the presence of intrinsic thermoacoustic feedback and noise, Combust. Theory Model. 22 (3) (2018) 613–634.

[35] M. Weilenmann, Y. Xiong, N. Noiray, On the dispersion of entropy waves in turbulent flows, J. Fluid Mech. 903 (2020) R1.

[36] W. Polifke, Modeling and analysis of premixed flame dynamics by means of distributed time delays, Prog. Energy Combust. Sci. 79 (2020) 100845.

[37] T.L. Kaiser, K. Oberleithner, Modeling the transport of fuel mixture perturbations and entropy waves in the linearized framework, J. Eng. Gas Turbines Power 143 (11) (2021) 111001.

[38] T.L. Kaiser, K. Oberleithner, A global linearized framework for modelling shear dispersion and turbulent diffusion of passive scalar fluctuations, J. Fluid Mech. 915 (2021) A111.

[39] T.L. Kaiser, N. Noiray, Q. Male, K. Oberleithner, Modeling the convection of entropy waves in strongly non-parallel turbulent flows, in: ASME Turbo Expo 2022, ASME, Rotterdam, Netherlands, 2022, V03BT04A039.

7

Alexander J. Eder[1]
TUM School of Engineering and Design,
Technical University of Munich,
Garching D-85748, Germany
e-mail: alexander.eder@tum.de

Bayu Dharmaputra
CAPS Laboratory,
Department of Mechanical and
Process Engineering,
ETH Zurich,
Zurich CH-8092, Switzerland

Marcel Désor
TUM School of Engineering and Design,
Technical University of Munich,
Garching D-85748, Germany

Camilo F. Silva
TUM School of Engineering and Design,
Technical University of Munich,
Garching D-85748, Germany

Alex M. Garcia
Siemens Digital Industries Software,
Leuven BE-3001, Belgium

Bruno Schuermans
CAPS Laboratory,
Department of Mechanical and
Process Engineering,
ETH Zurich,
Zurich CH-8092, Switzerland

Nicolas Noiray
CAPS Laboratory,
Department of Mechanical and
Process Engineering,
ETH Zurich,
Zurich CH-8092, Switzerland

Wolfgang Polifke
TUM School of Engineering and Design,
Technical University of Munich,
Garching D-85748, Germany

Generation of Entropy Waves by Fully Premixed Flames in a Non-Adiabatic Combustor With Hydrogen Enrichment

Thermoacoustic combustion instability is a major concern in gas turbine combustors with hydrogen-enriched fuels. Unsteady combustion not only generates acoustic waves but it may also result in fluctuations of burnt gas temperature, referred to as entropy waves. They are convected by the mean flow through the combustor and can cause indirect combustion noise when they are accelerated at the exit. In this work, we demonstrate that entropy waves occur in a fully premixed burner due to unsteady heat transfer at the combustion chamber wall. This mechanism of entropy generation is often neglected in the literature. This work shows an additional mechanism in CH_4-H_2-air flames, through which entropy may be created even in the fully premixed case. This is due to differential diffusion which generates local fluctuations in equivalence and carbon-to-hydrogen ratios. An adiabatic flame temperature is defined based on these two quantities to examine the influence of differential diffusion on the generation of entropy fluctuations. The generation of entropy waves is investigated by applying system identification (SI) to time series data obtained from a broadband forced large eddy simulation (LES) coupled with a heat conduction solver. The entropy transfer function (ETF) and flame transfer function (FTF) identified with LES/SI are then compared to experimental data obtained with tunable diode laser absorption spectroscopy with wavelength modulation spectroscopy (TDLAS-WMS) for measuring temperature fluctuations, and the multimicrophone method, respectively. After validating the computational setup, the entropy frequency response is identified at various positions within the combustion chamber, and the effects of generation and convective dispersion of entropy waves are qualitatively investigated. We show that a fully premixed turbulent system may exhibit significant entropy waves caused by wall heat losses and differential diffusion of hydrogen.
[DOI: 10.1115/1.4063283]

1 Introduction

Advanced gas turbines are operated with hydrogen-enriched fuels at lean-premixed conditions to reduce NOx and CO_2 emissions. These combustion systems are prone to self-excited thermoacoustic instabilities, which arise from the feedback between the combustion process and the combustor acoustics [1–3]. The mean flow of hot gases in such combustion chambers may contain regions of temperature inhomogeneities, often referred to as "hot spots" or "entropy waves." In gas turbine combustors, such entropy waves are accelerated at the entry of the high-pressure turbine and thereby generate acoustic disturbances, which propagate away from the sound source. The upstream traveling acoustic waves may then couple with the unsteady heat release of the flame and cause self-excited thermoacoustic instability, particularly at low frequencies ("rumble") [4,5]. The so-called "indirect combustion noise" significantly contributes to the overall engine noise and should be suppressed [6]. The pioneering work of Marble and Candel [7]

analyzed the generation of sound through the aforementioned conversion from entropy to acoustic waves. That work was followed by numerous studies aimed at improving the theoretical models [8], and providing experimental data for validation, e.g., Weilenmann and Noiray [9].

Many studies on entropy waves and indirect noise directly relate the generation of entropy fluctuations s' to those of the global heat release rate (HRR) $\dot{Q}'$ [10–12]. However, Chen et al. [13–15] have clarified the interdependence between $\dot{Q}'$ and s' and demonstrated that this simple relation may lead to invalid results. Dowling [16] was the first to consider the heat release rate per unit mass rather than unit volume, which is crucial for a correct prediction of entropy wave generation. Keller [17] argued in an early work that equivalence ratio fluctuations are the dominant mechanism for the generation of temperature inhomogeneities in technically premixed flames. As a result, entropy waves are predominantly associated with technically premixed systems, which exhibit fluctuations in heat release rate per mass of the premixture due to strong equivalence ratio fluctuations [13,18–21], assuming "complete combustion without heat loss" [13]. Poinsot [2] emphasized other sources of entropy fluctuations, such as dilution jets and heat losses due to convective or radiative heat transfer. Note that heat losses are most often neglected or considered a lower-order term [22]. Christodoulou et al. [23] and Rodrigues et al. [24] have addressed the influence of wall heat losses on the propagation of entropy waves in turbulent nonreactive flows.

This paper deals with fully premixed flames in a non-adiabatic combustor with a CH_4-H_2 fuel blend. We identify and analyze two mechanisms that generate entropy fluctuations, namely,

(1) wall heat losses due to unsteady heat transfer and
(2) local variations in equivalence ratio ϕ' and local segregation of fuel components X'_{H_2} due to differential diffusion.

In fully premixed CH_4-H_2-air flames, these local changes occur along the flame front. Consequently, entropy fluctuations due to differential diffusion—a mechanism examined in this study for the first time—are produced, as illustrated in Fig. 1. Temperature inhomogeneities are then convected downstream until reaching the nozzle exit, attenuated by dispersion due to turbulent mixing and spatial variations in the velocity field [19,25]. The latter is often referred to as "shear dispersion," a term coined by Morgans et al. [25,26]. The convective dispersion rate highly depends on the flow details inside the combustor [2,19] as well as the large-scale turbulent structures which disperse temperature inhomogeneities [27]. In short combustion chambers (as in aero-engines), entropy waves are more likely non-negligible when reaching the turbine stage. In addition, as some walls of the test rig considered in this work are water-cooled, the influence of heat losses on entropy wave production is expected to be relevant. Experimental work on entropy waves in (fully and technically) premixed combustion (see Refs. [28–31]) is sparse because measuring exhaust gas temperature with sufficiently fine temporal resolution is difficult [32]. Recently, Dharmaputra et al. [33] introduced tunable diode laser absorption spectroscopy with wavelength modulation spectroscopy (TDLAS-WMS) for entropy wave measurements, a technique that produces
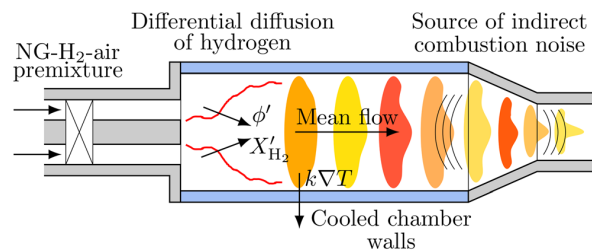
compact data sizes even for measurement rates in the order of kilohertz and megahertz. TDLAS-WMS was used to measure the entropy transfer function (ETF) of a fully premixed burner fueled with CH_4-H_2 in this work.

This work aims to analyze entropy wave generation and the associated frequency response over a wide frequency range. Fundamental concepts of the entropy transfer function are described in Sec. 2. The experimental setup of the premixed burner is presented in Sec. 3. Since an accurate prediction of wall heat losses is desired in this work, a flow solver is coupled with a conjugate heat transfer (CHT) code to account for heat conduction in solid materials. The second mechanism identified for entropy generation in hydrogen-enriched combustion is differential diffusion. Hence, the large eddy simulation (LES) solver is extended by a simplified diffusion model based on constant Lewis numbers of each species, see Sec. 4. The generation of entropy waves is scrutinized in Sec. 5. For this purpose, the predicted flame heat release rate is first compared with OH* chemiluminescence images from the experiment and the results of the CHT simulation are illustrated. The entropy response estimated with methods from system identification (SI) is compared with the experimental one. Furthermore, the ETF is identified at various positions in the combustor to investigate the convective dispersion of entropy waves. Finally, the main results are summarized and a brief outlook is given.

2 Entropy and Flame Response in Premixed Combustion

For an ideal gas mixture with small fluctuations $(\cdot)'$ around its temporal mean value $\overline{(\cdot)}$, the fluctuations in sensible-plus-chemical entropy s, density ρ, temperature T, and pressure p are related as follows:

$$\frac{s'}{\bar{c}_p} = \frac{1}{\gamma}\frac{p'}{\bar{p}} - \frac{\rho'}{\bar{\rho}} \approx \frac{T'}{\bar{T}} - \frac{\gamma-1}{\gamma}\frac{p'}{\bar{p}} \qquad (1)$$

where the linearized expression for the ideal gas law $\rho'/\bar{\rho} = p'/\bar{p} - T'/\bar{T}$ is used and compositional inhomogeneities in the Gibbs equation are neglected [34]. Equation (1) can be locally applied at any point in the domain. In the absence of large amplitude acoustic fluctuations and for low Mach number flow, temperature fluctuations dominate [18,35,36]. This simplifies the right-hand side of Eq. (1) to

$$\frac{s'}{\bar{c}_p} \approx \frac{T'}{\bar{T}} \qquad (2)$$

With this simplification, the entropy response (extracted either as an area average, line integral, or local scalar value) to upstream velocity perturbations u'_{ref} at a reference position, known as ETF, can be defined as

$$\mathcal{E}(\omega) \equiv \frac{T'(\omega)/\bar{T}}{u'_{\text{ref}}(\omega)/\bar{u}_{\text{ref}}} \qquad (3)$$

where temperature fluctuations downstream of the flame are considered coherent [33,37]. The ETF can be measured at various locations along the combustion chamber to investigate the convective dispersion of entropy waves generated at both the flame (differential diffusion) and the combustor walls (heat losses).

Since any real combustor has nonadiabatic walls to a greater or lesser extent [38], it suffers from heat losses due to convective heat transfer between the hot gases and the cooled combustion chamber walls. An unsteady flow may cause unsteady heat transfer, resulting in entropy waves generated by fluctuating heat losses per unit mass of products. Additionally, hydrogen-enriched flames may produce temperature fluctuation associated with local variations of the CH_4-H_2-air mixture due to the differential diffusion of species. It may be challenging to distinguish these two sources of entropy generation

Fig. 1 Sources of entropy fluctuations ($k\nabla T$, ϕ', and X'_{H_2}) and indirect combustion noise in a fully premixed combustor with nozzle exit. The pockets represent entropy fluctuations.

from the temperature measurements T' in experiments. In numerical investigations, one option to suppress the effect of differential diffusion is to use an equal Lewis number for all species while keeping the same mixture Prandtl number and the same laminar flame speed. However, since this approach requires one additional simulation and manipulates the underlying physics, an alternative is proposed in this work. The entropy waves produced by differential diffusion are related to the local variations of the flame temperature due to changes in species concentration. This temperature can be linked to the adiabatic flame temperature T_{ad}, which is equal to the burnt gas temperature in an adiabatic combustor. Therefore, an additional entropy transfer function that only considers differential diffusion can be defined based on T_{ad} as follows:

$$\mathcal{E}_{ad}(\omega) \equiv \frac{T'_{ad}(\omega)/\overline{T}_{ad}}{u'_{ref}(\omega)/\overline{u}_{ref}} \tag{4}$$

The adiabatic flame temperature is dependent on the local CH_4-H_2-air mixture, which is characterized in this work by the equivalence ratio ϕ and the carbon-to-hydrogen ratio ζ. The equivalence ratio, which captures changes in the fuel–air mixture, is calculated in this work as follows [39]:

$$\phi \equiv \frac{\sum_i (2n_{C,i} + 0.5n_{H,i})X_i}{\sum_i n_{O,i}X_i} \tag{5}$$

where $n_{C,i}$, $n_{H,i}$, and $n_{O,i}$ are the numbers of carbon, hydrogen, and oxygen atoms, respectively, and X_i is the volume fraction of species i. This definition takes into account differential diffusion and is equivalent to a definition based on Bilger's mixture fraction [40]. The carbon-to-hydrogen ratio captures changes in the CH_4-H_2 mixture due to differential diffusion and is introduced as follows:

$$\zeta \equiv \frac{\sum_i n_{C,i}X_i}{\sum_i n_{H,i}X_i} \tag{6}$$

In Sec. 5, both $\mathcal{E}$ and $\mathcal{E}_{ad}$ are estimated using methods from system identification. The difference between the two enables an evaluation of the impact of wall heat losses on the entropy response, expressed as $\mathcal{E}_{\dot{q}_w}(\omega) = \mathcal{E}(\omega) - \mathcal{E}_{ad}(\omega)$. This effect is the dominant one in the present combustion chamber, resulting in $\mathcal{E}(\omega) \approx \mathcal{E}_{\dot{q}_w}(\omega)$.

In addition to estimating the entropy response to velocity modulations, the flame transfer function (FTF) is identified as

$$\mathcal{F}(\omega) \equiv \frac{\dot{Q}'(\omega)/\overline{\dot{Q}}}{u'_{ref}(\omega)/\overline{u}_{ref}} \tag{7}$$

where $\dot{Q}$ is the volume-integrated heat release rate.

3 Experimental Setup

The schematic of the experimental setup is shown in Fig. 2 and consists of a plenum section ($l_{plenum} = 0.40$ m), a burner ($l_{burner} = 0.10$ m) with an axial swirler and a bluff body for flame anchoring, and a combustion chamber ($l_{chamber} = 0.75$ m) with a square section of 62×62 mm^2 that comprises three modules of the same type as for the plenum. Some of these modules feature air-cooled quartz windows, and others are water-cooled aluminum walls. Two loudspeakers are mounted on the walls of the most upstream and downstream modules. Fourteen flush-mounted water-cooled GRAS microphones are employed to reconstruct the acoustic pressure and particle velocity upstream and downstream of the burner using the multi-microphone method. By using upstream and downstream excitation through loudspeakers and reconstructing the acoustic variables, the flame transfer function is obtained as part of a
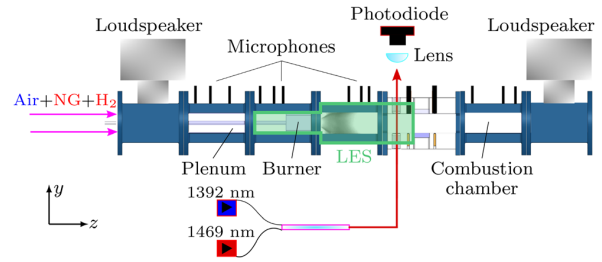

Fig. 2 Schematic of the experimental setup for ETF and FTF measurements of the fully premixed turbulent flame. The computational domain is shown in a frame.

flame transfer matrix [41]. Note that only the upstream loudspeaker is actuated and only the upstream acoustic variables are reconstructed for the measurement of the entropy transfer function. The combustor outlet is equipped with an adjustable orifice to ensure thermoacoustically stable conditions. The optical access for the laser beam, denoted as TDLAS-LOS (line-of-sight), is enabled through two wedged windows mounted on the sidewalls located around 28 cm downstream of the burner outlet, as shown in Fig. 2.

Regarding the TDLAS setup, two lasers (DFB-NEL) centered at around 1392 nm and 1469 nm are employed to probe the absorption transition of water vapor at 7185.59 cm^{-1} and 6806.03 cm^{-1}, respectively. The lasers are powered by two identical laser diode controllers (LDC-501). The scanning frequency for both lasers are set to 5 kHz, and the modulation frequencies are 150 kHz and 200 kHz for the laser centered at 1392 nm and 1469 nm, respectively. The two beams from both lasers are combined with a fiber combiner and guided through an optical fiber to the TDLAS port. After the beam passes the hot gas section, it is detected by a photodiode. Following the method presented in Ref. [33], the raw signals from the photodiode are converted into temperature signals. The ETF is obtained by taking the ratio of the temperature signals to the acoustic velocity upstream of the burner. A more detailed description of the experimental setup can be found in Ref. [33].

4 Computational Setup

The large eddy simulation is performed using the finite volume based OpenFOAM 10 library [42] solving the reactive Navier–Stokes equations. A previously developed reactive flow solver [43] based on reactingFoam is coupled with the conjugate heat transfer solver chtMultiRegionFoam to account for unsteady heat transfer at combustor walls. A low Mach number formulation is used to decouple acoustics and flame response, thereby suppressing self-excited instabilities or resonances in the system [44]. For time integration, a fully implicit, second-order accurate Euler scheme is used, and the velocity–pressure coupling is solved with the PISO-consistent algorithm (four inner iterations). The time-step in the fluid domain is $\Delta t = 7 \times 10^{-7}$ s and assures a Courant–Friedrich–Lewis number below 0.3 in the flame region. The computational domain, shown in Fig. 3, is discretized with 18×10^6 hexahedral elements and is refined in the swirler and flame region, with a typical cell size of about $250\,\mu m$ (laminar flame thickness of about $267\,\mu m$). Additional wall layers ensure an almost unity $\overline{y}^+$ value at the tip of the bluff body ($\overline{y}^+ < 1$), backplane ($\overline{y}^+ < 2$), and the chamber walls ($\overline{y}^+ < 1$), to correctly resolve the temperature boundary layers. Velocity inlet and total pressure outlet boundary conditions are used, and all walls are treated as no-slip. The effects of small-scale fluid motions are modeled with the WALE [45] subgrid scale model in a wall-resolved manner.

4.1 Combustion Model. An extension of the thickened flame model (TFLES) [46,47] with a local sensor $S(\phi)$ [48] and the Charlette efficiency function [49] is applied to account for turbulence–chemistry interaction. The flame front is resolved with
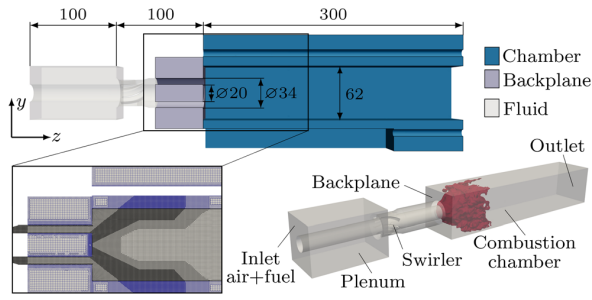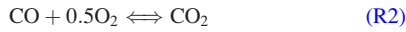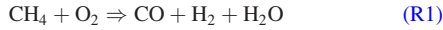
Fig. 3 Computational domain used in CHT-LES with a detailed view of the computational grid of fluid and solid region. Dimensions are given in millimeters.

$n = 12$ points, corresponding to a maximum thickening factor $F_{max} \approx 11$ [49]

$$F = 1 + \left(n \frac{\Delta_{LES}}{\delta_l^0(\phi)} - 1 \right) S(\phi) \qquad (8)$$

where δ_l^0 is the laminar flame thickness defined from the temperature profile gradient [47]. The flame sensor and thickness depend on the local equivalence ratio to capture the effects of differential diffusion. Future studies should also consider local segregation (variation in X_{H_2}) and preheating due to conjugate heat transfer [50].

4.2 Chemical Kinetics. A global chemical kinetics mechanism was calibrated for $\phi = 0.9$ and $X_{H_2} = 0.31$ based on target reaction progress rates computed from a one-dimensional freely propagating flame using the detailed kinetic mechanism UC San Diego [51] (UC-SD; 57 species and 268 reactions) as described by Garcia et al. [52]. The calibrated parameters are shown in Table 1 and the following three reactions are utilized in the simulation:

$$CH_4 + O_2 \Rightarrow CO + H_2 + H_2O \qquad (R1)$$

$$CO + 0.5O_2 \Longleftrightarrow CO_2 \qquad (R2)$$

$$H_2 + 0.5O_2 \Rightarrow H_2O \qquad (R3)$$

The local equivalence ratio fluctuations in the LES caused by differential diffusion are captured well by the global mechanism, which satisfactorily reproduces laminar flame speed, thermal flame thickness, and adiabatic flame temperature for a wide range around the operating condition $\phi = 0.9$, as shown in Fig. 4. Note that multicomponent diffusion was used in the Cantera simulations, hence the small deviations between Cantera and OpenFOAM. For larger variations in the equivalence ratio, especially in technically premixed systems, a mechanism with rate coefficients that vary with ϕ will be used in future studies. The reaction equations contain seven species, which lead to the following definition of equivalence and carbon-to-hydrogen ratios introduced in Eqs. (5) and (6), respectively,

$$\phi = \frac{2X_{CO_2} + 2X_{CO} + X_{H_2O} + 4X_{CH_4} + X_{H_2}}{2X_{CO_2} + 2X_{O_2} + X_{CO} + X_{H_2O}} \qquad (9)$$

Table 1 Global kinetic mechanism calibrated for CH_4-H_2-air flame ($\phi = 0.9$, $X_{H_2} = 0.31$). Units: J, K, kmol, s.

	A	b	T_a	ν'_{CH_4}	ν'_{H_2}	ν'_{O_2}
(R1)	4.53×10^7	0.66	13,160	0.65	—	0.18
(R2)	2.11×10^7	0.23	9257	—	—	—
(R3)	1.02×10^8	0.76	10,256	—	1.55	0.10
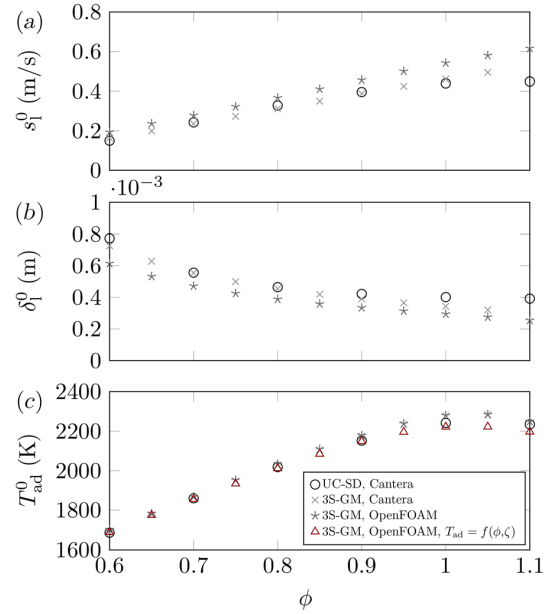
Fig. 4 Variation of: (a) laminar flame speed s_l^0, (b) laminar flame thickness δ_l^0, and (c) adiabatic flame temperature T_{ad}^0 with equivalence ratio ϕ. $X_{H_2} = 0.31$.

and

$$\zeta = \frac{X_{CO_2} + X_{CO} + X_{CH_4}}{2X_{H_2O} + 4X_{CH_4} + 2X_{H_2}} \qquad (10)$$

The adiabatic flame temperature T_{ad} is computed for various CH_4-H_2-air mixtures using Cantera. It is determined as the equilibrium temperature at constant enthalpy and pressure. A fifth-order polynomial function was then fitted as a function of ϕ and ζ to obtain $T_{ad} = f(\phi, \zeta)$ (see Fig. 5) for on-the-fly calculation in the LES. Note that with this approach, T_{ad} is not a scalar diffused and advected with the flow, but a quantity associated with the local mixture composition. Therefore, the diffusion and advection of T_{ad} results from the species transport instead of the heat transport.

4.3 Diffusion Model. The reactive solver was extended by a mixture-averaged based diffusion model for Fick's law with constant Lewis numbers Le_i for each species i, see Table 2 (note the difference between H_2 and CH_4), and a mixture Prandtl number
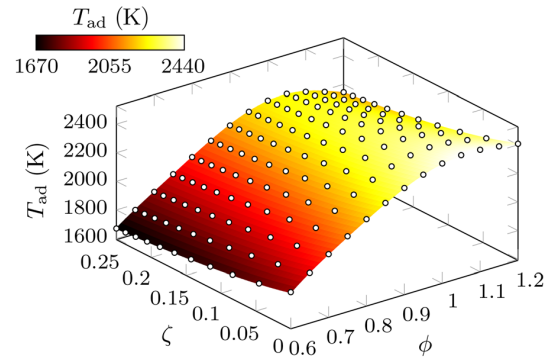
Fig. 5 Polynomial surface of chemical equilibrium data of adiabatic flame temperature from Cantera calculations (○)

118

Table 2 Constant Lewis number for each species used in the transport model

H_2	H_2O	N_2	CH_4	CO	O_2	CO_2
0.308	0.878	1.000	1.014	1.128	1.134	1.417

$Pr = 0.678$. The diffusion model is adapted to the TFLES model as discussed by Agostinelli [50] and enthalpy transport by species diffusion is considered. To enforce mass conservation $\sum_i Y_i = 1$ [53], nitrogen is used as a buffer species. The diffusion flux in the species conservation equation is modeled as

$$\mathbf{j}_i = -\frac{1}{Le_i}\frac{k}{c_p}\nabla Y_i \qquad (11)$$

where k is the thermal conductivity, c_p is the isobaric heat capacity, and ∇Y_i is the mass fraction gradient of species i.

4.4 Thermal Boundary Condition. Since no temperature measurements are available and adiabatic or Dirichlet temperature boundary conditions seem to be inappropriate for correctly resolving temperature inhomogeneities (which is the base for a correct prediction of entropy response), the LES solver is coupled with a conjugate heat transfer code to solve for heat conduction in solid materials. This is done using the time-dependent energy equation with Fourier's law. Since typical time scales in solid materials are much larger than in fluids, an approach similar to the ones proposed by Konle et al. [54] and Agostinelli et al. [55] is adopted for the heating phase of the solids. The solid time-step Δt_{solid} (used to integrate the heat conduction equation in time) is increased by a factor of 50×10^3 (10^3 is used in Ref. [55]) to accelerate the heating process, and at the same time, allow the fluid flow to react to the temperature changes. After the solid has reached thermal equilibrium (about 40 ms in fluid time, corresponding to about 30 min in solid time), the fluid and solid time steps are synchronized. The computational domain used in CHT-LES is shown in Fig. 3. It is discretized with 11×10^6 hexahedral elements for the solids. Note that only the first 30 cm of the combustion chamber are modeled in the LES, as the remaining sections do not influence entropy and flame response to upstream velocity perturbation.

The bluff body and backplane are modeled with the same material as in the rig, which is heat-resistant steel. The chamber walls are modeled as a material with increased thermal conductivity compared to the experiment. The objective is to consider the effect of radiative heat transfer, i.e., increased wall heat flux due to high adiabatic flame temperatures of hydrogen in a very simplified manner without using a computationally expensive radiation model as in Ref. [54]. The thermal properties of the chamber walls have been determined through heuristic analysis and adjusted to ensure decent agreement with experimental results in terms of flame shape and dynamics. Based on that agreement, the LES results are used to analyze and quantify the mechanisms of entropy wave generation in Sec. 5. The outer heat transfer coefficient of the actively air-cooled chamber walls is estimated as $h_{force} = 16$ W/m^{2}K by a Nusselt correlation for forced convection, whereby additionally the emissivity $\epsilon = 0.7$ for thermal radiation to the atmosphere is taken into account by the Stefan-Boltzmann law. The outer surfaces of the backplane body are assumed to experience natural convection, yielding an estimated outer heat transfer coefficient of $h_{nat} = 15$ W/m^{2}K. The specific heat at constant volume c_v and the thermal conductivity k depend on local temperature variations.

After the heating process of the solid materials described above and after reaching a statistically converged solution of the fluid, the entropy and flame responses to upstream velocity perturbation are identified with the well-established LES/SI approach [56], where LES is combined with methods from system identification. In the simulation, the velocity at the upstream boundary is modulated with an excitation signal, which is comparable to the acoustic excitation of the mass flow by loudspeakers in the experiment. To estimate the ETF and FTF over a wide frequency range, a frequency-limited (≈ 700 Hz) Daubechies wavelets-based signal [57] with constant power spectrum up the cutoff frequency $f_{cut} \approx 500$ Hz and a maximum amplitude of 10% of $\bar{u}_{inlet}$ is used to avoid nonlinear flame response and at the same time ensure high signal-to-noise ratio.

5 Results and Discussion

A fully premixed burner with a constant thermal power of 51 kW is analyzed. The burner is operated at constant fuel composition and the CH_4-H_2 fuel blend has a volumetric concentration of $X_{H_2} = 0.31$, which corresponds to $Y_{H_2} = 0.056$ by mass. Hydrogen was introduced to assure thermoacoustic stability in the experimental rig. The fuel–air mixture exhibits a constant equivalence ratio $\phi = 0.9$, resulting from the mass fluxes $\dot{m}_{CH_4} = 0.9$ g/s, $\dot{m}_{H_2} = 0.05$ g/s, and $\dot{m}_{air} = 19$ g/s. This leads to a mean velocity $\bar{u}_z = 5.124$ m/s at the inlet of the computational domain, shown in Fig. 3.

5.1 Mean Flame Shape. The time-averaged LOS OH* chemiluminescence image from the experiment is compared with the predicted LOS field of the time-averaged heat release rate $\left\langle \overline{\dot{Q}} \right\rangle$ in Figs. 6(a) and 6(b). This comparison is valid since OH* light intensity is proportional to the heat release rate in fully premixed flames [58]. However, it is worth noting that in the case of CH$_4$-H$_2$ mixtures, the local variations of the equivalent ratio could reach the levels seen in technically premixed flames, where OH* light intensity reacts stronger to ϕ' than to u' [59]. Therefore, further studies on the validity of the correlation between OH* light intensity and HRR for fully premixed flames with high local equivalence ratio variations (H$_2$-enriched flames) need to be done.

Both experiment and LES show a pure V-shape with no OH* concentration and HRR present in the outer recirculation zone, respectively. The slight asymmetry due to the different material thicknesses at the top and bottom side of the combustion chamber is noticeable. Both flames are lifted from the bluff body. The angle between the flame base and wall impingement is well recovered, whereas the area of maximum intensity is more blurred in the LES. The latter might be related to inaccuracies in the correlation between OH* and HRR in the present case. For a quantitative comparison of flame height and position of maximum intensity, the one-
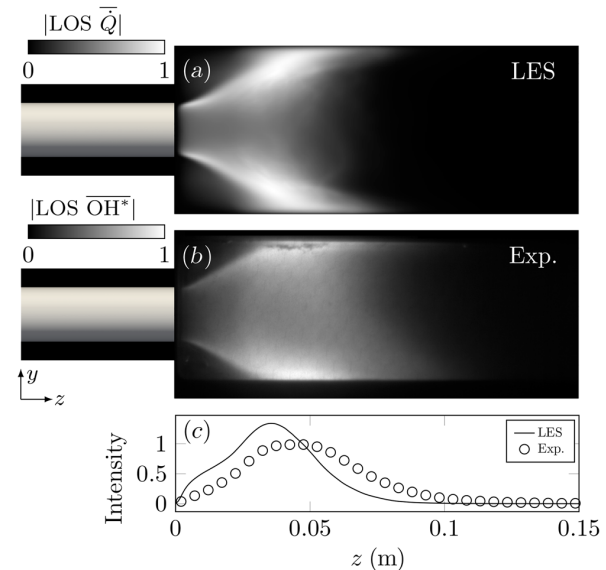

Fig. 6 LOS integration of: (a) time-averaged HRR from LES and (b) measured time-averaged OH* chemiluminescence. Corresponding (c) normalized axial distributions.

dimensional axial distribution of OH* and HRR intensities is obtained from another LOS integration $(1/l_y) \int \langle \overrightarrow{\dot{Q}} \rangle (y, z) \, dy$ across the width of the combustion chamber l_y, shown in Fig. 6(c) normalized with the area under the experimental curve. The flame length is underestimated by the LES, which may result from the simplifications of the chamber material (reduced thermal conductivity to heuristically consider thermal radiation) in the CHT simulation and associated inaccuracies in the absolute wall temperature and heat distribution.

5.2 Differential Diffusion of Hydrogen. Instantaneous and the time-averaged mass fraction fields of methane Y_{CH_4} and hydrogen Y_{H_2} are shown in Figs. 7(a) and 7(b). The hydrogen fields are significantly more blurred across the flame front than the methane fields, which is a manifestation of the differential diffusion of hydrogen. This effect occurs when the molecular transport of the mixture species is unequal [60]. Table 2 shows that the Lewis number of hydrogen ($Le_{H_2} \approx 0.3$) is significantly different than that of the remaining species (e.g., $Le_{CH_4} \approx 1$). Figure 7(c) shows the characteristic profiles of methane and hydrogen mass fraction along a flamelet (local coordinate ξ) on the mean turbulent flame brush. Hydrogen diffuses faster into the flame than methane, resulting in a faster reaction of hydrogen. After the maximum heat release rate hydrogen continues burning longer, because hydrogen is produced by the methane oxidation [61] (see reaction R1) in the present turbulent flame.

The differential diffusion of hydrogen causes local changes in the fuel–air mixture (equivalence ratio ϕ in Eq. (9)) and the fuel composition, described in this work with the carbon-to-hydrogen ratio ζ in Eq. (10). The instantaneous and time-averaged equivalence ratio fields are shown in Fig. 8(a) overlaid with an instantaneous and time-averaged isocontour of the heat release rate at 20% of its maximum value, respectively. This specific isocontour is used to cut off the primary reaction zone from the CO-CO$_2$ equilibrium (see reversible reaction R2) which blurs the heat release distribution in the burnt gas region and to account for all relevant flame features (i.e., tip, root, wrinkling). The local equivalence ratio is constant in front of the flame, equal to the global equivalence ratio
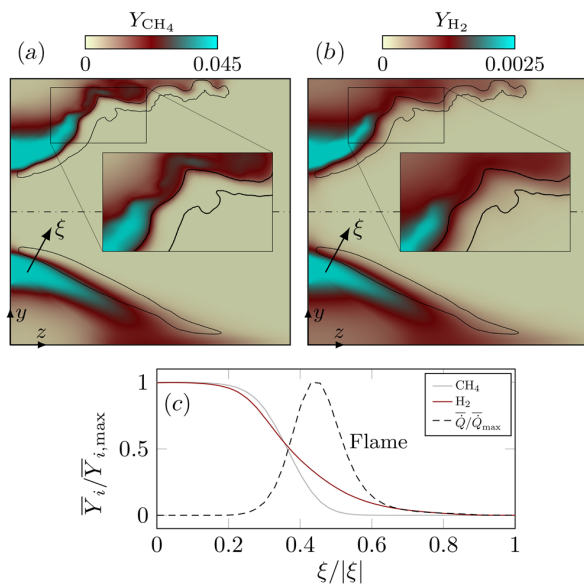

Fig. 7 Instantaneous (upper half) and time-averaged (lower half) mass fractions of: (*a*) methane and (*b*) hydrogen with isocontour of heat release rate at 20% of maximum value. (*c*) Characteristic profiles along the ξ axis.
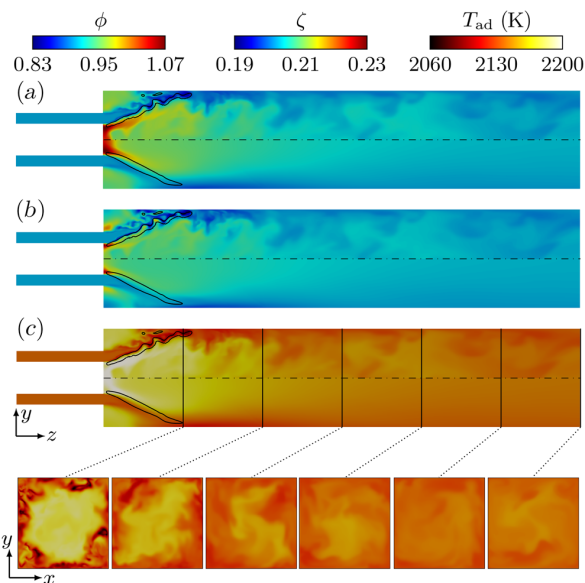
Fig. 8 Instantaneous (upper half) and time-averaged (lower half) contours of: (*a*) equivalence ratio, (*b*) carbon-to-hydrogen ratio, and (*c*) adiabatic temperature with slices at various axial positions. Isocontour (black) of instantaneous and time-averaged heat release rates at 20% of maximum value.

($\phi^{global} = 0.9$). The equivalence ratio decreases in front of the flame front as the Lewis number of the fuel is lower than that of oxygen. This locally leaner mixture is convected downstream along the flame toward the flame tip by the swirling turbulent flow. The latter produces a rise in the local equivalence ratio after the flame front, which is reinforced by the flow field in the inner recirculation zone (IRZ). It increases to its maximum values ($\phi_{max}^{local} < 1.1$) behind the IRZ at the tip of the bluff body. Along the flame front to the tip, the local equivalence ratio reaches minimum values of $\phi_{min}^{local} > 0.8$. This interplay between species diffusion and convection mechanisms is referred to as convection–diffusion interaction. Toward the combustor exit, the equivalence ratio recovers its global value. The instantaneous and time-averaged carbon-to-hydrogen ratio ($\zeta^{global} = 0.204$) field (see Fig. 8(b)) exhibit similar characteristics, but differ in local magnitude. The increase of hydrogen atoms (i.e., decrease in ζ) on the reactants side of the flame front along the whole flame brush (see blue region in the instantaneous field) may seem counterintuitive when considering the enhanced diffusion and faster reaction of H$_2$ mentioned above. However, two diffusive effects compete with each other, namely, the diffusion of hydrogen from the reactants (fresh gas) into the flame and the diffusion of hydrogen from the reaction zone (intermediate product from methane oxidation reaction R1) in both the upstream and downstream direction [61]. For a pure methane-air flame, only the latter effect would be present. In a CH$_4$-H$_2$-air flame, the hydrogen concentration in the fuel determines which of the two mechanisms dominates. Given the comparatively low volume fraction of hydrogen $X_{H_2} = 0.31$ in the present flame, the diffusion of hydrogen from the reaction zone predominates, hence the carbon-to-hydrogen ratio decreases upstream of the flame and increases inside of the reaction zone. With increasing hydrogen concentration, a reversal of the dominant mechanism would be expected. The same convection–diffusion interaction described for the equivalence ratio takes place for the carbon-to-hydrogen ratio, resulting in a lower ζ region at the flame tip and a higher ζ region at the IRZ. The change in the air–fuel mixture (i.e., equivalence ratio) and local segregation (i.e., carbon-to-hydrogen ratio) are correlated and mutually dependent, which is also confirmed by the similar flow patterns in both fields. However,
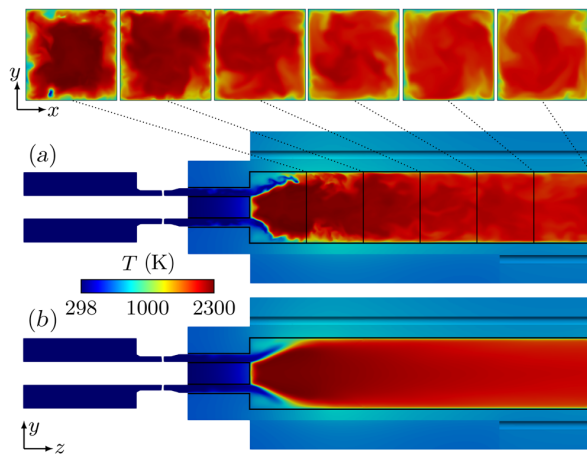
Fig. 9 (*a*) **Instantaneous field of temperature with slices at various axial positions and** (*b*) **time-averaged field of temperature. Black line as separator between fluid and solid domains.**

the relation is not trivial, as $\phi = f(\zeta, X_i)$ cannot be obtained by a linear mapping.

5.3 Adiabatic Flame Temperature. The adiabatic flame temperature (Fig. 8(*c*)) was calculated on-the-fly from local ϕ and ζ values using the dataset shown in Fig. 5. Variations in species concentration (ϕ and ζ) result in varying local adiabatic flame temperatures along the combustor. In the lean zone, the adiabatic temperature rises with an increase in the equivalence ratio, but decreases with an increase in the carbon-to-hydrogen ratio, leading to a competition between ϕ and ζ on the adiabatic flame temperature for the hydrogen concentration evaluated in this work. The adiabatic flame temperature is higher at the IRZ and lower at the flame tip, revealing a predominant effect of the equivalence ratio. Temperature inhomogeneities are produced by the interaction of cold and hot burnt gases, which are then convected by the mean flow through the combustor. Turbulent mixing and shear dispersion lead to a decay of the entropy waves caused by differential diffusion (i.e., "adiabatic" entropy waves) toward the end of the combustor, as shown with adiabatic temperatures slices at various positions in Fig. 8(*c*).

5.4 Temperature Inhomogeneities. The instantaneous fields of solid and fluid temperature are shown in Fig. 9(*a*). The maximum surface temperature in the combustion chamber is about 1070 K at 70 mm behind the backplane. The slightly lifted flame, as seen in Figs. 6(*a*) and 6(*b*), results in the heating of the bluff body tip up to 650 K. The increase of thermal conductivity in the wall material causes the backplane to heat up significantly—an effect that cannot be achieved with real wall materials without additional models for gas radiation. The hot backplane body leads to local preheating of the fresh gases ($T_{inlet} = 298$ K). The flow reaches around 2250 K in the IRZ where the burnt gases are present and lower temperatures in the outer recirculation zone of around 900 K (well visible also in the time-averaged field). In the instantaneous temperature field, large structures of cold pockets are visible along the combustion chamber walls, with a reflectional asymmetry of the structures' roll-up in the corners due to the swirling flow. These thermal boundary layers can be qualitatively compared to the experimental data obtained by Weilenmann et al. [31] (Fig. 3 in Ref. [31]), which were obtained by performing OH-LIF thermometry downstream of a natural gas flame anchored on a similar burner. The pockets are more pronounced after the flame zone, where the highest temperature gradients are present. However, temperature fluctuations are also visible around the centerline of the combustor. From a purely qualitative point of view, generation of temperature inhomogeneities in the postflame region and decreased intensity of entropy waves to the combustor exit are
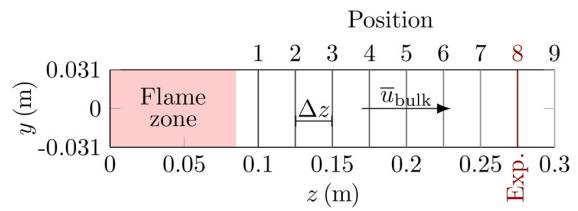

Fig. 10 Sampling positions 1 to 9 in the combustion chamber. Position 8 corresponds to the location of the experimental measurements.

already shown in Fig. 9. It is not evident whether the entropy waves are generated along the entire combustor wall or only in the region of the near-wall flame and then convected through the chamber.

5.5 Evaluation of Temperature Time Series. The statistically steady-state LES is excited with a broadband signal at the upstream boundary to determine the entropy response to velocity perturbations over a wide frequency range. The thermodynamic and adiabatic temperatures are area-averaged (with no significant difference to the line integral) at nine positions in the combustion chamber for the subsequent system identification, indicated in Fig. 10. Position 1 is located behind the flame zone and position 8 corresponds to the TDLAS-LOS location from the experiment. The distance between the sampling planes is $\Delta z = 0.025$ m and the bulk velocity in the combustion chamber is $\overline{u}_{bulk} \approx 32$ m/s. Portions of the inferred temperature time series at various positions are shown in Fig. 11(*a*). After the flame region (position 1), temperature fluctuations of 4% are observed. As the axial location progresses, the amplitude of inhomogeneities decreases continuously. The decrease in amplitudes of entropy waves is owed to turbulent mixing and alteration of mean flow profiles (shear dispersion). By characteristic minima and maxima in the time domain, the convection of entropy waves is observed. Shifting the time series by a characteristic time lag $\Delta\tau = \Delta z/\overline{u}_{bulk}$ (described in more detail below) and superposing them makes the convective behavior more evident. The superposition reveals very similar temporal positions of the minima and maxima as seen in Fig. 11(*b*), indicating one major source of the entropy fluctuations in the near-wall flame region. If heat losses along the entire combustion chamber walls are continuously generating entropy fluctuations, the superposed time signals would not coincide in basic features and would exhibit regions with significant differences, but this is not the case. Hence, we conclude that the origin of the temperature fluctuations is the interaction of the flame with the cold wall.

Figure 11(*c*) shows the time series of adiabatic temperatures at various positions. The adiabatic entropy fluctuations right after the flame zone, generated due to differential diffusion, are one order of magnitude smaller than the overall entropy fluctuations. The adiabatic temperature decreases significantly toward the combustor exit as shown in Fig. 8(*c*). Compared to the time series in Fig. 11(*a*), the adiabatic temperature signals are less affected by noise. By definition, only convective dispersion can affect their strength. Continuous generation in the combustion chamber is not possible as differential diffusion (hence ϕ' and ζ') acts only across the flame front. Superimposing the various time series in Fig. 11(*d*) highlights the convective nature of adiabatic entropy waves. Since both entropy and adiabatic entropy waves are convectively transported by the mean flow, the effect of the decaying mechanism may be equivalent in both [26].

5.6 Convective Transport of Entropy Waves. The cross-correlations γ_{pq} between the temperature signal at position 3 and the subsequent positions (cross-correlation of T'_1 with itself yields the autocorrelation) are evaluated to determine the convective transport of entropy waves. The cross-correlation between two positions p and q is defined as
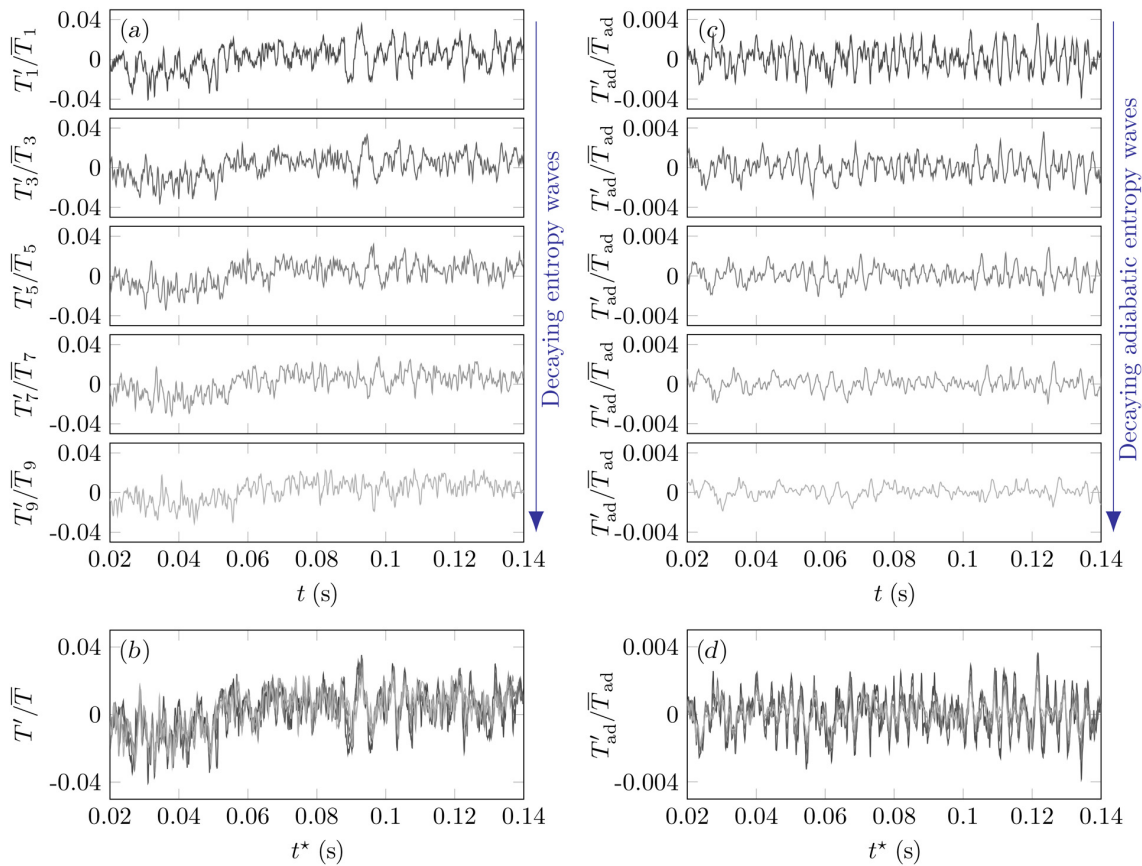
Fig. 11 (*a*) Normalized temperature and (*c*) normalized adiabatic temperature signals at various positions along the combustor and superposition of shifted (*b*) normalized temperature and (*d*) normalized adiabatic temperature time series by the characteristic time lag $\Delta\tau$. Note the different order of magnitude between temperature and adiabatic temperature fluctuations.

$$\gamma_{pq} \equiv \frac{1}{N-k} \sum_{i=1}^{N-k} \left(T'_{p,i} - \overline{T}_p \right) \left(T'_{q,i+k} - \overline{T}_q \right) \tag{12}$$

where k is a certain time lag. The normalized cross-correlation gives the correlation coefficient, where $|\gamma_{pq}| = 1$ indicates a perfect correlation. The cross-correlation of T'_1 with all subsequent temperature signals is shown in Figs. 12(*a*)–12(*c*). As the axial position increases, the correlation decreases, which is expected due to the decay mechanisms of a turbulent flow. Furthermore, the correlation is increasingly disturbed and obliterates its shape compared to the autocorrelation of T'_1. Different mechanisms can be associated with the dispersion of entropy waves, as discussed by Sattelmayer [19], Morgans et al. [26], Weilenmann et al. [27], and Polifke [32]. In simplified fully developed turbulent channel flows, turbulent mixing attenuates entropy waves particularly when the wavelength of temperature fluctuations is small compared to the turbulent length scale [19,30]. Recent experiments and large eddy simulations [27] have shown that when the integral length scale is of the order of the convective wavelength of the entropy waves, shear dispersion models based on the axial velocity profile significantly underestimate the decay rate of entropy waves. On the other hand, when the wavelength of entropy fluctuations is large compared to turbulent length scales, turbulent fluctuations do not lead to significant entropy waves [62]. The fully premixed burner under the investigated operating conditions exhibits convective wave-lengths longer than the largest turbulent structures (in the order of the chamber height $H = 62\,\text{mm}$) for all relevant frequencies $f < 500\,\text{Hz}$, hence the effect of turbulent mixing on the decay of entropy waves is considered to be negligible and shear dispersion

may be the dominant effect in this work. As the entropy waves travel at the bulk velocity, the maximum cross-correlation may be used to quantify the time delay $\Delta\tau = \Delta z / \overline{u}_{\text{bulk}}$ between each position. The obtained $\Delta\tau$ from the cross-correlation maxima in Fig. 12(*c*) correlates well with the convective transport. The cross-correlations are also evaluated for the adiabatic temperatures, as shown in Figs. 12(*d*)–12(*f*). The shape of the correlation hardly changes toward the end of the combustor, only the correlation coefficient decreases due to dispersion mechanisms. The time delay obtained from the distance between cross-correlation maxima in Fig. 12(*f*) is identical for all signals and slightly shorter compared to Fig. 12(*c*). From the analysis of the time series in Figs. 11(*a*) and 11(*c*), it is concluded that the overall and adiabatic entropy responses to upstream mass flow modulations decrease across the combustor, mainly due to shear dispersion.

5.7 Entropy and Flame Response. Figure 13 shows the transfer functions between temperature, adiabatic temperature, and heat release rate response to upstream velocity perturbations, respectively, estimated with the finite impulse response filter from $0.175\,\text{s}$ time series data discussed above. The $\mathcal{E}$ and $\mathcal{F}$ were additionally measured experimentally with the techniques described in Sec. 3 and Ref. [33], where the lowest excitation frequencies are $40\,\text{Hz}$ and $50\,\text{Hz}$, respectively. The frequency responses $\mathcal{G}(\omega) = |\mathcal{G}(\omega)| \exp(i\angle\mathcal{G}(\omega))$ are shown as Bode plots, where $|\mathcal{G}(\omega)|$ is the gain and $\angle\mathcal{G}(\omega)$ is the phase. The error bars of each temperature measurement and the predicted transfer functions are shown with a respective standard deviation of $\sigma = 1.96$ (95% confidence interval [63]) to consider the aleatoric uncertainty of the spectroscopic
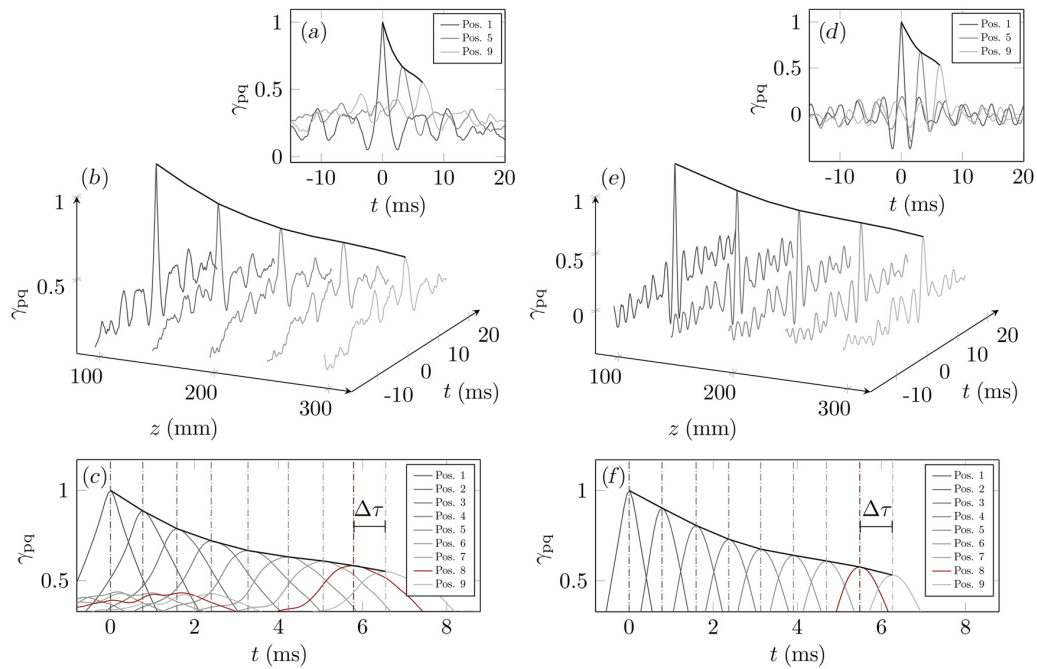
122

Fig. 12 Cross-correlation of (a)–(c) temperature and (d)–(f) adiabatic temperature output signals along the combustion chamber

database and system identification. The $\mathcal{E}$ gain in Fig. 13(a) from LES and experiment shows remarkable agreement and exhibits a low-pass behavior due to the convective dispersion of entropy waves. For low frequencies $f < 50$ Hz, the comparatively short time series length combined with long time delays between the burner outlet and combustor exit lead to large confidence intervals. The phase slope in Fig. 13(b) is predicted in accordance with experiments up to 120 Hz. The $\mathcal{E}$ phase represents the time delay of the velocity perturbations from the burner outlet to the measuring plane at position 8 in Fig. 10, which are transported convectively with the mean flow. Here, a decrease in the phase slope implies an acceleration of the bulk velocity, a behavior that was not observed in the simulation. As no velocity measurements inside the chamber are available for the present operating condition, the prediction of flame–turbulence interaction in LES cannot be fully validated. The low-frequency limit $\omega \rightarrow 0$ of the $\mathcal{E}$ phase in can be understood in the sense that a change of a quantity (e.g., u'_{ref}) results in a new steady-state of the system [64]. Since an increase in mean flow velocity (i.e., $u'_{\text{ref}}(\omega \rightarrow 0)$) results in an increase in mean burnt gas temperature (i.e., $T'(\omega \rightarrow 0)$), the input u'_{ref} and output T' are in phase ($\angle \mathcal{E}(\omega \rightarrow 0) \rightarrow 0$).

An adiabatic ETF based on the response of adiabatic temperature to upstream velocity perturbations is estimated and shown in Figs. 13(c) and 13(d). Note here the different order of magnitude in $\mathcal{E}_{\text{ad}}$ gain compared to $\mathcal{E}$. The maxima show amplifications by the effect of differential diffusion, which contributes about 30% to the gain of the overall ETF at these frequencies and is therefore considered to be non-negligible. $\mathcal{E}$ and $\mathcal{E}_{\text{ad}}$ reveal a very similar time lag as already shown in Figs. 12(c) and 12(f).

The flame response to upstream velocity perturbations is shown in Figs. 13(e) and 13(f) to provide a comprehensive representation of the system's frequency description. The estimated FTF gain corresponds well with that obtained from the experiment. The characteristic features of a fully premixed flame transfer function are well predicted [32]. The phase, which is of particular importance for thermoacoustic stability analysis, deviates significantly from the experimental measurements. This deviation is attributed to the shorter flame in the LES, as seen in Fig. 6(c), which leads to an

underestimation of the time delay between the burner outlet and the maximum heat release rate, and as a result, an overestimation of the phase slope.

As recently stated by Dharmaputra et al. [33] for technically premixed flames, similarities between $\mathcal{E}$ and $\mathcal{F}$ are also found in this work. The gain of both transfer functions exhibits its maximum at 180 Hz. After declining to a minimum at around 410 Hz, the $\mathcal{E}$ gain increases to a local maximum at about 540 Hz, which corresponds to the frequency of the second maximum of the FTF. Except for the low-frequency limit, the trend of both transfer functions coincides well with more undulations in the $\mathcal{E}$. In this work, fluctuations of the fuel supply (global equivalence ratio) can be ruled out as a possible reason for the similarities between $\mathcal{E}$ and $\mathcal{F}$, as the system is fully premixed. This leaves the influence of velocity fluctuations on wall heat losses and large coherent structures of swirling flows.

Having compared the transfer functions at the reference plane from the experiment, the predicted thermodynamic and adiabatic temperature fluctuations are now evaluated on various planes (see positions in Fig. 10) in the combustion chamber. The gain of $\mathcal{E}$ and $\mathcal{E}_{\text{ad}}$ in Figs. 14(a) and 14(c), respectively, exhibit similar trends. Note that the low-frequency range $f < 50$ Hz of the $\mathcal{E}$ gain is excluded from the discussions below due to its low confidence. With increasing distance from the combustor inlet, the gain decreases continuously. This trend is consistent with the decay of entropy responses shown in Fig. 12. The continuous decrease in gain suggests that the entropy waves (both due to differential diffusion and wall heat losses) originate in the flame region and are being propagated through the combustion chamber without noticeable generation. If the cold chamber walls were continuously generating entropy fluctuations induced by acoustic velocity perturbations, the gain toward the outlet would have to remain constant or increase at least for some frequencies. While the impingement of hot gases on the cold walls does result in additional heat losses throughout the combustor (as can be seen in Fig. 9(a)), these resulting temperature fluctuations are not strongly correlated with the upstream acoustic velocity perturbations. The change in phase of the two entropy transfer functions in Figs. 14(b) and 14(d) along the combustor fits the predicted convective transport, which is constant for a constant

123
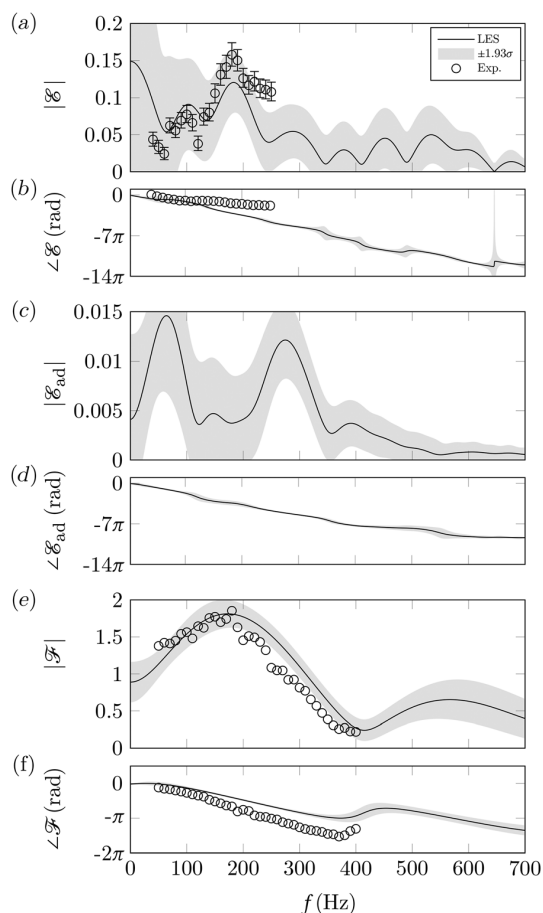
Fig. 13 Entropy transfer function (*a*) gain and (*b*) phase, adiabatic entropy transfer function (*c*) gain and (*d*) phase and corresponding flame transfer function (*e*) gain and (*f*) phase

Fig. 14 Entropy transfer function (*a*) gain and (*b*) phase, and adiabatic entropy transfer function (*c*) gain and (*d*) phase at various positions in the chamber. Confidence intervals (not shown) are comparable to Figs. 13(*a*)–13(*d*).

bulk velocity $\overline{u}_{\text{bulk}}$ and equal time delays $\Delta\tau$ between each position 1 to 9. As expected, the phases collapse in one slope when nondimensionalizing the abscissa using a Strouhal number $\text{St} = f z/\overline{u}_{\text{bulk}}$ (not shown).

6 Conclusion

This work identifies and analyzes two sources of entropy waves in fully premixed combustion with hydrogen enrichment of $X_{H_2} = 0.31$, namely, wall heat losses and differential diffusion. The wall heat losses dominate the generation of entropy waves in the present configuration, but this may change

- in a combustor with less severe wall cooling (e.g., thermal barrier coating),
- in a combustor where the flame is not close to the wall,
- in a larger combustor (smaller surface-to-volume ratio),
- at leaner conditions, or
- with increasing amount of H_2 in the fuel.

To the authors' best knowledge, this is the first time that these two effects have been analyzed in the context of entropy wave generation. The ETF is measured with the TDLAS-WMS method and estimated with LES/SI, both showing remarkable agreement in gain up to 200 Hz and phase up to 120 Hz. A strong correlation between ETF and FTF was found, similar to a previous study by Dharmaputra et al. [33] on technically premixed flames. The definition of an adiabatic flame temperature based on equivalence

and carbon-to-hydrogen ratios allowed the isolated investigation of the effect of differential diffusion with an additional adiabatic entropy transfer function. The entropy and adiabatic entropy responses to upstream velocity excitation were identified at various positions in the combustion chamber to discuss the effect of convective dispersion and generation. A subsequent study will apply the concepts developed in this paper to a technically premixed configuration of the present burner. This is of interest because such systems exhibit modulations of the fuel supply, adding another important source of entropy wave generation. This work has shown that the correct modeling of thermal boundaries is crucial for the prediction of entropy fluctuations. The effect of radiative heat transfer was considered only heuristically by increasing the thermal conductivity in the combustor walls. Therefore, the CHT-LES solver presented in this paper should be extended by a radiation model for future studies.

Data Availability Statement

The datasets generated and supporting the findings of this article are obtainable from the corresponding author upon reasonable request.

Nomenclature

Roman

c_p = specific isobaric heat capacity (J kg^{-1} K^{-1})
$\mathcal{E}$ = entropy transfer function
f = frequency (Hz)
F = thickening factor
$\mathcal{F}$ = flame transfer function
h = heat transfer coefficient (W m^{-2} K^{-1})
j = Fickian diffusion flux (mol s m^{-2})
k = thermal conductivity (W m^{-1} K^{-1})
Le = Lewis number
$\dot{Q}$ = volume-integrated heat release rate (W m^{-3})
s = sensible-plus-chemical entropy (J kg^{-1} K^{-1})
s_l^0 = laminar flame speed (m s^{-1})
T = temperature (K)
u = velocity (m s^{-1})
X = mole fraction
Y = mass fraction

Greek Symbols

γ = heat capacity ratio
γ_{pq} = cross-correlation
δ_l^0 = laminar flame thickness (m)
ζ = carbon-to-hydrogen ratio
ρ = density (kg m^{-1})
τ = time delay (s)
ϕ = equivalence ratio
ω = angular frequency, $\omega = 2\pi f$ (Hz)

Subscripts

ad = adiabatic
ref = reference position

References

[1] Candel, S., Durox, D., Ducruix, S., Birbaud, A.-L., Noiray, N., and Schuller, T., 2009, "Flame Dynamics and Combustion Noise: Progress and Challenges," Int. J. Aeroacoustics, **8**(1), pp. 1–56.

[2] Poinsot, T., 2017, "Prediction and Control of Combustion Instabilities in Real Engines," Proc. Combust. Inst., **36**(1), pp. 1–28.

[3] Chterev, I., and Boxx, I., 2021, "Effect of Hydrogen Enrichment on the Dynamics of a Lean Technically Premixed Elevated Pressure Flame," Combust. Flame, **225**, pp. 149–159.

[4] Zhu, M., Dowling, A. P., and Bray, K. N. C., 2000, "Self-Excited Oscillations in Combustors With Spray Atomisers," ASME J. Eng. Gas Turbines Power, **123**(4), pp. 779–786.

[5] Eckstein, J., Freitag, E., Hirsch, C., and Sattelmayer, T., 2006, "Experimental Study on the Role of Entropy Waves in Low-Frequency Oscillations in a RQL Combustor," ASME J. Eng. Gas Turbines Power, **128**(2), pp. 264–270.

[6] Ihme, M., 2017, "Combustion and Engine-Core Noise," Annu. Rev. Fluid Mech., **49**(1), pp. 277–310.

[7] Marble, F. E., and Candel, S., 1977, "Acoustic Disturbance From Gas Non-Uniformities Convected Through a Nozzle," J. Sound Vib., **55**(2), pp. 225–243.

[8] De Domenico, F., Rolland, E. O., Rodrigues, J., Magri, L., and Hochgreb, S., 2021, "Compositional and Entropy Indirect Noise Generated in Subsonic Non-Isentropic Nozzles," J. Fluid Mech., **910**, p. A5.

[9] Weilenmann, M., and Noiray, N., 2020, "Experiments on Sound Reflection and Production by Choked Nozzle Flows Subject to Acoustic and Entropy Waves," J. Sound Vib., **492**, p. 115799.

[10] Leyko, M., Nicoud, F., and Poinsot, T., 2009, "Comparison of Direct and Indirect Combustion Noise Mechanisms in a Model Combustor," AIAA J., **47**(11), pp. 2709–2716.

[11] Hield, P. A., Brear, M. J., and Jin, S. H., 2009, "Thermoacoustic Limit Cycles in a Premixed Laboratory Combustor With Open and Choked Exits," Combust. Flame, **156**(9), pp. 1683–1697.

[12] Goh, C. S., and Morgans, A. S., 2013, "The Influence of Entropy Waves on the Thermoacoustic Stability of a Model Combustor," Combust. Sci. Technol., **185**(2), pp. 249–268.

[13] Chen, L. S., Bomberg, S., and Polifke, W., 2016, "Propagation and Generation of Acoustic and Entropy Waves Across a Moving Flame Front," Combust. Flame, **166**, pp. 170–180.

[14] Chen, L. S., Steinbacher, T., Silva, C. F., and Polifke, W., 2016, "On Generation of Entropy Waves Across a Premixed Flame," ASME Paper No. GT2016-57026.

[15] Chen, L. S., 2016, "Scattering and Generation of Acoustic and Entropy Waves Across Moving and Fixed Heat Sources," Ph.D. thesis, TU Munich, Munich, Germany.

[16] Dowling, A. P., 1995, "The Calculation of Thermoacoustic Oscillation," J. Sound Vib., **180**(4), pp. 557–581.

[17] Keller, J. J., 1995, "Thermoacoustic Oscillations in Combustion Chambers of Gas Turbines," AIAA J., **33**(12), pp. 2280–2287.

[18] Polifke, W., Paschereit, C. O., and Döbbeling, K., 2001, "Constructive and Destructive Interference of Acoustic and Entropy Waves in a Premixed Combustor With a Choked Exit," Int. J. Acoust. Vib., **6**(3), pp. 135–146.

[19] Sattelmayer, T., 2003, "Influence of the Combustor Aerodynamics on Combustion Instabilities From Equivalence Ratio Fluctuations," ASME J. Eng. Gas Turbines Power, **125**(1), pp. 11–19.

[20] Motheau, E., Nicoud, F., and Poinsot, T., 2014, "Mixed Acoustic-Entropy Combustion Instabilities in Gas Turbines," J. Fluid Mech., **749**, pp. 542–576.

[21] Steinbacher, T., Meindl, M., and Polifke, W., 2018, "Modeling the Generation of Temperature Inhomogeneities by a Premixed Flame," Int. J. Spray Combust. Dyn., **10**(2), pp. 111–130.

[22] Brookes, S. J., Cant, R. S., Dupere, I. D. J., and Dowling, A. P., 2001, "Computational Modelling of Self-Excited Combustion Instabilities," ASME J. Eng. Gas Turbines Power, **123**(2), pp. 322–326.

[23] Christodoulou, L., Karimi, N., Cammarano, A., Paul, M., and Navarro-Martinez, S., 2020, "State Prediction of an Entropy Wave Advecting Through a Turbulent Channel Flow," J. Fluid Mech., **882**, p. A8.

[24] Rodrigues, J., Busseti, A., and Hochgreb, S., 2020, "Numerical Investigation on the Generation, Mixing and Convection of Entropic and Compositional Waves in a Flow Duct," J. Sound Vib., **472**, p. 115155.

[25] Xia, Y., Duran, I., Morgans, A. S., and Han, X., 2018, "Dispersion of Entropy Perturbations Transporting Through an Industrial Gas Turbine Combustor," Flow, Turbul. Combust., **100**(2), pp. 481–502.

[26] Morgans, A. S., Goh, C. S., and Dahan, J. A., 2013, "The Dissipation and Shear Dispersion of Entropy Waves in Combustor Thermoacoustics," J. Fluid Mech., **733**, p. R2.

[27] Weilenmann, M., Xiong, Y., and Noiray, N., 2020, "On the Dispersion of Entropy Waves in Turbulent Flows," J. Fluid Mech., **903**, p. R1.

[28] Bake, F., Richter, C., Mühlbauer, B., Kings, N., Röhle, I., Thiele, F., and Noll, B., 2009, "The Entropy Wave Generator (EWG): A Reference Case on Entropy Noise," J. Sound Vib., **326**(3–5), pp. 574–598.

[29] Wassmer, D., Schuermans, B., Paschereit, C. O., and Moeck, J. P., 2017, "Measurement and Modeling of the Generation and the Transport of Entropy Waves in a Model Gas Turbine Combustor," Int. J. Spray Combust. Dyn., **9**(4), pp. 299–309.

[30] Giusti, A., Worth, N. A., Mastorakos, E., and Dowling, A. P., 2017, "Experimental and Numerical Investigation Into the Propagation of Entropy Waves," AIAA J., **55**(2), pp. 446–458.

[31] Weilenmann, M., Doll, U., Bombach, R., Blondé, A., Ebi, D., Xiong, Y., and Noiray, N., 2021, "Linear and Nonlinear Entropy-Wave Response of Technically-Premixed Jet-Flames-Array and Swirled Flame to Acoustic Forcing," Proc. Combust. Inst., **38**(4), pp. 6135–6143.

[32] Polifke, W., 2020, "Modeling and Analysis of Premixed Flame Dynamics by Means of Distributed Time Delays," Prog. Energy Combust. Sci., **79**, p. 100845.

[33] Dharmaputra, B., Shcherbanev, S., Blondé, A., Schuermans, B., and Noiray, N., 2022, "Entropy Transfer Function Measurement With Tunable Diode Laser Absorption Spectroscopy," Proc. Combust. Inst., **39**(4), pp. 4621–4630.

[34] Magri, L., O'Brien, J., and Ihme, M., 2016, "Compositional Inhomogeneities as a Source of Indirect Combustion Noise," J. Fluid Mech., **799**, p. R4.

[35] Cumpsty, N. A., and Marble, F. E., 1977, "The Interaction of Entropy Fluctuations With Turbine Blade Rows; A Mechanism of Turbojet Engine Noise," Proc. R. Soc. A: Math., Phys. Eng. Sci., **357**(1690), pp. 323–344.

[36] Morgans, A. S., and Duran, I., 2016, "Entropy Noise: A Review of Theory, Progress and Challenges," Int. J. Spray Combust. Dyn., **8**(4), pp. 285–298.

[37] Meindl, M., Silva, C. F., and Polifke, W., 2021, "On the Spurious Entropy Generation Encountered in Hybrid Linear Thermoacoustic Models," Combust. Flame, **223**, pp. 525–540.

[38] Kraus, C., Selle, L., and Poinsot, T., 2018, "Coupling Heat Transfer and Large Eddy Simulation for Combustion Instability Prediction in a Swirl Burner," Combust. Flame, **191**, pp. 239–251.

[39] Cazéres, Q., 2021, "Analysis and Reduction of Chemical Kinetics for Combustion Applications," Ph.D. thesis, L'Institut National Polytechnique de Toulouse, Toulouse, France.

[40] Bilger, R. W., Stårner, S. H., and Kee, R. J., 1990, "On Reduced Mechanisms for Methane-Air Combustion in Nonpremixed Flames," Combust. Flame, **80**(2), pp. 135–149.

[41] Schuermans, B., Bellucci, V., Guethe, F., Meili, F., Flohr, P., and Paschereit, C. O., 2004, "A Detailed Analysis of Thermoacoustic Interaction Mechanisms in a Turbulent Premixed Flame," ASME Paper No. GT2004-53831.

[42] Weller, H. G., Tabor, G., Jasak, H., and Fureby, C., 1998, "A Tensorial Approach to Computational Continuum Mechanics Using Object-Oriented Techniques," Comput. Phys., **12**(6), pp. 620–631.

125

[43] Kuhlmann, J., Lampmann, A., Pfitzner, M., and Polifke, W., 2022, "Assessing Accuracy, Reliability and Efficiency of Combustion Models for Prediction of Flame Dynamics With Large Eddy Simulation," Phys. Fluids, **34**(9), p. 095117.

[44] Eder, A. J., Silva, C. F., Haeringer, M., Kuhlmann, J., and Polifke, W., 2023, "Incompressible versus Compressible Large Eddy Simulation for the Identification of Premixed Flame Dynamics," Int. J. Spray Combust. Dyn., **15**(1), pp. 16–32.

[45] Nicoud, F., and Ducros, F., 1999, "Subgrid-Scale Stress Modelling Based on the Square of the Velocity Gradient Tensor," Flow, Turbul. Combust., **62**(3), pp. 183–200.

[46] Colin, O., Ducros, F., Veynante, D., and Poinsot, T., 2000, "A Thickened Flame Model for Large Eddy Simulation of Turbulent Premixed Combustion," Phys. Fluids, **12**(7), pp. 1843–1863.

[47] Légier, J.-P., Poinsot, T., and Veynante, D., 2000, "Dynamically Thickened Flame LES Model for Premixed and Non-Premixed Turbulent Combustion," Proceedings of the Summer Program 2000, Stanford, CA, pp. 157–168.

[48] Oberleithner, K., and Albayrak, A., 2018, "Vorhersage von Flammentransferfunktionen: Abschätzung der Flammentransferfunktion aus stationären Strömungsfeldern," FVV/Informationstagung Turbomaschinen, Bad Neuenahr, Germany, Abschlussbericht 1151.

[49] Charlette, F., Meneveau, C., and Veynante, D., 2002, "A Power-Law Flame Wrinkling Model for LES of Premixed Turbulent Combustion Part i: Non-Dynamic Formulation and Initial Tests," Combust. Flame, **131**(1–2), pp. 159–180.

[50] Agostinelli, P. W., 2022, "Assessment of Large Eddy Simulation in the Conjugate Heat Transfer Context for Engine Operability: Application to Hydrogen Enrichment and Spinning Combustion Technology," Ph.D. thesis, Toulouse INP, Toulouse, France.

[51] Mechanical and Aerospace Engineering (Combustion Research), University of California at San Diego, 2016, "Chemical-Kinetic Mechanisms for Combustion Applications," University of California at San Diego, La Jolla, CA.

[52] Garcia, A. M., Le Bras, S., Prager, J., Haeringer, M., and Polifke, W., 2022, "Large Eddy Simulation of the Dynamics of Lean Premixed Flames Using Global Reaction Mechanisms Calibrated for CH$_4$-H$_2$ Fuel Blends," Phys. Fluids, **34**(9), p. 095105.

[53] Hirschfelder, J. O., Bird, R. B., and Cutriss, C. F., 1966, *Molecular Theory of Gases and Liquids*, Wiley, New York.

[54] Konle, M., de Guillebon, L., and Cottier, F., 2014, "Multi-Physics Simulations of an Aero Engine Combustor With OpenFOAM," Proceedings of the 1st Global Power and Propulsion Forum, Zurich, Switzerland, Paper No. GPPF-2017-0045.

[55] Agostinelli, P. W., Laera, D., Boxx, I., Gicquel, L., and Poinsot, T., 2021, "Impact of Wall Heat Transfer in Large Eddy Simulation of Flame Dynamics in a Swirled Combustion Chamber," Combust. Flame, **234**, p. 111728.

[56] Polifke, W., 2014, "Black-Box System Identification for Reduced Order Model Construction," Ann. Nucl. Energy, **67**, pp. 109–128.

[57] Föller, S., and Polifke, W., 2011, "Advances in Identification Techniques for Aero-Acoustic Scattering Coefficients From Large Eddy Simulation," Proceedings of the 18th International Congress on Sound and Vibration (ICSV18), Rio de Janeiro, Brazil, July 10–14, pp. 3122–3129.

[58] Higgins, B. S., McQuay, M. Q., Lacas, F., Rolon, J. C., Darabiha, N., and Candel, S., 2001, "Systematic Measurements of OH Chemiluminescence for Fuel-Lean, High-Pressure, Premixed, Laminar Flames," Fuel, **80**(1), pp. 67–74.

[59] Schuermans, B., Guethe, F., and Mohr, W., 2010, "Optical Transfer Function Measurements for Technically Premixed Flames," ASME J. Eng. Gas Turbines Power, **132**(8), p. 081501.

[60] Bilger, R. W., and Dibble, R. W., 1982, "Differential Molecular Diffusion Effects in Turbulent Mixing," Combust. Sci. Technol., **28**(3–4), pp. 161–172.

[61] Wang, J., Huang, Z., Tang, C., Miao, H., and Wang, X., 2009, "Numerical Study of the Effect of Hydrogen Addition on Methane-Air Mixtures Combustion," Int. J. Hydrogen Energy, **34**(2), pp. 1084–1096.

[62] Huet, M., and Giauque, A., 2013, "A Nonlinear Model for Indirect Combustion Noise Through a Compact Nozzle," J. Fluid Mech., **733**, pp. 268–301.

[63] Sovardi, C., Jaensch, S., and Polifke, W., 2016, "Concurrent Identification of Aero-Acoustic Scattering and Noise Sources at a Flow Duct Singularity in Low Mach Number Flow," J. Sound Vib., **377**, pp. 90–105.

[64] Polifke, W., and Lawn, C. J., 2007, "On the Low-Frequency Limit of Flame Transfer Functions," Combust. Flame, **151**(3), pp. 437–451.

126

An Arbitrary Lagrangian–Eulerian framework for the consistent analysis of entropy wave generation

Moritz Merk [*,1], Alexander J. Eder[1], Wolfgang Polifke

Technical University of Munich, TUM School of Engineering and Design, Department of Engineering Physics and Computation, Boltzmannstr. 15, Garching, 85747, Germany

ARTICLE INFO

ABSTRACT

Entropy waves are generated in many technically relevant flow processes such as combustion, mixing, or convective heat transfer. When accelerated, entropy waves generate acoustic waves that contribute to the overall sound emission and can lead to self-excited thermoacoustic instabilities, especially at low frequencies. In order to reduce or prevent these undesirable byproducts of the flow, an understanding of the generation mechanisms of entropy waves is key. This study derives the analytical source terms of entropy disturbances for moving sources in general three-dimensional reactive flows. In this general setup, the consistent derivation of the generation mechanisms requires the tracking of the moving source for which an Arbitrary Lagrangian–Eulerian (ALE) framework is utilized. The derived differential equations provide a fundamental understanding of the underlying source mechanisms.

In addition, the general three-dimensional differential equations are reduced to a quasi-one-dimensional jump condition to unify the analysis of the entropy wave generation. This unified framework is used for an in-depth analysis of a premixed flame, where all source terms that generate entropy disturbances are analyzed and their relative importance are quantified. The dominant contribution of unsteady heat addition per unit mass to the generation of entropy waves is reaffirmed for lean premixed flames. Finally, by comparison with the entropy generation mechanisms of a heated gauze at rest, it is emphasized once more that a heat source at rest is an invalid model for a premixed flame.

Novelty and significance statement

The analytical terms of entropy wave generation are derived consistently for moving sources in a general three-dimensional reactive flow. It is shown and emphasized that a consistent derivation requires the tracking of the local entropy sources. Therefore, an Arbitrary Lagrangian–Eulerian framework is used.

The derived equations provide a fundamental insight into the generation of entropy disturbances in reactive flows, e.g. premixed flames. Furthermore, the derived equations can be seen as a starting point to consistently extract sources of entropy waves from numerical simulations.

1. Introduction

Isobaric and irrotational disturbances [1] – so-called *entropy waves* – occur in many technically relevant unsteady flow processes such as combustion, mixing, or convective heat transfer. These entropic disturbances are convected with the mean flow velocity and generate a dipole-type acoustic sound source when accelerated [2–5]. In gas turbines, aero-engines, or rocket engines, entropy waves generated in the combustion chamber are accelerated as they enter a high-pressure turbine stage or a downstream nozzle. The acoustic waves generated – some leaving the combustor and some propagating back – affect the system in two ways. The outward propagating acoustic wave contributes

to the overall sound emission of the engine [6–8], while the inward propagating wave can result in self-excited low-frequency thermoacoustic combustion instability. This type of oscillation, often referred to as "rumble" [9–11], has been an active area of research [12–16] since the early work of Keller et al. [17,18] in the 1980's and can lead to reduced combustor lifetime or even system failure [6,19,20]. In order to prevent instability or to reduce the contribution to overall sound emissions, an understanding and accurate modeling of the generation, dispersion, and convection of entropy waves, and their conversion to acoustic energy is essential. This work focuses on a consistent description of entropy wave generation by unsteady combustion.

Nomenclature

Roman letters

A_s	Surface of source region (m^2)
c_p	Isobaric heat capacity ($\frac{\mathrm{J}}{\mathrm{kgK}}$)
f	Frequency (Hz)
g	Mass specific sensible-plus-chemical Gibbs' free enthalpy ($\frac{\mathrm{J}}{\mathrm{kg}}$)
h	Mass specific sensible-plus-chemical enthalpy ($\frac{\mathrm{J}}{\mathrm{kg}}$)
h_s	Mass specific sensible enthalpy ($\frac{\mathrm{J}}{\mathrm{kg}}$)
H	Mass specific total non-chemical enthalpy ($\frac{\mathrm{J}}{\mathrm{kg}}$)
$\dot{m}_\mathrm{s}$	Mass flux density relative to the local entropy source region ($\frac{\mathrm{kg}}{\mathrm{m}^2\mathrm{s}}$)
M	Mach number (-)
$\dot{M}_\mathrm{s}$	Mass flux relative to the local entropy source region ($\frac{\mathrm{kg}}{\mathrm{s}}$)
n	Normal vector (-)
p	Pressure ($\frac{\mathrm{kg}}{\mathrm{ms}^2}$)
$\dot{q}$	Volumetric heat release rate ($\frac{\mathrm{W}}{\mathrm{m}^3}$)
$\dot{Q}$	Integral heat release rate (W)
s	Mass specific sensible-plus-chemical entropy ($\frac{\mathrm{J}}{\mathrm{kgK}}$)
t	Time (s)
T	Temperature (K)
u	Flow velocity ($\frac{\mathrm{m}}{\mathrm{s}}$)
u_s	Velocity of entropy source region ($\frac{\mathrm{m}}{\mathrm{s}}$)
V	Volume (m^3)
V_k	Diffusion velocity of species k ($\frac{\mathrm{m}}{\mathrm{s}}$)
x	Eulerian coordinate (spatially fixed) (m)
x_s	(Eulerian) coordinate of the entropy source region (m)
Y	Mass fraction (-)

Greek letters

α	Heat transfer coefficient ($\frac{\mathrm{W}}{\mathrm{m}^2\mathrm{K}}$)
γ	Ratio of specific heats (-)
λ	Heat conductivity ($\frac{\mathrm{W}}{\mathrm{mK}}$)
ρ	Mass density ($\frac{\mathrm{kg}}{\mathrm{m}^3}$)
τ_{ij}	Viscous stress tensor ($\frac{\mathrm{kg}}{\mathrm{ms}^2}$)
ϕ	Equivalence ratio (-)
χ	ALE coordinate (moving with u_s) (m)
ψ	Source term of entropy generation ($\frac{\mathrm{W}}{\mathrm{m}^3\mathrm{K}}$)
Ψ	Integral source term of entropy generation ($\frac{\mathrm{W}}{\mathrm{K}}$)
$\dot{\omega}_k$	Volumetric reaction rate of species k ($\frac{\mathrm{kg}}{\mathrm{m}^3\mathrm{s}}$)
$\dot{\Omega}_k$	Integral reaction rate of species k ($\frac{\mathrm{kg}}{\mathrm{s}}$)

Operators

δ	Delta distribution
Δ	Difference
$\mathcal{H}$	Heaviside function
$\mathcal{O}$	Order of magnitude

Subscript

diff	Due to diffusive effects
gen	Generated
p	Acoustic contribution
$\vert_p$	Derivative at constant pressure
ref	Reference value
s	Entropic contribution
$\vert_s$	Derivative at constant sensible-plus-chemical entropy
$\vert_x$	Derivative at fixed Eulerian coordinate x
$\vert_\chi$	Derivative at fixed Arbitrary Lagrangian–Eulerian coordinate χ
Y	Compositional contribution
$\vert_Y$	Derivative at constant mass fraction
$\dot{\omega}_k$	Due to chemical reaction
1	Gas state in front of the reaction zone
2	Gas state behind the reaction zone
$\parallel$	Parallel to the local $\bar{s}$ gradient

Superscript

$^-$	Mean
$'$	Perturbation

Abbreviations

ALE	Arbitrary Lagrangian–Eulerian
LHS	Left-hand side
Q1D	Quasi one-dimensional
RHS	Right-hand side

To develop a fundamental understanding of the processes leading to the generation of entropy waves in exothermic reaction zones, analytical [21–24] and numerical [25–29] procedures are the methods of choice in the literature. Many experimental studies concentrate on the convection and acoustic response of entropy waves [30–33] and on the conversion to acoustic energy when accelerated [34,35], but not on the underlying generation mechanisms, except e.g. [36]. In contrast, numerical calculations provide comprehensive access to the fields of all relevant physical quantities. Depending on the trade-off between accuracy and computational time, there are numerical methods of varying complexity, ranging from high-fidelity simulations, e.g., large eddy simulation, to semi-analytic network models, some of which use simplistic analytical solutions such as quasi-one dimensional (Q1D) jump conditions. In any case, analytical tools are needed to provide *a priori* the underlying system of equations and *a posteriori* guidelines for visualizing and interpreting effects of interest in the simulation results. Closed-form analytical solutions exist only for simplistic situations but can provide an in-depth understanding of physical mechanisms. A proper understanding of the analytical equations is essential for the correct interpretation of both numerical and analytical results.

Starting from analytically derived entropy balance equations in differential form, several studies such as Morgans and Duran [8] or Duran et al. [7] argue that the total unsteady heat release rate of a flame contributes to the generation of entropy waves and that a perturbation of the heat-to-flow power ratio is the origin of entropic perturbations [37]. Derived from the same balance equations, several analytically reduced quasi-one-dimensional jump conditions agree with this conclusion [36,38–40]. However, all of these studies consider the flame as a heat source at rest. In contrast, a premixed flame front exhibits local displacements in response to various disturbances (e.g. acoustics, upstream flow velocity, vortical flow structures, turbulence, fuel concentration). This neglect of flame motion leads problematically to the spurious generation of entropy waves, as shown by Strobio Chen et al. [22] for a Q1D jump condition across a premixed flame, or by Meindl et al. [27] in one- and two-dimensional numerical simulations. This conclusion is widely accepted for quasi-one-dimensional jump conditions [41–46]. However, especially in differential/integral equations, the effect of flame motion on the source term of entropy waves is not

obvious, and the resulting source terms have been misinterpreted [23, 47].

Other studies, e.g. [13,17,37,48,49], argue from theoretical considerations or the derivation of one-dimensional jump conditions that perturbations of the heat added per unit mass are the only important generation mechanism of entropy waves in exothermic reaction zones. However, to the best of the authors' knowledge, the corresponding source terms have never been isolated adequately in differential/integral equations.

The objective of this work is (i) to consistently derive the source terms of entropy disturbances for moving sources in general three-dimensional reactive flows, and (ii) to unify the description of entropy wave generation of moving sources from the three-dimensional differential equations to the limit of quasi-one-dimensional jump conditions. An Arbitrary Lagrangian–Eulerian (ALE) reference frame [50] is used to explicitly take into account the movement of the source region.

The paper is structured as follows: In Section 2.1, the general three-dimensional differential balance equation for entropy disturbances is derived, and the entropy source terms of general sources in motion are identified. Section 2.2 reduces the differential equation to a quasi-one-dimensional jump condition to simplify the subsequent analysis of the individual source terms and recover the results of Strobio Chen et al. [22]. Section 3 evaluates the jump condition for two exemplary cases – a moving lean premixed flame front and a fixed heated source such as a heated gauze – including a detailed source term analysis for the lean premixed flame. Section 4 provides a conclusion and outlook for future work.

2. Analytical framework

Analyzing the source terms of entropy perturbations in flow differential equations provides an insight into the underlying physical mechanisms *and* their importance in various physical configurations. For a meaningful analysis, the isolation of terms generating entropy perturbations from simple transport terms is crucial. In the most general case of a moving entropy source region, the displacement of its time-invariant part does not generate entropy perturbations [22, 27,51]. The strict separation between mechanisms of transport and generation in the differential equations requires the tracking of the local displacement of the entropy source region. Analytically, this is achieved by using an Arbitrary Lagrangian–Eulerian coordinate system [50] following the entropy source region as proposed by Heilmann et al. [51].

This paragraph utilizes the example of a one-dimensional, perfectly premixed exothermic reaction zone in the limit of negligible diffusive effects to illustrate the need for entropy source tracking to strictly separate the generation and transport mechanisms of entropy disturbances. The investigated reaction zone is kinematically stabilized and responds to incoming velocity perturbations by a displacement of the reaction zone. No entropy disturbances are generated [22] since the global entropy generation remains time-invariant. This simplistic example is shown in Fig. 1(a) in an Eulerian coordinate system x (spatially fixed) with a relative motion between the coordinate system and the entropy source region. In the subfigure on the left, the spatial distribution of entropy is displayed. The subfigure on the right shows the respective temporal entropy signal observed at the fixed coordinate x^*. In the case of the fixed coordinate system, a *non-constant, time-dependent* entropy signal is observed at x^*, which might be interpreted as the result of a source of entropy waves. However, this signal is not evidence for the generation of a convected entropy disturbance but merely an artifact of the relative motion of the entropy source region relative to x^*. This artifact disappears when the exothermic reaction zone is expressed in an ALE coordinate system χ that perfectly tracks the entropy source region (see Fig. 1(b)). In this case there is no relative movement between the entropy source region and the coordinate system (Fig. 1(b) (left))

(a) Fixed coordinate system x

(b) Moving coordinate system χ
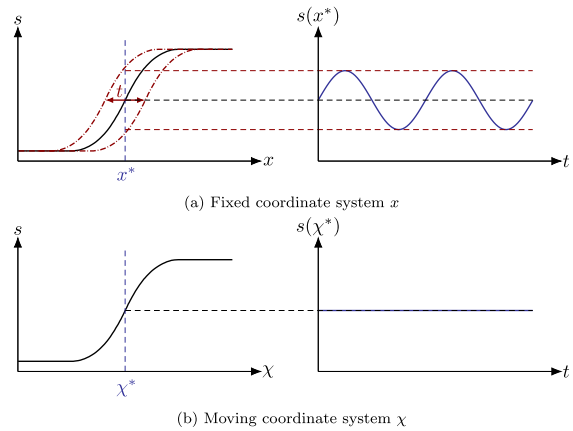
Fig. 1. One-dimensional fully premixed exothermic reaction zone perturbed by incoming velocity perturbations expressed in (a) a fixed (Eulerian) coordinate system x and (b) a moving (ALE) coordinate system χ perfectly tracking the corresponding entropy source region. The subplots on the left depict the spatial entropy distribution in the different coordinate system. The subplots on the right show the temporal entropy signal at the fixed coordinates x^* and χ^*, respectively.

and the expected *constant, time-invariant* entropy signal is observed at the coordinate χ^* (Fig. 1(b) (right)).

In this work, the ALE framework [50] is used to unify the analytical source formulation of entropy disturbances from the general three-dimensional balance equations to the quasi-one-dimensional jump condition. The derivations throughout this work involve the transformation between the ALE, the Eulerian, and the Lagrangian (coordinate system moving with a reference mass) frameworks. Expressed in the fixed spatial coordinates x, the three-dimensional coordinate transformation between the different systems is performed by simply rewriting the convective operator [50]. Using Einstein notation, the convective operator of the different coordinate systems expressed in the fixed spatial coordinates x reads

$$\underbrace{\frac{\mathrm{D}}{\mathrm{D}t}}_{\text{Lagrangian}} = \underbrace{\frac{\partial}{\partial t}\bigg|_{\chi} + (u_j - u_{\mathrm{s},j})\frac{\partial}{\partial x_j}}_{\text{ALE}} = \underbrace{\frac{\partial}{\partial t}\bigg|_{x} + u_j\frac{\partial}{\partial x_j}}_{\text{Eulerian}}. \tag{1}$$

This expression of the ALE framework in the non-moving coordinates x is chosen for a more straightforward application in numerical simulations. We refer to Donéa and Huerta [50] for a detailed derivation of this corresponding coordinate transformation. In Eq. (1), $u_{\mathrm{s},j}$ is the local velocity between the moving ALE coordinates χ and the fixed Eulerian coordinates x. Since the ALE framework perfectly tracks the entropy source regions throughout this work, $u_{\mathrm{s},j}$ is equal the local movement of these regions. $\partial/\partial t|_x$ and $\partial/\partial t|_\chi$ refer to the time derivatives at the fixed coordinate x and χ, respectively. The difference between the two time derivatives is the displacement operator

$$\frac{\partial}{\partial t}\bigg|_{x} - \frac{\partial}{\partial t}\bigg|_{\chi} = -u_{\mathrm{s},j}\frac{\partial}{\partial x_j}. \tag{2}$$

Its effect is visualized in Fig. 1(a) (right) for the perturbed one-dimensional fully premixed flame. The explicit appearance of the displacement operator in (Eq. (2)) in the ALE framework is key to the strict separation of generation and transport mechanisms in differential equations.

2.1. General balance equation for entropy disturbance

The derivation of the balance equation for entropy disturbances in general three-dimensional reacting flows of an ideal gas mixture starts

3

from the Gibbs' equation of a multi-component gas [52–55]:

$$T\,\mathrm{d}s = \mathrm{d}h - \frac{\mathrm{d}p}{\rho} - \sum_{k=1}^{N} g_k \,\mathrm{d}Y_k \,, \tag{3}$$

where ρ, p, T, $h = \sum_{k=1}^{N} h_k Y_k$ and $s = \sum_{k=1}^{N} s_k Y_k$ are the density, the pressure, the temperature, the sensible-plus-chemical enthalpy, and entropy. Y_k and $g_k = h_k - T s_k$ are the mass fraction and the sensible-plus-chemical Gibbs' free enthalpy of the kth of N species, respectively.

For flow problems, the total differentials d in Eq. (3) are replaced by the material derivatives D/Dt (Lagrangian framework) and after multiplication with ρ/T, Eq. (3) reads

$$\rho \frac{\mathrm{D}s}{\mathrm{D}t} = \frac{1}{T}\left(\rho \frac{\mathrm{D}h}{\mathrm{D}t} - \frac{\mathrm{D}p}{\mathrm{D}t}\right) - \sum_{k=1}^{N} \frac{g_k}{T}\rho \frac{\mathrm{D}Y_k}{\mathrm{D}t} \,. \tag{4}$$

Next, the balance equation for sensible-plus-chemical enthalpy [55,56]

$$\rho \frac{\mathrm{D}h}{\mathrm{D}t} - \frac{\mathrm{D}p}{\mathrm{D}t} = \tau_{ji}\frac{\partial u_j}{\partial x_i} + \frac{\partial}{\partial x_j}\left(\lambda \frac{\partial T}{\partial x_j}\right) - \frac{\partial}{\partial x_j}\left(\rho \sum_{k=1}^{N} h_k Y_k V_{k,j}\right)\,, \tag{5}$$

and the species balance equations [56]

$$\rho \frac{\mathrm{D}Y_k}{\mathrm{D}t} = -\frac{\partial}{\partial x_j}\left(\rho Y_k V_{k,j}\right) + \dot{\omega}_k \,, \tag{6}$$

are used to gain a better insight into the mechanisms of entropy generation. In Eqs. (5) and (6), volume forces and volumetric heat sources (e.g. an electric spark or a radiative flux) are neglected. τ_{ij}, λ, V_k and $\dot{\omega}_k$ are the viscous stress tensor, the heat conductivity, the diffusion velocity and the volumetric reaction rate of specie k. Substituting Eqs. (5) and (6) into Eq. (4) and transforming from the Lagrangian to the ALE framework (see Eq. (1)) yields the entropy balance equation for a general three-dimensional reacting flow

$$\rho \frac{\mathrm{D}s}{\mathrm{D}t} = \underbrace{\rho \left.\frac{\partial s}{\partial t}\right|_\chi + \rho\left(u_j - u_{\mathrm{s},j}\right)\frac{\partial s}{\partial x_j}}_{\dot{m}_{\mathrm{s},j}} = \psi_{\dot{\omega}_k} + \psi_{\mathrm{diff}} \,. \tag{7}$$

The mass flux density $\dot{m}_{\mathrm{s},j}$ is introduced for brevity and describes the local mass flux density relative to the local entropy source region, which is moving with the local velocity $u_{\mathrm{s},j}$. The two source terms on the right-hand side (RHS) of Eq. (7)

$$\psi_{\dot{\omega}_k} = -\sum_{k=1}^{N} \frac{g_k}{T}\dot{\omega}_k = \frac{\dot{q}}{T} - \sum_{k=1}^{N} \frac{h_{\mathrm{s},k}}{T}\dot{\omega}_k + \sum_{k=1}^{N} s_k \dot{\omega}_k \,, \tag{8}$$

and

$$\psi_{\mathrm{diff}} = \frac{1}{T}\tau_{ji}\frac{\partial u_j}{\partial x_i} + \frac{1}{T}\frac{\partial}{\partial x_j}\left(\lambda\frac{\partial T}{\partial x_j}\right) + \sum_{k=1}^{N} s_k \frac{\partial}{\partial x_j}\left(\rho Y_k V_{k,j}\right) - \frac{1}{T}\sum_{k=1}^{N}\frac{\partial h_k}{\partial x_j}\rho Y_k V_{k,j} \,, \tag{9}$$

correspond to the entropy generation due to chemical reactions and due to diffusive effects, respectively. In Eq. (8), $\psi_{\dot{\omega}_k}$ is further divided into three processes [28]. The first term corresponds to the entropy generation due to the volumetric chemical heat release rate $\dot{q} = -\sum_{k=1}^{N} \Delta h_{f,k}^0 \dot{\omega}_k$ - the energy conversion process from chemical into sensible enthalpy. The second and third terms take into account the changes in sensible[2] enthalpy h_{s} and the sensible-plus-chemical entropy due to a change in the composition of the gas mixture. The source term ψ_{diff} is divided into four contributions, namely (from left to right in Eq. (9)) viscous dissipation, heat conduction, entropy transport by species diffusion and enthalpy transport by species diffusion.

---

[2] Note that the "chemical part" of the sensible-plus-chemical enthalpy h is already included in the first term $\dot{q}/T$ via the definition of the volumetric heat release rate.
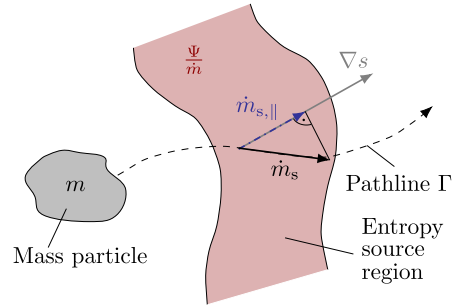

Fig. 2. Mass particle m convects along its pathline Γ across a source region with the entropy source density $\psi/\dot{m}_{\mathrm{s},\parallel} = \left(\psi_{\dot{\omega}_k} + \psi_{\mathrm{diff}}\right)/\dot{m}_{\mathrm{s},\parallel}$.

Eq. (7) is valid for general unsteady flows. The aim of the following paragraph is to derive the balance equation for low-amplitude entropy perturbations based on a first-order perturbation ansatz, which is introduced into Eq. (7) by expressing all physical quantities $Y(x,t) = \overline{Y}(x) + Y'(x,t)$ as the sum of a time-invariant mean $\overline{Y}(x)$ and a small fluctuating part $Y'(x,t) \ll \overline{Y}(x)$. Then, applying a subsequent separation of scales allows to split Eq. (7) into its mean (zeroth-order perturbation)

$$\overline{\dot{m}}_{\mathrm{s},j}\frac{\partial \overline{s}}{\partial x_j} = \overline{\psi}_{\dot{\omega}_k} + \overline{\psi}_{\mathrm{diff}} \,, \tag{10}$$

and its linearized (first-order perturbation) part

$$\overline{\rho}\left.\frac{\partial s'}{\partial t}\right|_\chi + \overline{\dot{m}}_{\mathrm{s},j}\frac{\partial s'}{\partial x_j} = -\dot{m}'_{\mathrm{s},j}\frac{\partial \overline{s}}{\partial x_j} + \psi'_{\dot{\omega}_k} + \psi'_{\mathrm{diff}}. \tag{11}$$

In Eqs. (10) and (11), the terms $\overline{\dot{m}}_{\mathrm{s},j}\frac{\partial \overline{s}}{\partial x_j}$ and $\dot{m}'_{\mathrm{s},j}\frac{\partial \overline{s}}{\partial x_j}$ represent the projection of the mean and perturbed mass flux densities onto the local mean sensible-plus-chemical entropy gradient and can be reformulated as

$$\overline{\dot{m}}_{\mathrm{s},j}\frac{\partial \overline{s}}{\partial x_j} = \overline{\dot{m}}_{\mathrm{s},\parallel} n_j \frac{\partial \overline{s}}{\partial x_j} \qquad \text{and} \qquad \dot{m}'_{\mathrm{s},j}\frac{\partial \overline{s}}{\partial x_j} = \dot{m}'_{\mathrm{s},\parallel} n_j \frac{\partial \overline{s}}{\partial x_j} \,, \tag{12}$$

with the amplitudes of the mean $\overline{\dot{m}}_{\mathrm{s},\parallel}$ and perturbed $\dot{m}'_{\mathrm{s},\parallel}$ mass flux densities in the direction of the mean sensible-plus-chemical entropy gradient $\partial\overline{s}/\partial x_j$ (see Fig. 2), and the corresponding normal vector

$$n_j = \frac{\frac{\partial \overline{s}}{\partial x_j}}{\left|\frac{\partial \overline{s}}{\partial x_i}\right|}. \tag{13}$$

Then, by taking advantage of the projection property in Eq. (12), the mean sensible-plus-chemical entropy gradient in the linearized entropy balance equation (11) is substituted with the mean entropy balance equation (10), yielding

$$\underbrace{\overline{\rho}\left.\frac{\partial s'}{\partial t}\right|_\chi + \overline{\dot{m}}_{\mathrm{s},j}\frac{\partial s'}{\partial x_j}}_{\text{Transport}} = \overline{\psi}_{\dot{\omega}_k}\left(\frac{\psi'_{\dot{\omega}_k}}{\overline{\psi}_{\dot{\omega}_k}} - \frac{\dot{m}'_{\mathrm{s},\parallel}}{\overline{\dot{m}}_{\mathrm{s},\parallel}}\right) + \overline{\psi}_{\mathrm{diff}}\left(\frac{\psi'_{\mathrm{diff}}}{\overline{\psi}_{\mathrm{diff}}} - \frac{\dot{m}'_{\mathrm{s},\parallel}}{\overline{\dot{m}}_{\mathrm{s},\parallel}}\right)$$

$$= \underbrace{\overline{\dot{m}}_{\mathrm{s},\parallel}\left(\frac{\psi_{\dot{\omega}_k}}{\dot{m}_{\mathrm{s},\parallel}}\right)' + \overline{\dot{m}}_{\mathrm{s},\parallel}\left(\frac{\psi_{\mathrm{diff}}}{\dot{m}_{\mathrm{s},\parallel}}\right)'}_{\text{Generation}} \,, \tag{14}$$

with

$$
\left(\frac{\Psi_{\dot\omega_k}}{\dot m_{\mathrm{s},\parallel}}\right)' = \frac{\overline{\dot q}}{\overline{\dot m}_{\mathrm{s},\parallel}\overline T}\left[\frac{\left(\frac{\dot q}{\dot m_{\mathrm{s},\parallel}}\right)'}{\left(\frac{\dot q}{\dot m_{\mathrm{s},\parallel}}\right)} - \frac{T'}{T}\right]
$$

$$
- \sum_{k=1}^{N}\frac{\overline h_{s,k}}{\overline T}\frac{\overline{\dot\omega}_k}{\overline{\dot m}_{\mathrm{s},\parallel}}\left[\frac{\left(\frac{\dot\omega_k}{\dot m_{\mathrm{s},\parallel}}\right)'}{\left(\frac{\dot\omega_k}{\dot m_{\mathrm{s},\parallel}}\right)} + \left(\frac{\overline c_{\mathrm{p},k}\overline T}{\overline h_{s,k}} - 1\right)\frac{T'}{\overline T}\right] \tag{15}
$$

$$
+ \sum_{k=1}^{N}\overline s_k\frac{\overline{\dot\omega}_k}{\overline{\dot m}_{\mathrm{s},\parallel}}\left[\frac{\left(\frac{\dot\omega_k}{\dot m_{\mathrm{s},\parallel}}\right)'}{\left(\frac{\dot\omega_k}{\dot m_{\mathrm{s},\parallel}}\right)} + \frac{s_k'}{\overline s_k}\right]
$$

and

$$
\left(\frac{\Psi_{\mathrm{diff}}}{\dot m_{\mathrm{s},\parallel}}\right)' = \left(\frac{\tau_{ji}\frac{\partial u_j}{\partial x_i}}{\dot m_{\mathrm{s},\parallel}T}\right)' + \left(\frac{\frac{\partial}{\partial x_j}\left(\lambda\frac{\partial T}{\partial x_j}\right)}{\dot m_{\mathrm{s},\parallel}T}\right)'
$$

$$
+ \left(\frac{\sum_{k=1}^{N} s_k\frac{\partial\rho Y_k V_{k,j}}{\partial x_j}}{\dot m_{\mathrm{s},\parallel}}\right)' - \left(\frac{\sum_{k=1}^{N}\frac{\partial h_k}{\partial x_j}\rho Y_k V_{k,j}}{\dot m_{\mathrm{s},\parallel}T}\right)' . \tag{16}
$$

Eq. (14) is the balance equation for small sensible-plus-chemical entropy perturbations strictly separating terms related to transport (left-hand side (LHS)) and generation (RHS).

The generation terms on the RHS of Eq. (14) show that small-scale entropy perturbations are generated only by disturbances of the local sources $\psi_{\dot\omega_k}/\dot m_{\mathrm{s},\parallel}$ (unit J/(kg m K)) or $\psi_{\mathrm{diff}}/\dot m_{\mathrm{s},\parallel}$ (unit J/(kg m K)). By analyzing the corresponding units, two important contributions can be identified: First, the length-based density[3] (unit 1/m) of the local energy addition per unit mass (unit J/kg). Integration of this quantity along the path of a mass particle moving through an entropy source region gives its total energy change per unit mass. To the local entropy generation, only the mass flux density parallel to the local entropy gradient contributes. The second important effect is the temperature at which the local energy addition per unit mass density takes place (unit J/(kg m)). The local entropy generation decreases with increasing temperature for a constant length-based density of the local energy addition per unit mass. The total entropy generated per unit mass across an entropy source region is then given by the path integral

$$
s_{\mathrm{gen}} = \int_\Gamma \frac{\psi_{\dot\omega_k} + \psi_{\mathrm{diff}}}{\dot m_{\mathrm{s},\parallel}}\, \mathrm{d}x \tag{17}
$$

as shown in Fig. 2.

2.2. Jump condition for entropy disturbance across a moving heat source

This section derives a Q1D jump condition that models the generation of entropy perturbations across a source region. The Q1D jump condition is an explicit analytical solution of the general balance equation (14) of entropy perturbations integrated over a convectively compact control volume enclosing an infinitesimally thin source sheet (see Fig. 3). Diffusive effects are assumed to be negligible ($\psi_{\mathrm{diff}} \approx 0$). The source sheet is a continuous, two-dimensional surface in motion. All state variables Y (e.g. $\dot m_{\mathrm{s}}$, ρ, p, T, s) are modeled via step functions

$$
Y \equiv Y_1 + (Y_2 - Y_1)\mathcal H\left(\mathbf x - \mathbf x_{\mathrm s}(t)\right) , \tag{18}
$$

---

[3] A length-based density of a quantity Y refers to this quantity per unit length. This definition is analogous to area-based densities such as the mass flux density $\dot m_{\mathrm s}$ (mass flux $\dot M_{\mathrm s}$ per unit area) or to volume-based densities such as the mass density ρ (mass per unit volume).
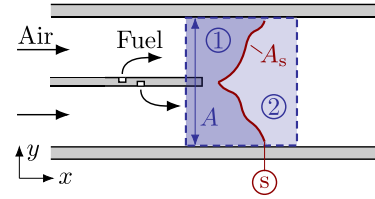

Fig. 3. Spatially fixed control volume V (dark blue, dashed line) enclosing an entropy source region in motion (s, dark red, wrinkled solid line). The flow states in front (1, dark blue) and after (2, light blue) the source region are indicated. The example is based on a generic partially premixed burner. (For interpretation of the references to color in this figure legend, the reader is referred to the web version of this article.)

with the Heaviside function defined as

$$
\mathcal H\left(\mathbf x - \mathbf x_{\mathrm s}(t)\right) \equiv \begin{cases} 0, & \mathbf x < \mathbf x_{\mathrm s}(t) \\ \mathrm{ref}, & \mathbf x = \mathbf x_{\mathrm s}(t) \\ 1, & \mathbf x > \mathbf x_{\mathrm s}(t) \end{cases} . \tag{19}
$$

State variables upstream and downstream of the entropy source region are assumed to be constant and are denoted by $(\cdot)_1$ and $(\cdot)_2$, respectively. $\mathbf x$ is the spatial coordinate and $\mathbf x_{\mathrm s}(t)$ is the time-dependent location of the source region. 'ref' denotes a reference value of the variable in the source region. We refer to Laksana et al. [57] for how to choose this reference value for reactive flows.

The volumetric heat release rate $\dot q$ as well as the volumetric reaction rates $\dot\omega_k$ are modeled as

$$
\dot q \equiv \frac{\dot Q}{A_{\mathrm s}}\delta\left(\mathbf x - \mathbf x_{\mathrm s}(t)\right) \qquad \Rightarrow \qquad \dot Q = \int \dot q\,\mathrm dV
$$
$$
\dot\omega_k \equiv \frac{\dot\Omega_k}{A_{\mathrm s}}\delta\left(\mathbf x - \mathbf x_{\mathrm s}(t)\right) \qquad \Rightarrow \qquad \dot\Omega_k = \int \dot\omega_k\,\mathrm dV \tag{20}
$$

with the integral heat release rate $\dot Q$, the integral reaction rates $\dot\Omega_k$, the delta distribution δ and the surface of the source region $A_{\mathrm s}$ (see Fig. 3).

Integrating over a control volume V as shown in Fig. 3 under the Q1D assumptions and for negligible diffusive effects, Eq. (7) simplifies to

$$
\dot M_{\mathrm s}\left(s_2 - s_1\right) = \Psi_{\dot\omega_k} , \tag{21}
$$

with

$$
\Psi_{\dot\omega_k} = \frac{\dot Q}{T_{\mathrm{ref}}} - \sum_{k=1}^{N}\left(\frac{h_{s,k}}{T}\right)_{\mathrm{ref}}\dot\Omega_k + \sum_{k=1}^{N} s_{k,\mathrm{ref}}\dot\Omega_k , \tag{22}
$$

where $\dot M_{\mathrm s} = \int \dot m_{\mathrm{s},j}\mathrm dA_{\mathrm s}$ is the mass flux across the entropy source region. Analogous to Section 2.1, the introduction of the first-order perturbation ansatz and the subsequent separation of scales yields the Q1D entropy jump condition as

$$
\underbrace{\overline M_{\mathrm s}\left(s_2' - s_1'\right)}_{\text{Transport}} = \underbrace{\overline M_{\mathrm s}\left(\frac{\Psi_{\dot\omega_k}}{\dot M_{\mathrm s}}\right)'}_{\text{Generation}} , \tag{23}
$$

with the source term

$$
\left(\frac{\Psi_{\dot\omega_k}}{\dot M_{\mathrm s}}\right)' = \frac{\overline Q}{\overline M_{\mathrm s}\overline T_{\mathrm{ref}}}\left[\frac{\left(\frac{\dot Q}{\dot M_{\mathrm s}}\right)'}{\left(\frac{\dot Q}{\dot M_{\mathrm s}}\right)} - \frac{T_{\mathrm{ref}}'}{\overline T_{\mathrm{ref}}}\right]
$$

$$
- \sum_{k=1}^{N}\left(\frac{\overline h_{s,k}}{\overline T}\right)_{\mathrm{ref}}\frac{\overline\Omega_k}{\overline M_{\mathrm s}}\left[\frac{\left(\frac{\dot\Omega_k}{\dot M_{\mathrm s}}\right)'}{\left(\frac{\dot\Omega_k}{\dot M_{\mathrm s}}\right)} + \left(\frac{\overline c_{\mathrm p,k}\overline T}{\overline h_{s,k}} - 1\right)_{\mathrm{ref}}\frac{T_{\mathrm{ref}}'}{\overline T_{\mathrm{ref}}}\right] \tag{24}
$$

$$
+ \sum_{k=1}^{N}\overline s_{k,\mathrm{ref}}\frac{\overline\Omega_k}{\overline M_{\mathrm s}}\left[\frac{\left(\frac{\dot\Omega_k}{\dot M_{\mathrm s}}\right)'}{\left(\frac{\dot\Omega_k}{\dot M_{\mathrm s}}\right)} + \frac{s_{k,\mathrm{ref}}'}{\overline s_{k,\mathrm{ref}}}\right] .
$$

An extensive derivation of the Q1D jump condition is given in Section 1 of the supplementary material.

Comparing the reactive entropy source term of the Q1D jump condition in Eq. (24) and the general 3D formulation in Eq. (15), their identical structure is evident. Note that the vectorial mass flux density $\dot{m}_{s,j}$ and the amplitude of the mass flux density parallel $\dot{m}_{s,\parallel}$ to the mean density gradient in Eq. (15) both coincide in the mass flux $\dot{M}_s$ in Eq. (24) due to the quasi-one-dimensional assumption. In analogy to Section 2, the source term of entropy disturbances (Eq. (24)) in the quasi-one-dimensional limit results from an energy addition per unit mass added at a given temperature level. It includes a contribution of the heat addition per unit mass.

For consistency, the derivation of the jump condition (Eq. (23)) in this work is based on the general entropy balance equation derived in Section 2.1. However, this approach requires the explicit definition of a reference state within the source region to approximate integrals such as $\int \dot{q}/T \, \mathrm{d}V$. This difficulty is avoided if the derivation of the entropy disturbance jump condition is based on the energy equation as is usually done in the literature [22,43]. Both derivation approaches are equivalent if the reference temperature is chosen as

$$T_{\text{ref}} = \frac{h_{s,2} - h_{s,1}}{s_2 - s_1} - \frac{1}{2}\frac{u_2^2 - u_1^2}{s_2 - s_1}. \tag{25}$$

Utilizing this reference temperature and introducing constant gas properties, no species fluctuations and an approximation to the first and third order in Mach number into Eq. (23) yields the jump conditions derived by Strobio Chen et al. [22] and Gant et al. [43], respectively. More details are found in Section 2 of the supplementary material.

In the following section, the similarity between the three-dimensional balance equation of entropy disturbances Eq. (14) and the quasi-one-dimensional jump condition Eq. (23) is used to better understand the general source terms.

3. Generation of entropy waves by moving and fixed heat sources

Numerous unsteady physical processes generate entropy waves, and Section 2 presents a unified framework for consistently analyzing the underlying mechanisms responsible for their generation. In this section, the framework is applied to two exemplary cases – a lean premixed flame in convective balance and a heated wire at rest – to understand the dominant mechanisms that generate entropy waves in both cases. The comparison of the two cases highlights the inherent difference in the generation of entropy waves for sources at rest and in motion.

3.1. Heat source in motion - A lean premixed flame

A *lean premixed flame* is an exothermic reaction zone, where fuel reacts with an excess of oxidizer. In analytical descriptions, the reaction mechanism models the reaction kinetics, while the species balance equations express the transport of individual species. The analysis of the dominant entropy generation mechanism in a premixed flame is divided into two parts. The first part investigates the non-diffusive entropy source terms based on the formulation of the Q1D jump condition in Eq. (24) following an order of magnitude analysis. In addition, the non-diffusive generation mechanisms are explained using temperature-entropy diagrams. The second part provides a rule of thumb for the consideration of diffusive terms (see Eq. (16)).

3.1.1. The non-diffusive entropy generation mechanisms of a premixed flame

Assuming complete combustion and infinitely fast reaction, the heat added per unit mass and the mass of species k reacting per unit mass of a lean premixed flame can be written as [22,58,59]

$$\frac{\dot{Q}}{\dot{M}_s} = \Delta h_r \phi \quad \text{and} \quad \frac{\dot{\Omega}_k}{\dot{M}_s} = Y_{2,k} - Y_{1,k} = \Delta Y_k , \tag{26}$$

with the heat of reaction Δh_r and the equivalence ratio ϕ. Then, the linearization of Eq. (26) under the assumption of a constant fuel composition ($\Delta h_r' = 0$) yields

$$\frac{\left(\frac{\dot{Q}}{\dot{M}_s}\right)'}{\left(\frac{\dot{Q}}{\dot{M}_s}\right)} = \frac{\phi'}{\overline{\phi}} \quad \text{and} \quad \frac{\left(\frac{\dot{\Omega}_k}{\dot{M}_s}\right)'}{\left(\frac{\dot{\Omega}_k}{\dot{M}_s}\right)} = \frac{Y_{2,k}' - Y_{1,k}'}{\overline{Y}_{2,k} - \overline{Y}_{1,k}} = \frac{\Delta Y_k'}{\Delta \overline{Y}_k} . \tag{27}$$

Substituting Eq. (27) into Eq. (23) leads to the Q1D balance equation for entropy waves of a lean premixed flame

$$\overline{M}_s\left(s_2' - s_1'\right) = \overline{M}_s\left[\left(\frac{\Psi_{\dot{\omega}_k}}{\dot{M}_s}\right)'_{\mathrm{I}} + \left(\frac{\Psi_{\dot{\omega}_k}}{\dot{M}_s}\right)'_{\mathrm{II}} + \left(\frac{\Psi_{\dot{\omega}_k}}{\dot{M}_s}\right)'_{\mathrm{III}}\right], \tag{28}$$

where the generation of entropy waves by the energy conversion from chemical to internal energy at a specific temperature level T_{ref} is expressed as

$$\left(\frac{\Psi_{\dot{\omega}_k}}{\dot{M}_s}\right)'_{\mathrm{I}} = \frac{\overline{\dot{Q}}}{\overline{\dot{M}}_s \overline{T}_{\text{ref}}}\left(\frac{\phi'}{\overline{\phi}} - \frac{T_{\text{ref}}'}{\overline{T}_{\text{ref}}}\right) . \tag{29}$$

The remaining source terms in Eq. (28) refer to a change in sensible enthalpy due to either a change in composition or due to the temperature dependence of the gas properties

$$\left(\frac{\Psi_{\dot{\omega}_k}}{\dot{M}_s}\right)'_{\mathrm{II}} = -\sum_{k=1}^{N}\left(\frac{\overline{h}_{s,k}}{\overline{T}}\right)_{\text{ref}} \Delta \overline{Y}_k\left[\frac{\Delta Y_k'}{\Delta \overline{Y}_k} + \left(\frac{\overline{c}_{p,k}\overline{T}}{\overline{h}_{s,k}} - 1\right)_{\text{ref}}\frac{T_{\text{ref}}'}{\overline{T}_{\text{ref}}}\right] , \tag{30}$$

and a change in the chemical-plus-sensible entropy once again either due to a change in composition or its dependency on a temperature or pressure change

$$\left(\frac{\Psi_{\dot{\omega}_k}}{\dot{M}_s}\right)'_{\mathrm{III}} = \sum_{k=1}^{N} \overline{s}_{k,\text{ref}} \Delta \overline{Y}_k\left[\frac{\Delta Y_k'}{\Delta \overline{Y}_k} + \frac{s_{k,\text{ref}}'}{\overline{s}_{k,\text{ref}}}\right] , \tag{31}$$

respectively.

The source terms on the RHS of Eq. (28) originate from the interaction of an incoming perturbation with the exothermic reaction zone. In the small perturbation limit, incoming disturbances are considered as a superposition of acoustic (p'), entropic (s'), and compositional (ϕ', Y_k') waves.[4] This decomposition may be introduced into Eqs. (29), (30) and (31) by the substitution of the temperature fluctuations with the linearization of the Gibbs equation (3)

$$\frac{T'}{\overline{T}} = \underbrace{\frac{\gamma - 1}{\gamma}\frac{p'}{\overline{p}}}_{\text{acoustic}} + \underbrace{\frac{s'}{\overline{c}_p}}_{\text{entropic}} - \underbrace{\sum_k \frac{\overline{s}_k}{\overline{c}_p}Y_k'}_{\text{compositional}} , \tag{32}$$

and the linearization of the sensible-plus-chemical entropy of species k

$$s_k' = \underbrace{\left.\frac{\overline{\partial s_k}}{\partial p}\right|_{s,Y_k} p'}_{\text{acoustic}} + \underbrace{\left.\frac{\overline{\partial s_k}}{\partial s}\right|_{p,Y_k} s'}_{\text{entropic}} + \underbrace{\left.\frac{\overline{\partial s_k}}{\partial Y_k}\right|_{p,s,Y_{l\neq k}} Y_k'}_{\text{compositional}} . \tag{33}$$

In Eq. (33), the explicit formulation of the acoustic, entropic, and compositional subcontributions is omitted here for the sake of simplicity. Instead, Fig. 4 shows individual source mechanisms resulting from the incoming compositional (Fig. 4(a)), acoustic (Fig. 4(b)), and entropic (Fig. 4(c)) waves in the low Mach number (M → 0) and zero frequency (f → 0) limit via temperature-entropy (T-s) diagrams. In the limit of these assumptions, all perturbations are spatially independent offsets

---

[4] In the small perturbation limit, only (incoming) acoustic waves affect the pressure fluctuations p'; only (incoming) entropy waves impact the entropy fluctuations s', and solely (incoming) compositional waves affect the mass fraction Y_k' and the equivalence ratio ϕ'. This fact is easily derived from a characteristic decomposition of the 1D reactive Euler equations.
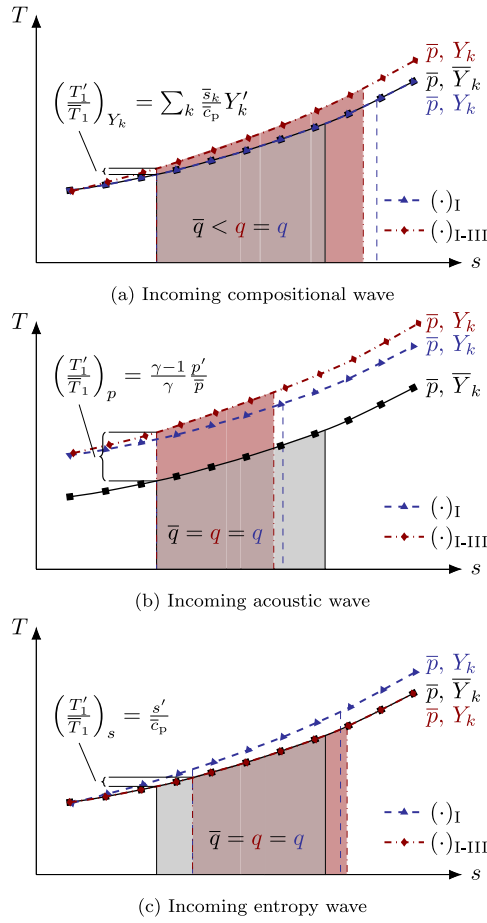
Fig. 4. Temperature-entropy (T-s) diagrams of an exothermic reaction zone in the low Mach number and zero frequency limit visualizing the entropy wave generation mechanisms $(\Psi_{\dot{\omega}_k}/\dot{M}_s)'$ and $(\Psi_{\dot{\omega}_k}/\dot{M}_s)'_I$ for (a) an incoming compositional wave Y'_k ($\phi' > 0$), (b) an incoming acoustic perturbation $p'_I > 0$, (c) an incoming entropy wave $s'_I > 0$. The black (solid), dark blue (dashed) and dark red (dash-dotted) lines correspond to the unperturbed mean state, the perturbed case considering solely $(\Psi_{\dot{\omega}_k}/\dot{M}_s)'_I$ and the perturbed case considering the full source term $(\Psi_{\dot{\omega}_k}/\dot{M}_s)'$.

($f \to 0$) and the combustion process is isobaric [56] (M $\to$ 0). In this case, the *mass-specific* heat released by the reaction,

$$q = \frac{\dot{Q}}{\dot{M}_s} = \int T\,\mathrm{d}s \, , \tag{34}$$

is equivalent to the area under the isobaric lines in the T-s diagram. In Fig. 4, each sub-figure shows the mean process in black (solid line) and the perturbed process in dark red (dash-dotted line). To visualize the individual effects of the entropy wave sources (Eqs. (29), (30) and (31)) and since neglecting the sources $(\Psi_{\dot{\omega}_k}/\dot{M}_s)'_{II} + (\Psi_{\dot{\omega}_k}/\dot{M}_s)'_{III}$ is a common assumption in the literature [6,8,28], the additional process shown in dark red (dashed line) considers solely the effect of the heat release source term $(\Psi_{\dot{\omega}_k}/\dot{M}_s)'_I$.

Fig. 4(a) shows the effect of an incoming compositional wave $Y'_{k,1}$ in the form of an equivalence ratio perturbation $\phi'_I > 0$ ($p'_I = 0$, $s'_I = 0$) of a lean premixed flame. In this case, the incoming perturbation shifts the gas mixture closer to the stoichiometric condition. Consequently, it increases the mass-specific heat release $q > \overline{q}$ (see Eq. (26)) by the chemical reaction. This effect corresponds to the entropy source term

$(\Psi_{\dot{\omega}_k}/\dot{M}_s)'_I$ (see Eq. (29)) and is shown by the increased area enclosed by the dark blue dashed lines in Fig. 4a. The effect of the sources $(\Psi_{\dot{\omega}_k}/\dot{M}_s)'_{II} + (\Psi_{\dot{\omega}_k}/\dot{M}_s)'_{III}$ is a modulation of the shape of the isobaric curve in the T-s diagram. The modulation results from the change in local gas composition and the corresponding perturbations in gas properties and entropy sensitivities (see Eqs. (30) and (31)). Overall, incoming equivalence ratio fluctuations generate entropy waves in phase.

In Fig. 4(b), an incoming acoustic perturbation $p'_I > 0$ ($s'_I = 0$, $\phi' = 0$, $Y'_k = 0$) shifts the incoming pressure to a higher isobaric line and therefore to higher temperatures, while the mass-specific heat remains unchanged ($q' = 0$, $q = \overline{q}$). Thus, an acoustic wave generates entropy waves solely by changing T_{ref} (and $s_{k,\mathrm{ref}}$). The generated entropy wave is π out of phase with the acoustic wave. The contribution of the entropy source $(\Psi_{\dot{\omega}_k}/\dot{M}_s)'_I$ in this mechanism can be formulated as a shift to another isobaric line, assuming unchanged specific heat $c_{p,k}$ and entropy s_k compared to the mean state. The sources $(\Psi_{\dot{\omega}_k}/\dot{M}_s)'_{II} + (\Psi_{\dot{\omega}_k}/\dot{M}_s)'_{III}$ again modulate the new isobaric line by incorporating the temperature (and pressure) dependence of $c_{p,k}$ and s_k.

In Fig. 4(c), an incoming entropy wave $s'_I > 0$ ($p'_I = 0$, $\phi' = 0$, $Y'_k = 0$) at constant pressure shifts the mass-specific heat release to higher entropy levels and thus to higher temperatures. In contrast, the mass-specific heat release $q = \overline{q}$ remains constant. Similar to an acoustic wave, an incoming entropy wave generates additional entropy waves simply by changing T_{ref} (and $s_{k,\mathrm{ref}}$). The generated entropy wave is in antiphase with the incoming wave. Destructive interference typically weakens the resulting entropy wave. In addition to the shift to higher entropy levels, the effect of the source $(\Psi_{\dot{\omega}_k}/\dot{M}_s)'_I$ leads to a modulation of the isobaric line due to the neglect of changes in specific heat $c_{p,k}$ and entropy s_k relative to the mean state. Considering the full source term $(\dot{\omega}_k/\dot{M}_s)'$, the modulation of the isobaric line of $(\dot{\omega}_k/\dot{M}_s)'_I$ is compensated by $(\Psi_{\dot{\omega}_k}/\dot{M}_s)'_{II} + (\Psi_{\dot{\omega}_k}/\dot{M}_s)'_{III}$ and the isobaric line remains unchanged.

The understanding of the entropy wave generation mechanisms for the Q1D description in the low Mach number and zero frequency limit gained from Fig. 4 can be extrapolated to higher Mach numbers, higher frequencies as well as to the full three-dimensional description (Section 2.1). At higher frequencies, the integral generation of entropy waves across the flame front exhibits a low-pass filter behavior [23], resulting from the partial cancellation effects across the flame front. The shape of this low-pass filter determines the frequency at which the acoustic/convective compactness assumption and the Q1D jump condition are no longer valid. At higher Mach numbers, the isentropic acceleration of the gas across the flame front becomes significant. Since the acceleration is isentropic, it does not directly affect the generation of entropy waves. However, a distributed flame can modulate the acoustic source mechanism by altering local pressure values. Expanding the interpretation of sub-mechanisms for the non-diffusive three-dimensional flow requires considering the analysis depicted in Fig. 4 as a local analysis, where the reference values $(\cdot)_{\mathrm{ref}}$ only pertain to local quantities.

After gaining a qualitative understanding of the individual source mechanisms from Fig. 4, the following paragraph focuses on an order of magnitude analysis. This analysis aims to quantify the importance of the compositional, acoustic, or entropic source contributions. To simplify the analysis, and since in premixed flames, the source term $(\Psi_{\dot{\omega}_k}/\dot{M}_s)'_I$ is generally the main contributor to entropy wave generation [28,60], this is the only term considered in the following analysis. However, the derived results are assumed to be reasonable estimates even for cases where the source terms $(\Psi_{\dot{\omega}_k}/\dot{M}_s)'_{II} + (\Psi_{\dot{\omega}_k}/\dot{M}_s)'_{III}$ are more prominent, since previous analysis showed that the source $(\Psi_{\dot{\omega}_k}/\dot{M}_s)'_{II} + (\Psi_{\dot{\omega}_k}/\dot{M}_s)'_{III}$ may be of the same order of magnitude as $(\Psi_{\dot{\omega}_k}/\dot{M}_s)'_I$, but is generally not the dominant contributor [28].

First, the relative order of magnitude of the different perturbations must be clarified. This study employs the normalized velocity perturbation $u_1'/\bar{u}_1$ in front of the reaction zone as a standard reference for other perturbations. All remaining perturbations are related to this quantity as follows:

1. Equivalence ratio perturbations are typically generated by a velocity perturbation at the fuel injector. The corresponding normalized equivalence ratio perturbation is of the same order of magnitude as the velocity perturbation [61–63]

$$\mathcal{O}\left(\frac{\phi'}{\bar{\phi}}\right) \approx \mathcal{O}\left(\frac{u_1'}{\bar{u}_1}\right). \tag{35}$$

2. Perturbations in the incoming normalized equivalence ratio $\phi'/\bar{\phi}$ can be expressed by perturbations in the incoming species mass fraction $Y_{k,1}'/\bar{Y}_{k,1}$ with a similar order of magnitude. In addition, the order of magnitude of $Y_k'/\bar{Y}_k$ can be assumed constant throughout the exothermic reaction zone due to the chosen normalization:

$$\mathcal{O}\left(\frac{Y_{k,1}'}{\bar{Y}_{k,1}}\right) \approx \mathcal{O}\left(\frac{Y_{k,\text{ref}}'}{\bar{Y}_{k,\text{ref}}}\right) \approx \mathcal{O}\left(\frac{\phi'}{\bar{\phi}}\right) \approx \mathcal{O}\left(\frac{u_1'}{\bar{u}_1}\right). \tag{36}$$

3. In the absence of acoustic sources, the acoustic characteristic variables

$$\Pi^{\pm} = \frac{1}{2}\left(\frac{p'}{\bar{p}} \pm \gamma \text{M}_1 \frac{u'}{\bar{u}}\right), \tag{37}$$

remain constant. At the inlet, the normalized pressure perturbation relates to the normalized velocity disturbance via the Mach number M. Furthermore, the order of magnitude of the normalized pressure fluctuations remains constant throughout the reaction zone for low to moderate Mach numbers [22,43]:

$$\mathcal{O}\left(\frac{p_1'}{\bar{p}_1}\right) \approx \mathcal{O}\left(\frac{p_{\text{ref}}'}{\bar{p}_{\text{ref}}}\right) \approx \mathcal{O}\left(\text{M}\frac{u_1'}{\bar{u}_1}\right). \tag{38}$$

4. The entropy perturbations at the reference point are generated either by incoming compositional, acoustic or entropic waves (see Fig. 4):

$$\left(\frac{s'}{\bar{c}_p}\right)_{\text{ref}} = \underbrace{\left(\frac{s'}{\bar{c}_p}\right)_{\text{ref},Y_k}}_{\text{compositional}} + \underbrace{\left(\frac{s'}{\bar{c}_p}\right)_{\text{ref},p}}_{\text{acoustic}} + \underbrace{\left(\frac{s'}{\bar{c}_p}\right)_{\text{ref},s}}_{\text{entropic}}. \tag{39}$$

Assuming that incoming acoustic, entropic, and compositional waves continuously generate entropy waves, it can be inferred that the entropy fluctuation at the reference point and behind the flame follow the same functional dependence. In the low Mach number limit, the order of magnitude of the sources in Eq. (39) are known, deriving from the Q1D jump condition proposed by Strobio Chen et al. [22, Eq. (42)]:

$$\mathcal{O}\left(\left(\frac{s'}{\bar{c}_p}\right)_{\text{ref},Y_k}\right) \lessapprox \mathcal{O}\left(\frac{\phi'}{\bar{\phi}}\right) = \mathcal{O}\left(\frac{u_1'}{\bar{u}_1}\right),$$

$$\mathcal{O}\left(\left(\frac{s'}{\bar{c}_p}\right)_{\text{ref},p}\right) \lessapprox \mathcal{O}\left(\frac{p_1'}{\bar{p}_1}\right) = \mathcal{O}\left(\text{M}_1\frac{u_1'}{\bar{u}_1}\right), \tag{40}$$

$$\mathcal{O}\left(\left(\frac{s'}{\bar{c}_p}\right)_{\text{ref},s}\right) = \mathcal{O}\left(\frac{s_1'}{\bar{c}_p}\right).$$

The Q1D jump condition for the generation of entropy waves is given in Eq. (28). Considering only the heat release source mechanism, the generation of entropy waves normalized with $\zeta = \bar{Q}/(\bar{\dot{M}}_s \bar{T}_{\text{ref}})$ reads

$$\frac{s_2'}{\zeta} - \frac{s_1'}{\zeta} = \frac{\phi'}{\bar{\phi}} + \left(\sum_k \frac{\bar{s}_k \bar{Y}_k}{\bar{c}_p}\frac{Y_k'}{\bar{Y}_k}\right)_{\text{ref}} - \left(\frac{\bar{\gamma}-1}{\bar{\gamma}}\frac{p'}{\bar{p}}\right)_{\text{ref}} - \left(\frac{s'}{\bar{c}_p}\right)_{\text{ref}}. \tag{41}$$

If present, the non-diffusive generation of entropy waves is dominated by fluctuations in incoming equivalence ratio

$$\mathcal{O}\left(\frac{\phi'}{\bar{\phi}} + \left(\frac{s'}{\bar{c}_p}\right)_{\text{ref},Y_k}\right) = \mathcal{O}\left(\frac{u_1'}{\bar{u}_1}\right). \tag{42}$$

Compositional temperature fluctuations at the reference point,

$$\mathcal{O}\left(\left(\frac{T'}{\bar{T}}\right)_{\text{ref},Y_k}\right) = \mathcal{O}\left(-\sum_k \left(\frac{\bar{s}_k \bar{Y}_k}{\bar{c}_p}\right)_{\text{ref}} \frac{Y_{k,1}'}{\bar{Y}_{k,1}}\right) \lessgtr \mathcal{O}\left(10^{-1}\frac{\phi'}{\bar{\phi}}\right), \tag{43}$$

are typically at least an order of magnitude smaller than the effect of the equivalence ratio perturbation, as shown by Patki et al. [28]. This is true even though $\mathcal{O}\left(Y_k'/\bar{Y}_k\right) \approx \mathcal{O}\left(\phi'/\bar{\phi}\right)$ and results from a partial cancellation of the summands due to different signs of the species mass fraction fluctuations $Y_k'/\bar{Y}_k$ for different species.

The contribution of incoming acoustic waves to the generation of entropy waves

$$\mathcal{O}\left(-\frac{\bar{\gamma}-1}{\bar{\gamma}}\frac{p'}{\bar{p}} - \left(\frac{s'}{\bar{c}_p}\right)_{\text{ref},p}\right) \approx \mathcal{O}\left(-\text{M}_1\frac{u_1'}{\bar{u}_1}\right) \tag{44}$$

increases proportionally with the equivalence ratio and the Mach number M_1 upstream of the flame. As the Mach number approaches zero, this term vanishes. For $\text{M} \to 1$, the acoustic contribution equals the importance of equivalence ratio perturbations.

Incoming entropy waves generate entropy waves of the same order of magnitude

$$\mathcal{O}\left(-\left(\frac{s'}{\bar{c}_p}\right)_{\text{ref},s}\right) = \mathcal{O}\left(\frac{s_1'}{\bar{c}_{p,1}}\right). \tag{45}$$

However, the generated entropy waves are out of phase by π (see Fig. 4), resulting in destructive interference across the flame front. Typically, the amplitude of the incoming entropy wave is reduced across the flame front.

3.1.2. The diffusive entropy generation mechanisms of a premixed flame

Diffusion effects are essential to most flames. Species diffusion is necessary for mixing fuel and oxidizer in diffusion flames [64] and is responsible for local equivalence ratio fluctuations in hydrogen fuel blends [29]. Thermal diffusion is essential for stabilizing and anchoring many flames, while viscous heating gains significance in high-speed flows due to strong velocity gradients. Due to the dissipative nature of all diffusion effects, they contribute to the generation of entropy (see Eq. (9)) and their perturbations — to the generation of entropy waves (see Eq. (16)). However, an order of magnitude analysis as performed for the non-diffusive mechanisms in Section 3.1.1 to estimate their relative importance for the generation of entropy waves is not straightforward. As a conservative rule of thumb, the contribution of the diffusive mechanisms to the local generation of entropy disturbances should be considered non-negligible in regions with leading order contributions of the diffusive mechanisms to the generation of entropy in the mean flow.

3.2. Heat source at rest - A heated wire gauze

In this section, a *heated wire gauze* in a flow field, as applied in a typical Rijke tube [65], is used as an example for the generation of entropy waves in a heat source at rest ($u_s = 0$). In this case, incoming flow field perturbations affect the heat transfer between the flow and the heated wire grid, leading to entropy wave generation. This mechanism is analyzed in more detail using the Q1D jump condition

(Section 2.2). Therefore, the heat flux between the wire gauze and the flow is modeled by Newton's law

$$\dot{Q} = \alpha A_s \Delta T,\tag{46}$$

with the heat transfer coefficient α, the surface area of the heated wire A_s and the temperature difference between the fluid and the wire surface ΔT. For a given geometry and fluid, the heat transfer coefficient

$$\alpha(\dot{M}_s, T_{\text{ref}})\tag{47}$$

depends only on the mass flux $\dot{M}_s$ and a reference temperature T_{ref} for the temperature-dependent fluid properties. The exact functional form of Eq. (47) is typically given via correlations. Then, the mass-specific heat flux is given by

$$\frac{\dot{Q}}{\dot{M}_s} = \frac{\alpha(\dot{M}_s, T_{\text{ref}})A_s \Delta T}{\dot{M}_s} \, ,\tag{48}$$

and the corresponding linearization

$$\left(\frac{\dot{Q}}{\dot{M}_s} \right)' \Big/ \left(\frac{\dot{Q}}{\dot{M}_s} \right) = \left(\frac{\frac{\partial \alpha}{\partial \dot{M}_s}\big|_{\overline{T}_{\text{ref}}}}{\overline{\alpha}} - 1 \right) \frac{\dot{M}_s'}{\overline{\dot{M}}_s} + \frac{\frac{\partial \alpha}{\partial T_{\text{ref}}}\big|_{\overline{\dot{M}}_s}}{\overline{\alpha}} \left(\frac{T'}{T} \right)_{\text{ref}} + \frac{\Delta T'}{\overline{\Delta T}}\tag{49}$$

with

$$\frac{\dot{M}_s'}{\overline{\dot{M}}_s} = \frac{u_1'}{\overline{u}_1} + \frac{1}{\gamma_1}\frac{p_1'}{\overline{p}_1} - \frac{s_1'}{\overline{c}_{p,1}}.\tag{50}$$

The index $(\cdot)_1$ denotes the inflow condition. Then, the generation of entropy waves is given by

$$\overline{\dot{M}}_s \left(s_2' - s_1' \right) = \frac{\overline{\dot{Q}}}{\overline{T}_{\text{ref}}} \left[\varsigma \frac{\dot{M}_s'}{\overline{\dot{M}}_s} + \left(\frac{\frac{\partial \alpha}{\partial T_{\text{ref}}}\big|_{\overline{\dot{M}}_s}}{\overline{\alpha}} - 1 \right) \left(\frac{T'}{T} \right)_{\text{ref}} + \frac{\Delta T'}{\overline{\Delta T}} \right]\tag{51}$$

with the prefactor of the perturbed mass flux

$$\varsigma = \left(\frac{\frac{\partial \alpha}{\partial \dot{M}_s}\big|_{\overline{T}_{\text{ref}}}}{\overline{\alpha}} - 1 \right) \neq 0.\tag{52}$$

Since the prefactor ς does not vanish, the interaction of incoming velocity perturbations with the heated wire gauze generates entropy waves due to a perturbation of the convective heat transfer. This is in contrast to the lean premixed flame in Section 3.1, which is insensitive to velocity perturbations.

A similar effect of a non-vanishing prefactor ς of the perturbed mass flux appears when the flame in Section 3.1 is assumed to be at rest. However, although this assumption is often made in the literature [36,38–40], the corresponding velocity sensitivity of the entropy wave generation is spurious [22].

4. Conclusion

This study provides an analytical framework for the consistent analysis of moving sources of entropy disturbances for general three-dimensional reactive flows and in the limit of a quasi-one-dimensional jump condition. The source terms of entropy perturbations are strictly separated from transport mechanisms by an Arbitrary Lagrangian–Eulerian framework that moves with the source itself.

The unified framework for the analysis of entropy perturbations derived in this study provides a deep insight into the underlying physical processes. As an example, the analytical framework is applied to a lean premixed flame (entropy source in kinematic balance with the flow) and a heated wire gauze (entropy source at rest). For the lean premixed flame, temperature-entropy diagrams and an

order of magnitude analysis are used to explain the different non-diffusive mechanisms of entropy wave generation and quantify their relative importance. In addition, and in agreement with earlier studies in quasi-one-dimensional frameworks, this analysis reaffirms the dominant contribution of equivalence ratio perturbations to the generation of entropy disturbances [13,22,25,48]. Furthermore, it highlights the heat release per unit mass as the key quantity for entropy wave generation in premixed flames. A comparison between the premixed flame and a heated wire gauze shows the fundamentally different mechanisms of entropy wave generation of sources in motion and at rest. In agreement with Strobio Chen et al. [22] and Meindl et al. [27], this reemphasizes the fact that premixed flames cannot be modeled via heat sources at rest.

The necessity of the Arbitrary Lagrangian–Eulerian framework for a clear separation between transport and generation effects has direct implications for the source analysis in numerical simulations. The derived analytical framework can be understood as a first step towards correcting the numerical analysis of entropy wave generation mechanisms.

CRediT authorship contribution statement

Moritz Merk: Conducted research, Wrote paper. **Alexander J. Eder:** Conducted research, Wrote paper. **Wolfgang Polifke:** Supervised research, Wrote paper.

Declaration of competing interest

The authors declare that they have no known competing financial interests or personal relationships that could have appeared to influence the work reported in this paper.

Data availability

No data and code used in the present work.

Acknowledgments

Appendix A. Supplementary data

Supplementary material related to this article can be found online at https://doi.org/10.1016/j.combustflame.2024.113334.

References

[1] B.T. Chu, L.S.G. Kovasznay, Non-linear interactions in a viscous heat-conducting compressible gas, J. Fluid Mech. 3 (1957) 495–514.

[2] J.E. Ffowcs Williams, M.S. Howe, The generation of sound by density inhomogeneities in low Mach number nozzle flows, J. Fluid Mech. 70 (1975) 605–622.

[3] N.A. Cumpsty, F.E. Marble, The interaction of entropy fluctuations with turbine blade rows; A mechanism of turbojet engine noise, Proc. R. Soc. A: Math. 357 (1977) 323–344.

[4] F.E. Marble, S.M. Candel, Acoustic disturbance from gas non-uniformities convected through a nozzle, J. Sound Vib. 55 (1977) 225–243.

[5] J.J. Keller, Production and propagation of sound in a duct, J. Acoust. Soc. Am. 65 (1979) 25–31.

[6] A.P. Dowling, Y. Mahmoudi, Combustion noise, Proc. Combust. Inst. 35 (2015) 65–100.

[7] I. Duran, S. Moreau, F. Nicoud, T. Livebardon, E. Bouty, T. Poinsot, Combustion noise in modern aero-engines, AerospaceLab 7 (2014) 1–11.

[8] A.S. Morgans, I. Duran, Entropy noise: A review of theory, progress and challenges, Int. J. Spray Combust. Dyn. 8 (4) (2016) 285–298.

9

[9] G.E. Abouseif, J.A. Keklak, T.Y. Toong, Ramjet rumble: The low-frequency instability mechanism in coaxial dump combustors, Combust. Sci. Technol. 36 (1984) 83–108.

[10] J. Eckstein, E. Freitag, C. Hirsch, T. Sattelmayer, Experimental study on the role of entropy waves in low-frequency oscillations in a RQL combustor, J. Eng. Gas Turbines Power 128 (2006) 264–270.

[11] Z. Yao, Y. Gao, M. Zhu, A.P. Dowling, K.N.C. Bray, Combustion rumble prediction with integrated computational-fluid-dynamics/low-order-model methods, J. Propuls. Power 28 (2012) 1015–1025.

[12] M.A. Macquisten, A.P. Dowling, Low-frequency combustion oscillations in a model afterburner, Combust. Flame 94 (1993) 253–264.

[13] W. Polifke, C.O. Paschereit, K. Döbbeling, Constructive and destructive interference of acoustic and entropy waves in a premixed combustor with a choked exit, Int. J. Acoust. Vib. 6 (2001) 135–146.

[14] F. Nicoud, T. Poinsot, Thermoacoustic instabilities: Should the Rayleigh criterion be extended to include entropy changes? Combust. Flame 142 (2005) 153–159.

[15] C.S. Goh, A.S. Morgans, The influence of entropy waves on the thermoacoustic stability of a model combustor, Combust. Sci. Technol. 185 (2013) 249–268.

[16] E. Motheau, F. Nicoud, T. Poinsot, Mixed acoustic-entropy combustion instabilities in gas turbines, J. Fluid Mech. 749 (2014) 542–576.

[17] J.J. Keller, W. Egli, J. Hellat, Thermally induced low-frequency oscillations, Z. Angew. Math. Phys. 36 (1985) 250–274.

[18] J.J. Keller, Thermoacoustic oscillations in combustion chambers of gas turbines, AIAA J. 33 (1995) 2280–2287.

[19] T. Lieuwen, Modeling premixed combustion - acoustic wave interactions: A review, J. Propuls. Power 19 (2003) 765–781.

[20] T. Poinsot, Prediction and control of combustion instabilities in real engines, Proc. Combust. Inst. 36 (2017) 1–28.

[21] K. Nishida, T. Takagi, S. Kinoshita, Analysis of entropy generation and exergy loss during combustion, Proc. Combust. Inst. 29 (2002) 869–874.

[22] L. Strobio Chen, S. Bomberg, W. Polifke, Propagation and generation of acoustic and entropy waves across a moving flame front, Combust. Flame 166 (2016) 170–180.

[23] M. Yoon, The entropy wave generation in a heated one-dimensional duct, J. Fluid Mech. 883 (2020) A44.

[24] J. Nan, J. Li, A.S. Morgans, L. Qin, L. Yang, Theoretical analysis of sound propagation and entropy generation across a distributed steady heat source, J. Sound Vib. 536 (2022) 117170.

[25] T. Steinbacher, M. Meindl, W. Polifke, Modeling the generation of temperature inhomogeneities by a premixed flame, Int. J. Spray Combust. Dyn. 10 (2018) 111–130.

[26] B. Semlitsch, T. Hynes, I. Langella, N. Swaminathan, A.P. Dowling, Entropy and vorticity wave generation in realistic gas turbine combustors, J. Propuls. Power 35 (2019) 839–849.

[27] M. Meindl, C.F. Silva, W. Polifke, On the spurious entropy generation encountered in hybrid linear thermoacoustic models, Combust. Flame 223 (2021) 525–540.

[28] P. Patki, V. Acharya, T. Lieuwen, Entropy generation mechanisms from exothermic chemical reactions in laminar, premixed flames, Proc. Combust. Inst. 39 (2022) 1607–1614.

[29] A.J. Eder, B. Dharmaputra, M. Désor, C.F. Silva, A.M. Garcia, B. Schuermans, N. Noiray, W. Polifke, Generation of entropy waves by fully premixed flames in a non-adiabatic combustor with hydrogen enrichment, J. Eng. Gas Turbines Power 145 (2023) 111001.

[30] A. Giusti, N.A. Worth, E. Mastorakos, A.P. Dowling, Experimental and numerical investigation on the propagation of entropy waves, AIAA J. 55 (2017) 446–458.

[31] D. Wassmer, B. Schuermans, C. Paschereit, J.P. Moeck, Measurement and modeling of the generation and the transport of entropy waves in a model gas turbine combustor, Int. J. Spray Combust. Dyn. 9 (2017) 299–309.

[32] M. Weilenmann, U. Doll, R. Bombach, A. Blondé, D. Ebi, Y. Xiong, N. Noiray, Linear and nonlinear entropy-wave response of technically-premixed jet-flames-array and swirled flame to acoustic forcing, Proc. Combust. Inst. 38 (2021) 6135–6143.

[33] B. Dharmaputra, S. Shcherbanev, A. Blondé, B. Schuermans, N. Noiray, Entropy transfer function measurement with tunable diode laser absorption spectroscopy, Proc. Combust. Inst. 39 (2022) 4621–4630.

[34] F. Bake, C. Richter, B. Mühlbauer, N. Kings, I. Röhle, F. Thiele, B. Noll, The entropy wave generator (EWG): A reference case on entropy noise, J. Sound Vib. 326 (2009) 574–598.

[35] F. De Domenico, E.O. Rolland, J. Rodrigues, L. Magri, S. Hochgreb, Compositional and entropy indirect noise generated in subsonic non-isentropic nozzles, J. Fluid Mech. 910 (2021) A5.

[36] G. Wang, X. Liu, S. Wang, L. Li, F. Qi, Experimental investigation of entropy waves generated from acoustically excited premixed swirling flame, Combust. Flame 204 (2019) 85–102.

[37] A.P. Dowling, The calculation of thermoacoustic oscillation, J. Sound Vib. 180 (1995) 557–581.

[38] A.P. Dowling, S.R. Stow, Acoustic analysis of gas turbine combustors, J. Propul. Power 19 (2003) 751–764.

[39] P.A. Hield, M.J. Brear, S.H. Jin, Thermoacoustic limit cycles in a premixed laboratory combustor with open and choked exits, Combust. Flame 156 (2009) 1683–1697.

[40] M. Leyko, F. Nicoud, T. Poinsot, Comparison of direct and indirect combustion noise mechanisms in a model combustor, AIAA J. 47 (2009) 2709–2716.

[41] Y. Méry, Dynamical response of a perfectly premixed flame and limit behavior for high power density systems, Combust. Flame 192 (2018) 410–425.

[42] Y. Chen, L.J. Ayton, D. Zhao, Modelling of intrinsic thermoacoustic instability of premixed flame in combustors with changes in cross section, Combust. Sci. Technol. 192 (2019) 832–851.

[43] F. Gant, A. Cuquel, M.R. Bothien, Autoignition flame transfer matrix: Analytical model versus large eddy simulations, Int. J. Spray Combust. Dyn. 14 (2022) 72–81.

[44] Y. Song, X. Liu, J. Li, L. Yang, Effect of the flame motion on azimuthal combustion instabilities, Aerosp. Sci. Technol. 130 (2022) 107930.

[45] Y. Song, J. Li, L. Yang, Effect of flame motion on longitudinal combustion instabilities, Aerosp. Sci. Technol. 122 (2022) 107427.

[46] H.S. Gopalakrishnan, A. Gruber, J.P. Moeck, Computation and prediction of intrinsic thermoacoustic oscillations associated with autoignition fronts, Combust. Flame 254 (2023) 112844.

[47] A. Fattahi, N. Karimi, N. Hajialigol, Dynamics of entropy wave generation in a simplified model of gas turbine combustor: A theoretical investigation, Phys. Fluids 32 (2020) 106107.

[48] T. Sattelmayer, Influence of the combustor aerodynamics on combustion instabilities from equivalence ratio fluctuations, J. Eng. Gas Turbines Power 125 (2003) 11–19.

[49] B. Schuermans, Modeling and Control of Thermoacoustic Instabilities (Ph.D. thesis), École Polytechnique Fédérale de Lausanne, Lausanne, Switzerland, 2003.

[50] J. Donéa, A. Huerta, Finite Element Methods for Flow Problems, Wiley, Hoboken, NJ, USA, 2003.

[51] G. Heilmann, T. Liu, P. Romero Vega, T. Sattelmayer, A novel decomposition approach preventing spurious entropy generation in hybrid thermoacoustic stability computations, J. Eng. Gas Turbines Power 144 (2022) 091013.

[52] L. Magri, On indirect noise in multicomponent nozzle flows, J. Fluid Mech. 828 (2017) R2.

[53] L. Magri, J. O'Brien, M. Ihme, Effects of nozzle Helmholtz number on indirect combustion noise by compositional perturbations, J. Eng. Gas Turbines Power 140 (2018) 031501.

[54] E.O. Rolland, Sound Produced by Entropic and Compositional Inhomogeneities (Ph.D. thesis), University of Cambridge, Cambridge, UK, 2018.

[55] T.C. Lieuwen, Unsteady Combustor Physics, Cambridge University Press, New York, NY, USA, 2021.

[56] T. Poinsot, D. Veynante, Theoretical and Numerical Combustion, Edwards, Philadelphia, PA, USA, 2005.

[57] A. Laksana, P. Patki, T. John, V. Acharya, T. Lieuwen, Distributed heat release effects on entropy generation by premixed, laminar flames, Int. J. Spray Combust. Dyn. 15 (2023) 139–146.

[58] B. Schuermans, V. Bellucci, F. Guethe, F. Meili, P. Flohr, O. Paschereit, A Detailed Analysis of Thermoacoustic Interaction Mechanisms in a Turbulent Premixed Flame, ASME Turbo Expo 2004, 2004.

[59] T. Schuller, T. Poinsot, S. Candel, Dynamics and control of premixed combustion systems based on flame transfer and describing functions, J. Fluid Mech. 894 (2020) P1.

[60] J.M. Truffaut, G. Searby, L. Boyer, Sound emission by non-isomolar combustion at low Mach numbers, Combust. Theory Model. 2 (1998) 423–428.

[61] W. Polifke, C.J. Lawn, On the low-frequency limit of flame transfer functions, Combust. Flame 151 (2007) 437–451.

[62] A. Huber, W. Polifke, Dynamics of practical premix flames, part I: Model structure and identification, Int. J. Spray Combust. Dyn. 1 (2009) 199–228.

[63] H. Schwarz, L. Zimmer, D. Durox, S. Candel, Detailed measurements of equivalence ratio modulations in premixed flames using laser Rayleigh scattering and absorption spectroscopy, Exp. Fluids 49 (2010) 809–821.

[64] N. Peters, Turbulent Combustion, Cambridge University Press, Cambridge, UK, 2000.

[65] P.L. Rijke, Notiz über eine neue Art, die in einer an beiden Enden offenen Röhre enthaltene Luft in Schwingungen zu versetzen, Ann. Physics 183 (1859) 339–343.

10